

**Development and Evaluation of a Dose Monitoring System
for Modern Radiotherapy**

Von der Fakultät für Medizin und Gesundheitswissenschaften
der Carl von Ossietzky Universität Oldenburg
zur Erlangung des Grades und des Titels einer

Doktorin der Naturwissenschaften Dr. rer. nat

angenommene Dissertation

von

Frau Frauke Eenboom

geboren am 17.09.1981 in Eutin (Plön)

1. Gutachter: Prof. Dr. Björn Poppe

2. Gutachter: Prof. Dr. Dietmar Georg

Tag der Disputation: 8. Juli 2015

Abstract

In medical linear accelerators the dose monitoring system controls the applied dose and the symmetry and flatness of the applied beam to the patient. It consists of a monitoring device, which is in most cases an ionisation chamber, and control loop electronics which evaluate the signal from the monitoring device and stops irradiation in case of malfunction. Therefore the dose monitoring system is the most important safety mechanism in a medical linear accelerator.

The aim of this work was to develop a new dose monitoring system for medical linear accelerators which gains more information on the beam besides the required parameters applied dose, symmetry and flatness.

To analyse the drawbacks and capabilities of a typical dose monitoring system used nowadays and to gain information on the ambient radiation field in the linear accelerator head, simulations and measurements with the two dose monitor chambers used by Siemens were done. Based on these results and on requirements from prospective linear accelerators a new dose monitor chamber was designed.

First of all, a new beam sensing principle was introduced which senses the beam in two directions by parallel wires or strip electrodes instead of radially segmented electrodes. This sensing principle allows a reconstruction of the beam profile and not only comparison of the left and right side of the beam profile, as done nowadays. By knowing the profile of the beam, errors in beam generation can be analysed more exactly and countermeasures could be taken during beam generation. Moreover a better knowledge of the beam profile would allow to reduce the acceptable error margins in beam profile and thus lead to a more precise agreement between planned and applied dose distribution.

The geometric dimensions as well as the channel and wire distance were determined theoretically by modelling the response of such an ionisation chamber to typical radiation beams of different beam qualities. A single dose monitor chamber for monitoring photon and electron beams was designed.

Moreover a pre-selection on suitable filling media was done, based on required signal level and ion mobility. These investigations revealed that a fluid is not suitable for this kind of ionisation chamber and as filling gases nitrogen, a nitrogen-carbon dioxide mixture as well as an argon-carbon dioxide mixture are best suited.

The materials of the ionisation chamber were selected such that they do not adversely alter the beam profile, have a long durability even after applying high doses and form a favourable electric field.

By changing the concept from two monitor chambers to a single one, alternative solutions for the secondary scattering foil in electron mode and the mirror in photon mode had to be found. A concept for a secondary scattering foil and a mirror permanently in the beam path are presented in this work.

Based on the theoretical results for wire segmentation and material selection, and first measurements with a multi-wire chamber operated in ionisation mode, a first basic prototype open to air was built to show the feasibility of using a wire chamber to monitor the beam profile of a medical linear accelerator.

Finally a second prototype with sealed ionisation chambers was investigated. For this suitable electronics were developed and three gas fillings were analysed. These measurements showed that nitrogen is the best suited gas.

During measurements with the second prototype in the head of a medical linear accelerator the performance concerning repeatability, detection of symmetry changes and measurement of the beam profile were analysed. Moreover the effect of varying

field size on the monitor chamber signals was investigated. These measurements pointed out that the performance of the new monitor chamber is adequate and that the theoretically derived wire segmentation is sufficient to monitor the radiation beam.

The investigations in this work showed that a unified dose chamber for photon and electron radiation with wire electrodes can monitor the beam adequately and fulfil the main criteria for such a novel dose monitor system.

Zusammenfassung

In medizinischen Linearbeschleunigern überwacht das Dosismonitorsystem die applizierte Dosis sowie die Symmetrie und Ebenheit des auf den Patienten applizierten Strahlenfeldes. Es besteht aus einer Überwachungseinheit, typischerweise einer Ionisationskammer, und Regelungselektronik, die das Signal der Überwachungseinheit auswertet und die Bestrahlung im Falle eines Fehlers gestoppt. Daher ist das Dosismonitorsystem der wichtigste Sicherheitsmechanismus eines medizinischen Linearbeschleunigers.

Ziel dieser Arbeit war es ein neues Dosismonitorsystem für medizinische Linearbeschleuniger zu entwickeln, das neben den benötigten Werten applizierte Dosis, Symmetrie und Ebenheit mehr Information über den Strahl gewinnt.

Um die Nachteile und das Leistungsvermögen heutzutage typischerweise eingesetzter Dosismonitorsysteme zu untersuchen und um Informationen über das umgebende Strahlenfeld im Kopf eines Linearbeschleunigers zu erhalten, wurden Simulationen und Messungen mit den zwei Dosismonitorkammern von Siemens durchgeführt. Auf diesen Untersuchungen und auf Anforderungen an künftige Linearbeschleuniger basierend wurde ein neues Dosismonitorsystem entwickelt.

Zunächst wurde ein neues Prinzip zur Strahlabtastung eingeführt, das den Strahl in zwei Richtungen durch parallele Drähte oder Streifenelektroden statt durch radial segmentierte Elektroden abtastet. Dieses Abtastprinzip erlaubt die Rekonstruktion des Strahlprofils und nicht nur den Vergleich der rechten und linken Hälfte des Strahlprofils, wie dies heutzutage geschieht. Durch Kenntnis des Strahlprofils können Fehler bei der Strahlerzeugung exakter analysiert werden und Gegenmaßnahmen können bereits während der Strahlerzeugung ergriffen werden. Des Weiteren würde es eine genauere Kenntnis des Strahlprofils erlauben, die akzeptierbaren Fehlergrenzen für das Strahlprofil zu reduzieren und so zu einer besseren Übereinstimmung von geplanter und applizierter Dosisverteilung führen.

Die geometrischen Abmessungen sowie der Kanalabstand wurden theoretisch ermittelt indem die Antwort einer solchen Ionisationskammer auf typische Strahlenfelder unterschiedlicher Strahlenqualität modelliert wurde. Es wurde eine einzige Kammer für die Überwachung von Photonen- sowie Elektronenstrahlung entwickelt.

Des Weiteren wurde auf Basis der notwendigen Signalstärke und Ionenmobilität eine Vorauswahl geeigneter Füllmedien getroffen. Diese Untersuchungen zeigten, dass Flüssigkeiten für diese Art von Kammer nicht geeignet sind und dass die Gase Stickstoff, eine Stickstoff-Kohlendioxid-Mischung sowie eine Argon-Kohlendioxid-Mischung am besten geeignet sind.

Die Materialien der Ionisationskammer wurden so gewählt, dass sie das Strahlprofil nicht negativ beeinflussen, eine hohe Alterungsbeständigkeit auch nach hohen Strahlendosen haben und ein günstiges elektrisches Feld bilden.

Durch die Verwendung nur noch einer Ionisationskammer statt zwei musste eine alternative Lösung für die zweite Streufole im Elektronenmodus sowie für den Spiegel im Photonenmodus gefunden werden. Ein Konzept permanent im Strahlengang installierter zweiter Streufole und Spiegel wird in dieser Arbeit vorgestellt.

Basierend auf den Untersuchungen zur Segmentierung und Materialauswahl und ersten Messungen mit einer Drahtkammer, die im Ionisationsbereich betrieben wurde, wurde ein erster einfacher Prototyp gebaut, der offen gegenüber der Umgebungsluft ist. Mit diesem wurde die Verwendbarkeit einer Drahtkammer zur Überwachung des Strahlprofils eines medizinischen Linearbeschleunigers gezeigt.

Schließlich wurde ein zweiter Prototyp mit geschlossenen Ionisationskammern untersucht. Für diesen wurde eine passende Elektronik entwickelt und drei Füllgase wurden untersucht. Diese Untersuchungen zeigten, dass Stickstoff die beste Wahl ist. Während der Messungen mit dem zweiten Prototypen im Kopf eines medizinischen Linearbeschleunigers wurde die Leistungsfähigkeit bezüglich Wiederholbarkeit, Detektierbarkeit von Symmetrieänderungen und Messung des Strahlprofils untersucht. Des Weiteren wurde der Einfluss sich ändernder Feldgrößen auf die Signale der Ionisationskammer geprüft. Diese Messungen zeigten, dass die Leistungsfähigkeit der neuen Dosismonitorkammer ausreicht und dass die theoretisch bestimmte Segmentierung der Kammer genügt, um den Strahlengang zu überwachen.

Die Untersuchungen dieser Arbeit zeigen, dass eine Ionisationskammer für Photonen- und Elektronenstrahlung mit Drahtelektroden den Strahlengang adäquat überwachen kann und die Hauptanforderungen an ein solches neues Dosismonitorsystem erfüllt.

Table of Content

1	Introduction	1
2	Dose Monitor Chambers.....	7
2.1	Physics of Ionisation Chambers.....	7
2.1.1	Ionisation of Gases and Fluids	7
2.1.2	Signal Generation	8
2.1.3	Collection Efficiency and Recombination	10
2.2	Monitoring Beam Flatness and Symmetry.....	12
2.3	Normative Requirements.....	13
2.4	Examples of Dose Monitor Chambers	14
2.4.1	Siemens	14
2.4.2	Varian	15
2.4.3	Elekta.....	16
2.4.4	Other Gas Filled Dose Chambers.....	16
2.4.5	Liquid Filled Dose Chambers.....	18
2.5	External Conditions	19
2.5.1	Dose Rate	19
2.5.2	Temperature, Pressure and Humidity.....	19
2.5.3	Head Scatter and Backscatter	20
3	Evaluation of a Current Monitor System	23
3.1	Simulations	23
3.1.1	Materials and Methods.....	23
3.1.2	Results and Discussion.....	25
3.2	Measurements.....	29
3.2.1	Materials and Methods.....	29
3.2.2	Results.....	31
3.2.3	Discussion	35
3.3	Conclusion	36
4	Development of the Unified Dose Chamber	37
4.1	Evaluation Principles	38
4.1.1	Sampling of Beam Profile	38
4.1.2	Monitoring of Symmetry and Flatness.....	39
4.2	Geometric Dimensions	41
4.2.1	Entrance Window Size	41
4.2.2	Height of Ionisation Volume	42
4.3	Channel and Wire Distance	44
4.3.1	Analytical Model	44
4.3.2	Error Detection and Non-Symmetric Profiles	55
4.3.3	Comparison to Current Photon Chamber	58
4.4	Electric Field and Ion Velocity	59

4.5	Filling Medium	60
4.5.1	Gas vs. Fluid	60
4.5.2	Induced Charge.....	61
4.5.3	Ion Mobility and Recombination.....	62
4.6	Further Components	64
4.6.1	Wires	64
4.6.2	Foils.....	67
4.6.3	Other Materials.....	72
4.7	Activation	74
4.8	Ageing.....	75
4.9	Summary of Optimal Parameters.....	75
5	Effects of Changes in Monitor Chamber on Linear Accelerator	77
5.1	Secondary Foil.....	77
5.2	Mirror	79
6	Preliminary Investigations.....	81
6.1	Construction of first prototype	81
6.2	Measurements.....	82
6.2.1	X-Ray	82
6.2.2	Linear Accelerator	83
6.3	Results.....	84
6.3.1	X-Ray	84
6.3.2	Linear Accelerator	85
6.4	Discussion and Conclusion	88
7	Second Prototype of UDC	89
7.1	Construction	89
7.2	Electronics	90
7.2.1	Hard- and Software	90
7.2.2	Accuracy.....	93
7.2.3	Tests.....	94
7.3	Measurements.....	97
7.3.1	Determination of Gas Filling	97
7.3.2	Performance Measurements	105
7.3.3	Conclusion.....	122
7.4	Conclusion on Applicability of the New Dose Monitor Concept	123
8	Summary and Outlook.....	125
A	Recombination Correction for Continuous Sweeping of Dose Rate.....	A-1
B	Monte Carlo Simulation	B-1
C	Channel and Wire Distance Results	C-1
D	Activation of Chamber Materials	D-1
E	Preliminary Investigations with MWPC	E-1
F	Prototype Two.....	F-1

Glossary and Abbreviations I
Table of Figures II
Table of Tables VIII
References IX
Erklärungen XVI
Curriculum Vitae XVII

1 Introduction

In medical radiotherapy linear accelerators are used to treat malignant and benign diseases. The aim is to deposit a well-defined amount of dose in a target volume which consists of the tumour and a safety margin. The total dose is normally applied in several fractions, typically around 25 to 30 with one fraction per day. The tumours may be treated by electron or photon radiation, depending on the type, shape and location. Photon radiation is created when the electron beam accelerated in the linear accelerators waveguide hits a target, after being collimated and guided to the correct path by bending magnets. This photon radiation is collimated by a primary collimator and for conventional flat photon fields flattened by a cone-shaped flattening filter. For electron radiation the target is removed and the electron beam is flattened and broadened by scattering foils.

Switching between different energies and radiation types is currently realized in linear accelerators by mechanically moving the respective setup into the radiation beam. This limits the number of available configurations per machine. Classically 2 photon energies and 5 - 6 electron energies are available.

Typically nowadays photon radiation is applied from several directions and in several segments of varying shape per direction. By this the intensity across the radiation field from one direction can be modulated to spare critical organs and to apply the desired dose to the tumour. This modulation is achieved by collimating the beam by a so called multi-leaf collimator (MLC).

The treatment is planned first of all in a treatment planning system based on the anatomy of the patient, determined by a planning CT, and measured physical properties, like depth-dose curve or beam profile, of the radiation beam of the linear accelerator.

For the success of the treatment it is crucial that the applied dose is the same as the planned one. Moreover excessive radiation may harm the patient. For these reasons the most important safety system of a linear accelerator is the dose monitoring system. According to IEC 60601-2-1 two independent measuring systems have to monitor the total applied dose. Moreover, monitoring of symmetry and flatness of the radiation field is demanded [IEC 60601-2-1 1998]. Symmetry is the ratio of the dose at two points anywhere in the radiation field located symmetrically to the central beam axis. Flatness is the ratio of the dose at any two points in the radiation field (for details see chapter 2.2). Further normative requirements for a dose monitoring system are given in chapter 2.3.

Besides the conventional radiation therapy with flat beam profiles, the unflat beam is used, especially in stereotaxis. By removing the flattening filter the dose rate can be increased which significantly reduces treatment time [Fu, et al. 2004, U. Titt, O. Vassiliev, et al. 2006]. Moreover the use of the unflat beam in intensity modulated radiation therapy (IMRT) is discussed [U. Titt, O. N. Vassiliev, et al. 2006]. The meaning of the quality criterion flatness is no longer valid for such fields. Only symmetry can be determined.

Currently ionisation chambers open to air or filled with ionisation gas are used to monitor these parameters. Depending on the supplier of the linear accelerator, two separate chambers for photons and electrons [Kubo 1989, Duzenli, McClean and Field 1993, Lam, Muthuswamy and Ten Haken 1996, Zhu, Bjärngard, et al. 2001] or one chamber for both beam qualities are used [Duzenli, McClean and Field 1993, Lam, Muthuswamy and Ten Haken 1996, Verhaegen, Symonds-Taylor, et al. 2000, Ravikumar and Ravichandran 2001, Zhu, Bjärngard, et al. 2001, Haryanto 2003].

These dose monitor chambers are located in the treatment head of the linear accelerator. The electrodes of the monitor chambers used for photon and electron radiation mostly consist of thermoplastics, coated with a conducting layer [Haryanto 2003, Sjörgen, Karlsson and Karlsson 1999]. Dose chambers only used for photon radiation consist of alumina or mica [Duzenli, McClean and Field 1993, Zhu, Bjärngard, et al. 2001]. Besides these established monitor chamber, several other concepts for dose measurement and beam monitoring were developed [Taumann 1984, McIntyre und Johnson 1990, Yi Yao 1997, Arndt and Kyte 2000]. A detailed review of some dose monitor chamber concepts is given in chapter 2.4.

The main cause for an incorrect application of dose is a primary beam from the waveguide not hitting the target or scattering foils correctly. Figure 1-1 shows errors in field symmetry and flatness that can occur in flattened photon radiation therapy beams. (a) shows a symmetric and flat beam profile. In (b) the incident electron beam on the target is tilted and thus the radiation field is tilted as well. Moreover, the electron beam might hit the target off axis (c), thus producing a two-plateau profile. In (d) a diverging beam, e.g. caused by bending magnet problems, is observed, which leads to a beam profile with two peaks at the rim of the beam profile.

Similar errors occur for electron radiation, as the secondary scattering foil is also cone-shaped and flattens the beam.

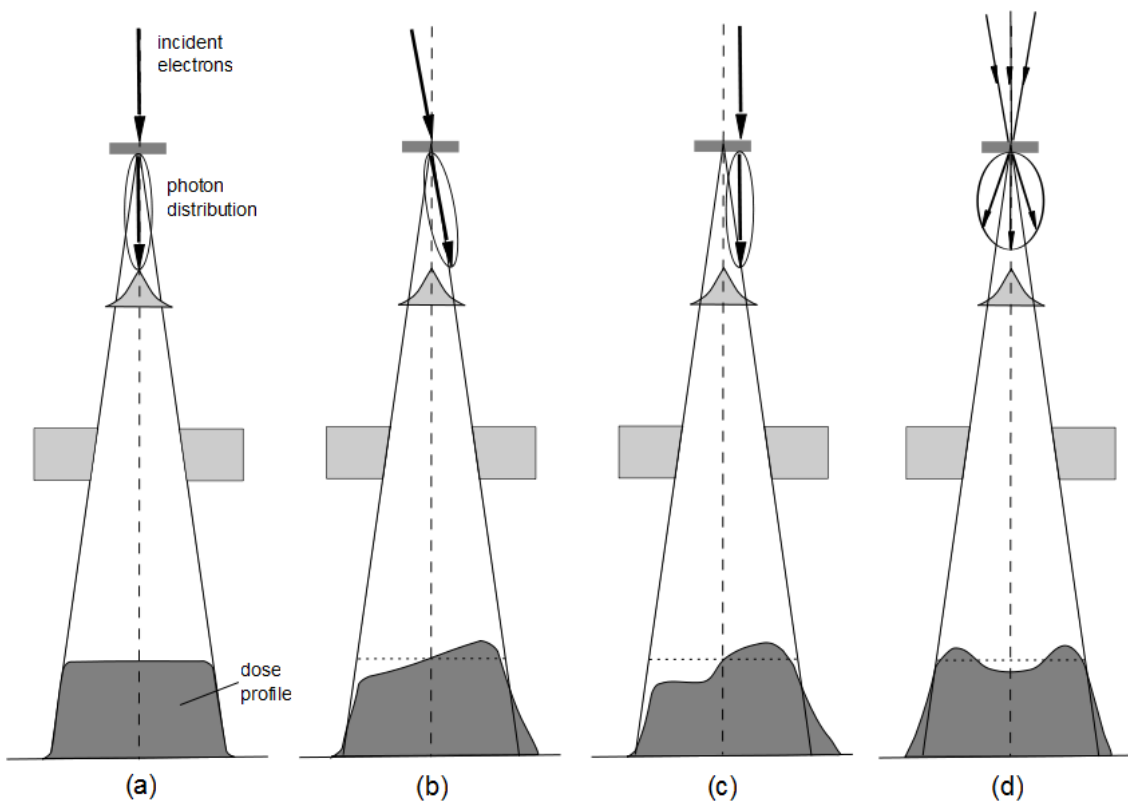


Figure 1-1: Potential errors in beam symmetry and flatness for flattened beams: (a) correct beam direction and divergence, (b) tilted incident electron beam, (c) displaced incident electron beam, (d) divergent beam (adapted from [Krieger 2005])

In unflattened beams the errors in symmetry given in figure 1-2 may occur. (a) gives a symmetric profile. Error causes (b) to (d) are the same as for flattened beams.

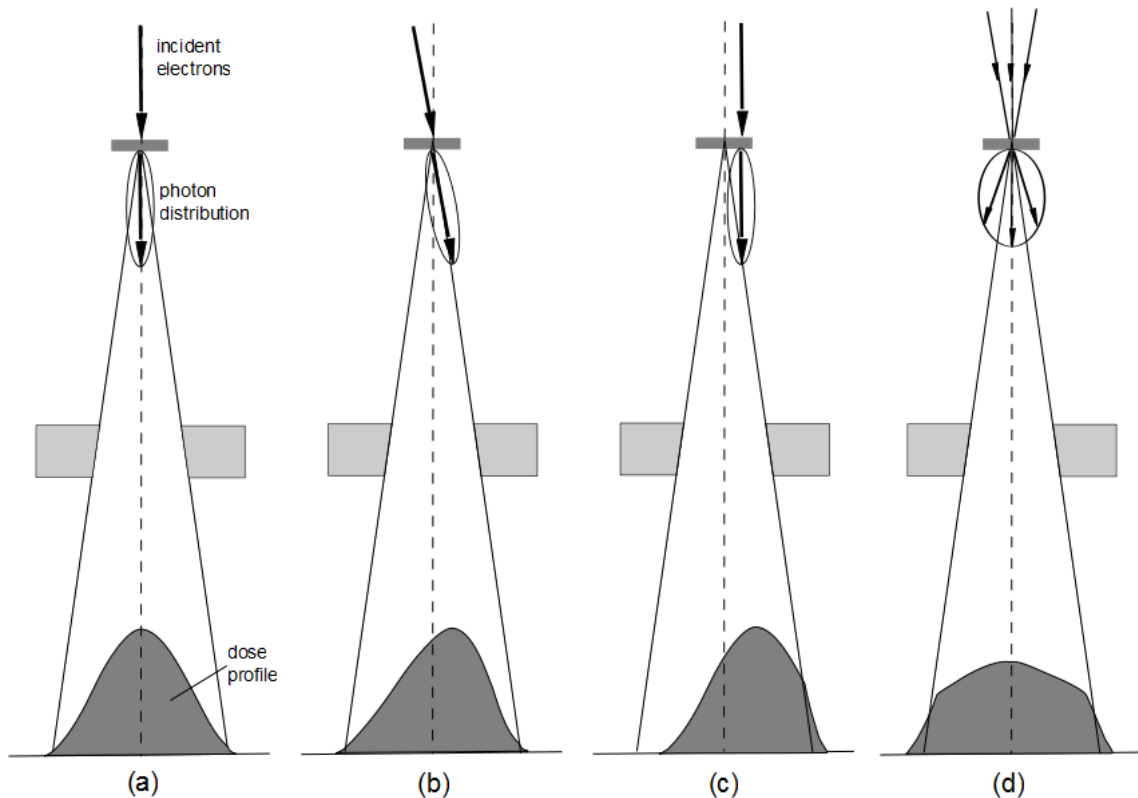


Figure 1-2: (a) Potential errors in beam symmetry and flatness for unflattened beams: (a) correct beam direction and divergence, (b) tilted incident electron beam, (c) displaced incident electron beam, (d) divergent beam (adapted from [Krieger 2005])

Currently used dose monitor chambers always sum the signal over a larger area and thus cannot detect small changes in the beam profile. The dose monitor systems used by Siemens cannot distinguish between the errors (b) and (c) in figure 1-1 and figure 1-2 as these integrate over the areas on the left and right side of the central axis and compare these two values. Moreover case (d) is hard to detect as the sum of applied dose on both sides is the same and thus similar to case (a). Only the drop in maximum can be detected.

In conventional fractionation schemes a small error in one of the fractions does not have a high significance. IEC 60601-2-1 demands to stop the beam if the measured dose exceeds the planned one by more than 10 % [IEC 60601-2-1 1998]. In hypofractionated treatment with higher dose per fraction, such errors have greater consequences.

Moreover the use of two separate dose chambers is non-favourable. The error-proneness is higher due to moving parts in the linac head. The dose chamber slide mechanics may wear and thus lead to a stuck chamber slide. Moreover the position of the chamber slide has to be monitored to ensure that the correct chamber is in the beam path. This leads to additional potential errors and control effort.

Furthermore the diameter of the current electron chamber in Siemens linacs is too small such that radiation hits the rim and is scattered into the dose chamber. As it is also open to air, a temperature and pressure correction has to be applied.

Additionally, nowadays only the symmetry and flatness of the beam is known, not its profile which would allow a finer steering and thus correction of the beam by changing the current to the steering coils such that the incident angle on the exit window is corrected.

To ensure a better monitoring of the treatment beam a higher spatial resolution is needed. Therefore in this work a new Unified Dose Chamber for electron and photon radiation was developed which monitors beam symmetry and flatness as well as the beam profile and overcomes the drawbacks of the current dose monitor system. This system could also be used for precise steering and failure analysis as more detailed

information on beam profile and changes therein is available, compared to the current dose monitor system.

Besides the normative requirements given in chapter 2.3, a new dose monitor chamber shall meet the following demands:

- sensing of beam profile
- detection of changes in beam symmetry and flatness at least as good as current system
- reliable measurement of applied dose
- fit into current linear accelerator head
- not disturb the beam in unwanted fashion
- lifetime of at least several years, preferably 10 years

External effects like temperature or backscatter on the dose chamber which influence its performance are analysed in chapter 2.5 to consider these in the design.

To assess the capabilities of nowadays dose monitoring systems, the currently used Siemens dose chambers for photon and electron radiation as well as a chamber with thermoplastic foils intended for photon and electron radiation are examined in chapter 3. First of all, the effects of the primary collimator and the flattening filter on the photon beam are investigated. Moreover the effect of backscatter to the chamber volume is assessed. Afterwards measurements with these three dose chambers in a Siemens linear accelerator are conducted. The effect of backscatter for different field sizes is investigated as well as the proportionality of the signals and the ability to detect symmetry changes.

For the development of the new Unified Dose Chamber first all the principle how to sense the beam profile and to ensure detection of changes in symmetry and flatness is evaluated in chapters 4.1 and 4.3. The geometric dimension to fit to the current linear accelerator head and not disturb the beam is evaluated in chapter 4.2. Electric field configurations are briefly discussed in chapter 4.4.

A suitable filling gas is discussed in chapter 4.5 and a deeper look into several materials for dose monitor chambers and ageing phenomena is taken in chapters 4.6 and 4.8. As activation might influence the dose monitor signal and hinder easy replacement for service, this aspect is considered in chapter 4.7. A concept for a Unified Dose Chamber based on these results is presented.

The effect of such a chamber on the current linear accelerator architecture is evaluated in chapter 5. Integration of secondary scattering foil and change of mirror material are discussed.

To assess the capability of a foil chamber with the desired segmentation to measure electron beams, a preliminary investigation with a multi wire proportional chamber operated in ionisation mode is carried out. Afterwards a first prototype open to air, i.e. using ambient air as ionisation gas, is constructed and tested. The results of these preliminary investigations are given in chapter 6.

Based on these results and the investigation in chapter 4 concerning filling gas and materials, a second prototype is built. This one is closed and filled with different filling gases. Electronics to measure and record the chamber signals are developed and are presented in chapter 7.2.

Measurements are done to determine the best filling gas (chapter 7.3.1). To evaluate the performance of the Unified Dose Chamber the second prototype is mounted into the head of a Siemens linear accelerator and the dose rate proportionality, short- and

mid-term stability, effect of backscatter and the detection of symmetry changes as well as measurement of dose profile is investigated in chapter 7.3.2. Furthermore the effect of the dose chamber segments on the beam is evaluated.

Finally in chapter 8 an outlook on the use of the new Unified Dose Chamber in future developments of linear accelerators is given, including a better steering to control the beam profile by a feedback loop.

This work was realized in co-operation with Siemens AG, Healthcare. A patent application has been filed for the evaluation principle (patent application publication no. DE 10 2011 077 978 A1, disclosure date: 27.12.2012) [Eenboom 2012].

2 Dose Monitor Chambers

2.1 Physics of Ionisation Chambers

Dosimetry systems in linear accelerators monitor the dose applied to the patient by analysing the current induced in monitor chambers in the linac head. These chambers do not measure the applied dose directly, but their output is normalized to applied dose at isocentre.

The charge produced in the ionisation volume has to be removed before the next linac pulse occurs to prevent an addition of the contribution from several dose pulses. Therefore sufficiently high ion mobilities and electric fields are required.

2.1.1 Ionisation of Gases and Fluids

When ionising radiation like electron and photon beams passes the ionisation chamber, the medium in the chamber is ionised. This leads to positive ions and free electrons which might combine with electrically neutral molecules to negative ions. For indirectly ionising radiation like photon beams, primary ionisation occurs mostly via Compton scattering in the therapeutic energy range of 1 MeV to 25 MeV [Hofmann 2003].

The absorbed dose D to a chamber volume filled with a medium of mass m is given by

$$D = \frac{Q}{m} \cdot \frac{W}{e} \quad (1)$$

with e being the elementary charge and Q the produced charge. W/e is the mean energy needed to produce an electron-ion pair.

Smaller W -values lead to more electron-ion pairs per incident charged particle. Examples for W -values are given in table 2-1.

Table 2-1: W -values for different gases [Kolanoski 2004]

	Air	H ₂	N ₂	CO ₂	Ar	Xe	CH ₄
W /eV	34	37	35	33	26	22	28

For the number of primary electron-ion pairs n no simple expression exists. Nevertheless it is approximately linearly dependent on the average atomic number of the gas [Sauli 1977]. The statistics of primary ionisation follows a Poisson-like distribution

$$p_k^n = \frac{n^k}{k!} e^{-n} \quad (2)$$

with k being the actual number of ions in one event. This leads to an inefficiency of

$$1 - \varepsilon = p_0^n = e^{-n} \quad (3)$$

The amount of charge produced moreover depends on the density of the medium which is directly proportional to the probability of interaction. The denser the medium the more charge is produced. Therefore more electron-ion pairs are produced in fluid filled chambers compared to gas filled ones as the density is a factor of 10^3 higher in liquids compared to gases [Hofmann 2003].

2.1.2 Signal Generation

Without an electric field applied to the chamber, the electrons and ions diffuse by multiple collisions [Sauli 1977]. When an electric field E is applied to the chamber electrodes, the electrons and ions drift to the respective electrode.

For *ions* the drift velocity v_D^+ is linearly proportional to the reduced electric field E/P , with P being the atmospheric pressure. Their mobility μ is given by

$$\mu^+ = \frac{v_D^+}{E} \cdot \frac{P}{P_0} \quad (4)$$

with P_0 being 1013.25 mbar. μ^+ is constant up to high energies and specific for a certain gas. For a mixture of gases G_1, G_2, \dots, G_n the mobility μ_i^+ of the ion G_i^+ is given by Blanc's law

$$\frac{1}{\mu_i^+} = \sum_{j=1}^n \frac{p_j}{\mu_{ij}^+} \quad (5)$$

where p_j is the volume concentration of gas G_j in the mixture and μ_{ij}^+ the mobility of ion G_i^+ in gas G_j . In gas mixtures the gas with lowest ionisation energy dominates the characteristics as excited states are most readily de-excited via frequent ion gas collisions [Pettifer, Borowski and Loeffen 1999].

For *electrons* the mobility varies with the applied electric field and filling medium. The electrons can increase their energy between collisions due to their small mass. The drift time of electrons is given by

$$w = \frac{e}{2m} \cdot \frac{E}{\tau} \quad (6)$$

with τ being the mean time between collisions which is a function of the electric field E [Townsend 1947]. The mobilities may be 10^2 - 10^3 times higher than those of ions.

The moving charges in the electric field induce charges on the anode and cathode. For the dose chamber signal only the total induced charge is important. The induced charge difference dq is given by

$$dq = Q \frac{dU}{U_0} \quad (7)$$

with dU being the potential difference the ion or electron drifted through and U_0 being the potential difference between the electrodes.

2.1.2.1 Parallel Plate Chambers

In a parallel plate chamber with applied voltage U_0 and plate distance d , the electric field E is given by

$$E = \frac{U_0}{d} = \frac{Q}{Cd} = \frac{Ne}{Cd} \quad (8)$$

with C being the capacitance of the chamber and N the number of ions. e is the elemental charge. This leads to a homogeneous distribution of the field lines and therefore constant drift velocity of the produced ions and free electrons.

After a time t the ions drifted a distance $ds^+ = v_D^+ t$ and the electrons a distance $ds^- = v_D^- t$ over a potential difference

$$dU = E ds = E (ds^+ + ds^-) = \frac{Ne}{Cd} (v_D^+ + v_D^-) t \quad (9)$$

From (7) it follows that the resulting induced charge is

$$dq = Q \frac{E ds}{U_0} = \frac{Ne}{d} (v_D^+ + v_D^-) t \quad (10)$$

At a time $t = T^- = x/v_D^-$ all electrons reach the anode at a distance x and do not further induce charge on the electrodes. The induced charge becomes

$$dq = \frac{Ne}{d} (v_D^+ t + x) \quad (11)$$

After the ions reached the cathode after a time $t = T^+ = x/v_D^+$ the induced charge dq equals the total charge Q which was created in the chamber.

Depending on the measurement circuit, the signal shape might vary. For a circuit with a large time constant RC (upper red line in figure 2-1), the pulse shape follows the shape of the induced charge and reaches a maximum at U_{\max} .

For smaller time constants the pulse maximum is below the maximum. For electron sensitive detectors very small time constants are selected such that the ion contribution to the signal is not counted (lower red dotted line in figure 2-1) [Knoll 2000].

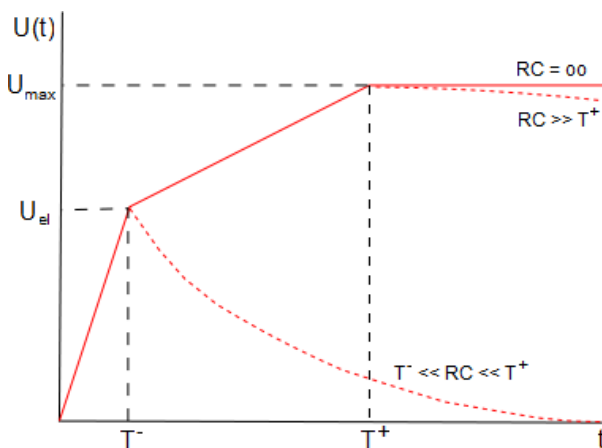


Figure 2-1: Pulse shape dependence on RC

2.1.2.2 Wire Chambers

In conventional multi-wire proportional chambers (MWPCs) with anode wires stretched at a distance s , and cathode plates, the electric field is illustrated in figure 2-2 and given by [Sauli 1977]

$$E(x, y) = \frac{CU_0}{2\varepsilon_0 s} \left(1 + \tan^2 \frac{\pi x}{s} \tanh^2 \frac{\pi y}{s}\right)^{1/2} \left(\tan^2 \frac{\pi x}{s} + \tanh^2 \frac{\pi y}{s}\right)^{-1/2} \quad (12)$$

$$\text{with } C = \frac{2\pi\varepsilon_0}{(\pi l/s) - \ln(2\pi a/s)}$$

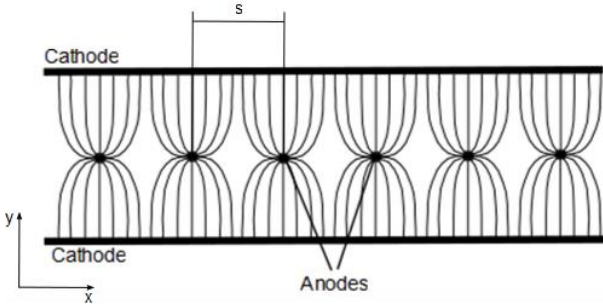


Figure 2-2: Electric field of a MWPC

It follows that

$$E_y = E(0, y) = \frac{CU_0}{2\varepsilon_0 s} \coth \frac{\pi y}{s} \quad (13)$$

$$E_x = E(x, 0) = \frac{CU_0}{2\varepsilon_0 s} \cotg \frac{\pi x}{s} \quad (14)$$

For $y \ll s$

$$E(x, y) = \frac{CU_0}{2\varepsilon_0 s} \frac{1}{r}; \quad r = (x^2 + y^2)^{1/2} \quad (15)$$

for $y \geq s$

$$E(x, y) = \frac{CU_0}{2\varepsilon_0 s} \quad (16)$$

The signal induction is in principle the same as in parallel plate chambers as long as the electric field is small enough to prevent electron avalanche. Nevertheless as v_D is a variable of the electric field E , the velocity is higher near the wires which leads to a slightly different charge over time distribution compared to figure 2-1.

2.1.3 Collection Efficiency and Recombination

Positive ions undergo multiple collisions while drifting to the cathode. They might get neutralized by recombination with a free electron or negative ion, or by extracting an electron at the walls of the chamber. Charge may also be transferred to molecules with equal or lower ionisations potentials. Free electrons can be neutralized by positive ions or might attach to a molecule with high electron affinity [Sauli 1977].

The collection efficiency is the amount of collected charge compared to the amount of produced charge and is influenced by three physical causes [Hochhäuser and Balk 1986, Reich 1990, Bruggmoser, et al. 2007].

In *diffusion loss* a part of the charge diffuses against the electric field to the “wrong” electrode. This part of recombination depends on the applied voltage U .

Initial recombination is the recombination of ions and electrons along the track of the ionising particle. It is proportional to the linear energy transfer (LET) and in parallel plate chambers with electrode spacing d indirectly proportional to the applied voltage U .

Volume recombination is caused by diffusion and electrostatic attraction of the charge carriers in the chamber volume. The collection efficiency for pulsed radiation is indirectly proportional to the electric field and directly proportional to the charge per volume and pulse q .

The total collection efficiency is the sum of the single collection efficiencies and is given by [Boag 1966, Boag 1987, Böhm 1976, Boag, Hochhäuser and Balk 1996, Roos and Derikum 2000]

$$f = f_a + f_i + f_v = 1 - \frac{2kT}{Ue} + \frac{E_i d}{U} + \frac{\mu q d^2}{2U} = 1 - \frac{2kT/e + E_i d + \frac{1}{2}\mu q d^2}{U} \quad (17)$$

with T being the gas temperature and k the Boltzmann constant. E_i is a constant and is 0.0044 for x-rays > 120 kV and is only meaningful for $U/d < 0.4$ V/mm [Reich 1990]. μ is a constant depending on the geometry of the chamber, the mobility of the charge carriers and the recombination coefficient.

For volume recombination this can be approximated with $u = \frac{\mu d^2 q}{U}$ by [Boag 1950]

$$f = \frac{1}{u} \ln(1 + u) \quad (18)$$

in case that nearly all electrons attach to molecules forming negative ions. This formula is valid up to about 5×10^{-4} C/kg [Hochhäuser and Balk 1986].

For high doses per pulse as they occur at monitor chambers in linear accelerators, volume recombination becomes more prominent. Due to a certain amount of free electrons not attaching to neutral molecules, Boag's theory is no longer applicable. The resulting collection efficiency also depends on the fraction of collected electrons p [Hochhäuser and Balk 1986, Boag, Hochhäuser and Balk 1996].

Hochhäuser and Balk (1986) suggested a collection efficiency based on the assumption that the negative ion density is uniform across the chamber

$$f = \frac{1}{u} \ln \left(1 + \frac{e^{pu} - 1}{p} \right) \quad (19)$$

Piermattei, et al. (2000) confirmed this approach for high doses per pulse from a Novac electron accelerator.

Moreover in gases with low electron attachment like noble gases or pure nitrogen, the electric field of the electrodes may be shielded by the positive ions [Boag, Hochhäuser and Balk 1996], leading to a lower field strength and thus longer drift times and increased recombination.

2.2 Monitoring Beam Flatness and Symmetry

The main purpose of a dose monitoring system is to monitor the applied dose as well as changes in symmetry and flatness of the treatment field. According to IEC 60601-2-1 (1998) the treatment should be terminated, if the signals from the dose monitor indicate a change greater than 10 % in the absorbed dose distribution.

The flatness for photon radiation is defined as “maximum value of the ratio of maximum absorbed dose (averaged over not more than 1 cm² anywhere in the flattened area) to the minimum absorbed dose (averaged over not more than 1 cm² anywhere in the flattened area)” [IEC 60976] and is measured on the major axes and the diagonals of the treatment field.

$$Flatness(IEC; Photons) = \frac{D_{max}}{D_{min}} \times 100\% \quad (20)$$

For electrons, flatness is defined as “ratio of the highest absorbed dose anywhere in the radiation field at standard measurement depth to absorbed dose on the radiation beam axis at the depth of dose maximum” [IEC 60976].

$$Flatness(IEC; Electrons) = \frac{\max(D_{d_{std}})}{D_{axis, d_{max}}} \quad (21)$$

Symmetry is defined as “maximum value of the ratio of the higher to the lower absorbed dose (averaged over not more than 1 cm²) at any two positions symmetrical to the radiation beam axis and inside the flattened area” [IEC 60976].

$$Symmetry(IEC) = \max\left(\frac{D(x, y)}{D(-x, -y)}\right) \times 100\% \quad (22)$$

IEC 60976 defines a flattened region in which the uniformity (flatness) of the treatment field in the patient plane is measured. For photons this area is defined by the radius and diagonals of the nominal field size F from which the values d_m on the main axis and d_d on the diagonals, given in table 2-2, have to be subtracted. For electrons, the flattened area is defined as the area surrounded by the 90 % isodose line minus 1 cm.

Table 2-2: Parameters for calculating flattened area for photon beams (data from [IEC 60976])

Square radiation field F /cm	Dimensions defining the flattened area	
	d _m	d _d
5 ≤ F ≤ 10	1 cm	2 cm
10 < F ≤ 30	0.1 F	0.2 F
30 < F	3 cm	6 cm

To monitor beam flatness and symmetry in the linac head, conventional dose chambers are segmented. In the monitor chambers used in Siemens linear accelerators, the segmented electrode has four segments to monitor beam flatness and symmetry (see chapter 2.4.1).

2.3 Normative Requirements

The following international regulations have to be met by all dose monitor chamber systems for linear accelerators:

- IEC 60601-1: Medical electrical equipment – Part 1: General requirements for basic safety and essential performance [IEC 60601-1]
- IEC 60601-1-2: Medical electrical equipment – Part 1-2: General requirements for basic safety and essential performance – Collateral standard: Electromagnetic compatibility – Requirements and tests [IEC 60601-1-2]
- IEC 60601-2-1: Medical electrical equipment – Part 2-1: Particular requirements for the safety of electron accelerators in the range 1 MeV to 50 MeV [IEC 60601-2-1]

Moreover a linear accelerator should operate according to the following performance characteristic guidelines. The dose monitoring system shall be capable of monitoring this performance.

- IEC 60976: Medical electrical equipment – Medical electron accelerators – Functional performance characteristics [IEC 60976]
- IEC 60977: Medical electrical equipment – Medical electron accelerators – Guidelines for functional performance characteristics [IEC 60977].

For the dose chamber in particular, the following most important requirements apply:

IEC 60601-2-1

- Two independent dose monitoring systems which can independently terminate radiation
- Malfunctioning of one system shall not affect the other system
- Performance for absorbed dose rate up to twice the specified maximum included in technical description if linear accelerator is under any circumstance capable of producing this dose rate
- At least one transmission detector centred on reference axis on patient side of all field flattening and beam scattering filters shall be provided
- Hermetically sealed detectors should be sealed independently of one another
- Detectors shall detect symmetrical and non-symmetrical changes of dose distribution
- Means shall be provided to terminate irradiation before additional 0.25 Gy is delivered, when absorbed dose distribution is distorted by more than 10 % or the signals from the radiation detectors indicate a change >10 % in absorbed dose distribution

IEC 60976/60977 (recommended performance stated in brackets)

- Reproducibility (0.5 %)
- Proportionality (2 %)
- Dependence on the shape of radiation field (statement sufficient)
- Stability after high absorbed dose (2 %)
- Stability throughout the day (2 %)
- Stability throughout the week (2 %)
- Flatness and symmetry of radiation field (symmetry: photons: 103 %; electrons: 105 %)

For the development of a new dose chamber, the flatness and symmetry requirements were translated to Siemens measurement convention which compares the signals from left and right side of the beam profile.

- Flatness < 3 % (< 5 % for 25 MeV)
- Symmetry < 2 %

2.4 Examples of Dose Monitor Chambers

For monitoring the radiation beam in medical linear accelerators, several concepts were proposed in the past. In the following chapters, first of all, the currently implemented solutions of the three main manufacturers with respect to the installed number of linacs are shown. Furthermore other published segmentation schemes are presented. Besides these typical gas filled ionisation chambers, liquid filled ones for different purposes are shown.

2.4.1 Siemens

In Siemens linear accelerators separate parallel plate ionisation chambers are used for photon and electron radiation, respectively. Both chambers are mounted on a carriage which moves the respective chamber into the beam during treatment.

For monitoring photon radiation a ceramic chamber made from alumina is used. The monitor chamber consists of two separate gas volumes, separated by the high voltage plate. Electrode one monitors the whole beam (monitor 1) while electrode two is separated into five segments to monitor the central part of the beam (monitor 2) and the beam flatness and symmetry (segments 1 - 4). Figure 2-3 shows the chamber and the segmentation of electrode two.

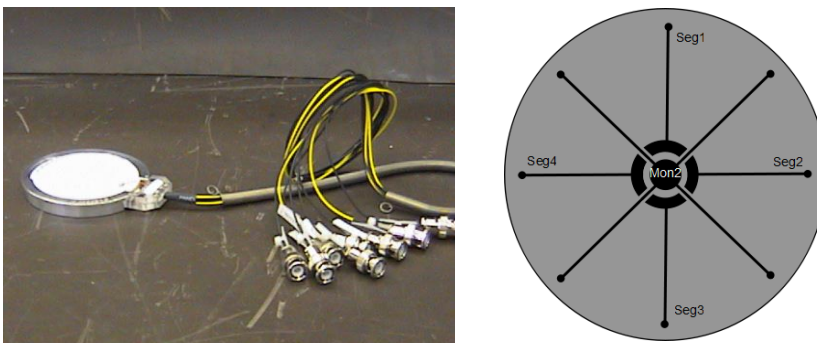


Figure 2-3: Siemens photon chamber (left) and segmentation of electrode two (right)

The top of the chamber is positioned 10.7 cm from the target. It is made from 1.52 mm thick alumina plates (0.93 g/cm^2) [Zhu, Bjärngard, et al. 2001] and filled with nitrogen slightly above ambient pressure. The chamber volumes are 1.52 mm high and have a diameter of 63.5 mm.

For monitoring electron radiation, a chamber with metalized Kapton¹ foils is used. Electrode two is segmented as shown in figure 2-4.

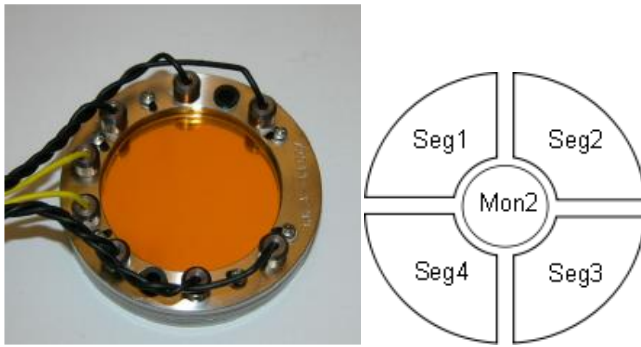


Figure 2-4: Siemens electron chamber (left) and segmentation of electrode two (right)

The first Kapton foil is 11.2 cm from the target. The secondary scattering foil is directly attached to the electron chamber within the chamber carriage. The Kapton foils are 25 μm thick and coated with gold. The chamber volumes are 1.5 mm high and the inner radius of the chamber volume is 20 mm.

2.4.2 Varian

In Varian medical linear accelerators two different chambers are used. For single photon energy linacs, such as the Clinac 600C and Clinac 6/100, and in some Clinac 1800 a mica ionisation chamber is used [Kubo 1989, Duzenli, McClean and Field 1993, Lam, Muthuswamy and Ten Haken 1998, Zhu, Bjärngard, et al. 2001]. The bottom of the chamber is 14.1 cm downstream of the target and 2.8 cm behind the flattening filter [Zhu, Bjärngard, et al. 2001]. Figure 2-5 shows a schematic drawing of this chamber.



Figure 2-5: Schematic cross-section of Varian mica chamber (adapted from [Duzenli, McClean and Field 1993])

For multi-energy linear accelerators, such as some Clinac 1800 and the Clinac 2100 and 2300 series, a sealed ionisation chamber with Kapton foils is used (see figure 2-6) [Duzenli, McClean and Field 1993, Lam, Muthuswamy and Ten Haken 1998, Verhaegen, Symonds-Taylor, et al. 2000, Ravikumar and Ravichandran 2001, Zhu, Bjärngard, et al. 2001]. The Kapton foils are 0.02 g/cm^2 thick. In the 2100 and 2300 series, the bottom of the chamber is 16.9 cm below the source and 4.4 cm below the flattening filter [Zhu, Bjärngard, et al. 2001]. Figure 2-7 shows the segmentation of the Varian chamber. The inner segments are used for beam angle steering, the outer ones for beam position steering [Chapman 2005].

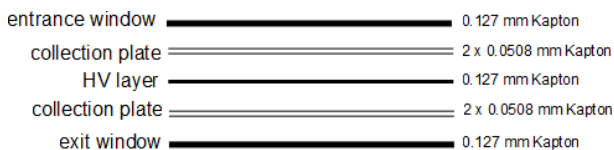


Figure 2-6: Schematic cross-section of Varian Kapton chamber (adapted from [Duzenli, McClean and Field 1993])

¹ Kapton is a polyimide

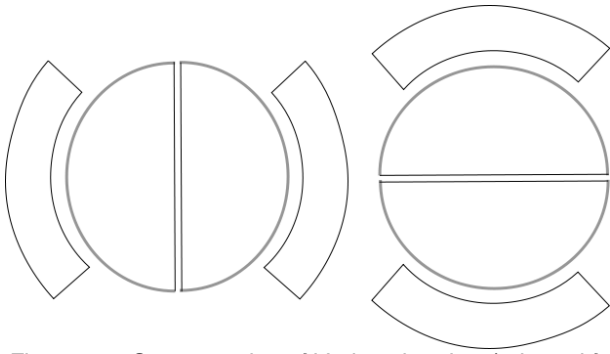


Figure 2-7: Segmentation of Varian chamber (adapted from [Chapman 2005])

2.4.3 Elekta

The beam monitor chamber used by Elekta is an open chamber made from six plates of 0.012 mm Mylar² each, which are coated with 0.15 μm carbon [Haryanto 2003]. These form 3 independent sensitive volumes [Barth 2007]. The circular spacer between two plates consists of aluminium with a density of 2.73 g/cm^3 and alumina [Haryanto 2003]. The first channel is 4 cm in diameter and the second channel 8 cm in diameter [Hounsell 1998]. For photon radiation an additional 3 mm thick backscatter plate made from aluminium alloy is placed 1.6 cm below the chamber [Hounsell 1998, Zhu, Bjärngard, et al. 2001]. A schematic sketch of the dose chamber is shown in figure 2-8. The sectors denoted by 2TB, 2RG, 2RT and 2TA are used to analyse backscatter effects. Inner and outer hump monitor the inner and outer energy level of the beam and are used to steer and monitor the beam.

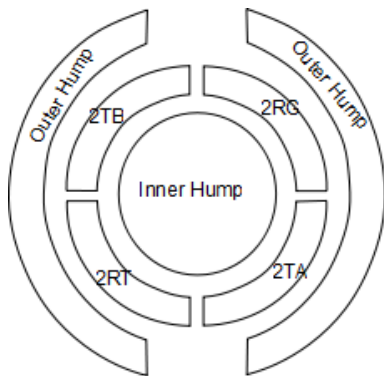


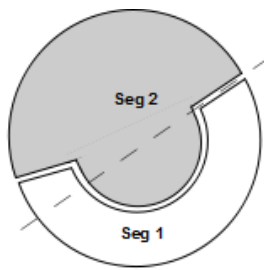
Figure 2-8: Segmentation of the Elekta dose monitor chamber (adapted from [Barth 2007])

2.4.4 Other Gas Filled Dose Chambers

Besides these monitor chambers used nowadays, other segmentations for gas filled chambers were proposed to monitor different parts of the beam. These chambers are not in use.

For Siemens a prototype of a chamber for electron and photon radiation was built in the past by PTW-Freiburg, Germany. This foil chamber consists of metalized Kapton foils with a diameter of 60 mm. Monitor 1 spreads over the whole area to monitor the total applied dose. The second monitor volume is segmented into eight non-symmetric segments.

² Mylar is a biaxially-oriented polyethylene terephthalate



Taumann (1984) proposed a simple segmentation into two electrodes, one being a ring portion extending from 0° to a little less or a little more than 180° , the other one being the rest of the ring portion plus an inner circle as depicted in figure 2-9. For determining symmetry, both electrode signals are weighted and compared. For flatness values the sum and weighted difference of both signals are related.

Figure 2-9: Schematic of chamber with two electrodes (adapted from [Taumann 1984])

McIntyre (1974) combined two segmented rings to monitor different parts of the beam. The inner four electrodes I1 to I4 (see figure 2-10) spread approximately one fourth of the radial distance of the chamber and are positioned under the flattening filter beneath the steepest slope of the filter. Thereby these electrodes are sensitive to changes in the position of the radiation lobe. The outer segments O1 to O4 are located at the shoulders of the lobe to detect a tilt of the beam.

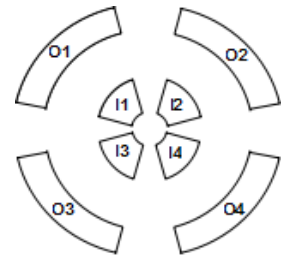
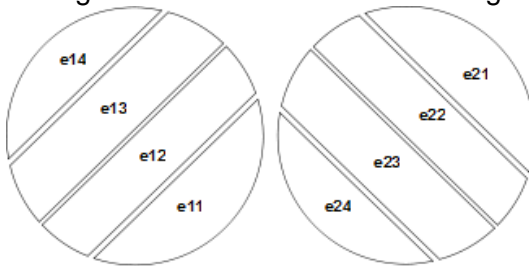


Figure 2-10: Schematic of chamber with four inner (I1-I4) and four outer segments (O1-O4) (adapted from [McIntyre 1974])

Boux (1976) constructed an ionisation chamber with strip electrodes. Two electrodes arranged 90° to each other are segmented into four strips each with equal areas.



Symmetry is determined by comparing the sum of the two segments on each side of an electrode, e.g. sum of e11 and e12 compared to the sum of e13 and e14 in figure 2-11. For flatness, the sum of the inner and the sum of the outer segments are compared.

Figure 2-11: Schematic of chamber with strip electrodes. left: electrode 1 with segments e11 to e14; right: electrode 2 with segments e21 to e24 (adapted from [Boux 1976])

Another chamber type, mostly used to monitor proton radiation, is the multi-wire proportional chamber (MWPC), invented by George Charpak in the 1960s [Charpak, et al. 1968]. A MWPC is a large-area gas-filled ionisation chamber with wires as anodes and cathodes. The chamber is operated in proportional mode with a sufficiently high voltage. Nowadays MWPCs are not only used in high energy physics but also in PET scanners [Ott 1993]. For monitoring proton beams, MWPCs are used for example at the Svedberg Laboratory, Uppsala, Sweden to monitor the vertical position of the beam [Tilly, et al. 2007].

Wire chambers are also used to monitor the beam in medical linear accelerators. Galbraith et al. (1990) proposed a single high voltage wire stretched along the centre of the secondary collimator to monitor the dose per pulse of an accelerator. Two grounded wires up- and downstream of the sense wire limit the ionisation volume. This simple chamber is used as a safety feature to stop the machine if an unexpected high dose per pulse is applied. It does not record the applied dose, nor does it monitor different parts of the beam.

Another wire chamber used to monitor the photon treatment beam is the DAVID chamber by PTW-Freiburg, Germany [Poppe, et al. 2006]. It is positioned in the accessory holder of the linear accelerator below the multi-leaf collimator. The wires spread along the travel axes of the leaf pairs of the MLC with one wire per leaf pair. It is used to monitor the opening of the leaves as the signal is directly proportional to the leaf opening and thus the line integral of the ionisation density along the wire. As the

DAVID chamber is below the secondary collimators, it cannot be used to monitor flatness or symmetry of an arbitrarily shaped radiation beam. Moreover it monitors only one dimension, such that symmetry and flatness could not be monitored in both required dimensions.

Other methods to monitor the beam below the secondary collimator include the COMPASS system by IBA Dosimetry (Uppsala, Sweden) which consist of an array of 40 x 40 ionisation chambers [Boggula, et al. 2010] and the integral quality monitoring (IQM) system which consists of a large area ionisation chamber with a gradient in the electrode plate separation along the direction of the MLC motion [Islam, et al. 2009, Chang, et al. 2013].

2.4.5 Liquid Filled Dose Chambers

Another monitor for the radiation field behind the secondary collimator consists of a liquid filled pixel ionisation chamber and was designed to work with a miniature MLC (ModuLeaf, MRC Systems GmbH, Heidelberg, Germany) [Hofmann 2003, Eberle, et al. 2003]. It is used gantry mounted and is filled with isooctane, a nonpolar liquid. The chamber volume consists of a read-out electrode on which 400 signal electrode pads are placed. Figure 2-12 shows the segmentation of the signal electrode. The pad rows are aligned to the collimator leaves.

The chamber is mainly used to monitor the individual settings of the leaf positions of a MLC under photon radiation. This prototype analyses the position of two MLCs with one pad row, so that the individual position cannot be monitored.

The main advantage of a liquid filled ionisation chamber is the higher density of the liquid compared to air or gas. Thus a smaller active volume is needed to gain a sufficient signal-to-noise ratio. The main disadvantage of the prototype is the dose rate dependence of the signals.

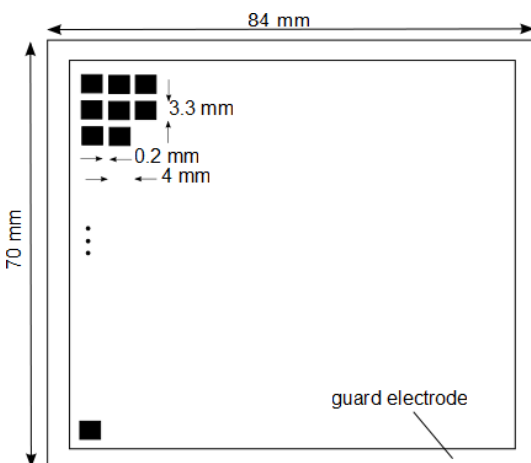


Figure 2-12: Segmentation of liquid filled chamber of German Research Cancer Centre (adapted from [Hofmann 2003])

In a further development of the chamber [Berghöfer, et al. 2005], the authors used tetramethylpentane (TMP) in a high purity grade, although Hofmann (2003) showed that the chamber signals are highly dependent on the purity of the liquid. The current signal can be increased by a factor of 4 with respect to isooctane.

The signal electrode has 24 x 20 interconnected square conductive pixels on each side. The pixels are 3.3 mm x 3.3 mm with a spacing of 0.2 mm.

With this chamber design the dose rate dependence persists. The relationship between the current and the dose rate is a non-linear function. Therefore for small currents the corresponding dose-rate is overestimated. The effect can be corrected by using the inverse function.

2.5 External Conditions

The monitor chamber signals are subject to several influences. The applied dose rate influences the signal level and chambers open to air are affected by temperature and pressure changes as well as by varying humidity. Besides the primary beam which the chamber shall monitor, head scatter from components like primary collimator and flattening filter as well as backscattered radiation from mirror and secondary collimator reach the chamber and thus affect the output factor of the linear accelerator.

Effects like quality of photon or electron radiation, polarity of applied voltage or incident beam's diameter don't change during operation in a selected mode for which the chamber is calibrated during installation. Therefore no corrections for these effects have to be applied.

2.5.1 Dose Rate

In radiotherapy different dose rates are applied to deliver the radiation to the patient. Varying the dose rate can be achieved by increasing the dose per pulse or by increasing the repetition rate. For electron radiation the dose rate is typically 3 Gy/min to 9 Gy/min. For photon radiation typically 2 Gy/min to 5 Gy/min are used. Low dose rates of 0.5 Gy/min are rarely applied. For flattening filter free configurations dose rates of up to 10 Gy/min are achieved which mainly is owed to the higher dose per pulse. The advantage of a higher dose rate is the faster delivery of the radiation such that the effect of intrafractional set-up errors of the patient is minimized. In further developments of accelerating systems, the dose rate might be increased further so that the question arises whether a higher dose rate has a significant effect on the requirements to the monitor chamber.

The dose per pulse influences the recombination of the gas in the monitor chamber. Higher doses per pulse produce more electron-ion pairs which lead to a higher recombination. Therefore the increase in signal is not proportional to the increase in dose (for details see chapter 2.1.3). For a linear accelerator operating at defined constant dose rates the chamber can be calibrated at these operating points.

If continuous sweeping of dose rate is realized by adapting the dose per pulse, a correction algorithm is needed. Such a correction is suggested in appendix A. Therefore for continuous change of dose rate a change in pulse repetition frequency (prf) is favoured. The prf has to be low enough to allow for the ions to drift to the electrodes before the next pulse occurs. For details see chapter 2.1.2.

2.5.2 Temperature, Pressure and Humidity

Temperature and pressure influence the density and thus the number of ionisable molecules of the gas in an unsealed ionisation chamber. Therefore the chamber signal has to be corrected in chambers open to air by

$$k_{\rho} = \frac{p_0 T}{p T_0} \quad (23)$$

with $p_0 = 101.3$ kPa and $T_0 = 293.2$ K [Reich 1990].

For extremely accurate measurements a correction for humidity is recommended [Johns und Cunningham 1974]. Besides this short term effect, humid air may lead to corrosion in chambers open to air. Blad, Nilsson and Knöös (1996) observed a corrosion effect for an unsealed chamber in a Philips SL linear accelerator with air of higher humidity. The effect is believed to be more pronounced in air containing acids or other aggressive substances [Blad, Nilsson and Knöös 1996].

2.5.3 Head Scatter and Backscatter

The energy fluence per monitor unit coming from the linear accelerator head to a point in air, e.g. the monitor chamber volume in the accelerator head, can be expressed as [Olofsson, Georg and Karlsson 2003]

$$\frac{\Psi_{tot}}{MU_{tot}} = \frac{\Psi_p + \Psi_e + \Psi_c + \Psi_m}{MU_p + MU_e + MU_c + MU_m} \quad (24)$$

where ψ is the energy fluence and MU the monitor signal. The indices p, e, c and m represent primary, extra-focal (head scatter), secondary collimator (backscatter), and beam modulator contributions. The contribution of head scatter and backscatter from secondary collimator to the monitor chamber has been investigated manifold.

Head scatter is also called extra-focal radiation as it is the radiation not originating from the primary source (primary radiation) but consists of particles scattered in the treatment head. Figure 2-13 shows a schematic drawing of a linear accelerator head.

Sources for head scatter are mainly the primary collimator, flattening filter and beam stopper below the target. Their relative contribution to the beam was determined to be around 3.7%, 2.5% and 1.7%, respectively, for a 28.6 x 28.6 cm² field in a 6 MV beam of a Siemens MD2 [Chaney, Cullip and Gabriel 1994]. The ratio of primary to scattered radiation in the isocentre plane was determined to be 10.4. This is in agreement with the finding of Dunscombe and Nieminen who derived a ratio of 11.5 from an empirical model of the Siemens MD2 [Dunscombe and Nieminen 1992]. Sheik-Bagheri and Rogers investigated several linear accelerators at several energies by Monte Carlo simulation and found a contribution of the primary beam of 92 % to 97 % at isocentre [Sheikh-Bagheri and Rogers 2002]. In flattening filter free linacs the amount of head scatter is reduced [Zhu, Kang and Gillin 2006, Vassiliev, et al. 2006].

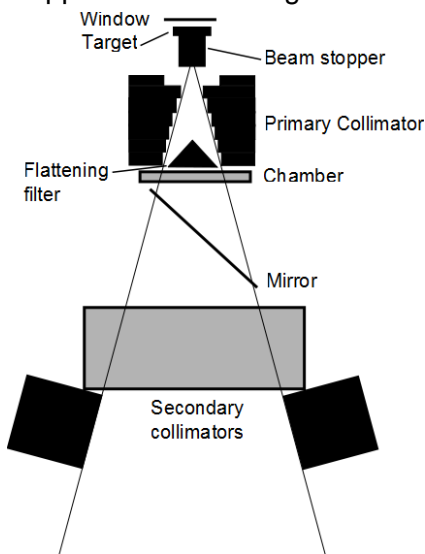


Figure 2-13: Schematic drawing of a linear accelerator head

Moreover, the radiation scattered back into the monitor chamber from the secondary collimators may contribute to the signal measured by the monitor chamber. At wider collimator settings less backscatter reaches the dose chamber and thus the probable distortion of the primary dose measurement is reduced.

The amount of backscattered radiation was quantified by photoactivation [Patterson and Shragge 1981], beam on time with beam current feedback disabled [Huang, Chu and Bjärngard 1987], measurement of number of beam pulses [Yu, Sloboda and Mansour 1996, Huang, Chu and Bjärngard 1987, Sharpe, et al. 1995], addition of an attenuator between the collimator and the monitor chamber [Luxton and Astrahan 1988], target charge [Watts and Ibbott 1987, Lam, Muthuswamy and Ten Haken 1998], and measurement of forward photon fluence from the target with telescopic pin-hole collimation [Lam, Muthuswamy and Ten Haken 1996, Kubo and Lo 1989, Duzenli, McClean and Field 1993, Yu, Sloboda and Mansour 1996, Hounsell 1998, Sanz, Alvarez and Nelli 2007], for several linear accelerators from various manufacturers.

Linear accelerators affected by backscatter include

- 18 MV AECL Therac-20 [Patterson and Shragge 1981, Kubo 1989, Kubo and Lo 1989]
- 23 MV CGR Saturne 25 [Luxton and Astrahan 1988]
- Saturne 41 [Sanz, Alvarez and Nelli 2007]
- Varian Clinac 2100/2300 and Clinac 1800 series [Duzenli, McClean and Field 1993, Yu, Sloboda and Mansour 1996, Lam, Muthuswamy and Ten Haken 1998, Liu, Mackie and McCullough 2000, Ravikumar and Ravichandran 2001].

The increase in backscatter of a small field (0.5 cm x 0.5 cm to 3 cm x 3 cm) compared to a 40 cm x 40 cm field is approx. 2 – 4 % in these linacs [Liu, Mackie and McCullough 1997, Verhaegen, Symonds-Taylor, et al. 2000, Ravikumar and Ravichandran 2001]. The amount of charge collected by the monitor chamber per photon generated in the target changes with collimator setting as the amount of backscattered radiation increases with decreasing field size. Therefore the output is reduced with decreasing field size in the above mentioned linacs.

In several other linacs, such as the 4 MV Varian Clinac-4, the Clinac 600C and 6/100 and a series of Siemens 6–15 MV linacs (Mevatron VI, XII, 74 and 77 and MD2), the output of the linacs is not affected by the backscatter to the monitor chamber [Huang, Chu and Bjärngard 1987, Muralidhar, et al. 2007, Lam, Muthuswamy and Ten Haken 1998, Verhaegen and Das 1999]. The reason for this difference was investigated by several authors.

Duzenli et al. compared the backscatter influence for two Varian accelerators, one equipped with a mica chamber with copper plated steel windows (Clinac 600C) and the other equipped with a Kapton beam monitor chamber (Clinac 2100C) [Duzenli, McClean and Field 1993]. They conclude that for the Clinac 600C the effect of backscatter is negligible, but for the Clinac 2100C, the effect has to be considered. This finding is supported by the results of Ravikumar and Ravichandran [Ravikumar and Ravichandran 2001] and Kubo and Lo [Kubo and Lo 1989] who found a decrease of 4% in machine output for the Clinac 1800 equipped with a Kapton chamber and negligible influence in a Clinac 1800 equipped with a mica chamber. Moreover the Siemens machines investigated are equipped with an alumina chamber, where no effect could be found. The chambers used in today's Siemens linacs are essentially the same.

For the Philips SL15 accelerator (now Elekta) Hounsell investigated the effect of the backscatter plate [Hounsell 1998]. The accelerator is equipped with a Mylar chamber and an additional aluminium alloy plate of 3 mm thickness situated 1.6 cm below the chamber. If this plate is removed, the output decreases for a 4 cm x 4 cm field compared to a 40 cm x 40 cm field by more than 4.5 %. With the plate present, the variation in output is within 0.3 %.

Kairn et al. simulated an Elekta linac and found backscatter of <0.35 % if the plate is present. With the plate removed, the backscatter increased up to 2.4 % for 6 MV and 4.4 % for 10 MV [Kairn, et al. 2009].

Therefore it can be concluded that the effect of backscatter depends strongly on the chamber design. If an exit window at the chamber is present which absorbs scattered electron radiation to a great extent, the effect of backscattered radiation is negligible. If the exit window is thin, so that backscattered electrons can reach the sensitive volume of the ion chamber, the backscatter effect has to be accounted for in dose calculations or a backscatter plate has to be added, as in Elekta linacs.

No difference concerning the backscatter factor was observed between flattening filter free linacs and configurations including the flattening filter [U. Titt, O. Vassiliev, et al. 2006, Zhu, Kang and Gillin 2006].

3 Evaluation of a Current Monitor System

In order to investigate the ambient radiation field in the linear accelerator head the new dose chamber will be designed for, Monte Carlo simulations were conducted for a Siemens linear accelerator. The effects of flattening filter and primary collimator on the photon beam as well as backscatter effects from components below the dose chamber were simulated to characterize the radiation field which a new dose monitor system has to detect.

Photon radiation was simulated and measured with and without the flattening filter (unflat), denoted by $x\text{ MV FF}$ and $x\text{ MV UF}$. Moreover a configuration without the primary collimator and flattening filter was simulated, denoted by $x\text{ MV UF w/o } 1^\circ\text{ colli}$. This configuration would allow moving a target into the electron beam setup to generate unflat photon energies without using one of the two setups for flat photon radiation and would thus increase the number of available photon configurations per linac which is limited by mechanical constraints.

In order to estimate the profile of the beam at the position of the dose chamber in the linear accelerator head, the energy fluence vs. position at this position for 6 MV and 15 MV photon beams was investigated. Spectra of the radiation fields were simulated to characterize the beam at the chamber position.

Furthermore as seen in chapter 2.5.3 some dose chambers are affected by backscattered radiation. This radiation is analysed and its amount at small field sizes is simulated to determine the influence under different configurations like flattened or unflattened beams with and without primary collimator. Moreover the effect of a plate to block backscattered radiation was investigated.

To evaluate the capabilities and drawbacks of the current Siemens dose chambers and other foil chambers to monitor the beam, measurements were done with three dose chambers. First of all the dose chambers currently used by Siemens were assessed. As described in chapter 2.4.1 the photon dose chamber used by Siemens is made from alumina and is filled with nitrogen. The electron chamber is made out of Kapton foils. Moreover a prototype of a foil chamber, provided by PTW-Freiburg, Germany was available.

First of all the behaviour of the linac at start-up was observed in order to eliminate adverse effects on the measurements and their interpretation. Moreover the effect of backscatter to the three monitor chambers in flat and unflat beams was investigated.

Furthermore the proportionality of the measured signal to the applied dose was examined to investigate whether chamber response is proportional at low monitor unit settings.

As one of the main tasks of a monitor chamber is to monitor the symmetry of the radiation field, the capability of the Siemens monitor chambers to do so was investigated by changing the beam profile.

3.1 Simulations

3.1.1 Materials and Methods

Monte Carlo simulations were conducted with the EGSnrc code and BEAMnrc. Geometry and material details were provided by Siemens Healthcare for a Siemens Primus with 3D-MLC (see appendix B). Figure 3-1 shows the set-up of the simulated linear accelerator for photon and electron radiation showing one representative scoring plane. Y-jaws are not shown in this view. 6 MV and 15 MV photon beams as well as six electron energies were simulated. Incident particles to the simulation were electrons of

different primary energy (see appendix B) which enter the simulation and hit first of all the target in photon mode or the primary scattering foil in electron mode.

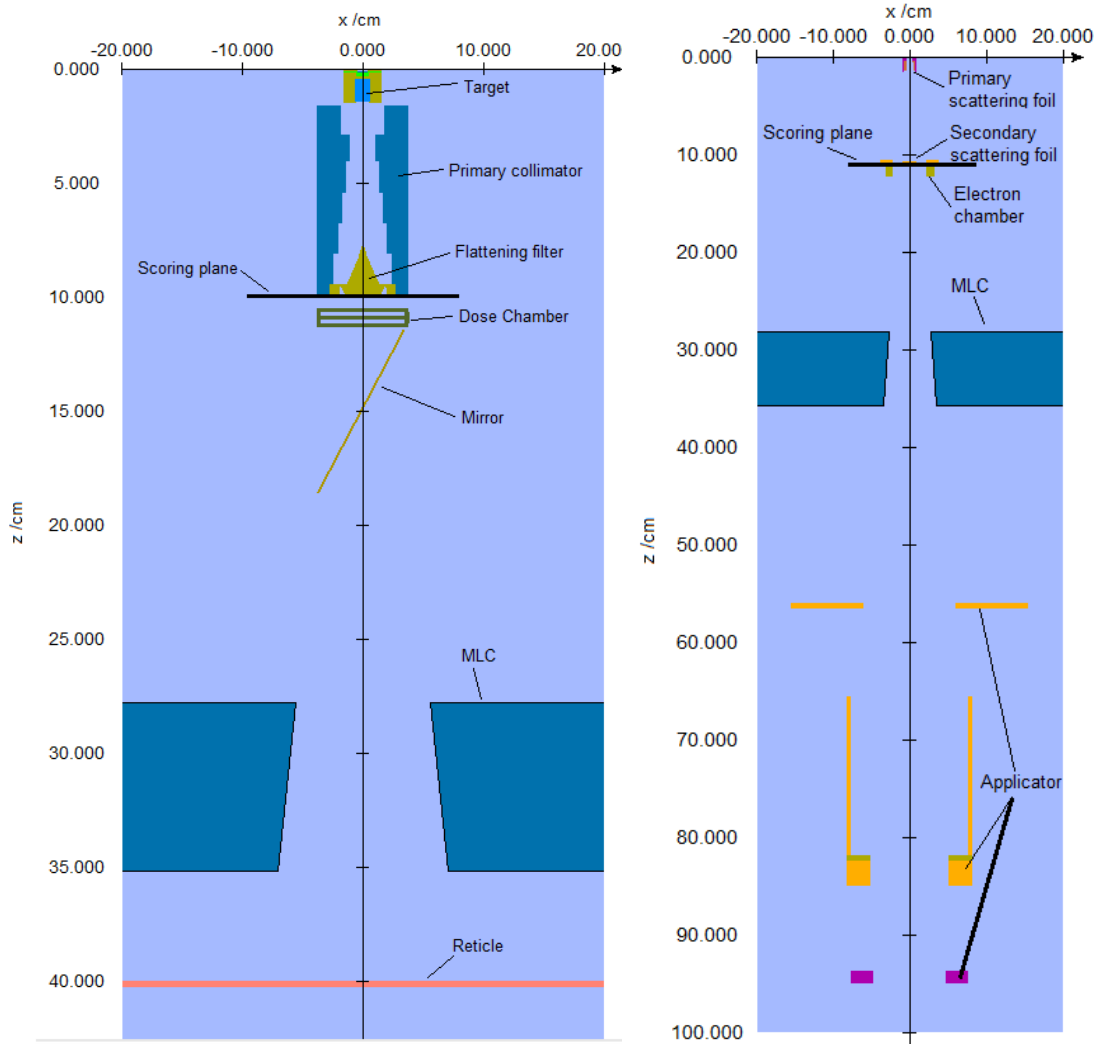


Figure 3-1: Simulated linac head with scoring planes; right: 6 MV photon; left: 17 MeV electron

For photon radiation target, primary collimator, absorber (only 15 MV), flattening filter, monitor chamber, Y-jaws, MLC and reticle were modelled. As monitor chamber the photon chamber and a prototype of a foil chamber was employed. The prototype of a foil chamber features essentially the same materials as the electron chamber but has a larger diameter of 3.175 cm. With the photon chamber present the mirror was modelled as well. When using the foil chamber, the mirror was replaced by a horizontal plane which consisted either of plexi glass of 3 mm thickness or air. The simulated field size was 5 cm x 5 cm at the isocentre with SID 100 cm.

For electron radiation primary and secondary scattering foil, foil monitor chamber, Y-jaws, MLC and a 10 cm x 10 cm applicator were simulated. SID was again 100 cm.

Each component was given a different latch bit, such that the origin of particles in each scoring plane could be evaluated (see appendix B). Three scoring planes were generated behind flattening filter, dose chamber and mirror. At such a plane the properties of all particles traversing this plane were stored in a file and could be analysed.

Dose zones were selected in the two ionisation volumes of the dose chambers.

The number of initial histories was chosen such that a minimum uncertainty is reached without getting aliasing effects caused by the analysis software which could not handle files larger than 2.3 GB. The uncertainty was between 0.3 % and 2.0 % for all simulations considering all particles.

Data analysis was carried out with BeamDP (National Research Council Canada 1999), the data processor for BEAMnrc. Energy fluence and energy fluence versus position for each configuration were evaluated by analysing the contribution of the particles at a scoring plane to the field. For energy fluence for example the energy fluence of all particles over the area of the scoring plane was summed.

The analysis was carried out for all particles (photons and electrons), all particles with latch bits 6, 7 or 8 (i.e. particles that interacted with Y-jaws, MLC or reticle), electrons and electrons with latch bits 6, 7 or 8.

Moreover for the dose zones in the ionisation volumes of the monitor chambers the dose fraction of backscatter originating from Y-jaws, MLC or reticle was evaluated to analyse the effect.

How the flattening filter and the primary collimator influence the beam profile was investigated by comparing three configurations for both photon energies:

- with flattening filter
- without flattening filter
- without flattening filter and without primary collimator

Investigations by other authors revealed no qualitative difference in backscattered radiation between flattened and unflattened beams [Zhu, Ahnesjö, et al. 2009]. In these simulations this effect was verified by scoring the energy fluence over the whole width of the dose chamber for particles with latch bits 6, 7, and 8, i.e. particles from components below the dose chamber. Moreover the effect of a backscatter plate comparable to the Elekta system (see chapter 2.4.3) was simulated.

The dose in the ionisation volume of the dose chamber, induced by backscattered particles was simulated to compare the current photon dose chamber and a chamber made of polyimide foils. Moreover the effect of a backscatter plate and the amount of backscattered radiation in electron mode were simulated.

3.1.2 Results and Discussion

3.1.2.1 Effect of Flattening Filter and Primary Collimator

The flattening filter is designed to shape a flat field in the isocentre plane by attenuating radiation in the inner part of the radiation field which can be seen in figure 3-2 and figure 3-3. The energy fluence scored behind the dose chamber is shown. No differences between configurations with and without the primary collimator (1° colli) are observed.

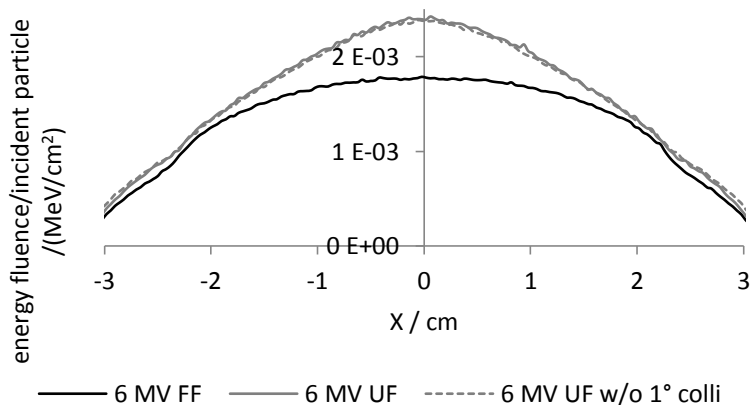


Figure 3-2: Energy fluence vs. position behind the dose chamber for 6 MV beams

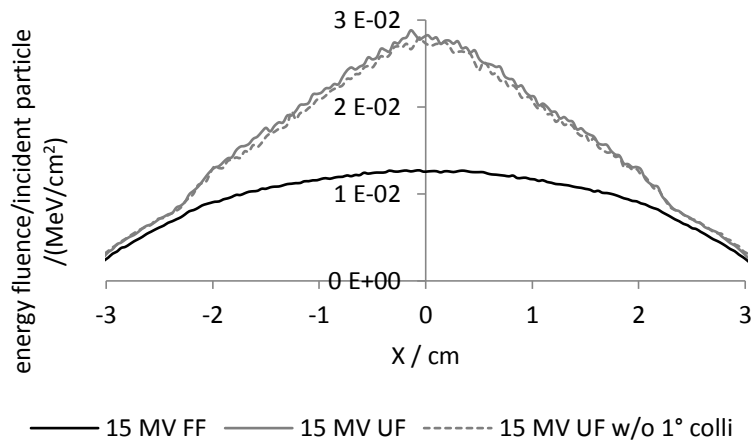


Figure 3-3: Energy fluence vs. position behind the dose chamber for 15 MV beams

The flattening filter has a beam hardening effect. As can be seen from the energy fluence distribution, the spectrum of the beam is shifted to higher energies for the flattened field (FF) (compare figure 3-4). For beams without the primary collimator (UF w/o 1° colli) even more low energy radiation is present (compare figure 3-4). For configurations with a primary collimator this low energy radiation is absorbed and thus does not reach the scoring plane. The pronounced peak at 511 keV due to annihilation photons is clearly visible.

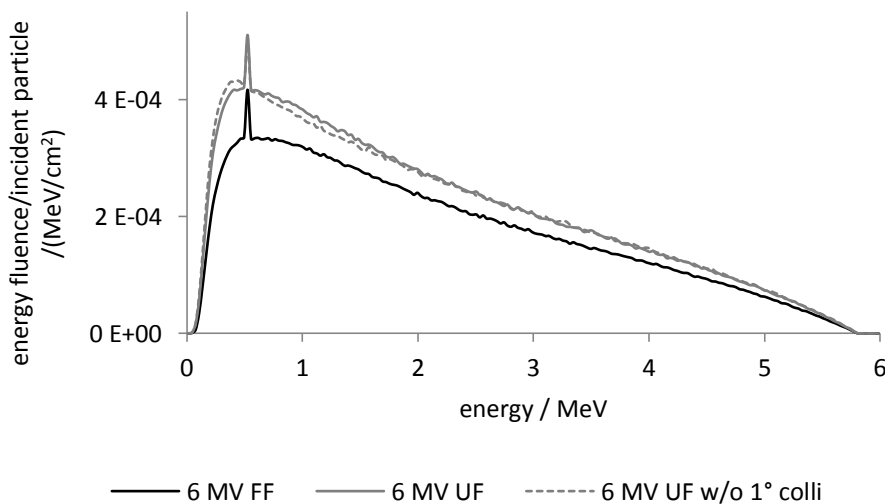


Figure 3-4: Energy fluence per incident particle behind the dose chamber for 6 MV beams

Several authors investigated the effect of removing the flattening filter, either by Monte Carlo simulations or by measurements. Sixel and Faddegon calculated spectra of a 6 MV Therac-6 accelerator (Theratronics Int. Ltd., Kanata, Ontario, Canada) used for radiosurgery without flattening filter [Sixel and Faddegon 1995]. Monte Carlo simulations were compared to calculations based on the small angle analytical Schiff spectrum and to simulations by Mohan et al. for a flattened beam [Mohan, Chui and Lidofsky 1985]. The spectra reveal that the unflattened beam is softer, i.e. more low-energy x-rays contribute to the spectrum which agrees with the conducted simulation.

3.1.2.2 Backscatter

Concerning backscatter no qualitative difference between flat and unflat beams could be observed which agrees with the findings of other authors [Zhu, Ahnesjö, et al. 2009]. In figure 3-5 the backscattered energy fluence for 6 MV beams is given. The spikes result from electrons with high energy. As the number of backscattered particles is low compared to the primary beam, the uncertainty in these simulations is around 20 % and single high energy particles lead to distortions in the distribution.

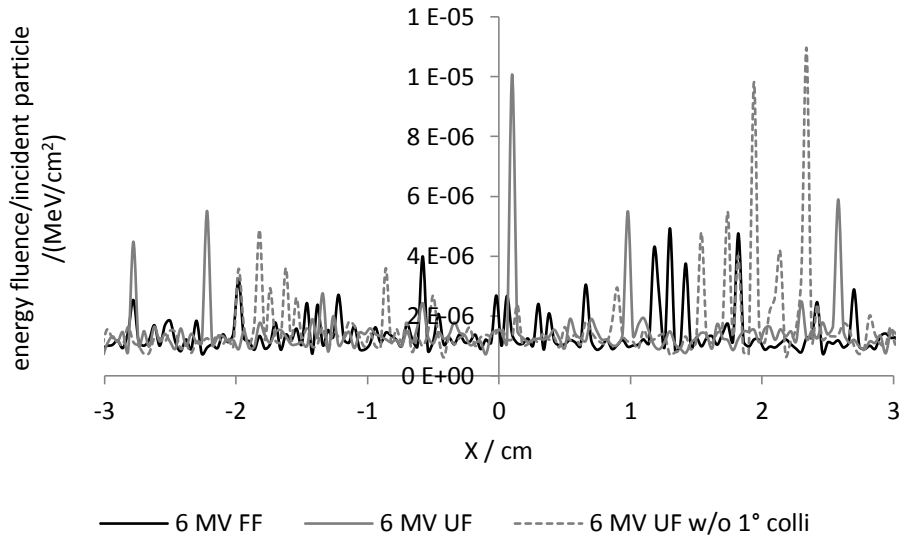


Figure 3-5: Energy fluence vs. position behind the dose chamber for 6 MV backscattered radiation

From Elekta it is known that the backscattered radiation is blocked by inserting an aluminium plate behind the dose chamber (see chapter 2.4.3). The dose from the backscattered radiation can also be significantly reduced when inserting an acrylic glass plate.

The energy fluence for radiation scattered back to a plane below the monitor chamber is given in figure 3-6. The peaks result from the backscattered high energy electrons (dotted lines). By inserting a 3 mm thick acrylic glass plate below the chamber, most electrons are blocked so that the mean energy distribution is flatter (red lines).

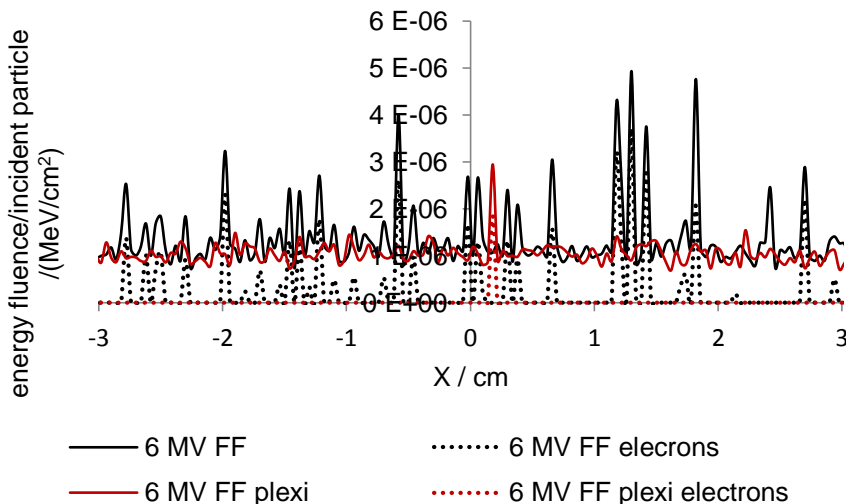


Figure 3-6: Energy fluence vs. position of radiation scattered back to monitor chamber from Y-jaws, MLC or reticle for a 6MV beam

Also for 15 MV a significant reduction in energy fluence of backscattered electrons is observed. As these backscattered electrons have higher energies not all of them are blocked (see figure 3-7).

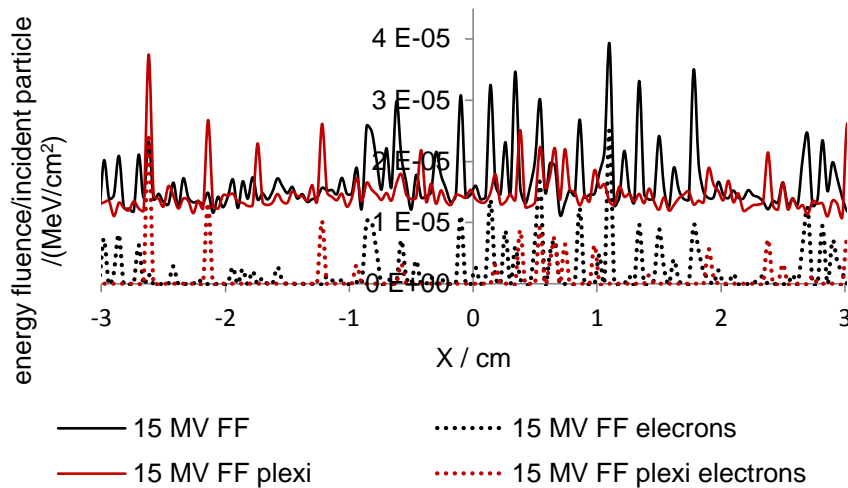


Figure 3-7: Energy fluence vs. position of radiation scattered back to monitor chamber from Y-jaws, MLC or reticle for a 15MV beam

Moreover for a 5 cm x 5 cm field the fraction of dose from radiation scattered back from the Y-jaws, MLC and reticle that enters the ionisation volumes of the chamber was scored.

For flat 6 MV no backscattered radiation is detected in the photon chamber (with or without mirror) which agrees with the investigation of Huang et al. and Muralidhar et al. [Huang, Chu and Bjärngard 1987, Muralidhar, et al. 2007].

For a chamber having foils as entrance and exit window, the dose originating from backscattered radiation is around $2.1 \% \pm 0.9 \%$ and $5.6 \% \pm 3.1 \%$ in upper and lower chamber volume, respectively. This is in the range of the amount of backscattered radiation observed by Ravikumar and Ravichandran who found 4 % backscattered radiation to the monitor chamber of a Varian Clinac 1800 linear accelerator equipped with a foil chamber [Ravikumar and Ravichandran 2001] and Hounsell who observed an increase of 4.5 % when reducing the field size from 40 cm x 40 cm to 4 cm x 4 cm [Hounsell 1998]. Verhaegen et al. found an increase of 2-3 % when reducing the field size from 40 cm x 40 cm to 0.5 cm x 0.5 cm [Verhaegen, Symonds-Taylor, et al. 2000].

The amount of backscattered radiation entering the ionisation volumes can be reduced to $0.2 \% \pm 0.2 \%$ by inserting a 3 mm acrylic glass plate behind the chamber. For flattening filter free configuration the dose fraction in the lower chamber volume is reduced from $2.0 \% \pm 1.2 \%$ to $0.2 \% \pm 0.2 \%$. The mirror leads to the same reduction. The effect of a plate between monitor chamber and secondary collimator has also been investigated by Hounsell for a Philips SL15 accelerator [Hounsell 1998]. When a 3 mm thick aluminium plate was in place, the increase in backscatter, when reducing the field size from 40 cm x 40 cm to 4 cm x 4 cm, was approximately 0.3 %.

For flat 15 MV a backscattered dose fraction of 0.1 % - 0.3 % is detected in the photon chamber (with or without mirror) which agrees with the finding of Huang et al. who did not observe a change in accelerator output while varying the field size [Huang, Chu and Bjärngard 1987].

For chambers with foils the dose fraction in the lower chamber volume from backscattered radiation is $5.1 \% \pm 1.9 \%$. This amount is comparable to the 4 % backscatter in 18 MV flat photon beams at a Varian Clinac 2100C accelerator equipped with a Kapton chamber found by Duzenli et al. [Duzenli, McClean and Field 1993]. The backscatter can be reduced to $1.4 \% \pm 0.5 \%$ by inserting a 3 mm acrylic glass plate.

For electrons the dose fraction in the lower ionisation volume from backscattered radiation is between $0.3 \% \pm 0.05 \%$ (17 MeV) and $0.7 \% \pm 0.02 \%$ (6 MeV).

3.2 Measurements

3.2.1 Materials and Methods

To investigate the capabilities of the current dose monitor system to monitor the beam and investigate the possibilities of a foil chamber, measurement with the current Siemens photon (PhCh) and electron chamber (ECh) (see chapter 2.4.1) and a prototype of a foil dose chamber (FCh), provided by PTW-Freiburg, Germany (see chapter 2.4.4), were made.

At a Siemens Oncor Expression equipped with 160 MLC the signals from the dose chambers were probed at a test point on the main dosimetry PCB G42 (Rev. E) after the first signal amplification and supplied to a LeCroy waverunner 6100A 1GHz oscilloscope (LeCroy Corporation, Chestnut Ridge, NY, USA) in front of the bunker. In figure 3-8 the dosimetry electronics for Monitor 1 for photon radiation (X Mon1) up to the first amplification stage is given. The variable resistors R_{var} X-Hi and R_{var} X-Lo are plug-in resistors to adjust the gain of the first amplification stage depending on the selected energy.

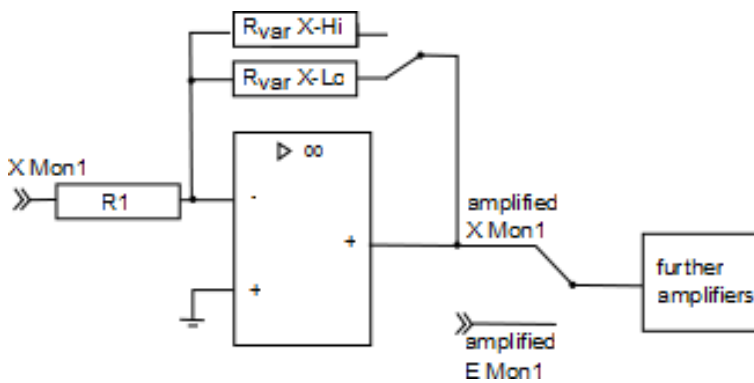


Figure 3-8: Dosimetry electronics

The linac was operated in open loop, i.e. in an operating mode in which the control loop is not active and therefore the applied dose rate is not controlled. By this the foil chamber prototype could be used as well. It would not give meaningful input to the control system due to its different segmentation.

The gantry was at 180° with the mirror removed. For output measurements an ionisation chamber was placed at the isocentre (see figure 3-9). For photon radiation a Farmer chamber (PTW-Freiburg, Germany, type 30013) and for electrons a Roos chamber (PTW-Freiburg, Germany, type 34001) was connected to a Multidos with TBA Control Unit (PTW-Freiburg, Germany). As built up 2 cm (6 MV, 6 MV UF, 6 MeV) or 4 cm (15 MV, 15 MV UF, 15 MeV) rigid water RW3 were used. Backscatter material was at least 10 cm of RW3. All measured signals were temperature and pressure corrected.

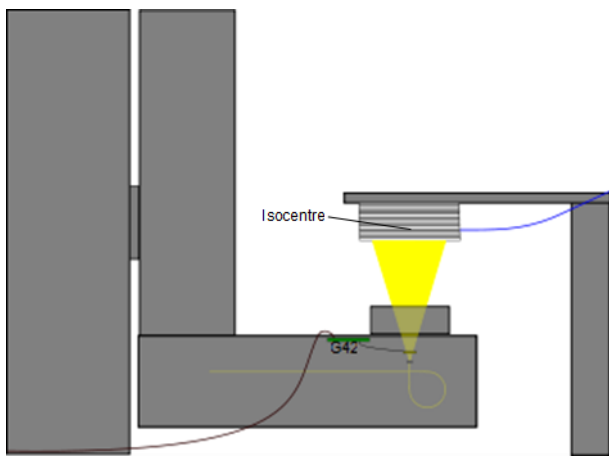


Figure 3-9: Set-up for evaluation of current dose monitor chambers

Measurements were done for 6 MV and 15 MV flattened, 6 MV and 15 MV unflattened photon beams and for 6 MeV and 15 MeV electron beams. When removing the flattening filter, the R_{var} X-Hi and R_{var} X-Lo determining the first amplification stage were changed for monitor 1 and monitor 2 to adapt the peak of the signal of the dose chamber to the electronics. Otherwise the current peak would be higher than the peaks the electronics are designed for. Moreover these resistors were used during the measurements with the foil chamber. In table 3-1 the used resistor values are given.

Table 3-1: Resistor on G42 for flat and unflat photon beams

	6 MV Mon1	6 MV Mon2	15 MV Mon1	15 MV Mon2
flat	51.3 M Ω	300 k Ω	82 M Ω	475 k Ω
unflat	27 M Ω	180 k Ω	51 M Ω	300 k Ω

First of all, the repeatability of the linac performance was checked for each energy by repeating ten measurements with 100 MU and measuring the output at the isocentre.

To assess the influence of the field size on the dose chamber signals, five consecutive measurements for 2 cm x 2 cm and 40 cm x 40 cm field size each were done. The dose chamber signals of one second were stored and their pulse peak values were averaged. This average was compared for both field sizes.

Furthermore the proportionality of the monitor 1 dose chamber signal to the applied dose was checked. This relation should be linear to secure a proper measurement of the applied dose over a wide range. This is checked for 6 MV, 6 MV UF and 6 MeV at high dose rate³ by summing the peak values of the dose pulses over 1 MU, 3 MU, 5 MU and 10 MU and normalizing the sum to the dose at isocentre. The field size was kept constant at 20 cm x 20 cm and three measurements per MU value were done.

In order to assess the capability of the current Siemens dose chambers to detect changes in beam symmetry, the electron beam was steered parallel to the direction of the waveguide (called inplane direction) by changing the current to the steering coils such that the incident angle on the exit window was not 90°. For measurement of the symmetry of the radiation field in the isocentre a StarCheck (PTW-Freiburg, Germany) was used, field size was 20 cm x 20 cm. The change of the dose chamber signals in inplane direction was analysed by investigating the change in the peak value, averaged over one second. From these values symmetry was calculated and compared to symmetry measured at isocentre for 6 MV, 6 MV UF and 6 MeV. Detection of symmetry changes was not examined for the foil chamber due to its segmentation which was not subject of this investigation.

³ 6 MV: 3 Gy/min at 222 Hz; 6 MV UF: 6.5 Gy/min at 222 Hz; 6 MeV: 9 Gy/min at 185 Hz

3.2.2 Results

3.2.2.1 Stability of Linac

The ten consecutive measurements showed that the recorded charge at isocentre was constant within 0.36 % (one relative standard deviation) so that the linac performance is considered to be constant for all energies under investigation for short-term comparison.

For 6 MV and 6 MV UF the linac starts up slowly and settles after a few pulses as can be seen in figure 3-10. For electrons (see figure 3-11) and higher energy photon beams this behaviour was not observed. Therefore all measurements except proportionality tests were done at least one second after the linac started.

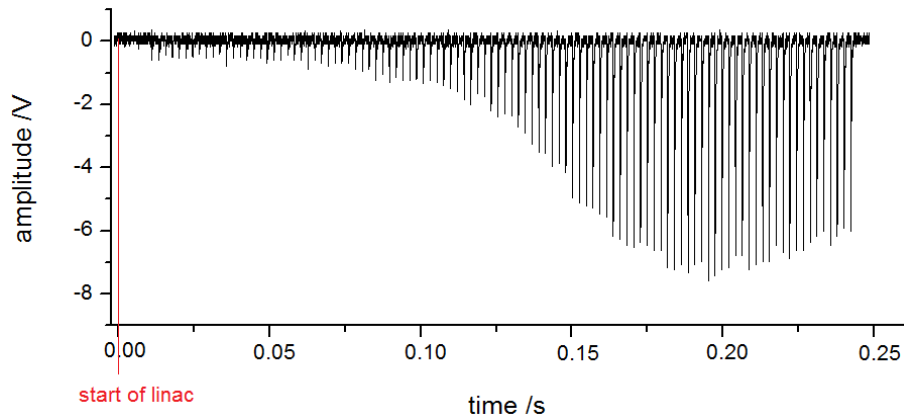


Figure 3-10: Foil chamber signals for 1 MU at 6 MV UF

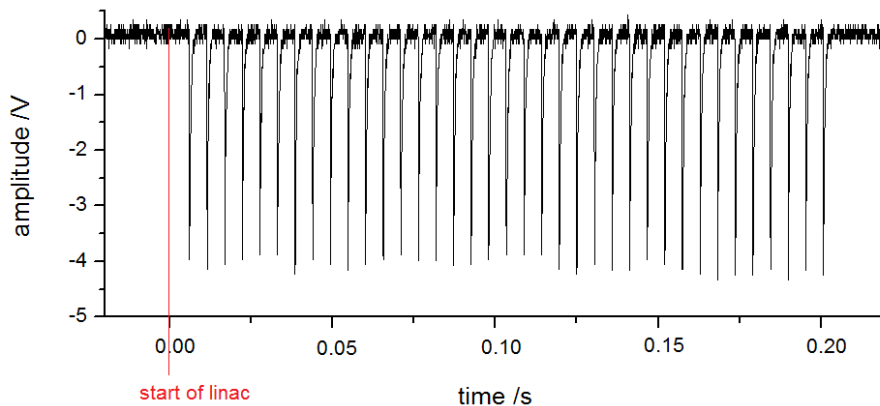


Figure 3-11: Foil chamber signals for 1 MU at 6 MeV

3.2.2.2 Backscatter

When decreasing the field size, more backscattered radiation from the MLC and Y-jaws reaches the dose chamber (see chapter 2.5.3). As can be seen in figure 3-12 for flattened photon beams the signal does not change significantly for the photon chamber. As the data for 15 MV was corrupted for the photon chamber, data for 5 cm x 5 cm field size is used for comparison. For unflat energies a slight increase can be observed.

More backscattered radiation can enter the Monitor 1 (Mon1) volume of the foil chamber. The signal of a 2 cm x 2 cm field is up to 6.3 % higher than for a 40 cm x 40 cm field (15 MV).

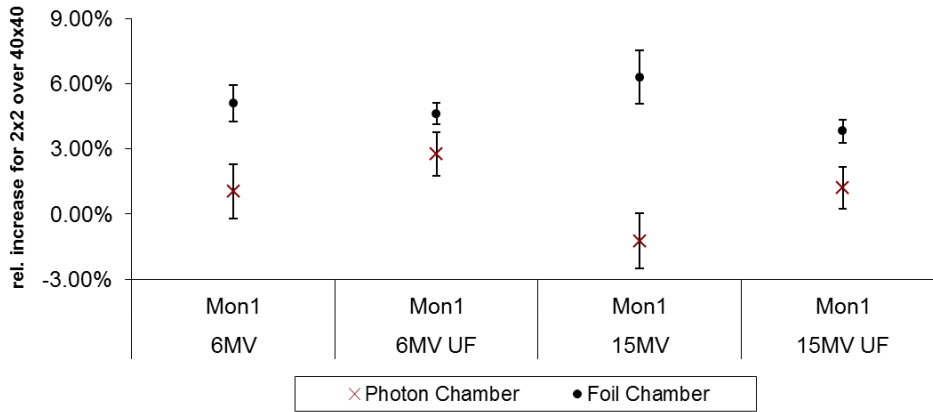


Figure 3-12: Backscatter to Monitor 1

For analysing the effect to the other chamber volume, the signal of some segments was analysed. Again the change in signal is much more pronounced for the foil chamber (compare figure 3-13; Segx = segment x). Segments 2 and 4 of the photon chamber and segments 3 and 7 of the foil chamber are in inplane direction. The amount of backscatter in the foil chamber is high due to the entrance window materials of the dose chambers. The alumina entrance window of the photon chamber blocks nearly all backscattered radiation whereas more backscatter can pass the polyimide foil of the foil chamber.

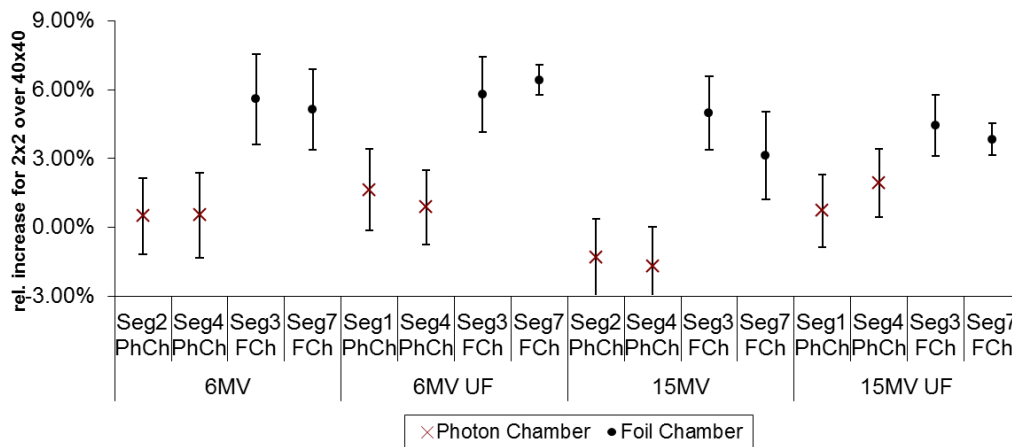


Figure 3-13: Backscatter to segments

3.2.2.3 Proportionality

For each MU value the sum of the dose peaks normalized to the dose at the isocentre was constant within 1 %. In figure 3-14 the average summed voltage per charge at isocentre is shown.

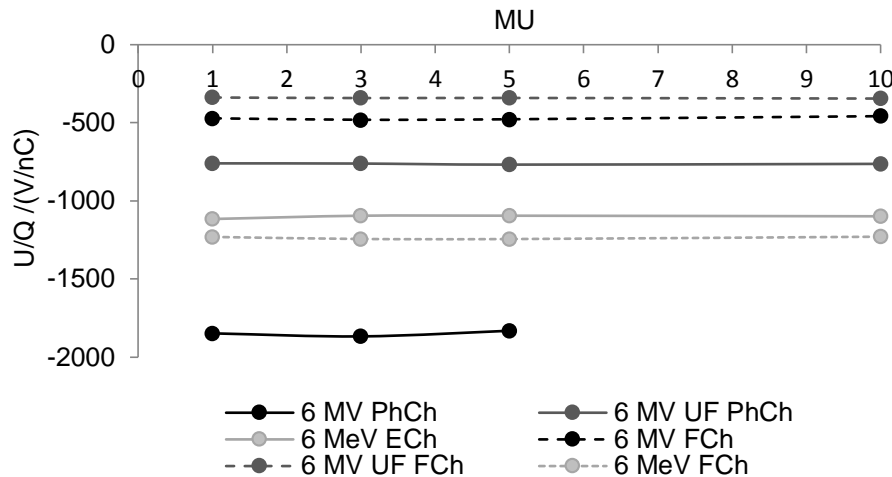


Figure 3-14: Sum of dose chamber voltage pulses per charge at isocentre for 1 MU to 10 MU

The higher V/nC values at flat 6 MV for the photon chamber compared to the foil chamber result from the use of the lower gain resistor values during the measurements with the foil chamber.

3.2.2.4 Symmetry Detection

For the photon and electron chamber symmetry was calculated from inplane segments. For photon radiation, the output with a steered beam is significantly lower compared to a beam hitting the target perpendicularly (see table 3-2). The symmetry given in table 3-2 is the maximum achievable distortion when steering the incident beam by the steering coils.

Table 3-2: Output change for steered beams

	Symmetry ([IEC 60976])	Signal level change
6 MV	110 %	-20 %
6 MV UF	105 %	-40 %
6 MeV	107 %	0 %

In table 3-3 the average peak of the dose chamber over 5 measurements across one second each is given for a non-steered beam (100%) and a steered beam (105 %, 107 % or 110 %). The percentage values in column two give the symmetry at isocentre according to IEC 60976 protocol.

In column four the symmetry based on the average voltage peak values is given. In the linac control system the dose pulse signals are multiplied by a factor with which the dose per pulse values at the control console result in a calculated symmetry of 0 % if the symmetry at isocentre is ok. As this factor is lacking at this stage of signal processing, the steered values are normalized to the non-steered ones and symmetry is calculated from these (column six). In the last column the difference between the symmetry values at isocentre measured with the StarCheck according to Siemens protocol for steered and non-steered beams (last but one column) are given.

For photon beams, the change in calculated symmetry from the dose chamber signals was not significant. For electrons, the change in symmetry could be detected, as can be seen by comparing columns six and eight of table 3-3.

Table 3-3: Symmetry changes for steered 6 MV, 6 MV UF and 6 MeV beams

		Avg. Voltage Peak /V	Sym- metry	Norm. to Sym. 100%	Norm. Sym- metry	Symmetry StarCheck	Difference Symmetry StarCheck
6MV	Seg 2 100%	-4.53		1.00			
	Seg 4 100%	-4.68	1.66%	1.00	0.00%	0.03%	
	Seg 2 110%	-3.55		0.78			
	Seg 4 110%	-3.71	2.28%	0.79	-0.62%	6.89%	6.86%
6MV UF	Seg 2 101%	-5.94		1.00			
	Seg 4 101%	-6.20	2.12%	1.00	0.00%	0.48%	
	Seg 2 105%	-3.49		0.59			
	Seg 4 105%	-3.60	1.51%	0.58	0.61%	2.78%	2.30%
6MeV	Seg 2 100%	-4.69		1.00			
	Seg 4 100%	-4.19	-5.70%	1.00	0.00%	0.67%	
	Seg 2 107%	-4.86		1.04			
	Seg 4 107%	-4.03	-9.41%	0.96	3.72%	4.16%	3.49%

This is due to two effects, the segment geometry and the beam profile at the chamber position. First of all, the photon chamber's segments sum the signal from 0.635 cm from the centre to 3.175 cm. To analyse the beam geometry a 6 MV photon beam was simulated resulting from an electron beam being tilted by 1°. The energy fluence was scored behind the chamber (at 11.327 cm from target) and at isocentre (SID 100) in air. As can be seen in figure 3-15 the profile of the beam at the chamber position does not change significantly from 2 cm to the edge of the chamber when the incident electron beam is tilted by 1°. The change in the inner 4 cm is moreover quite small. Therefore the signal change in the segments is not very high. The calculated symmetry of the non-tilted beam at the chamber position is 0.03 %, the symmetry of the tilted one 1.07 %.

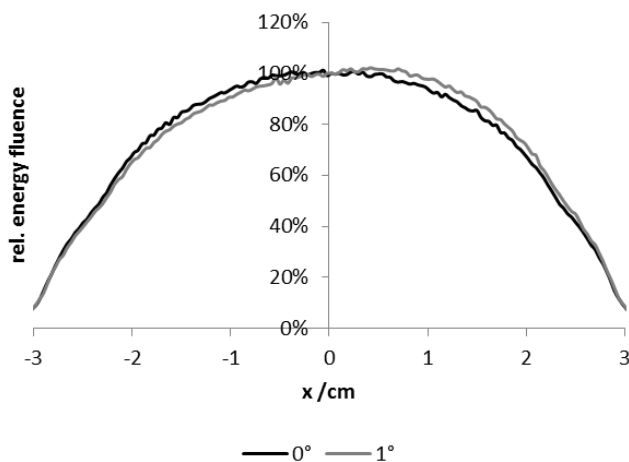


Figure 3-15: Simulated beam profile of a 6 MV photon beam scored at chamber position non-tilted (black line) and tilted by 1° (grey line)

The change in beam profile is much more pronounced at isocentre. Here the non-tilted beam has a symmetry of 0.06 % and the tilted one of 8.14 %.

Later measurements confirmed that the change in symmetry of the beam at the dose chamber position is not the same as in the isocentre plane. The change in symmetry is nevertheless proportional (see chapter 7.3.2.2.3).

As the diameter of the electron chamber is smaller and the beam's tilt is more pronounced at the chamber position, the segments detect changes more easily. Figure 3-16 shows the beam profile over the chamber diameter of a non-tilted and a tilted 17 MeV electron beam. At the chamber position the calculated symmetry is 0.35 % vs. 6.38 % whereas at a source to surface distance of 90 cm (SSD 90) it is 0.10 % vs. 3.08 % with a 10 cm x 10 cm applicator.

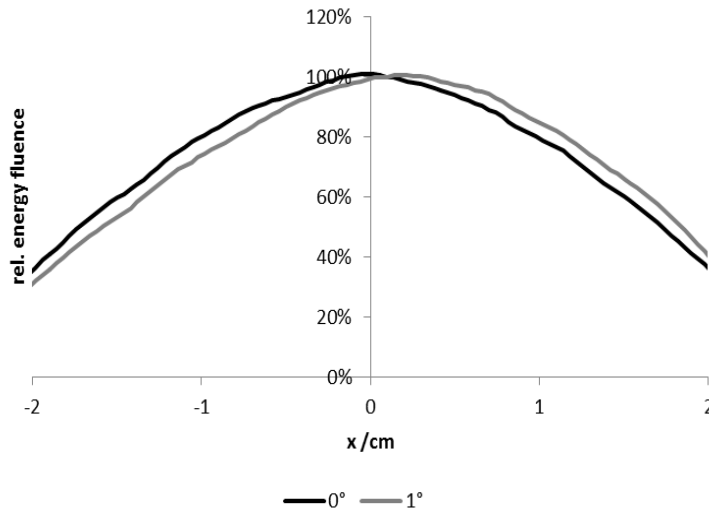


Figure 3-16: Simulated beam profile of a 17 MeV electron beam scored at chamber position, non-tilted (black line) and tilted by 1° (grey line)

3.2.3 Discussion

As the measurements were done during stable operation of the linac, the instable behaviour at the beginning of 6 MV photon beams is not relevant for the conducted measurements. Moreover it is not clinically relevant as in photon mode during start-up of the 6 MV beam less dose is applied per pulse but the total dose is correct. The start-up behaviour at 6 MV is due to the operation of the accelerator at the border of the acceptable limits. For rotational treatments this is corrected by the linac. The discussion of this behaviour is out of the scope of this work.

For the photon chamber the alumina plate at the bottom of the chamber blocks nearly all backscattered radiation such that the effect of changing field sizes is low as also observed by Huang et al. and Muralidhar et al. [Huang, Chu and Bjärngard 1987, Muralidhar, et al. 2007]. As the foil chamber lacks such a barrier, more backscattered radiation can reach the chamber. The increase in backscattered radiation by 3.5 - 6.3 % when reducing the field size from 40 cm x 40 cm to 2 cm x 2 cm agrees with the fraction of backscattered radiation found in the simulations (2.1 - 5.6 %). Moreover this is in the range of 2 - 4 % found by Ravikumar and Ravichandran, Hounsell and Verhaegen et al. when taking measurement uncertainty and differences in linac and chamber design into account [Ravikumar and Ravichandran 2001, Hounsell 1998, Verhaegen, Symonds-Taylor, et al. 2000].

Titt et al. and Zhu et al. investigated the effect of the flattening filter on backscatter in Varian linacs. They found no difference in the backscatter contribution between flattened and unflattened beams, which is in agreement with the measurements [U. Titt, O. Vassiliev, et al. 2006, Zhu, Kang and Gillin 2006].

From proportionality measurements during system validation tests it is known that the linearity of the current Siemens system is below 1 % for higher selected MUs and below 2 % for MU values up to 5 MU. This corresponds to the results seen here. No

significant difference between the foil chamber and the photon and electron chamber was observed such that these are considered to be similar in behaviour.

By steering the beam not only its incident angle on the target is changed, but also the position where it hits the target. Therefore a loss in signal is observed if the beam is significantly steered and does not fully hit the target. The electron chamber detects the change in symmetry quite well whereas the change in photon chamber signals is not as significant as for the electron chamber, due to the segment geometry and the beam profile at the chamber position.

3.3 Conclusion

The measurements with the three dose chambers show that the proportionality of the measured to applied dose does not deviate between these three and is within the specified range of 2 %, as expected.

Non-symmetric fields can be well detected in electron mode. For photon radiation only small changes in dose chamber signal were seen. Simulations show that for photon radiation the asymmetry of the beam in the head is not as pronounced as in the isocentre plane.

As seen from the simulations and measurements, a chamber with foils is sensitive to backscattered electrons from Y-jaws, MLC and reticle. For a 6 MV photon beam these electrons have an energy low enough such that they can be stopped to a large amount by a 3 mm thick acrylic glass plate or by the mirror. For 15 MV the effect is still significant. Backscatter is negligible under electron radiation.

The results from simulations and measurements agree well with those found in the literature. As pointed out in chapter 2.5.3, the current Siemens photon chamber is not prone to backscattered radiation. Also the simulations and measurements show this.

These investigations showed that for the current dose monitor system the main drawback is the detectability of non-symmetric fields in photon mode. Besides this, moving parts in the linear accelerator head, which might wear, are present and the diameter of the electron chamber is too small such that the main beam hits the rim and radiation is scattered into the ionisation volume.

Therefore, during the development of a Unified Dose Chamber special attention was paid on the detectability of non-symmetric fields. Moreover the effect of the field-size dependent backscatter into the monitor chamber was taken into account.

4 Development of the Unified Dose Chamber

As seen in chapter 3 the current dose chambers are suitable for detecting changes in symmetry and flatness. Nevertheless an improvement for photon radiation is desirable as small changes are not very well detected. Moreover, as pointed out in chapter 1, the use of two separate dose chambers is non-favourable due to moving mechanics and wear of these.

Additionally, nowadays only the symmetry and flatness of the beam at the position of the isocentre is known, not its profile. Moreover by summing the signal from both sides of the beam profile, the current dose monitor chambers cannot detect the root cause of the radiation field distortion. Knowing the beam profile would allow precise steering and failure analysis, besides giving detailed information on symmetry and flatness.

Therefore a new Unified Dose Chamber (UDC) for electron and photon radiation was designed which monitors beam symmetry and flatness as well as the beam profile by a better spatial resolution. It fulfils the normative criteria (see chapter 2.3) and the main criteria given in chapter 1 which are:

- sensing of beam profile
- detection of changes in beam symmetry and flatness at least as good as current system
- reliable measurement of applied dose
- fit into current linear accelerator head
- not disturb the beam in unwanted fashion (clipping of edge of radiation field, inhomogeneous field distribution in flattened beam)
- material selection such that sighted lifetime is at least several years, preferably 10 years

Therefore in chapter 4.1, first of all the principle of beam sampling is derived to adequately sample the beam profile. Then the necessary dimensions of the Unified Dose Chamber as well as the required channel distance for optimal sampling are derived in chapter 4.2 and 4.3. The electric field in a typical chamber with these dimensions is given in chapter 4.4.

The best gas filling suited for the UDC is determined in chapter 4.5. Finally a look at further materials like foils and wires is taken in chapter 4.6 to choose the appropriate material to meet the demands concerning lifetime and reliability. Potential activation of these materials and ageing phenomena are investigated in chapters 4.7 and 4.8.

4.1 Evaluation Principles

4.1.1 Sampling of Beam Profile

In order to gain additional information, besides total dose and changes in symmetry and flatness, the Unified Dose Chamber was designed to measure a projection of the beam profile in two directions orthogonal to the central axis, parallel to the waveguide (inplane) and orthogonal to it (crossplane). This is done by sampling different portions of the beam profile by parallel segments. By this the causes of the beam distortion in case of error can be detected.

In order to measure the beam profile accurately, the sampling frequency has to be high enough, i.e. there has to be a sufficient number of parallel channels that sample the profile.

The beam profile can be seen as a continuous function $f(x)$ in the space domain. The sampling frequency f_s has to be chosen such that the frequency spectrum $F(\omega)$ of the beam profile is zero for frequencies above half of the sampling frequency.

$$F\left(\omega > \frac{f_s}{2} = \Omega_{Nyq}\right) = 0 \quad (25)$$

The Nyquist frequency is

$$\Omega_{Nyq} = \frac{\pi}{\Delta x} \quad (26)$$

Then the sampling theorem can be applied to exactly reconstruct the original function $f(x)$ [Butz 2009]

$$f(x) = \sum_{k=-\infty}^{\infty} f(k\Delta x) \frac{\sin \Omega_{Nyq}(x - k\Delta x)}{\Omega_{Nyq}(x - k\Delta x)} \quad (27)$$

If the sampling frequency is not high enough, the high frequency components will show in other locations in the discrete spectrum. The consequence of choosing a sampling frequency below twice the Nyquist frequency can be seen in figure 4-1 (bottom). When a continuous function $f(x)$ is sampled with spatial frequency f_s , the frequency spectrum is replicated every f_s in the frequency domain (figure 4-1 middle). If f_s is chosen too small, the frequency spectra overlap and are thus corrupted (figure 4-1 bottom). An exact reconstruction of the profile is no longer possible in this case.

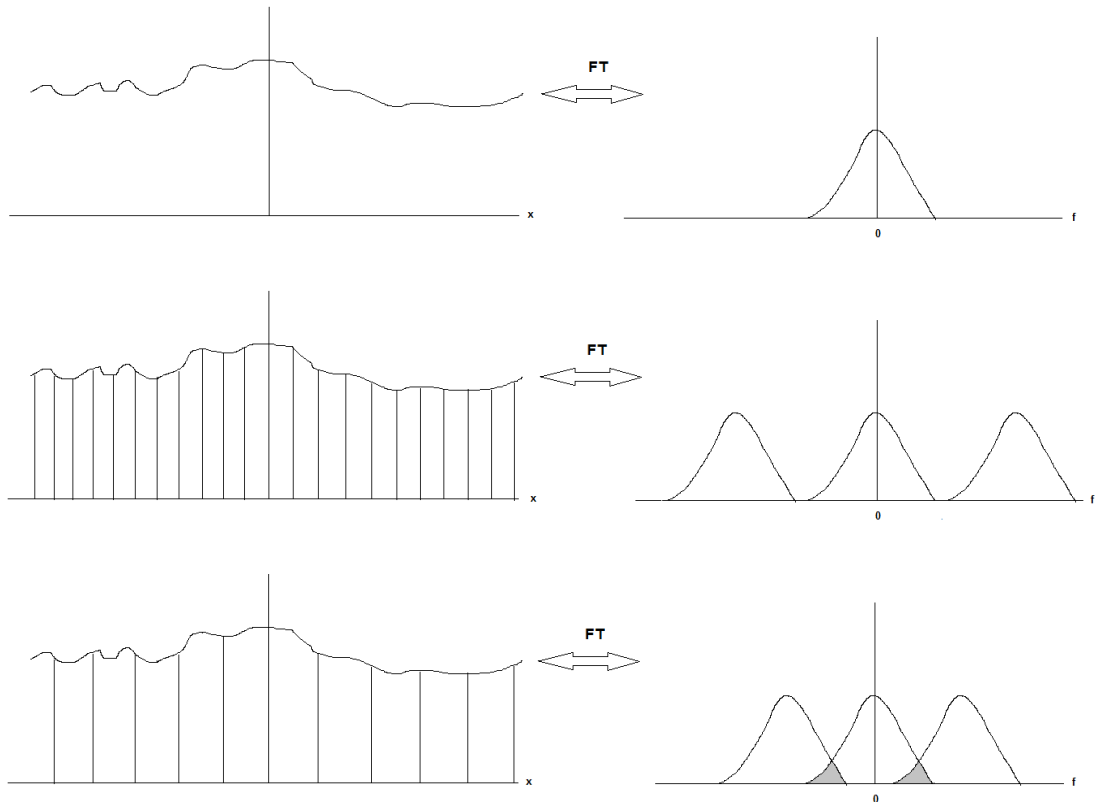


Figure 4-1: Fourier transformation of a continuous (top), sampled (middle) and undersampled (bottom) signal.

4.1.2 Monitoring of Symmetry and Flatness

The comparison of segments in conventional dose monitor chambers is very coarse as they integrate over a large area.

Figure 4-2 shows the sampling of the possible errors by the Siemens chambers. As the flattened region in the isocentre is 34 cm x 34 cm for a 40 cm x 40 cm field (see chapter 2.2), the region to be monitored at the position of the chamber at 11 cm from the source point is $34 \text{ cm} / (100/11) = 3.7 \text{ cm}$. The inner segment in figure 4-2 shows the monitor 2 electrode. The outer two segments are used to monitor symmetry and flatness. Each segment averages over the profile shaded in grey. As the outer segments average over a large area, the error they detect is not the maximal error calculated from the maximum and minimum dose at the edges of the profile but resembles the deviation at the position of the centre of the segment (at positions X_- and X_+).

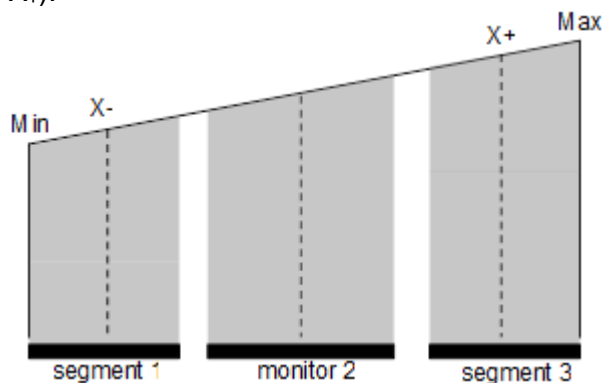


Figure 4-2: Schematic diagram of beam symmetry and flatness detection by current Siemens chamber

For crossplane direction, flatness and symmetry are defined as follows. For inplane, segments 2 and 4 are analysed.

$$\begin{aligned} & Flatness(Siemens) \\ &= \frac{\max(Seg1, Mon2, Seg3) - \min(Seg1, Mon2, Seg3)}{\max(Seg1, Mon2, Seg3) + \min(Seg1, Mon2, Seg3)} \times 100\% \end{aligned} \quad (28)$$

$$Symmetry(Siemens) = \frac{Seg1 - Seg3}{Seg1 + Seg3} \times 100\% \quad (29)$$

With the Unified Dose Chamber it is possible to compare smaller beam segments. For a chamber with n channels in the projected flattened region with signals $S(1...n)=1...N$, flatness could be calculated as

$$Flatness(UDC) = \frac{\max(1 \dots N) - \min(1 \dots N)}{\max(1 \dots N) + \min(1 \dots N)} \times 100\% \quad (30)$$

to state comparable values to the current Siemens chambers. Symmetry could be calculated by comparing the two sides of the radiation beam

$$Symmetry(UDC) = \frac{\sum_{m=1}^{\frac{n-1}{2}} S(m) - \sum_{m=\frac{n+3}{2}}^n S(m)}{\sum_{m=1}^{\frac{n-1}{2}} S(m) + \sum_{m=\frac{n+3}{2}}^n S(m)} \times 100\% \quad (31)$$

Definitions more closely to the IEC 60976 definition would be

$$Flatness(UDC) = \frac{\max(1 \dots N)}{\min(1 \dots N)} \times 100\% \quad (32)$$

$$Symmetry(UDC) = \frac{S\left(\frac{n+1}{2} + k\right)}{S\left(\frac{n+1}{2} - k\right)} \times 100\% \quad (33)$$

where $k=1...(n-1)/2$.

Especially for symmetry determination, the last definition is advised as it takes advantage of the finer segmentation.

4.2 Geometric Dimensions

4.2.1 Entrance Window Size

The size of the entrance and exit windows of the Unified Dose Chamber has to be chosen on the one hand such that the beam is not affected in the region of the maximal field size used at isocentre. On the other hand, scatter from the linac head entering the chamber would spoil the signals if the entrance and exit windows are too large.

Monte Carlo Simulations with BEAMnrc (see appendix B) were done to assess the beam diameter at the chamber position. Figure 4-3 shows the simulated beam profiles. It can be seen that the full width at half maximum (FWHM) is around 4 cm for photon beams and 17 MeV electron beams and 2.6 cm for 6 MeV electron beams.

To decrease the amount of radiation scattered back from the rim of the dose chamber into the ionisation volume, the entrance windows diameter should embrace most of the radiation beam.

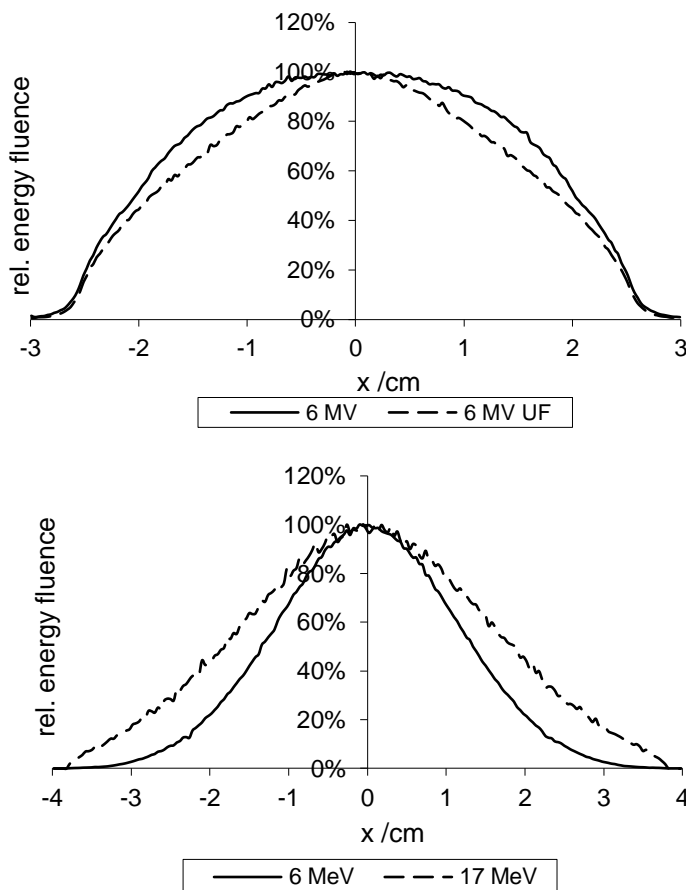


Figure 4-3: Beam profiles in chamber plane of incident radiation for 6 MV and 6 MV UF (top) and 6 MeV and 17 MeV (bottom) beams

To check the consistency between simulated and real beam profiles, the photon beam profiles were compared to film measurements with Gafchromic EBT films below the chamber slide (see figure 4-4). The FWHM of the film measurements is larger than for the simulations as the film is placed a few centimetres farther towards the isocentre where the beam is broader.

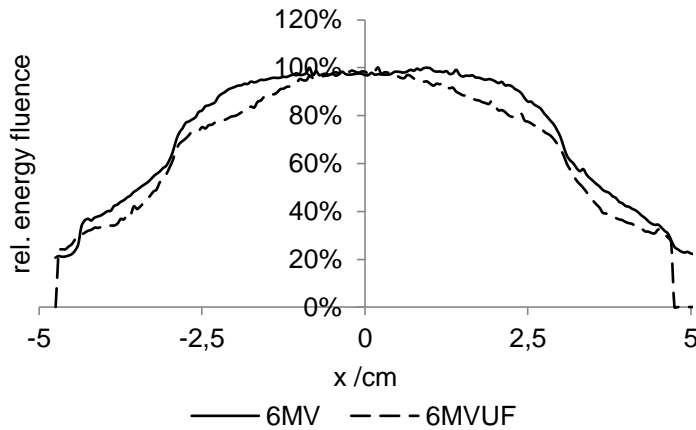


Figure 4-4: Measured 6 MV beam profiles with and without flattening filter

The deviations between the film measurements and simulations are also due to different scatter conditions as not all components like chamber slide, motors, etc. were simulated. The film measurements show a baseline of scattered radiation which can be seen in figure 4-4 from the measured dose outside the photon chamber radius of 30 mm.

It can be concluded that the chamber windows should be around 75 mm times 75 mm, or 75 mm in diameter to embrace most of the beam.

4.2.2 Height of Ionisation Volume

The distance between the HV layer and the wires in the monitor chamber determines the effective ionisation volume. A larger distance leads to higher signals as more molecules are ionised. But then a higher voltage has to be applied to prevent recombination (see chapter 2.1.3).

As the dose chambers are at 11 cm from the source, the dose per pulse values at isocentre have to be multiplied by $(100/11)^2=82.6$ as the dose changes with r^2 . This leads to dose pulses from 1.24 MU to 13.79 MU at the chamber position (see table 4-1), which roughly corresponds to 12.4 mGy and 138 mGy per pulse at a common normalization of 100 MU corresponding to 1 Gy.

From equation (1) it follows that the induced charge at 30 °C for the lowest pulse is

$$\frac{Q}{D \cdot V} = \frac{\rho}{\frac{W}{e}} = \frac{\frac{101325}{(287,058 \times 303,15)} \frac{kg}{m^3}}{34 \frac{J}{C}} = 0.034 \frac{C}{Gy m^3} \quad (34)$$

with

$$m = \rho \cdot V = \frac{p}{R_s \cdot T} \cdot V \quad (35)$$

R_s being the gas constant, p the pressure, T the temperature and V the volume. This results in $421 \mu C/m^3$ for the lowest pulse of 12.4 mGy. The typical beam settings to be monitored with the Unified Dose Chamber are summarized in table 4-1.

To detect the dose pulse with a reasonable signal to noise ratio, at least around a hundred pC have to be produced (personal communication HBS Elektrobau, Rudolstadt, April 2008). Otherwise electronics noise would have a significant influence. For the central channels the length of the wires in the ionisation volume is at most

75 mm and the width of the effective ionisation volume is determined by the distance between the channels. For 3 mm channel distance 94 pC per millimetre distance between wires and HV plane are expected, for 4 mm 126 pC/mm.

Table 4-1: Doses per pulse at patient plane and resulting dose at chamber and induced charge for an air-filled chamber for typical linac settings

Energy	Dose rate / (MU/min)	prf /Hz	Dose at isocentre / (MU/pulse)	Dose at chamber / (MU/pulse)	Induced charge /($\mu\text{C}/\text{m}^3$)
6 MV	50	40	0.021	1.73	588
	200	220	0.015	1.24	421
15 MV	50	20	0.042	3.47	1180
	500	220	0.038	3.14	1068
23 MV	50	20	0.042	3.47	1180
	500	220	0.038	3.14	1068
7 MV UF	2000	220	0.152	12.55	4267
17 MV UF	2000	200	0.167	13.79	4689
6MeV	300	90	0.056	4.63	1573
	900	180	0.083	6.86	2331
21 MeV	300	50	0.100	8.26	2808
	900	110	0.136	11.23	3819

Recombination effects in the chamber volume (see chapter 2.1.3) cause that not all of the potentially induced charge is collected and lead to a slightly lower signal. Moreover the dose distribution is not homogeneous over the area of the incident beam. This leads to lower signals at the outer parts of the chamber which are not on the central beam axis. This is illustrated in figure 4-5. The line integral cross the central red line would be much higher than across the red line at the edge of the radiation field.

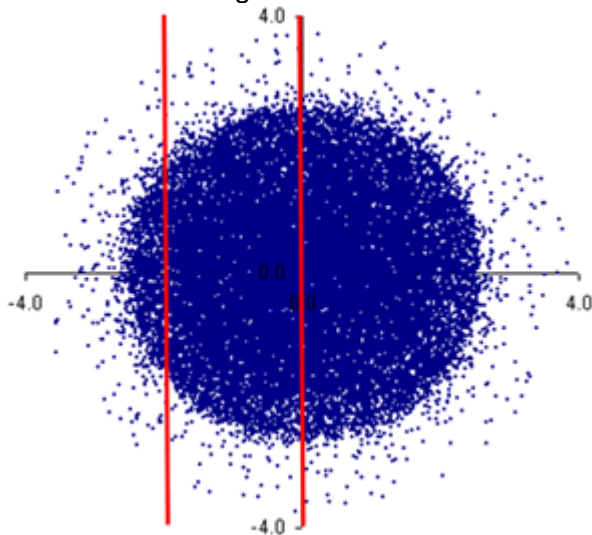


Figure 4-5: X-Y scatter plot of 6 MV beam. Red lines indicate the position of wires on central beam axis and at the edge of the radiation field

Taking these effects into account, the height of the ionisation volume should be at least 2.5 mm to 3 mm to get sufficiently high signal levels even at the edge of the radiation field.

4.3 Channel and Wire Distance

4.3.1 Analytical Model

As pointed out in chapter 4.1.1, the distance between the channels has to be small enough to measure a projection of the beam profile accurately. On the other hand too many channels increase the number of electronics channels. Moreover, the signal per channel is lower if more channels are present. Therefore the minimum number of channels for good profile reconstruction has to be found.

In this model, the beam profile is sampled by wires at a distance T and subsequently Fourier transformed. By looking at the Fourier spectrum, the maximum acceptable distance T_{\max} for a good profile reconstruction is estimated. It is first evaluated by looking at the frequency ω_{Nyquist} where the components in the Fourier spectrum fall below 1 % of the maximum as contributions to the beam with frequencies above ω_{Nyquist} are high frequency contributions with a low impact on the main profile. 1 % was selected as limit as a comparison of back-transformed Fourier spectra with and without contributions below 1 % showed very similar shapes. The aim of the Unified Dose Chamber is to monitor major changes in the beam profile and not smaller disturbances with a very high spatial frequency.

Subsequently T is varied around $1/\omega_{\text{Nyquist}}$ to refine the value of T_{\max} by looking at the difference between original and reconstructed profile. The acceptance criterion was set such that this difference has to be within 1.5 % for the main profile in the centre of the field to ensure a good agreement. Slightly larger differences at the border of the radiation field or at the outmost 5 mm on each side of the Unified Dose Chamber entrance window are tolerated. Moreover the reconstructed profile and an interpolated profile through the sampled points are compared to the original one. For the last analysis with the final model, a smaller acceptance criterion of 0.5 % is applied as technically smaller electrode distances are possible which still yield a signal which is high enough for common electronics.

In the first part the method is explained choosing a Gaussian beam profile and a sampling by a dirac comb. The model is refined throughout the chapter. At the end, the capability of detecting errors and the measurement of non-symmetric profiles are investigated.

4.3.1.1 Principle

Sampling a function at distances T apart is in the simplest way done by multiplying the function with a dirac comb, the so-called Shah function. The sampling is illustrated in figure 4-6.

$$\Delta_T(x) \stackrel{\text{def}}{=} \sum_{k=-\infty}^{\infty} \delta(x - kT) \quad (36)$$

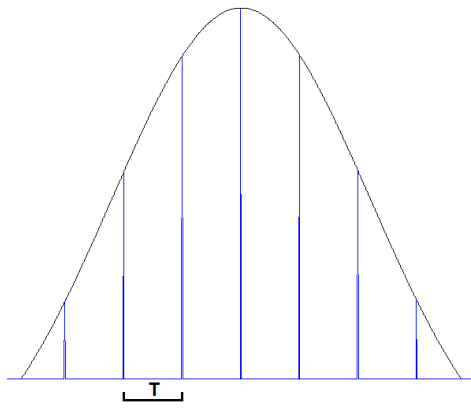


Figure 4-6: Sampling principle of a dirac comb

The fluence of the electrons leaving the bending magnet is approximately of Gaussian shape. The photon fluence produced in the target has a similar shape as at high energies the photons are mainly produced in forward direction. Hence as a first estimate of the beam profile, a broad Gaussian distribution is assumed.

The full width at half maximum (FWHM) of the radiation field is assumed to be 75 mm (see chapter 4.2.1). This field shape corresponds well to measured beam profiles of unflat 6 MV beams [Faddegon 2005].

The Fourier transform of the Gaussian profile shows that the spectral components above frequencies of 0.47 per cm are negligible. Thus a channel distance of 10.7 mm is necessary to measure the profile accurately.

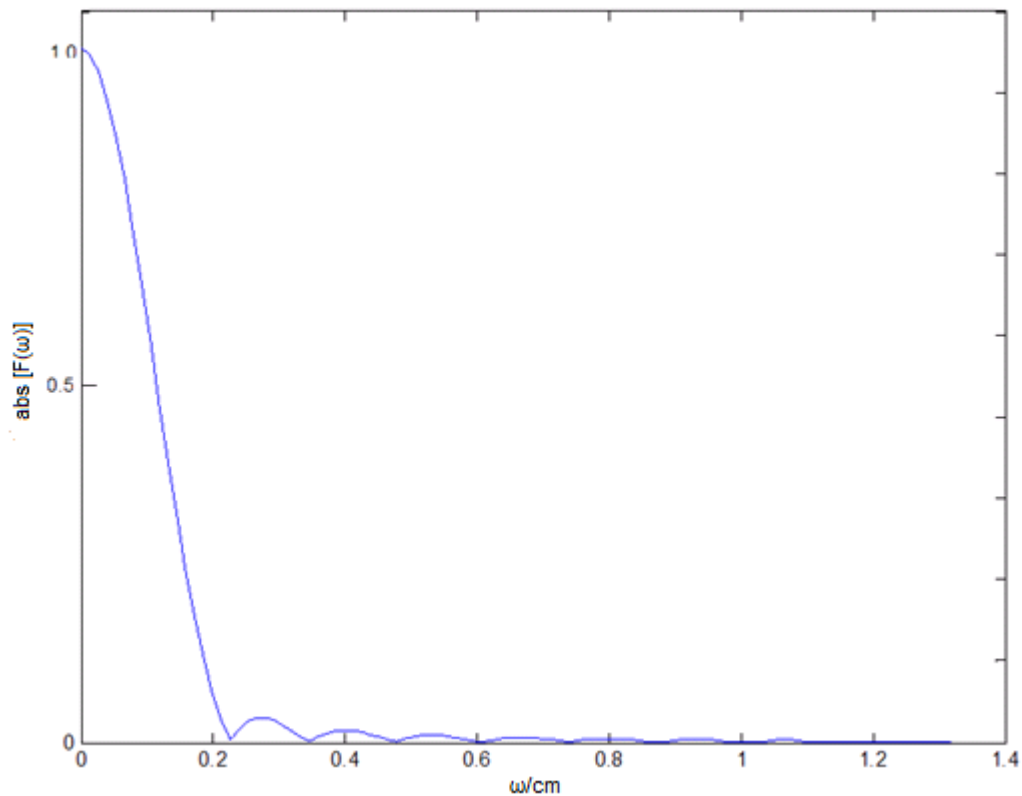


Figure 4-7: Fourier spectra of Gaussian distribution with FWHM=75mm

With larger sampling distances some of the information is lost but the agreement of a reconstructed profile by inverse Fourier transform with the original one is still quite good. T was varied from 25.0 mm to 5.0 mm in steps of 2.5 mm for the Gaussian

profile to verify the 10 mm sampling distance. Figure 4-8 shows the results for sampling distances T of 25.0 mm, 10.0 mm and 5.0 mm.

In the upper left corner, the original profile as well as the sampled one can be seen. On the upper right side the Fourier transform of the sampled profile can be observed. As can be seen, the Fourier spectrum repeats every $1/T$. If the distance between the Fourier spectra is too small, i.e. the sampling distance T is too large, an accurate reconstruction is not possible (original and reconstructed profile in lower left corner). The graph in the lower right corner shows the percentage difference between reconstructed and original profile. For 10.0 mm sampling distance the profile reconstruction is acceptable in the central area. The deviations between the original and reconstructed profile are at the edges of the radiation field which do not contribute to the collimated beam profile at the patient plane. The deviations at the field edges result from the abrupt transition to zero at the edge of the original profile.

At larger distances T the profile is not adequately sampled. The differences between original and reconstructed profile are also large in the inner part of the beam profile.

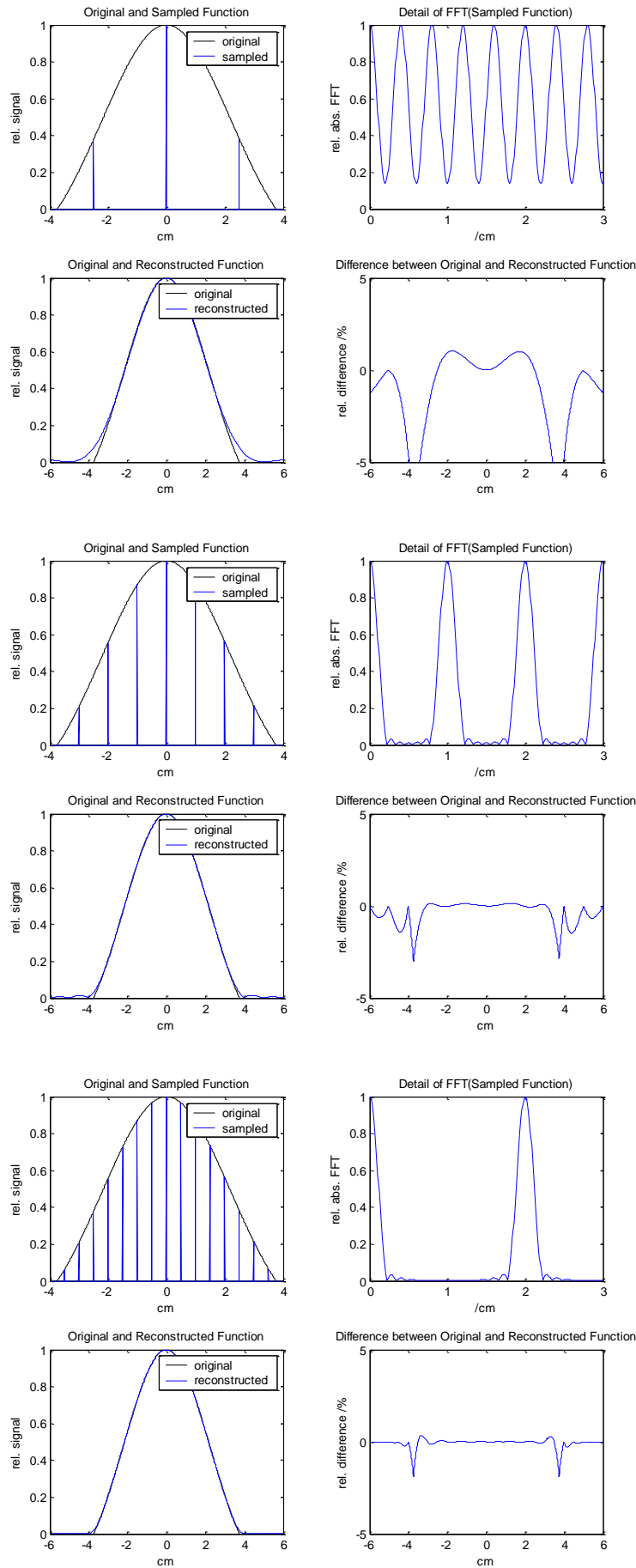


Figure 4-8: Sampling of a Gaussian profile with a dirac comb with sampling distance $T = 25.0$ mm (top), $T = 10.0$ mm (middle) and $T = 5.0$ mm (bottom)

4.3.1.2 Sampling by a Wire Chamber

When measuring a beam by an ionisation chamber, the measured dose profile $M(x)$ is a convolution of the original dose profile $D(x)$ and the response function of the ionisation chamber $K(x)$ [Looe, Stelljes, et al. 2013].

The response function of the dose chamber is not of dirac-comb shape as the beam is scattered at the entrance foils of the chamber and in the filling medium of the ionisation volume. These scattered secondary electrons induce currents in neighbouring wire channels and lead to a blurring of the measured profile. Moreover any detector averages over a volume such that the sampling is not point-like. Therefore sampling by a dirac-comb does not resemble the true sampling. The blurring effect of a detection wire can be characterized by determining the response of all detection wires when radiation is only incident on one wire [Looe, Harder, et al. 2010].

To determine the response function of a wire chamber, simulations with the Garfield simulation package were done [Veenhof 1984]. A pencil beam is incident on a chamber with wire distance $T = 3$ mm, wire diameter $a = 100$ μm and electrode – HV distance d which was chosen to be 3 mm. The filling medium was CO_2 .

The resulting induced current in the wires was scored and a Gaussian function fitted, as this is a sufficient estimate for the form of the response function $K(x)$ [Looe, Stelljes, et al. 2013]. This Gaussian function operates like a low-pass filter on the dose profile.

These simulations showed that the transfer function has a FWHM of approximately T , as can be seen in figure 4-9. The resulting standard deviation σ is

$$\sigma = \frac{FWHM}{2\sqrt{2\ln 2}} = \frac{T}{2.3548} \quad (37)$$

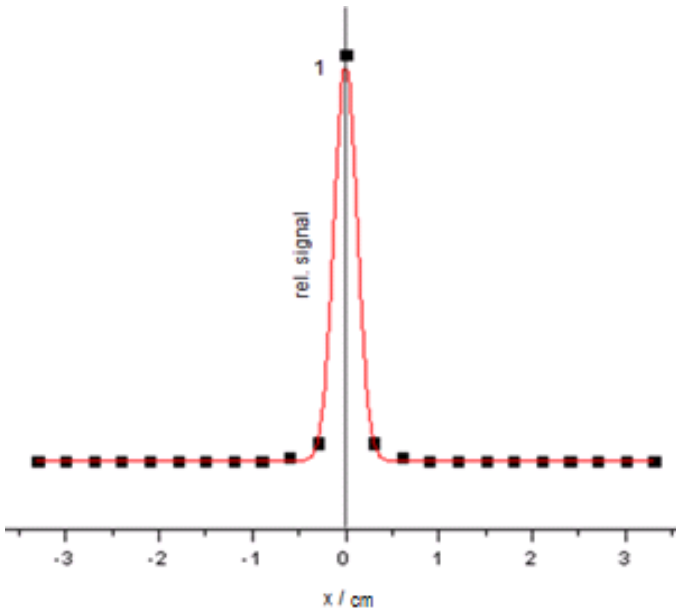


Figure 4-9: Induced current caused by a pencil beam incident at $x = 0$ mm

The Gaussian response function for sampling in the following models was calculated over a distance R to simulate a sampling over the width R . The resulting signal $S(n)$ at wire n is given by

$$S(n) = \sum_{i=-R/2}^{R/2} \left(F(i + (n-1)T) \times \frac{1}{\sqrt{2\pi}\sigma} e^{-\frac{1}{2\sigma^2}i^2} \right) \quad (38)$$

R was chosen to be 10 times T to ensure adequate sampling. Figure 4-10, which is not to scale as R is smaller, illustrates the sampling principle.

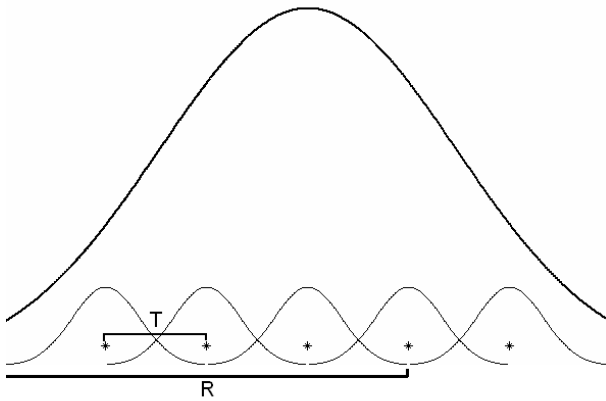


Figure 4-10: Sampling principle of a wire chamber

4.3.1.3 Sampling Measured Beam Profiles by a Wire Chamber

In reality the beam profile is not of exact Gaussian shape. To assess the needed sampling distance for real radiation fields, Gafchromic EBT film was placed on the chamber slide with the monitor chambers not in place to measure the beam profile directly. Two to four monitor units were applied for 6 MV, 6 MV UF, 15 MV and 15 MV UF photon beams and 6 MeV and 15 MeV electron beams to achieve a dose to properly darken the film.

The films were scanned several days after the measurements with a Vidar Dosimetry Pro scanner (VIDAR Systems Corporation, Herndon, VA, USA) with 16 bit and 142 dpi and read into Verisoft (version 2.11, PTW-Freiburg, Germany). The image was normalized to the maximum of the radiation field and the grey-scale image was exported. A projection of the beam profile was generated by summing the grey values along the x- and y-axis, respectively.

In figure 4-11 the scanned film as well as the 3D profile of a 6 MV beam can be observed. Moreover the projected profiles are given.

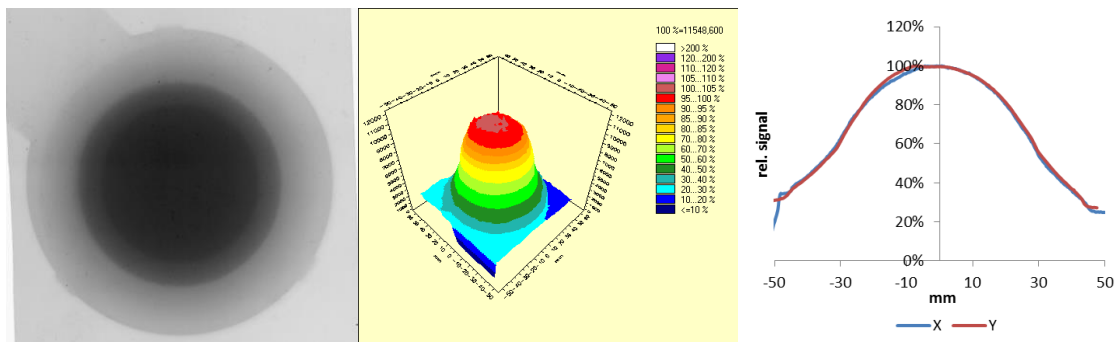


Figure 4-11 Film exposure, 3D profile and projected profiles in x- and y-direction of a 6 MV photon beam at the position of the chamber carriage

With the Unified Dose Chamber the profile can only be sampled in the area of the chamber, i.e. within the inner 75 mm. As the profile does not decline to zero at the edges of the sampling area due to scattered radiation, a reconstruction by inverse Fourier transform is not as adequate as in the case of sampling over the whole profile. To overcome this, the sampling value of the most outer wire is subtracted from the sampling values as a kind of background subtraction before Fourier transformation and the result scaled to the original range after reconstruction. In figure 4-12 these two possibilities are given with a sampling distance of 4.0 mm for a 6 MV beam. This shows that by subtracting the background radiation, a very good reconstruction with 4 mm

sampling distance is possible, well below the acceptance criterion of $\pm 1.5\%$. As can be seen in figure 4-12, interpolation of the sampled values also leads to good results. For electron beams the films only covered a smaller area so that the profile was only sampled in the respective area.

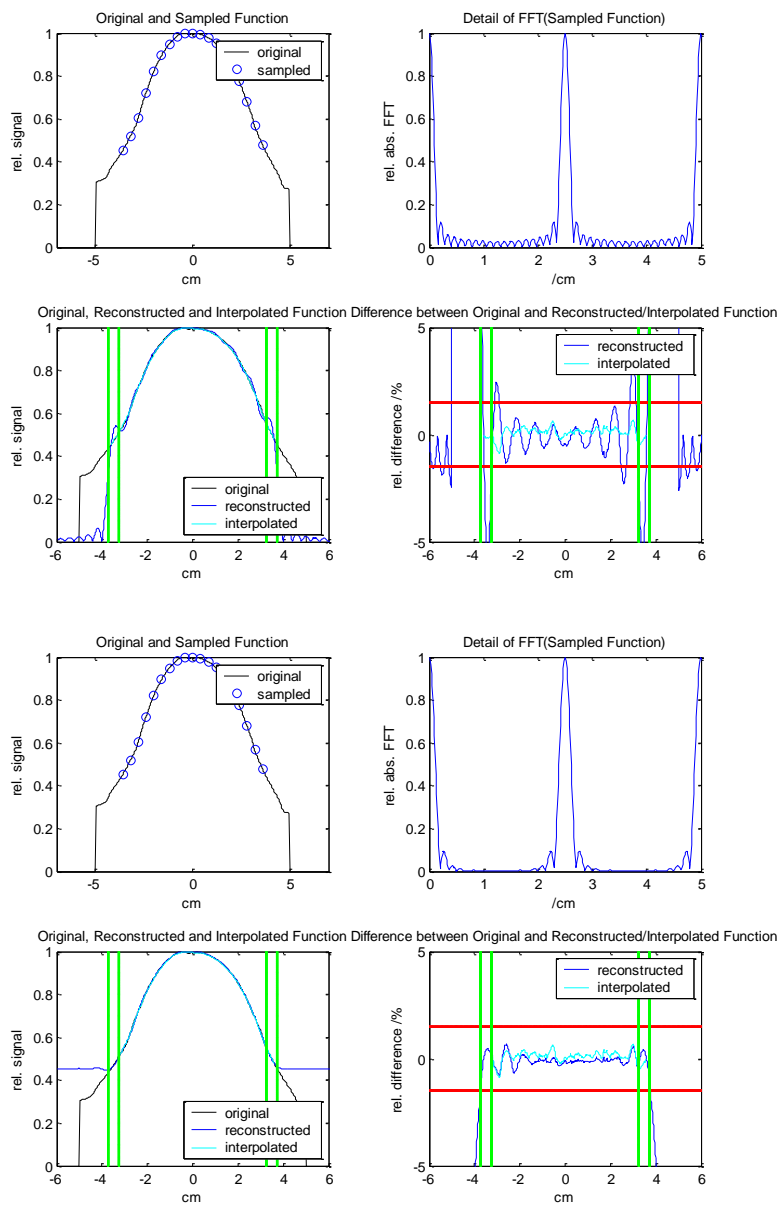


Figure 4-12: Sampling of a 6 MV photon beam film exposure profile with $T=4.0$ mm in the inner 7.5 cm of the radiation field and reconstruction without (top) and with (bottom) subtraction of outermost signal

In table 4-2 the required sampling distances to reconstruct the profile within $\pm 1.5\%$ are given. The analysis plot for 6 MV flattened photon beam is given in figure 4-13, for all energies in appendix C.

Table 4-2: Required sampling distance T_{max} for sampling measured profiles with wires

	6 MV	6 MV UF	15 MV	15 MV UF	6 MeV	15 MeV
T_{max} /mm	9.2	9.0	8.8	9.0	3.0	3.4

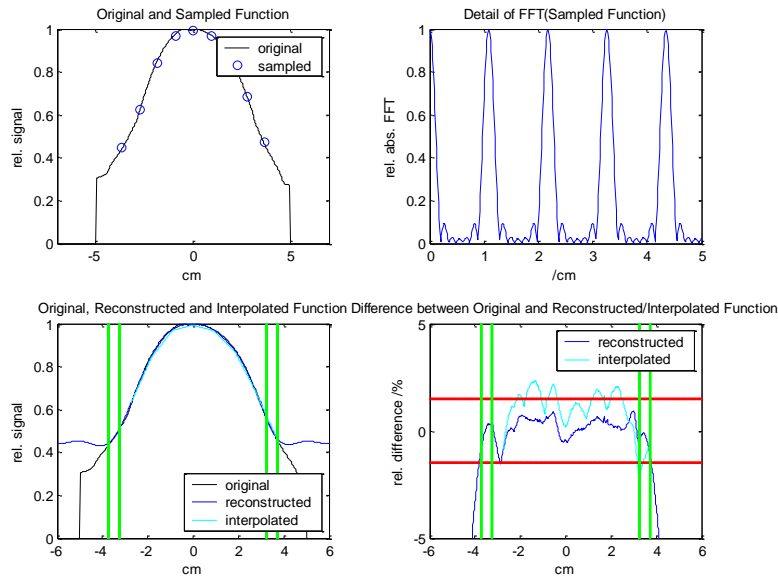


Figure 4-13: Sampling of measured profile of a 6 MV flattened photon beam with wires with Gaussian transfer function with $T = 9.2$ mm

4.3.1.4 Sampling with more than one Wire per Channel

When sampling a beam profile with a single wire per channel, the transfer function is of Gaussian shape. In order to achieve a transfer function of a more rectangular form to increase collection efficiency, several wires can be connected to form a single channel. By this the signal-to-noise ratio can be improved.

In figure 4-14 the transfer function of channels with two wires can be seen. In order to achieve a high resolution, the number of wires per channel shall be small, so that two wires per channel were chosen.

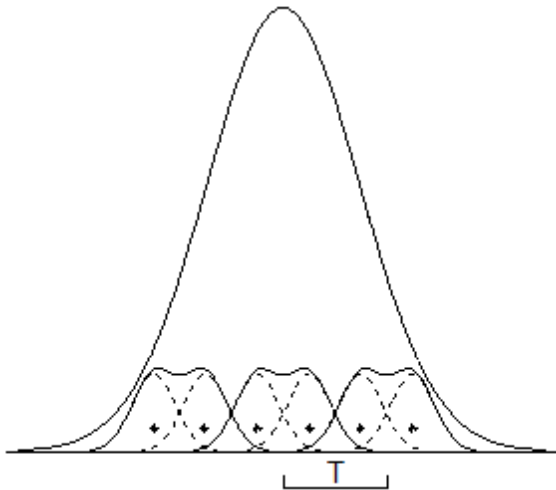


Figure 4-14: Sampling principle of multi-wire channels

Film measurements of the beam profile were analysed to get the required sampling distance. For photon radiation, the required maximal sampling distances are given in table 4-3. Figure 4-15 shows an analysis plot for a 6 MV flattened photon beam with $T = 9.2$ mm. In appendix C the plots for all energies are given.

Table 4-3: Required sampling distance T_{max} for sampling measured profiles with two wires per channel within $\pm 1.5\%$

	6 MV	6 MV UF	15 MV	15 MV UF
T_{max} /mm	9.2	8.8	9.2	9.2

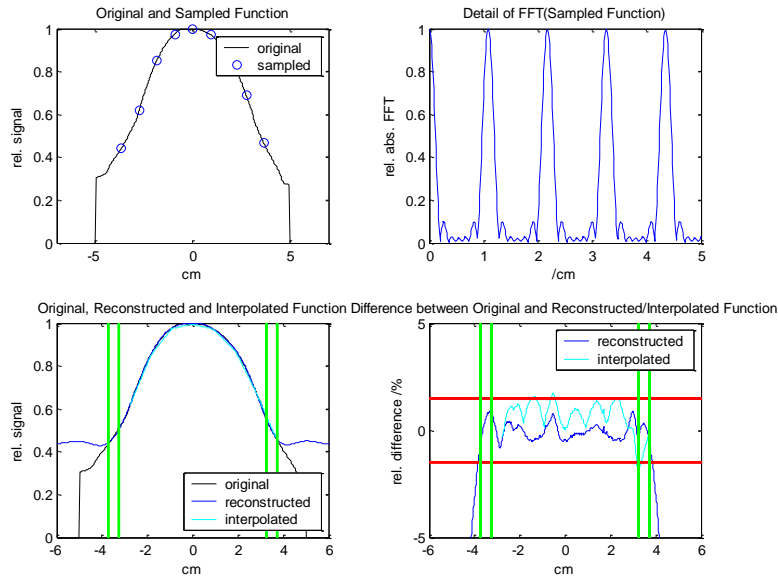
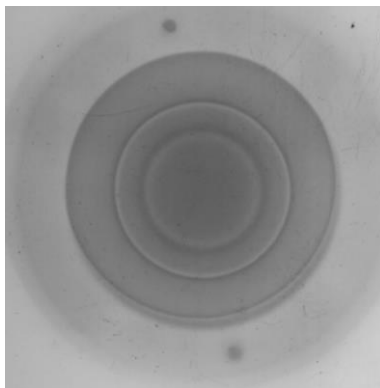


Figure 4-15: Sampling of measured profile of a 6 MV flattened photon beam with two wires with Gaussian transfer function per channel with $T = 9.2$ mm

The electron profiles have higher frequency components than the photon beams due to the secondary scattering foil. It imposes a ring pattern on the electron beam (see figure 4-16). To adequately map this pattern, higher sampling frequencies would be needed than for reconstructing the beam distribution alone.



To reconstruct the ring structure in the profile within $\pm 1.5\%$ in the central 5.0 cm, for 6 MeV and 15 MeV a sampling distance of at most 3.2 mm is required. Analysis plots are given in appendix C.

Due to multiple scattering during the travel path to the isocentre plane this ring structure is not observable at the isocentre plane and thus does not have an influence on the treatment. Therefore larger distances of the wires would be allowed.

Figure 4-16: Film exposure of a 15 MeV electron beam at the position of the chamber carriage

Smaller distances between the channels than the required 9 mm from the analysis for photon radiation above are technically possible. These are for example realized in the MWPC for the Heidelberg Ion Beam Therapy Center (HIT), see appendix E. Smaller sampling distances would allow sampling the beam profile with a higher precision. Therefore the acceptance criterion for photon radiation is lowered to $\pm 0.5\%$. The interpolated profiles also correspond mainly within $\pm 0.5\%$ to the original ones. Table 4-4 gives the corresponding maximal sampling distances for photon radiation. The analysis plots are given in appendix C. For 6 MV flattened photon beams, figure 4-17 illustrates the result.

Table 4-4: Required sampling distance T_{max} for sampling measured profiles with two wires per channel within $\pm 0.5\%$

	6 MV	6 MV UF	15 MV	15 MV UF
T_{max} /mm	3.6	3.6	3.6	4.0

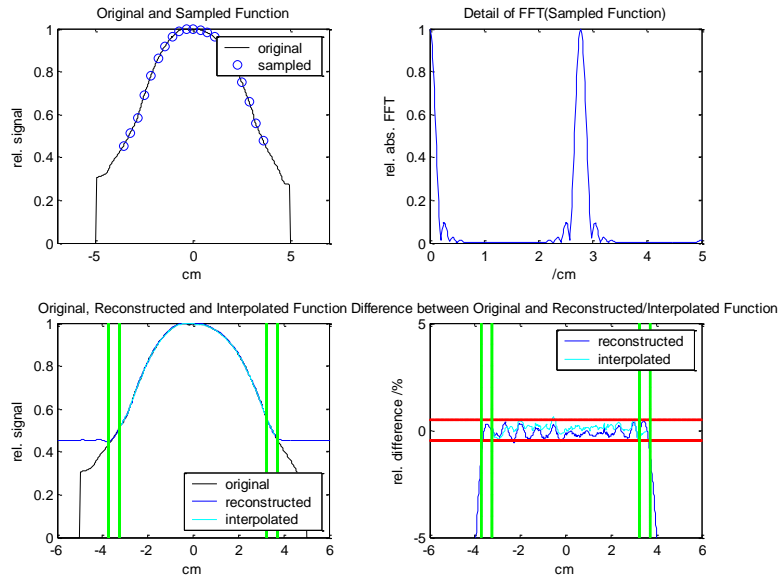


Figure 4-17: Sampling of measured profile of a 6 MV flattened photon beam with two wires with Gaussian transfer function per channel with $T = 3.6$ mm

4.3.1.5 Discussion and Conclusion

As the films were lying on the chamber slide with gantry at 180° , only the beam profile through the chamber outlets could be measured. Most of the scattered radiation from the head outside the main beam is absorbed by the chamber slide. A Unified Dose Chamber would measure more scattered radiation as no shielding carriage is in place. Assuming that the scattered radiation is homogeneous around the main beam in the area of the entrance window of a UDC, the radiation field of a 6 MV photon beam would be as in figure 4-18 on the right hand side. This image is obtained by filling the area of the film which is covered by the chamber slide with the same pixel values as in the upper left corner of the left image in figure 4-18.

The difference in projected profile can be seen in figure 4-19. The central 7.5 cm (grey shaded area) is not significantly affected. Due to the broadening of the profile the required sampling frequency would be even lower than those determined for the film measurements. Therefore the required maximal sampling distances found for the film measurements are a good estimate of required channel distance for a UDC.

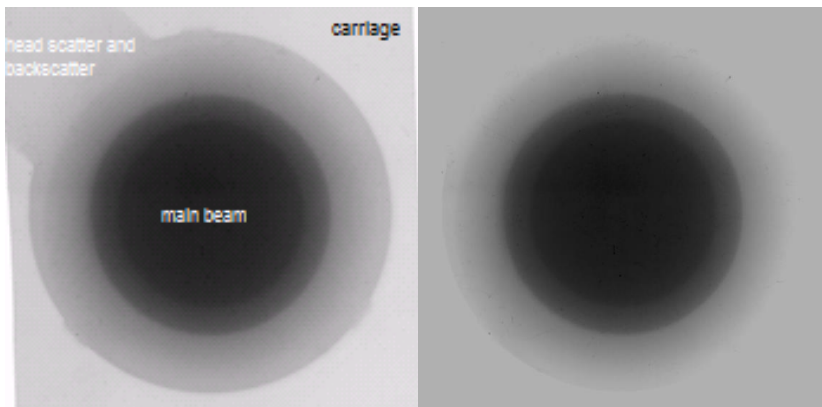


Figure 4-18: Film exposure of a 6 MV photon beam (left) and the same beam with homogeneous background (right) at the position of the chamber carriage

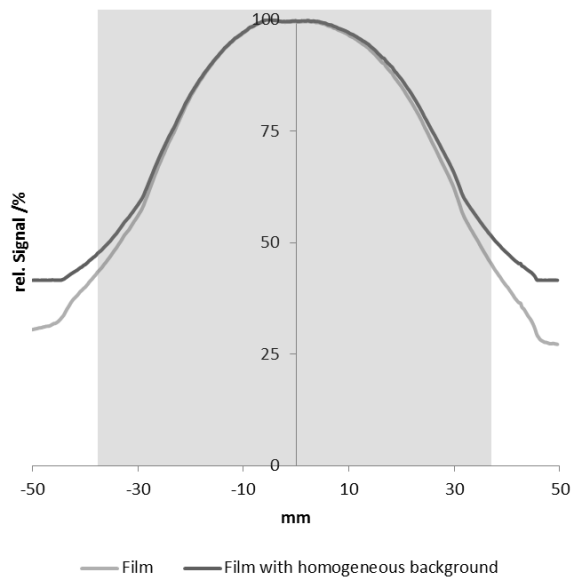


Figure 4-19: Projected profiles of film exposure and hypothetical film exposure with homogenous background of a 6 MV photon beam at the position of the chamber carriage

These are for photon radiation in the order of 3.6 mm for matching reconstructed and original profile within $\pm 0.5\%$ and 3.2 mm for electron radiation to reconstruct the ring structure within $\pm 1.5\%$, so that a channel distance of 3.0 mm to 3.5 mm would be required. The analysis also shows that with these sampling distances a representation of the profile by interpolation of the sampled values is possible.

4.3.2 Error Detection and Non-Symmetric Profiles

To analyse the capability of the UDC to detect changes in beam profile, the measured beam profiles were multiplied with ramp functions of different steepness to create tilted beam profiles. The ramp was defined over -5.00 cm to +5.00 cm with a change of the outermost value by $\pm 1\%$, $\pm 5\%$ and $\pm 10\%$ from the centre.

Figure 4-20 shows the original measured profile and the modified profile which is multiplied by a ramp such that the relative energy fluence at the left outermost point is 10 % higher than in the original profile.

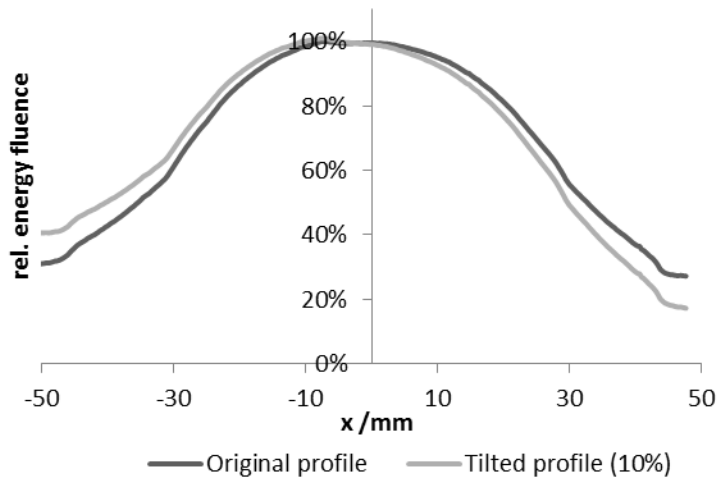


Figure 4-20: Original and by 10% tilted profile of an 6 MV photon beam

When the beams are tilted, the maximum error occurs at the outer half of the flanks. When a small number of wires is chosen, the detected change in signal is smaller than the real change, as the wires integrate over a greater volume. In figure 4-21 the difference between a non-tilted profile and a profile tilted by a ramp function of $\pm 1\%$ can be seen, on the top with a wire distance of 10.0 mm, on the bottom with 4.0 mm. For the larger sampling distance the detected signal changes are not as high as in the original profile.

The symmetry of the non-tilted profile was set to 100.00 % as this represents the symmetric and flat profile. Table 4-5 gives the changes in symmetry for the different ramp functions for the real profiles and the sampled profiles with $T = 10.0$ mm, 6.0 mm, 4.0 mm, 3.6 mm and 3.2 mm for a 6 MV flattened photon beam. For calculating symmetry, the formula according IEC definition is used, i.e. symmetric channels around the central axis are compared (see chapter 4.1.2).

Table 4-5: Detected symmetry changes for tilted profiles of a 6 MV flattened photon beam for different sampling distances T in %

Ramp	10.0 mm	6.0 mm	4.0 mm	3.6 mm	3.2 mm	real
$\pm 1\%$	100.71	100.72	100.72	100.73	100.73	100.73
Δ to real	-0.02	-0.01	-0.01	0.00	0.00	
$\pm 5\%$	103.60	103.64	103.65	103.68	103.68	103.69
Δ to real	-0.09	-0.05	-0.04	-0.01	-0.01	
$\pm 10\%$	107.32	107.42	107.44	107.49	107.50	107.51
Δ to real	-0.19	-0.09	-0.07	-0.02	-0.01	

As can be seen the changes in symmetry of 3.0 %, which have to be detectable by the dose monitoring system [IEC 60977], can be detected well within 0.05 % with the sampling distances of 4.0 mm and below required for profile reconstruction. With increasing sampling distance the accuracy of the error detection decreases.

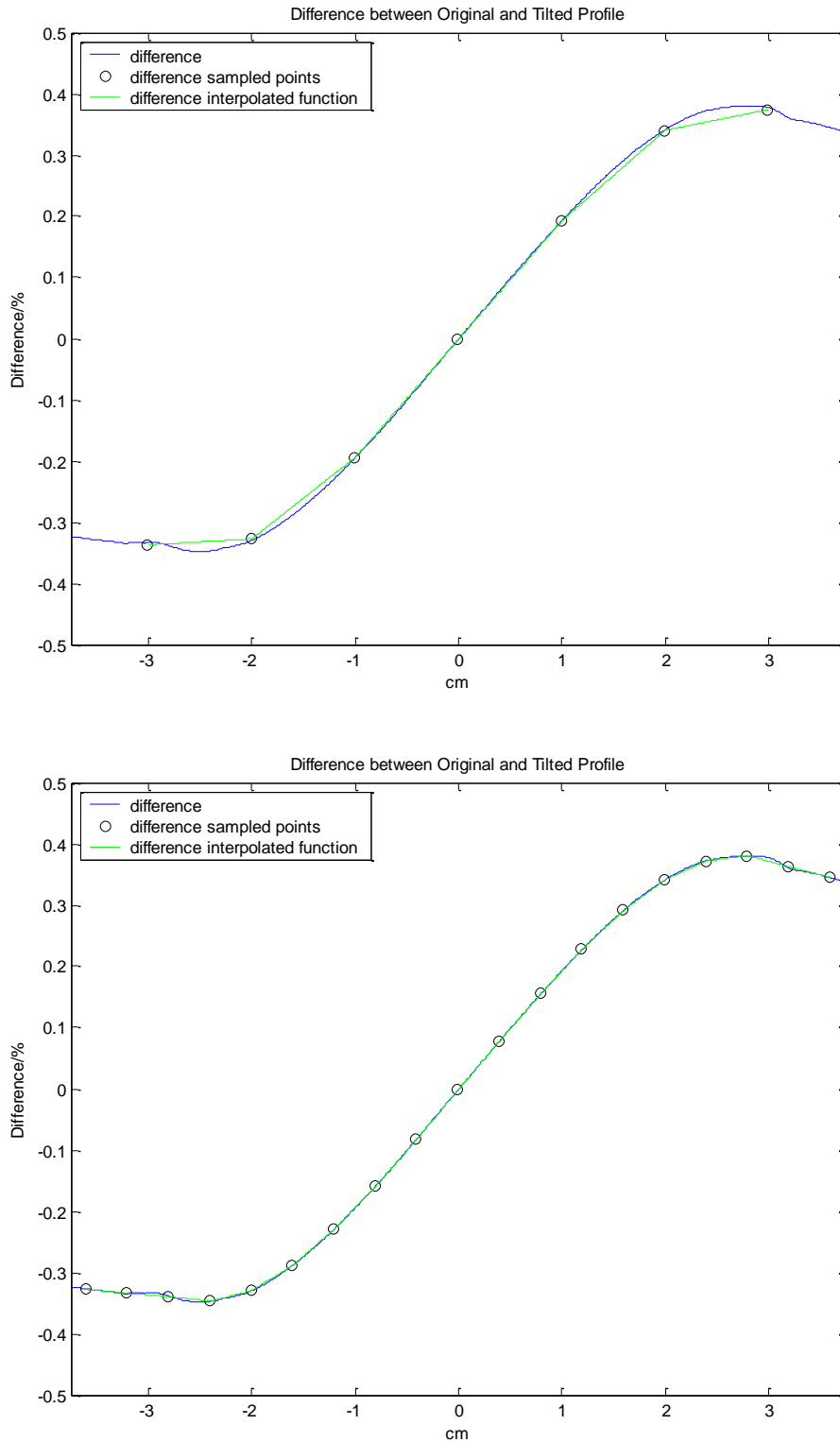


Figure 4-21: Difference between a symmetric profile and a profile with 100.73 % symmetry (blue line), the respective sampled values (black) and interpolated profiles (green) for sampling distances of $T = 10.0$ mm (top) and $T = 4.0$ mm (bottom)

For electron beams the profile spreads over a smaller area so that the changes in symmetry are not as high as for the photon beam when applying the same ramp function. Again a good determination of the real symmetry change can be measured with sampling distances below 4.0 mm as can be seen in table 4-6.

Table 4-6: Detected symmetry changes for tilted profiles of a 6 MeV electron beam for different sampling distances T in %

Ramp	10.0 mm	6.0 mm	4.0 mm	3.6 mm	3.2 mm	real
± 1 %	100.54	100.53	100.54	100.55	100.55	100.56
Δ to real	-0.02	-0.03	-0.02	-0.01	-0.01	
± 5 %	102.74	102.69	102.76	102.80	102.80	102.81
Δ to real	-0.07	-0.12	-0.05	-0.01	-0.01	
± 10 %	105.56	105.45	105.60	105.68	105.68	105.70
Δ to real	-0.14	-0.25	-0.10	-0.02	-0.02	

Symmetry changes of 3.0 %, which have to be detectable by the dose monitoring system [IEC 60977], are detectable with sampling distances of 4.0 mm and below within 0.05 % of the real value, which is accurate enough.

A reconstruction and interpolation of the tilted profiles is also possible with the sampling distances determined in chapter 4.3.1.4. Figure 4-22 shows the analysis plot for a 6 MV flat photon beam with ramp = 10 %, i.e. symmetry of 107.51 %, and $T = 3.6$ mm.

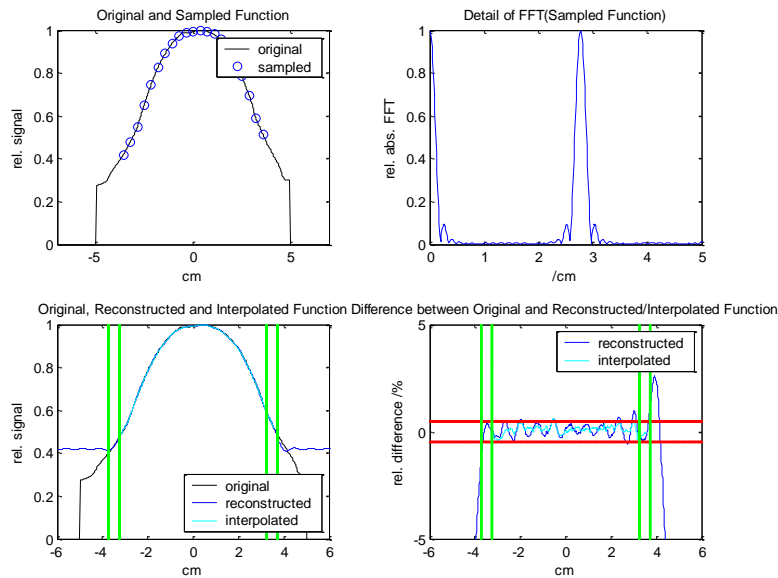


Figure 4-22: Sampling of measured and tilted profile of a 6 MV flattened photon beam with a symmetry of 107.51 % with two wires with Gaussian transfer function per channel with $T = 3.6$ mm

4.3.3 Comparison to Current Photon Chamber

The Unified Dose Chamber is not only constructed to sense the beam profile but also to detect changes in symmetry and flatness at least as good as the current photon chamber. Due to the segmentation of the Siemens photon chamber, in the following abbreviated by PhCh, (see chapter 2.4.1) it senses the beam over a wide area on each side of the central axis whereas the Unified Dose Chamber senses the beam at several positions in the radiation field.

To compare the ability to detect symmetry changes, 6 MV photon beam profiles multiplied with ramp functions with slopes of 0 % to 10 % were generated and sampled with the segmentation of the Siemens photon chamber and the Unified Dose Chamber with sense wires every 4 mm. In table 4-7 the symmetry according to IEC 60976 calculated from the field size which corresponds to the flattened region at isocentre is given in column two. The difference of the tilted profiles to the non-tilted can be seen in column three. The symmetry calculated from the sensed profile is given in column 4 and 7 for UDC and PhCh, respectively. Columns 5 and 8 give the respective difference to the non-tilted profile. In the 6th and 9th column the quotient of the difference in original profile and sensed profile is given. As can be seen the differences are proportional.

Table 4-7: Symmetry detection by UDC and Siemens photon chamber in inner 3.4 cm of radiation field

Ramp function	Original profile (flattened region)	diff. to 0%	Symmetry UDC	diff. to 0%	diff. original / diff. UDC	Symmetry PhCh	diff. to 0%	diff. original / diff. PhCh
0%	102.65		102.00			104.17		
1%	103.35	0.70	102.65	0.65	1.077	104.92	0.75	0.933
5%	106.21	3.56	105.31	3.31	1.076	107.97	3.80	0.937
10%	109.89	7.24	108.74	6.74	1.074	111.92	7.75	0.934

Table 4-8 gives the same analysis for the UDC but for the inner 7.5 cm instead of the flattened region which corresponds to 3.4 cm at chamber position. The last column gives the quotient of the difference of the tilted profiles to the non-tilted ones for the original profile within the inner 3.4 cm over the difference in these profiles sensed with the UDC within the inner 7.5 cm of the radiation field. The change in signal of the UDC is higher at the outer edges. Therefore the outer wires are favoured for sensing the symmetry change.

Table 4-8: Symmetry detection by UDC in inner 7.5 cm of radiation field

Ramp function	Original profile (inner 7.5 cm)	diff. to 0%	Symmetry UDC	diff. to 0%	diff. original / diff. UDC	diff. original 3.4 cm / diff. UDC 7.5 cm
+0%	114.32		112.58			
+1%	115.65	1.33	113.85	1.27	1.047	0.55
5%	121.18	6.86	119.07	6.49	1.057	0.55
10%	128.42	14.1	125.94	13.36	1.055	0.54

4.4 Electric Field and Ion Velocity

The electric field in a multiwire chamber with cathode wires and anode plates is given by (compare chapter 2.1.2.2)

for $y \ll s$

$$E(x, y) = -\frac{CU}{2\varepsilon_0 s r}; \quad r = (x^2 + y^2)^{1/2} \quad (39)$$

for $y \geq s$

$$E(x, y) = -\frac{CU}{2\varepsilon_0 s} \quad (40)$$

$$\text{with } C = \frac{2\pi\varepsilon_0}{(\pi l/s) - \ln(2\pi a/s)}$$

Due to the shape of the electric field in a wire chamber, the velocity of the ions is larger near the wires as here the field is higher. For ions with higher mobility the velocity is higher. In figure 4-23 the velocity of CO_2^+ and N_2^+ ions with respect to the y position is given which is orthogonal to the wires in the direction of the cathodes, assuming a trajectory on a line through a wire. An electric field of 1000 V over 4 mm gap between the plate and wires of 7 cm length with 3 mm separation are assumed.

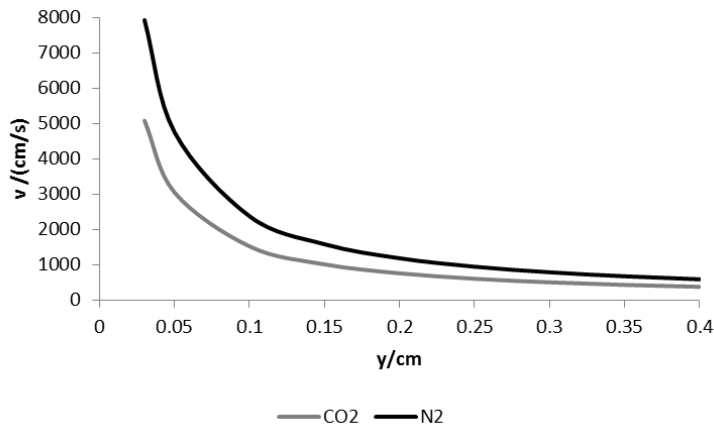


Figure 4-23: Ion velocity in a wire chamber with 1000 V applied to the electrodes, wire length $l = 7$ cm, wire spacing $s = 3$ mm, gap size $d = 4$ mm and at position $x = 0$

4.5 Filling Medium

4.5.1 Gas vs. Fluid

Sealed ionisation chambers used to monitor the spatial distribution of radiation fields may be filled with pure gases, gas mixtures or liquids. Suitable filling gases are noble gases, hydrogen, nitrogen, carbon dioxide and methane [O'Kelly 1962] or a mixture of these. Suitable filling liquids at room temperature are isooctane (C_8H_{18}), tetramethylpentane (TMP) and tetramethylsilane (TMS; $Si(CH_3)_4$).

The advantage of liquids is their higher density and the resulting higher charge per incident dose. Thus the ionisation chambers can be made smaller or the signal level can be increased. But liquid ionisation chambers have severe drawbacks. First of all, the signal strongly depends on the purity of the liquid. Residual current as well as initial and general recombination depend on the amount and type of trace concentrations of impurities present in the liquid [Wickman and Nyström 1992]. Moreover, signals are temperature dependent and increase for example for isooctane by 0.14 % - 0.22 % per °C, depending on the applied voltage and is not linear for TMS [Wickman and Nyström 1992]. The two most severe effects are the increasing recombination and thus decreasing collection efficiency with increasing dose per pulse [van Herk 1991, Berghöfer, et al. 2005] and the slow mobility of the ions.

In gases, the mobility is in the order of $1 - 2 \times 10^{-4} \text{ m}^2 \text{ V}^{-1} \text{ s}^{-1}$ (see table 4-12). For liquids, mobilities in the range of $0.58 - 12 \times 10^{-8} \text{ m}^2 \text{ V}^{-1} \text{ s}^{-1}$ are reported (see table 4-9). The wide range of the given mobilities results from different purity grades in the analysed liquids.

For a gap of 3 mm as technically feasible for the UDC and an applied voltage of 1000 V, this would lead to transit times of at least 75 ms. As the linac pulse spacing is in the order of a few milliseconds, the charge in the chamber would not be cleared before the next pulse, thus leading to the formation of a charge cloud and even higher recombination.

Table 4-9: Ion mobilities for filling liquids (in $\text{m}^2 \text{ V}^{-1} \text{ s}^{-1}$)

	Isooctane	TMS
[Wickman and Nyström 1992]	3.5×10^{-8}	0.58×10^{-8}
[Pardo, et al. 2005]	μ_+ : 3.5×10^{-8} μ_- : 2.3×10^{-8}	-
[Eberle, et al. 2003]	5.3×10^{-8}	12×10^{-8}

Due to the drawbacks of liquids, especially the slow mobility, it was decided to fill the Unified Dose Chamber with a gas. In the following chapters the properties of different possible gases are compared.

4.5.2 Induced Charge

The charge Q induced in an ionisation chamber is proportional to the applied dose D (see chapter 2.1.2).

$$D = \frac{Q}{m} \cdot \frac{W}{e} \quad (41)$$

The total number of induced electron-ion pairs n_t , which determines the induced charge Q , is

$$n_t = \frac{dE/dx}{W} \quad (42)$$

For measurements a high induced charge Q per dose D is favourable to increase signal levels. Therefore the filling gas should have a high collision stopping power dE/dx and a low mean energy to produce an electron-ion pair W . In table 4-10 the properties of some gases are summarized. Figure 4-24 gives the total number of induced electron-ion pairs per centimetre for a range of energies.

Table 4-10: Collision stopping power dE/dx , mean energy to produce an electron-ion pair W and resulting total number of electron-ion pairs per centimetre n_t for different filling gases for a minimal ionising particle

	Air	H ₂	N ₂	CO ₂	Ar	Xe	CH ₄
dE/dx / (keV cm ⁻¹) [Kolanoski 2004, Berger, et al. 2009]	1.99	0.34	1.96	3.01	2.44	6.76	1.48
W / eV [Kolanoski 2004]	34	37	35	33	26	22	28
Total no. e-ion pairs n_t /cm ⁻¹	58	9.2	56	91	94	307	53

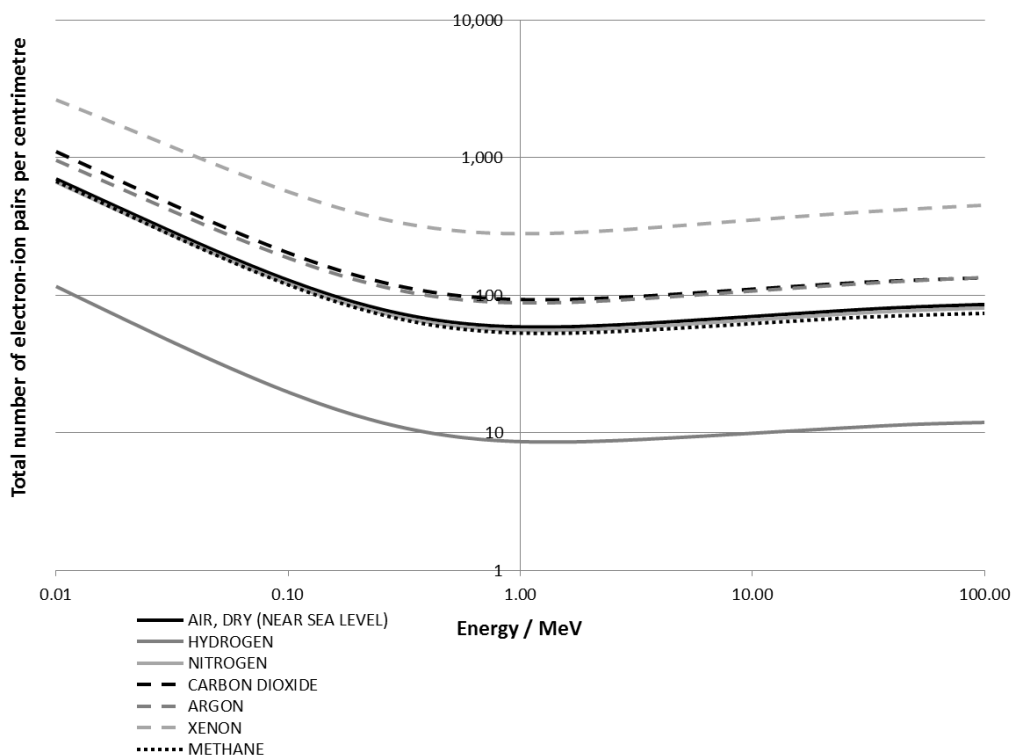


Figure 4-24: Total number of electron-ion pairs per centimetre in different filling gases (calculated from data from [Berger, et al. 2009] and [Kolanoski 2004])

The inefficiency of the ionisation process depends on the number of initial electron-ion pairs n (compare chapter 2.1.3).

$$1 - \varepsilon = p_0^n = e^{-n} \quad (43)$$

Table 4-11 gives the number of primary electron-ion pairs and the resulting inefficiency. For all gases, except H₂, the resulting efficiency is above 99.99 %.

Table 4-11: Number of primary electron-ion pairs [Kolanoski 2004] and resulting inefficiency

	H ₂	N ₂	CO ₂	Ar	Xe	CH ₄
n	5.2	10	35	29.4	44	16
$1 - \varepsilon$	5.5×10^{-3}	4.5×10^{-5}	6.3×10^{-16}	1.7×10^{-13}	7.8×10^{-20}	1.1×10^{-7}

Concerning the number of produced electron-ion pairs, argon and carbon dioxide are superior to nitrogen, air or methane. Admixtures of Xenon would further increase signal levels. Hydrogen is excluded from further investigations as the charge yield is low and hydrogen is highly flammable and thus a hazardous material. For the same reason, methane is excluded from further investigations.

4.5.3 Ion Mobility and Recombination

The mobility of different gas fillings (see table 4-12) is not critical with respect to clearance before the next dose pulse occurs. The ion transit time t_{ion} is in the order of several microseconds for a gap d of a few millimetres and an applied voltage of several hundred volts. It is thus far below the pulse repetition time which is in the order of milliseconds. The ion transit time is given by the ratio of the travel distance d divided by the velocity v which depends on the mobility μ and the reduced electric field E/P (see equation (4) in chapter 2.1.2).

$$t_{ion} = \frac{d}{v} = \frac{d}{\mu \frac{E}{P}} = \frac{d^2}{\mu P} \quad (44)$$

The recombination of the electron-ion pairs created by incident radiation depends on the field strength in the ionisation volume, the mobility of the ions and the applied dose (i.e. the charge density). To reduce recombination high field strength is advisable. Nevertheless the field strength has to be kept low enough to prevent avalanche. As rare gases have fewer excitation modes than polyatomic gases, the gas gain sets in at lower electric field strengths [Sauli 1977]. From this point of view, nitrogen and carbon dioxide are preferable for a chamber operated in the ionisation regime.

In noble gases and nitrogen, the free electrons do not attach to neutral components and thus do not form negative ions. In these gases recombination is less as the mobility of the electrons is approximately 1000 times faster than that of ions [Sauli 1977]. In all other gases and mixtures of nitrogen or noble gases with other species, as well as in technically pure gases [Dinter and Tesch 1974], the electrons attach to neutral atoms to form negative ions. Table 4-12 gives an overview on ion mobilities given in the literature for typical filling gases.

Table 4-12 Mobility μ (10^{-4} m²atm/(Vs)) of ions in gases at zero field

Ion in gas	[Buryakov 2004]	[Saporosch enko 1965]	[Moseley, Snuggs, et al. 1969]	[Keller, Martin and McDaniel 1965]	[Dotan, et al. 1976]	[Sharma 1998]	[Moseley, Cosby and Peterson 1976]	[Helm and Elford 1977]	[Madson and Oskam 1967]	[Hackam 1969]	[Varney 1952]
Air											
Benzene	1.94										
DMMP	1.95										
o-TLD	1.75										
MA	1.74										
Pyridine	1.7										
Aniline	1.81										
DMA	1.81										
DEA	1.71										
DPA	1.54										
N ₂											
N ⁺ in N ₂		2.54	2.97	2.47							
N ₂ ⁺ in N ₂		1.7	1.87	1.44							
N ₃ ⁺ in N ₂		1.9	2.26								
N ₄ ⁺ in N ₂		2.34	2.33	1.84							
CO ₂ ⁺ in N ₂					2.18						
CO ₂											
CO ₂ ⁺ in CO ₂						1.09					
CO ₃ ⁺ in CO ₂							1.34				
O ⁻ in CO ₂							1.92				
Ar											
Ar ⁺ in Ar						1.00		1.44	1.54		
CO ₂ ⁺ in Ar						1.72					
Xe ⁺ in Xe										0.54	0.67-0.77

4.6 Further Components

For the construction of a Unified Dose Chamber, the selection of appropriate materials is essential. The components should not adversely alter the beam, should not be activated and have to be radiation resistant to ensure a long life-time of the monitor chamber. In chapter 4.6.1 a deeper look into the selection of appropriate sense wires is taken, looking at the diameter, material selection and applied tension. Afterwards different materials for the foils are investigated. Subsequently a brief look at other components like gaskets, spacer rings, glue, etc. is taken.

4.6.1 Wires

For sense wires in wire chambers stainless steel, tungsten, tungsten-rhenium and molybdenum are common materials [Charpak, et al. 1968, Ott 1993, Poppe, et al. 2006, Tilly, et al. 2007] often coated with gold to increase surface quality and electrical conductivity. Typical diameters range from 0.02 mm to 0.4 mm, depending on field of application.

Important criteria for the selection of wire material are the electrical conductivity and the density of the material, which should be low to prevent sagging. For the same reason the modulus of elasticity shall be high in order to have a low elongation at a given tension T . The tension T applied to a wire is normally chosen to be 60% of the yield point [Hearty 1996]. Moreover the thermal expansion coefficient should be low to prevent elongation of the wire with temperature rise in the linear accelerator head. The surface quality of the wire shall be as good as possible to prevent the formation of whiskers. This is a more important issue in proportional chambers but may also be relevant in ionisation chambers. Table 4-13 gives an overview on the properties of some common wire materials.

Table 4-13: Properties of typical wire materials

	Au	W	W/ 3%Re	Mo	Stainless Steel
Electrical conductivity / (MS/m)	42.55 ¹ /48.8 ²	17.69 ¹ /18.2 ²	10.94 ³	19.2 ¹ /17.3 ²	1.33 ⁴
Density / (g/cm ³)	19.32 ²	19.26 ²	19.4 ³	10.28 ²	8 ⁴
Modulus of elasticity / GPa	74.5 ⁵	345 ⁵	403 ³	276 ⁵ /329 ⁶	≈200 ⁴
Yield Point / MPa	205 ⁷	550 ⁷		450-550 ⁸	502 ⁶
Thermal expansion coefficient / (μm/m*K)	14 ⁹	4.5 ⁵		4.8 ⁹ /5.4 ⁵	17.3 ⁹
1 [Seilnacht 2011]	4 [Inox 2007]		7 [Goodfellow 2003]		
2 [Hoppe 2011]	5 [Scientists 2004]		8 [Science at home 2011]		
3 [Rhenium Alloys Inc. 2011]	6 [The Engineering Toolbox 2011]		9 [Wikipedia 2011]		

Wire diameter

The diameter of the wires does not only determine the weight of the wires which determines the required tension, but is also critical with regard to the voltage that can be applied. The smaller the diameter, the higher is the potential around the wires which may lead to unwanted gas gain.

Garfield simulations [Veenhof 1984] were performed with tungsten wires with length $L=7$ cm, varying wire diameter a and tension T . The chamber parameters were $d=5$ mm, $s=3$ mm and $U_0=500$ V, with the gravitational force being perpendicular to the electrodes (see figure 4-25).

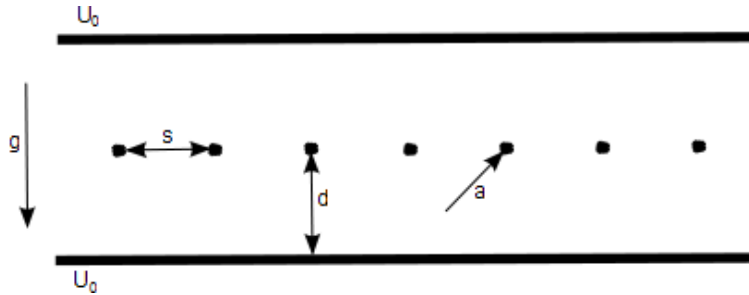


Figure 4-25: Chamber geometry and simulation parameters for Garfield simulations

For larger wire diameters the ratio between the electric field at the central wire and at the plane is smaller, i.e. the electric field is more homogeneous (see table 4-14).

Table 4-14: Simulated electric field strengths, sag and deflection for varying wire diameter

	$a=20\mu\text{m}$ $T=45\text{cN}$	$a=50\mu\text{m}$ $T=75\text{cN}$	$a=100\mu\text{m}$ $T=75\text{cN}$
Surface field central wire /(V/cm)	27,469.1	12,221.5	6,682.7
Field at 2*radius (central wire) /(V/cm)	13,738	6,118.6	3,355.4
Electric field E_x @plane /(V/cm)	788	820	850
Ratio E central wire / E plane	35	14.9	7.9
max sag x /nm	28.8	239	1160
max deflection y inner 6cm /nm	6.49	4.40	4.74
max deflection y most outer wire /nm	310	110	81.5

To prevent gas gain the electric field at a distance equal to twice the wire radius and directly on the wire surface is compared. As the electric field is smaller at these positions for larger wire diameters, higher voltages may be applied for larger diameters before gas gain sets in. Gas gain starts approximately at field strengths of a few 10^4 V/cm [Markert 2005], so that a wire diameter of 100 μm or above is advisable.

Wire tension

For accurate beam sensing it is essential, that the wires don't sag significantly. Applying a tension T on the wire of length L_0 and cross sectional area A causes an elongation ΔL

$$\Delta L = \frac{g \cdot T \cdot L_0}{A \cdot E} \quad (45)$$

with modulus of elasticity E , so that the total length of the wire is $L=L_0+ \Delta L$ [Hearty 1996]. The gravitational force on the wire causes sagging of the wire. The maximal sag of a wire of density ρ is [Hearty 1996]

$$sag = \rho \cdot A \cdot \frac{L^2}{8 \cdot T} \quad (46)$$

In table 4-15 the typical elongation and sag for wires made from different materials is given. The initial length L_0 is assumed to be 7.5 cm, the radius of the wires is 100 μm and a tension of $T \cdot g = 1 \text{ N}$ was assumed.

Table 4-15: Typical values for elongation and sag for different wire materials

Material	E /(kN/mm ²)	ΔL / μm	ρ /(g/cm ³)	Sag / μm
W	345	27.69	19.26	1.04
W/3%Re	403	23.70	19.4	1.05
Mo	300	31.83	10.28	0.56
Stainless Steel	200	47.74	8	0.43

Although the elongation for molybdenum and stainless steel wires is larger due to the lower modulus of elasticity, the sag is smaller due to the lower density.

As a result of the applied electric field in the chamber the wires are displaced from their equilibrium position if no initial tension T is applied. The deflection of wires was observed for large wire chambers with $L > 1 \text{ m}$. The minimal tension T on the wires has to be larger than the critical tension T_c that prevents the deflection of the wires due to electrostatic forces [Sauli 1977].

$$T \geq T_c = \frac{1}{4\pi\epsilon_0} \left(\frac{CV_0L}{s} \right)^2 = 4.65 \mu\text{N} \quad (47)$$

For the short wires in the Unified Dose Chamber this effect is negligible and with a commonly applied tension of several cN the deflection is prevented.

The yield point for all investigated materials is in the order of 500 MPa, so that for a wire with 100 μm diameter a tension of 2.35 N is proposed by Hearty [Hearty 1996]. If tungsten is alloyed with 3% rhenium, the strength of the material is further increased. Such reinforcement seems not to be necessary due to the short length of the wires.

As can be seen from table 4-15 the sag can be kept at very low values with lower tension values. The applicable tension has to be found out during the manufacturing process as exact wire quality depends on supplier and the material properties may deviate from the values given in table 4-13.

For a good electrical conductivity and fewer problems with wire ageing, wires should be of a good surface quality and gilded.

4.6.2 Foils

In the Unified Dose Chamber the entrance and exit window and the high voltage as well as the ground planes have to be made from thin foils which do not influence the beam in an unwanted way. The high voltage and ground plates are coated with a thin conductive layer. These foils have to fulfil the following criteria:

1. Low density
2. Thin material
3. Low Z material
4. Radiation resistant up to 3.2×10^7 Gy
5. High dielectric strength
6. Hard and unaffected by notches
7. It must be possible to make it in a uniform sheet and to metallize it

Requirements one through three ensure a low interaction of the chamber with the beam. Thin and low Z material reduces lateral scatter which enhances spatial resolution [Thomas and Symonds-Taylor 2003]. The radiation resistance is calculated based on a projected 10 year life-time of the chamber at normal clinical usage⁴. The high dielectric strength is needed as the foils isolate the electric field of the chamber volume from the surrounding. Requirement six ensures that the chamber is not easily damaged during install and service.

In principle, thin sheets of compounds of lithium, beryllium or boron, graphite or various plastics may be considered. The last requirement favours for plastics as graphite is too soft and can as well as the other materials not be manufactured as a thin and stable foil.

Foil material

In the following several plastics are compared. All of them are stiff and hard and metallizable [Domininghaus 1998]. Table 4-16 gives some mechanical and physical properties of favoured materials with low density, high dielectric strength, low water absorptions and usable in the temperature range found in a linac head (18°C to 60°C).

Ionising radiation leads to changes in the molecular structure of plastics. Most commonly the macromolecules degrade and ambient oxygen molecules diffuse into the plastic and occupy the valences which were released by the ionising radiation. This leads to a change of the mechanical properties like rigidity, stiffness, or hardness or to embrittlement [Ensinger 2012]. Figure 4-26 gives the radiation resistance for several plastics. Due to its high radiation resistance, polyimide (PI) and polyetheretherketon (PEEK) are favoured.

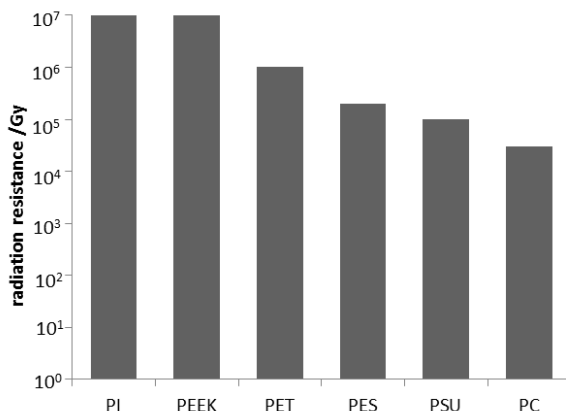


Figure 4-26: Radiation resistance of foil materials. For meaning of abbreviations see table 4-16 [Domininghaus 1998] and [Bay. Forschungsverbund Materialwissenschaften 2007]

⁴ 39,000 Gy per year at isocentre (personal communication, Siemens AG)

Table 4-16: Properties of foil materials [Dominghaus 1998]

Common trading name	PI	PEEK	PES	PSU	PET polyethylene-terephthalate	PC
	Polyimid	Polyetheretherketon	Polyethersulfon	Polysulfon		Polycarbonate
	Kapton				Mylar	Lexan
Density /(g/cm ³)	1.43	1.32	1.37	1.24	1.37	1.20
Temperature range for usage /°C	-200° to +260	-100 to 250	-100 to 200	-100 to +150	-20 to +100	-40 to +135
Dielectric strength /(kV/cm)	560	190	400	425	420	380
Water absorption /% (24h)	0.32	0.5	0.43	0.02	0.10	0.16
Flammability	After ignition source is removed, material extinguishes itself	flame retardant	flame retardant	flame retardant	flame retardant types available	flame retardant types available

Moreover the beam shall be disturbed as little as possible when passing the monitor chamber. The effect of additional material in the beam is far more pronounced in electron beams than in photon beams. Therefore the energy loss of an electron beam passing the chamber is analysed. In figure 4-27 the total stopping power for three materials is given from data available from the National Institute of Standards and Technology [NIST 2009]. The total stopping power of polyimide is higher than of polyethylene-terephthalate, followed by polycarbonate but is still small compared to other materials like alumina which is used in the current photon chamber.

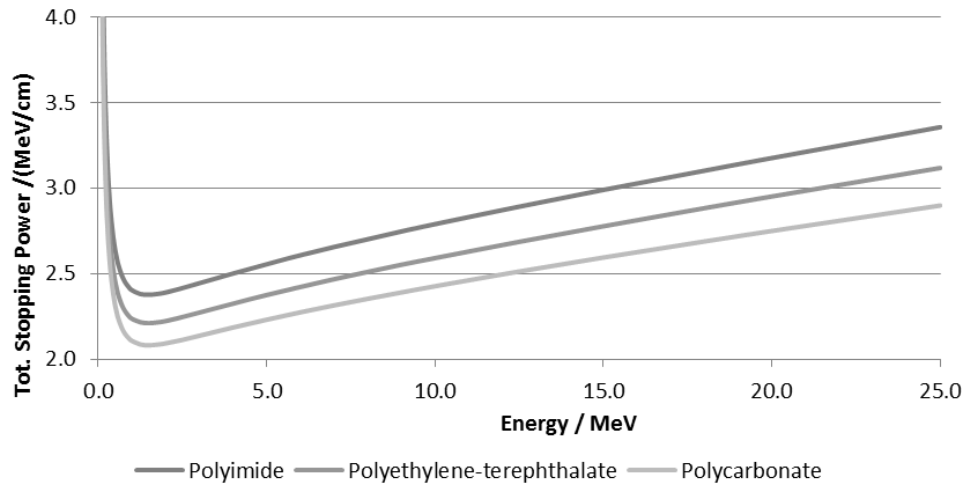


Figure 4-27: Total stopping power for polyimide (dark grey), polyethylene-terephthalate (grey) and polycarbonate (light grey) [NIST 2009]

In summary, PES, PSU and polycarbonate are not appropriate materials for the foils in the Unified Dose Chamber. PES and PSU are sensitive to notches or have a predisposition for stress cracks [Domininghaus 1998] and their radiation resistance as well as the one of polycarbonate and polyethylene-terephthalate (PET) is too low. The life-time of the foils would be below one year as their radiation resistance is below 1×10^6 Gy (compare figure 4-26). The typical yearly amount of applied dose to the isocentre is around 39 kGy (internal communication, Siemens AG). As the dose chamber is around 11 cm from the target, this would mean $(100/11)^2 \times 39 \times 10^3$ Gy = 3.2×10^6 Gy applied per year to the foils. Therefore these materials were excluded from further analysis.

Polyimide and PEEK are very radiation resistant and stable materials which are suitable for application in a monitor chamber. As good handling experiences with Kapton were made and it is a validated material at Siemens, it was decided to use this in the Unified Dose Chamber.

Foil Thickness

In order to make the entrance and exit foils as gastight and stable as possible, these should on the one hand be made as thick as possible to reduce bending and diffusion in and out of the chamber. Moreover thicker foils are more resistant to unintended damage by service personnel during handling. On the other hand thicker foils will disturb the beam. Therefore the influence of different thicknesses of chamber foils made from Kapton was investigated.

The change in energy fluence and spectral distribution was investigated for 6 MeV electron and 6 MV and 15 MV flattened photon beams by Monte Carlo simulations with BEAMnrc (see appendix B). For electrons an applicator of 25 cm x 25 cm was simulated, for photons a 40 cm x 40 cm field was used. The combined thickness of entrance and exit window was varied from 50 μ m to 200 μ m, keeping the inner three foils at 25 μ m, and the fluence was scored at isocentre in air.

Spectral distribution of a 6 MeV electron beam is plotted in figure 4-28. Below 5 MeV the distributions for all foil thicknesses are the same within simulation accuracy. Only small changes can be observed above 5 MeV. Moreover the initial energy of the particles can be adapted to match the desired distribution.

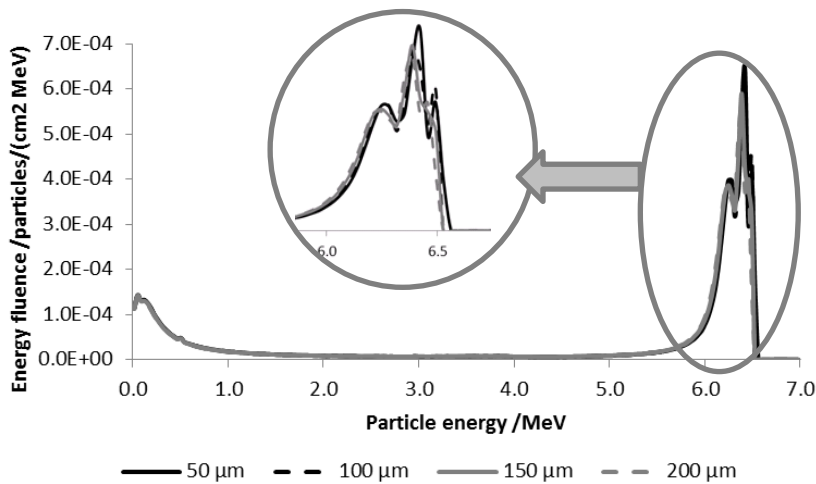


Figure 4-28: Energy fluence at isocentre of a 6 MeV beam for different combined thicknesses of entrance and exit foil

In figure 4-29 the energy fluence is shown. A small change is observed which is below 4 % in the central region and does not exceed 6 % for 150 μm thickness and 10% for 200 μm at the edges. By adapting the initial energy the distribution may be optimized.

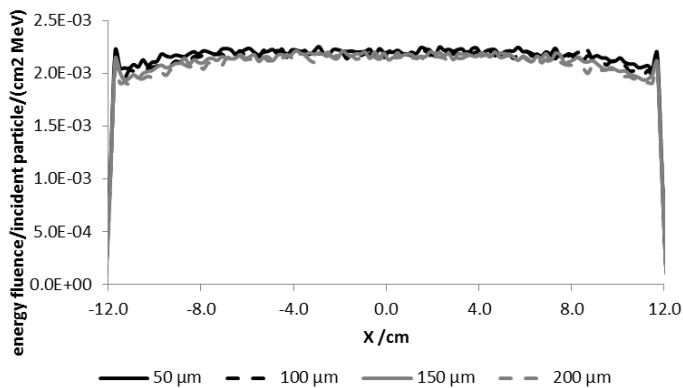


Figure 4-29: Energy fluence vs. position at isocentre of a 6 MeV beam for different combined thicknesses of entrance and exit foil

For photon radiation the changes in the scored parameters were well below 1.5 % for all foil thicknesses. The simulation uncertainty was mainly below 0.5 %, for 15 MV below 1 %.

Total attenuation is compared in figure 4-30 for chambers with varying entrance and exit foil thicknesses. The thickness of the inner foils was 25 μm each, four layers of 200 nm gold coating and 2 cm of nitrogen gas in the two chamber volumes was assumed. For all foil thicknesses the beam is not significantly attenuated. Above 40 kV the attenuation is below 1 %.

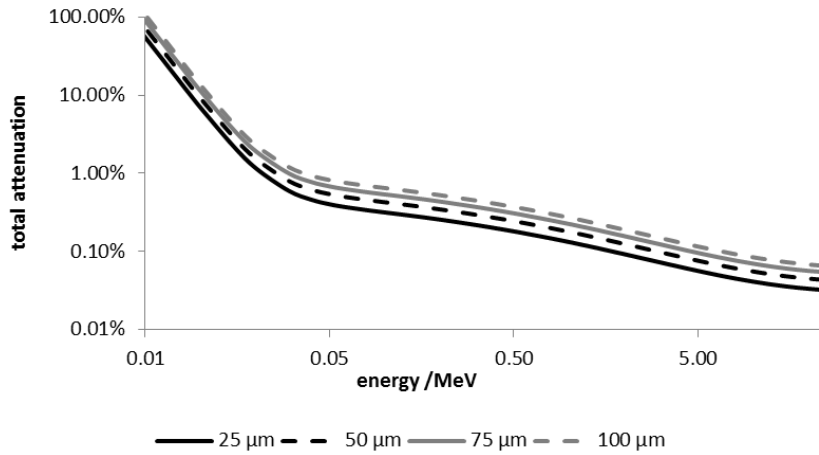


Figure 4-30: Total attenuation with coherent scattering for different entrance and exit foil thicknesses

Besides the influence on the beam, the permeability of the foils is a crucial parameter for determining the thickness of the foils.

The gas throughput Q depends on the area A through which the gas can flow, the thickness of the foil d , the partial pressure difference between the two volumes Δp and the permeability constant K [dos Santos, Veloso and Monteiro 2004].

$$Q = K \frac{A}{d} \Delta p \quad (48)$$

In table 4-17 permeability coefficients for Kapton type HN (25 μm thickness) for some gases are given.

Table 4-17: Permeability coefficients for different gases for Kapton in ($\text{cm}^3 \text{ mm}$) / ($\text{m}^2 \text{ day atm}$)

Gas	CO ₂	O ₂	H	N ₂	He
[Massey 2003]	17	10	100	2	163
[Goodfellow 2003]	43.8	8.75	87.5	2.6	-

The low permeability of nitrogen through Kapton favours for N₂ as filling gas. Moreover is the partial pressure difference between the gas filling and the surrounding air smaller than for other gases, as air consists out of 78 % nitrogen. Therefore the throughput is lower if nitrogen is used as a filling gas.

For example, the throughput for a chamber with exit windows of 75 mm x 75 mm and 25 μm thick Kapton foils, filled with nitrogen (95 % purity grade) at 20 hPa above air pressure, the throughput will be

$$Q = 2 \frac{\text{cm}^3 \cdot \text{mm}}{\text{m}^2 \cdot \text{day} \cdot \text{atm}} \frac{(0.075\text{m})^2}{0.025\text{mm}} 0.02\text{atm} = 0.009 \frac{\text{cm}^3}{\text{day}}$$

which is equivalent to 0.009 % of the total volume per day in a chamber volume with 1 cm height and 10 cm x 10 cm area.

More critical is the inflow of components like oxygen. Here the partial pressure difference between air and chamber volume with 95 % nitrogen and assumed 5 % oxygen is $0.21 \cdot 1013 \text{ hPa} - 0.05 \cdot 1030 \text{ hPa} = 162 \text{ hPa}$

$$Q = 10 \frac{\text{cm}^3 \cdot \text{mm}}{\text{m}^2 \cdot \text{day} \cdot \text{atm}} \frac{(0.075\text{m})^2}{0.025\text{mm}} 0.16\text{atm} = 0.36 \frac{\text{cm}^3}{\text{day}}$$

As the partial pressure difference decreases with increasing oxygen concentration in the chamber, the throughput decreases from day to day until equilibrium between chamber volume and air is reached.

The gas throughput depends inversely on the foil thickness d , thicker foils would minimize the gas loss and diffusion of unwanted components over time.

In the chamber metalized windows are used. The metallization further reduces the permeability. Aluminium is impermeable to oxygen if the coating has no pores. This is true for coating thicker than 18 μm . But even for thinner coatings with high porosity, the number of pores through which oxygen might reach the plastic foil is in the order of 0.001 % of the total area [Buchner 1999] so that permeability is significantly reduced by a factor of 10^5 .

Metallization

As coating on the foils, theoretically all conductive materials may be used. In practice, aluminium, gold and graphite are used as they can be vacuum coated on plastic foils. Table 4-18 gives some properties of these materials. As the layers are very thin (in the order of 50 - 200 nm), the density and atomic number are not critical. Photon and electron radiation have little influence on metallic properties such that these can be seen as radiation resistant [Choppin, Liljenzin and Rydberg 2002].

If the chamber design is open, metallization should be corrosion resistant. Therefore aluminium should not be considered in such a case [Blad, Nilsson and Knöös 1996].

Table 4-18: Properties of materials suited for metallization

	Aluminium	Gold	Graphite
Electrical conductivity /(MS/m)	37.66*	42.55*	0.2-0.3†
Density /(g/cm ³)	2.698*	19.282*	2.20†
Atomic number	13*	79*	6*

* [Hoppe 2011]

† [Pierson 1993]

4.6.3 Other Materials

Radiation resistance and permeability are also the main selection criteria for other component materials. Besides wires and foils, also gaskets, bolts, spacers, housing, screws, PCB and adhesive have to withstand the radiation conditions in the head of the linear accelerator. The gaskets and the housing have to be as gastight as possible.

The monitor chamber is only directly hit by the beam in the central area where the foils and sense wires can be found. Surrounding the main beam, the other materials only receive a lower dose.

At the outer rim of the current photon chamber, i.e. at a radius of approximately 3.5 cm from the central axis, a dose rate of 11.3 Gy/min was measured at a dose rate at isocentre of 2.0 Gy/min (internal measurements at Siemens AG). The typical yearly amount of applied dose to the isocentre is around 39 kGy (internal communication, Siemens AG). Thus the dose per year that materials in that position have to withstand is $11.3/2 \cdot 39 \text{ kGy/year} \approx 220 \text{ kGy/year}$. On the rails of the current carriage a dose rate of 87 % of the dose rate at isocentre was measured, so that at this position, only approximately 34 kGy are applied per year.

For housing and screws aluminium is chosen as it is easy to machine, readily available at low cost and stable.

Ionising radiation leads to changes in molecular structure of rubber and plastic materials which lead to changes in mechanical properties and to embrittlement [Ensinger 2012]. Brittle gaskets may be permeable to the filling gas. Moreover the glue used has to be radiation resistant enough such that it does not become brittle. This would lead to untight entrance and exit windows and such change the gas concentration in the chamber.

For the bolts, spacers and PCB radiation resistant materials were chosen to minimize the possibility of mechanical damages during service and to prevent the degradation of materials and outgassing [Titov, et al. 2002, Ensinger 2012]. For these components, the radiation resistance of common materials is given in table 4-19.

Table 4-19: Radiation resistance of materials used for ionisation chambers

Component	Material	Radiation resistance /Gy	life time /years
Gaskets	NBR*	1×10^5	0.45
	EPDM*	6×10^5	2.73
	FPM*	2.2×10^5	1.00
Bolts, Spacers	PEEK†	1×10^7	45.45
PCB	FR4†	1×10^7	45.45
Adhesive	Araldite two component glue†	1×10^6	4.54

NBR= Nitrile Butadiene Rubber

EPDM= Ethylene Propylene Diene Monomer

FPM= Fluorocarbon Rubber

FR4= Fire-Retardant glass laminate substrate material (epoxied fibre-glass)

* [Massey 2003]

† [Domininghaus 1998]

The permeability constants for nitrogen of the gasket materials in table 4-19 are given in table 4-20. EPDM was hence excluded as an option for the gaskets as the permeability constant is significantly higher than for NBR or FPM. For prototype 2 NBR was used.

Table 4-20: Permeability constants for nitrogen [Massey 2003]

	NBR	EPDM	FPM
permeability / $\frac{cm^3 * mm}{m^2 * Tag * atm}$	40	553	17.5

4.7 Activation

In the energy range covered by linear accelerators, materials in the treatment beam may be activated. The most important effect is the nuclear photo effect. When a photon of sufficient energy hits a nucleus, a neutron may be expelled which leads in most cases to a radioactive isotope which decays by emitting a positron or by electron capture in most cases.



A = number of nucleons

Z = nuclear charge

N = number of neutrons

This reaction depends on nuclear reactions cross section and the energy of the photon, which has to be higher than the binding energy of the neutron. Most reactions occur in the Giant Dipole Resonance (GDR) region of the nuclear reaction cross section in which “the electric field of the photon transfers its energy to the nucleus by inducing an oscillation in which the protons as a group move in opposite direction to the neutrons as a group” [Loi, et al. 2006]. (γ,n) reactions dominate the GDR cross sections of high atomic-number nuclei [Naeem 2006] and the neutron yield is proportional to the convolution of the (γ, n) cross-section and the bremsstrahlung spectrum [Loi, et al. 2006].

The neutron itself can activate further nuclei, in the energy range up to 25 MeV most likely by neutron capture. The resulting isotope is in most cases radioactive and decays most probably by β- decay.



Activation of target, primary collimator, flattening filters and jaws is a known issue [Becker, Brunckhorst and Schmidt 2007] and occurs mainly through the first process [Fischer, Tabot and Poppe 2006], but also other components like wedge filters in the beam may be activated [Fischer and Peick 2003].

In the Unified Dose Chamber, the only materials which can significantly be activated are the metal housing and the sense wires, which are made from aluminium, molybdenum or tungsten and gold. Table D-1 in appendix D gives the threshold energy for the most important photonuclear reactions as well as the peak energy and cross section of the processes.

The GDR in the principal cross section for photonuclear interactions peaks around 21 MeV for aluminium, at 18 MeV for molybdenum, at 12-15 MeV for tungsten and at 13.5 MeV for gold. The cross section in aluminium is small compared to the other materials, i.e. a low activation is expected. On the other hand, it is the only material where γ,p reaction has a significant cross section. For tungsten, gold and molybdenum, no significant γ,p cross section is observed, except for Mo-92 where a peak of 130 mbarn in the γ,p cross section occurs at approximately 15 MeV [Los Alamos National Laboratory 2008].

With respect to activation, materials with smaller cross sections for photonuclear reactions are advantageous. As the amount of gold on the wires is very small, their activation is not deemed as a problem. Molybdenum as material for wires is preferred over tungsten with respect to activation.

4.8 Ageing

For conventional wire chambers operated in the proportional region, ageing of the wires is a known and critical issue. Polymer growth on wires (whiskers) by polymerization caused by species produced in the avalanche due to impurities in the gas, etching away of aluminized surfaces and a uniform coating by a polymer or silicon are the main problems. Several investigators studied these effects and guidelines for wire chamber production and operation are suggested. Christo summarized the Do's and Don'ts in 1989 [Christo 1989] and in a workshop on aging phenomena in gaseous detectors in 2001 most suggestions were deemed still valid though with further limitation due to increased dose rates in newer detectors [Titov, et al. 2002].

To prevent or inhibit the ageing process, the use of CF_4 or CO_2 gas and high purity gases, increased wire diameter as well as gold plated wires with good surface quality, reduced relative voltage and a large distance between anode and cathode are recommended. PVC should not be used due to outgassing after high absorbed dose. Silicon impurities, hydrocarbons and fingerprints should be avoided.

In the Unified Dose Chamber the electric field is much smaller than in multi wire chambers such that most ageing phenomena will not be as pronounced as at high field strengths. Nevertheless, high purity gases shall be used and the chamber shall be assembled under clean room conditions.

To minimize the effect of outgassing materials, mainly material already selected for the MWPC for the detector used at HIT were used.

4.9 Summary of Optimal Parameters

The Unified Dose Chamber should work reliably for several years such that high quality materials should be used. For the foils polyimide metalized with gold or carbon is favourable. The thickness should be around 75 μm to 100 μm to minimize permeation in and out of the gas volume and to not influence the beam significantly.

Wires made from tungsten or molybdenum, preferably coated with gold to increase the electrical conductivity and minimize ageing effects, are preferred. The diameter should be as large as possible to lead to a homogeneous field distribution. 100 μm diameter wires are a good compromise between sag and field distribution. All other materials have to be radiation resistant as well and should be chosen according to table 4-19.

The diameter of the entrance window has to be around 75 mm to ensure that the whole beam passes the chamber. The height of the ionisation volume should be at least 2.5 mm to 3.0 mm to ensure a measurable amount of collected charge. To detect the beam profile the channel distance should be 3.5 mm or smaller. Moreover smaller distances between the wires and between the wires and foils lead to a more homogeneous field distribution.

The filling gas should be argon or nitrogen mixed with CO_2 due to the higher mobility and more produced electron-ion pairs per incident electron.

5 Effects of Changes in Monitor Chamber on Linear Accelerator

Changing the monitor chambers from two separate ones in a moving chamber slide to a fixed unified one has some impact on the layout of the linear accelerator. First of all, the secondary foil used to flatten electron radiation is normally attached in a container to the electron chamber such that it is moved with the chamber in the chamber slide. For a unified chamber a solution is discussed in the following.

Moreover the mirror is normally attached to the chamber slide below the photon chamber and is not in the beam during electron mode. As the mirror would influence the electron beam, another solution has to be found. One suggestion is discussed in chapter 5.2.

5.1 Secondary Foil

The secondary scattering foil consists of three conical layers of aluminium with decreasing diameter quenched between two Kapton foils, as can be seen in figure 5-1.

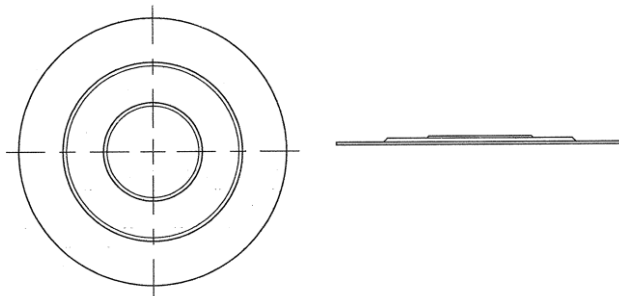


Figure 5-1: Secondary foil

In photon mode the secondary scattering foil is not in place. For a single dose chamber, there are two possibilities. The secondary scattering foil can be moved into the beam if electron mode is selected. This would counteract the advantage of less moving parts of a single dose chamber. Moreover the positioning of the scattering foil is quite critical. Even small deviations in the range of a few hundred micrometres can spoil the beam profile.

A better solution would be to keep the scattering foil in place, under electron as well as photon radiation. Therefore simulations were performed to assess the influence of the secondary scattering foil on photon beams.

The highest impact is assumed at low energies. Thus 6 MV and 15 MV flat photon beams with a foil chamber similar to the PTW-Freiburg prototype discussed in chapter 2.4.4 were simulated, with and without the secondary scattering foil in place. For the foil chamber, five Kapton foils of 25 μm thickness, coated with gold were simulated. Figure 5-2 gives the set-up of this chamber.

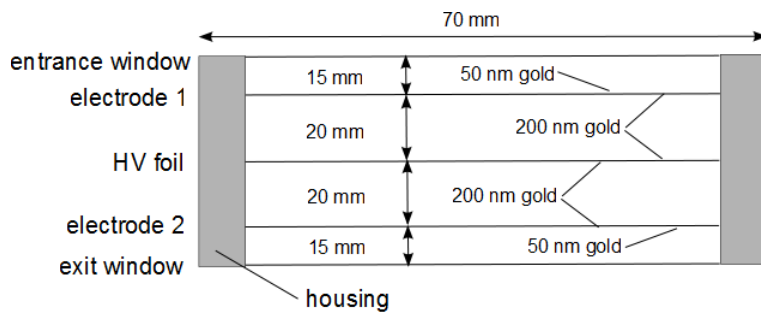


Figure 5-2: Simulated foil chamber

The energy fluence was scored at SSD 100 cm at a field size of 40 cm x 40 cm in a depth of 10 cm in a water phantom of 60 cm x 60 cm x 30 cm and in air. Figure 5-3 shows the simulated set-up. The number of incident particles was chosen such that the simulated profiles have an uncertainty below 0.5 %. For details of simulation parameters see appendix B.

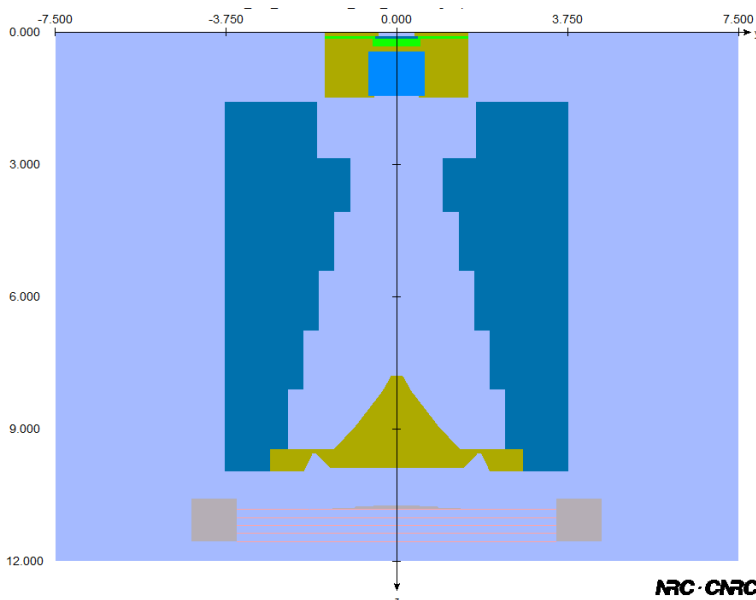


Figure 5-3: Detail of simulation set-up for a 6 MV flat photon beam with secondary scattering foil in place

The difference between the profile with and without scattering foil was calculated. For 15 MV photon beams the differences in energy fluence, spectral and angular distribution as well as mean energy distribution in the isocentre plane are mainly within ± 1.0 % such that no significant influence on the beam is observed.

When scoring the energy fluence in air for 6 MV photon beams a slight drop in the centre can be seen (figure 5-4 on the left). This vanishes when the beam is scored in water (see figure 5-4 on the right). This is due to scatter in the water volume. Therefore it is concluded that the secondary scattering foil can be kept in the photon beam without adversely affecting the beam.

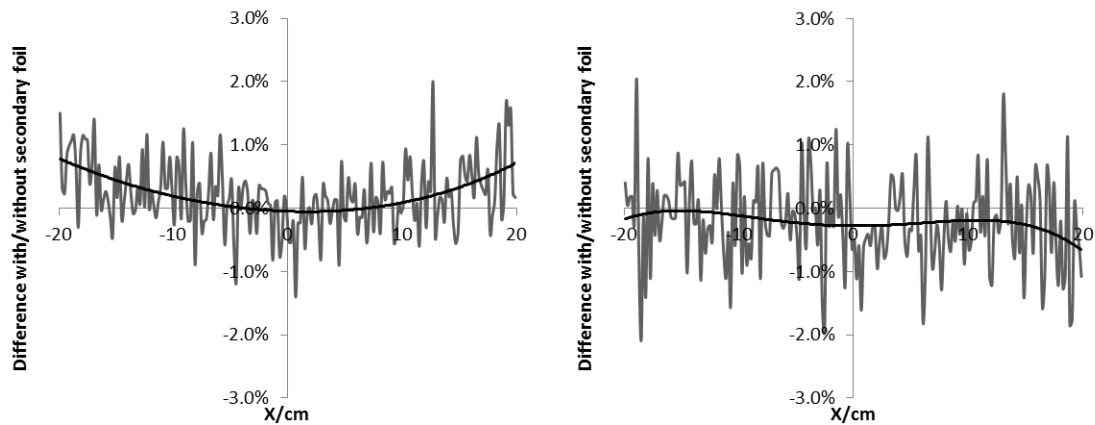


Figure 5-4: Difference in energy fluence between a simulated 6 MV flat photon beam without and with secondary foil in beam path, scored at 100 cm SSD in air (left) and in 10 cm of water (right). Black lines indicate a 4th order polynomial fit

5.2 Mirror

In current Siemens accelerators the mirror, which deflects the light from a light bulb into the patient plane, is mounted under the photon chamber and is thus not in the beamline during electron radiation. The current mirror consists of a rigid 1.6 mm thick glass layer coated with 50 μm aluminium which would undesirably influence the beam in electron mode. To prevent a moving mirror which is moved out of the beam in electron mode when using a single dose chamber, the mirror concept has to be changed.

A possible solution would be to replace the glass mirror by a thin metallised polyimide foil which does not adversely influence the electron beam and can thus be kept constantly in the beamline. For electrons a slight disturbance and filtering of low energy components from the spectrum is expected. For photon radiation the replacement may result in changes in the beam spectrum as fewer low energy photons are absorbed. This may lead to increased surface dose in the patient plane and thus to unwanted side effects like skin reddening when treating the patient.

To validate the feasibility of applying such a mirror, beam profiles and spectra in the patient plane from simulated 6 MV photon beams were analysed. The existing mirror setting and a setting with a 100 μm thick polyimide mirror coated with 200 nm aluminium in place were compared for a monitor chamber with 5 layers of 25 μm thick polyimide foils and a diameter of 7 cm.

In figure 5-5 the energy fluence distribution for both configurations at 100 cm SSD scored in air is plotted. The energy fluence for a polyimide mirror is higher than with a silicon mirror as fewer low energy particles are absorbed. The peak at 511 keV is approximately 4 % higher and the peak of the main distribution at approx. 1 MeV is 3 % higher.

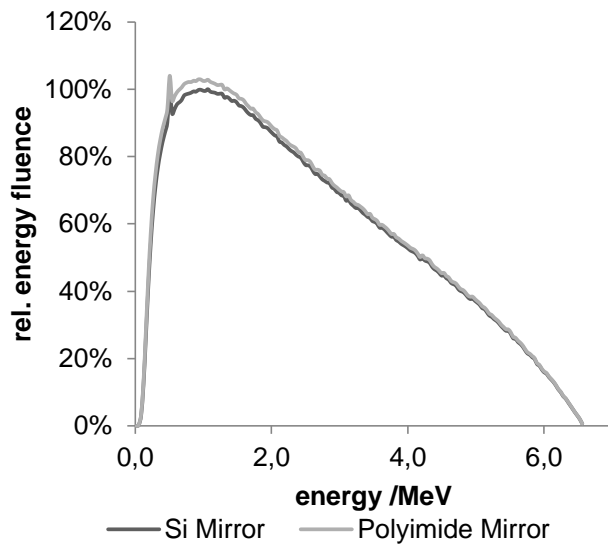


Figure 5-5: Energy fluence distribution for a 6 MV flat photon beam at 100 cm SSD with silicon (dark grey) or polyimide (light grey) mirror

The effect of a further layer of polyimide foil in the electron beam would be similar to having thicker entrance and exit foils which was analysed in chapter 4.6.2.

6 Preliminary Investigations

To test the feasibility of wire chambers for monitoring photon and electron radiation, first of all the usability of a multi-wire proportional chamber (MWPC) normally used in proportional mode to monitor proton and ion beams was analysed in ionisation mode under photon and electron radiation. Detailed results are presented in appendix E.

These preliminary investigations showed that in principle a wire ionisation chamber is a feasible mean for monitoring radiation from a linear accelerator. Therefore a first prototype of a Unified Dose Chamber was constructed.

6.1 Construction of first prototype

To test the basic concept of the design determined in chapter 4, a first prototype was built. To keep the design simple, this prototype is open to air. The main aim of this prototype was to be able to measure in the head of a linear accelerator which was not possible with the MWPC due to its size. The basic layout is shown in figure 6-1. Between two shielding planes a HV plane and a single signal layer are placed. The outer diameter is 112 mm x 112 mm, the central area for beam sensing is 76 mm x 76 mm.

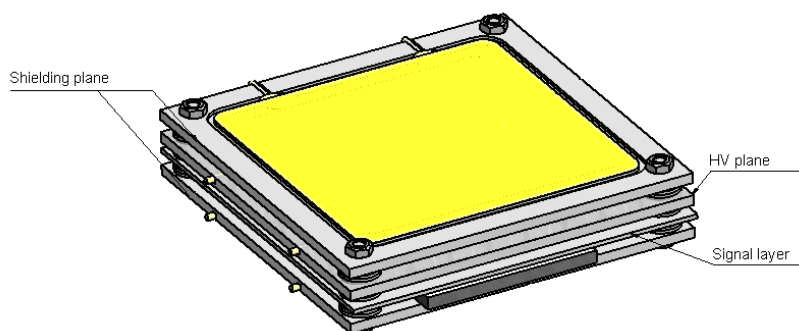


Figure 6-1: Layout of prototype 1 [Schirmer 2010]

The HV and shielding plane frames consist of 3.2 mm thick FR4. For the shielding planes a 25 μm thick polyimide foil, which is coated with aluminium on one side, is glued into the frame with the coated side facing the HV plane. For the HV plane a nickel-plated polyester mesh is used.



For the signal layer of the first prototype a signal frame from a MWPC detector was used. It was cut in the appropriate size and glued together. 50 μm gilded W/3%Re wires were used as these were readily available. The wire tension was 45 cN resulting in negligible sag of $<0.6 \mu\text{m}$ and the resistances of the wires varied between 2.2 Ω and 2.3 Ω . Figure 6-2 shows the first prototype.

Figure 6-2: Photo of prototype 1

As the channel distance in a MWPC detector is 2 mm, 3.5 mm as suggested by the theoretical model for the UDC was not achievable. Any two channels were bridged by tinned copper strands (\varnothing 0.25 mm) to achieve a channel distance of 4 mm. Wire to wire distance was 1 mm.

Due to the inexactness of the manufacturing process of the signal frame, the wires are not in parallel to the frame but displaced by 1 mm from one side to the other as illustrated in figure 6-3. The dotted lines show the optimal position of the wires, orthogonal to the frame. The solid lines indicate the actual position of the wires.

To define the distance between the planes, spacer rings made from PEEK were used. The distance from the HV nickel mesh to the wires of the signal layer was 4.8 mm.

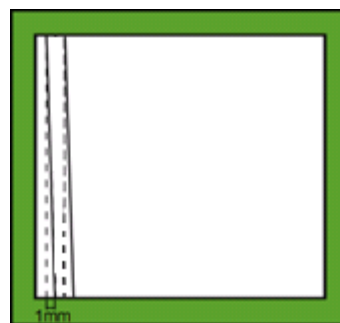
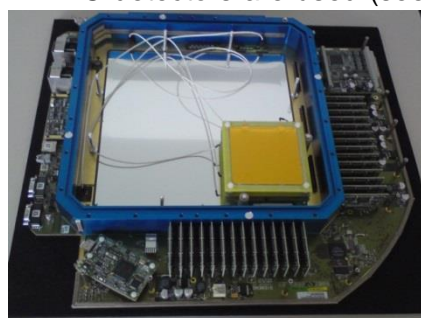


Figure 6-3: Displacement of wires of prototype 1

In order to log the signals from the wire channels, the electronics and software of the MWPC detectors are used (see appendix E). Figure 6-4 shows prototype 1 connected to a MWPC with the MWPC's wire and HV layers removed. The voltage could be set between zero and 2000 V at arbitrary integers. Ground potential was provided by the board as well.



For signal processing the ribbon cable was connected to one set of channels of the MWPC. The signals were integrated, amplified and digitized on the board and evaluated using the MWPC test software.

Figure 6-4: Prototype 1 with MWPC electronics

6.2 Measurements

6.2.1 X-Ray

For testing the functionality of the UDC, investigations at the MWPC beamtest were performed. The MWPC board with prototype 1 was mounted on a movable table in the test device. The x-ray tube of the test stand was set to 60 kV and 20 mA. The beam diameter at the position of the signal layer was verified by Gafchromic EBT films and is approx. 8 mm x 9 mm. The dose rate was calculated to be around 19 Gy/min [McGinnis 2009]. Integration time in the MWPC testing software was set to 200 μ s. The stated values are averaged over 2047 samples. In the short ribbon cable connecting the chamber and the electronics, every second channel was cut, such that every channel that was read corresponds to a single chamber channel. Temperature and pressure were constant over the time of measurements.

First of all, the high voltage was varied from 0 V to 1600 V to determine the plateau region and subsequently define the operating voltage. Afterwards the signal levels of the channels were compared by moving the chamber orthogonal to the wire orientation in steps of 1 mm. The value when the beam directly hits the channel was scored. Moreover, the signal of a single channel in the centre was scored, when the beam moves in orthogonal direction to the wire. For movement along a wire, measurements with a central wire and one at the edge of the chamber were done. In the end a control measurement of the signal level to compare the first and last measurement was carried out in order to judge the stability of the measurements.

6.2.2 Linear Accelerator

To test the first prototype under realistic conditions at a linear accelerator, the chamber was put through the opening of the jaws and laid onto the current photon chamber at a gantry angle of 180°. The electronics were placed onto the accessory holder (see figure 6-5 right).

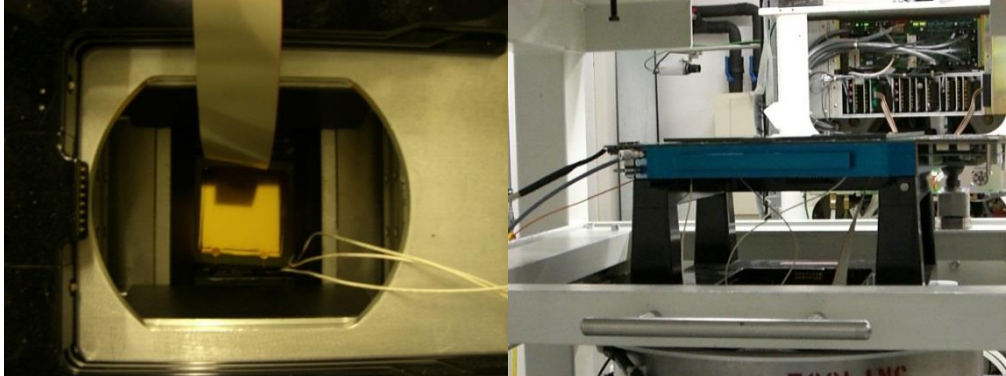


Figure 6-5: Set-up of prototype 1 at linear accelerator (left: chamber in head; right: electronics on accessory holder)

500 V were applied to the chamber. Temperature and pressure were constant during the measurements. The linear accelerator was configured as follows:

- 25 MV, 760 mGy/min at 220 Hz in 10 cm water at 100 cm SSD, 40 cm x 40 cm field size
- 6 MV, 880 mGy/min at 220 Hz in 10 cm water at 100 cm SSD, 40 cm x 40 cm field size

The dose rates were set to these values in order not to cause an overflow of the electronics. They are lower than for conventional linacs used in the clinic. To estimate the dose rate under normal clinical conditions (10 cm x 10 cm field; 10 cm SSD; measured at D_{max}), the measured dose rates were corrected.

For high energies, the percentage of ionisation at a depth of 10cm compared to the maximum dose (D_{10}) does not significantly depend on the field size, so that the measured D_{10} is approximately 81 % of the dose maximum D_{max} , as for a 10 cm x 10 cm field [Podgorsak and Hartman 2007]. Therefore the estimated dose rate at D_{max} for a 10 cm x 10 cm field is 0.94 Gy/min, which is approximately 31 % of the normal dose rate of 3 Gy/min.

For lower energies like 6 MV D_{10} depends on the field size [Podgorsak and Hartman 2007]. For Co-60 beams, the difference in D_{10} between a 10 cm x 10 cm and a 50 cm x 50 cm field is 8.6 % [Podgorsak and Hartman 2007]. For 6 MV the difference is estimated to be around 8 % as the peak of the spectrum of a 6 MV beam is near the cobalt spectrum. So the D_{10} for a 40 cm x 40 cm is estimated to be 75 % of D_{max} . The estimated dose rate at D_{max} is therefore 1.2 Gy/min, which is 40 % of the normal dose rate of 3 Gy/min.

The longer ribbon cable used in this setup was not cut, so that the signal from one chamber channel was split on two channels in the software. Integration time was 200 μ s. Thus the sampling frequency was too low so that the maximum sampled value in 2047 samples was assumed to be the true signal height. Synchronisation of the sampling and the linac pulse was not possible for this first test, as the electronics are normally used for a continuous beam. For each channel, noise and signal level were determined and two channels were summed to yield the true signal of the channel of the chamber. For 25 MV two measurements of the beam profile were done, for 6 MV one measurement was conducted.

Moreover the beam was steered with the steering coils to get a non-symmetric profile at the isocentre. Monitoring of the profile at 100 cm SSD was only possible in the inner 10 cm of the field with a Wellhöfer 1D water tank, so that only slight differences in symmetry were observed.

Moreover the induced charge in the chamber was analysed. Therefore for each channel the signal of the maximum pulse was integrated and the values of the two pins resembling a single channel of the chamber were summed.

6.3 Results

6.3.1 X-Ray

Due to the small diameter of the beam, the measured signal was only slightly higher than the noise which was 100 digital numbers. The average signal-to-noise ratio (SNR) was 1.12.

The variation of the high voltage supplied showed that the signals were fairly constant over a voltage range of 200 V to 800 V so that an operating voltage of 500 V was selected. Above 900 V the signal slowly increased. After going back to 500 V the signal was not back to the first measured value which was found to be due to heat dissipation from the nickel mesh. Before the following measurements were done, the prototype cooled down. At 500 V no heating of the chamber was observed.

Figure 6-6 shows the signal level minus the noise for all channels. The outer two channels show higher values because here more than four wires were bridged. The inner 13 channels show the same values within 4.3 % (one standard deviation). The deviation may be caused by varying amplification in different channels of the MWPC electronics.

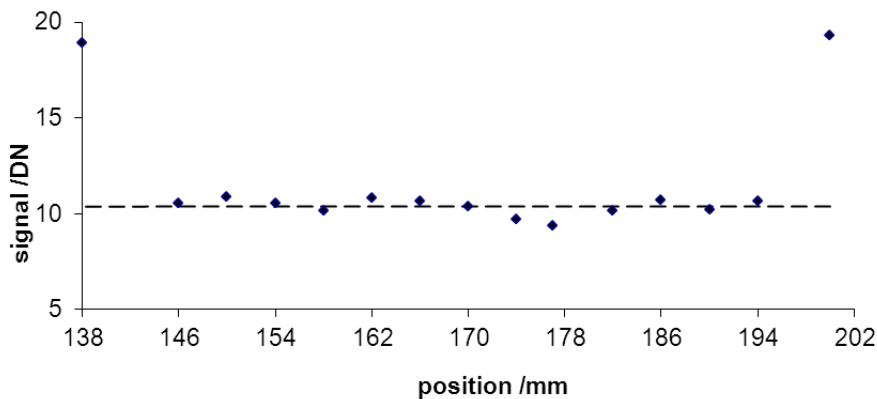


Figure 6-6: Signal levels of channels of prototype 1 at x-ray test stand

When moving the chamber orthogonal to the wire direction, a channel samples the beam profile. In figure 6-7 the measured profile can be seen. The FWHM of the beam profile is 7.3 mm.

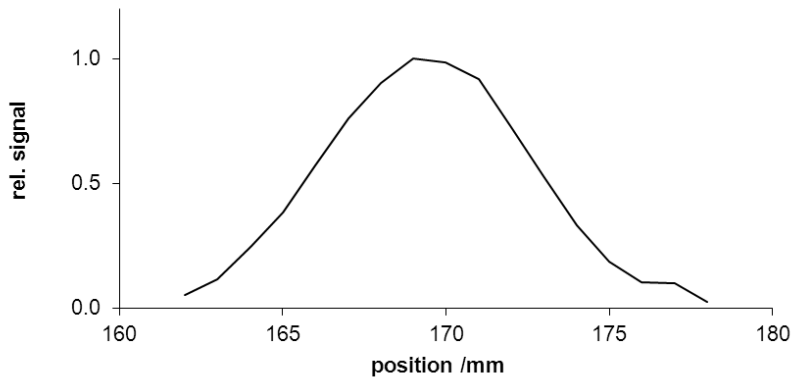


Figure 6-7: Scan of the x-ray beam from the test stand with a single channel of prototype 1

To investigate the homogeneity along a wire, the beam was moved along the central wire and along one at the edge. The decrease in signal intensity observed figure 6-8 is due to the misalignment of the wires. From one side to the other the signal decreases to approx. 90 % which corresponds to the results of the former measurement. 1 mm aside the maximum, the signal level is around 90 %. The plateau is 65 mm wide so that a beam of 60 mm diameter at a linear accelerator can be monitored well.

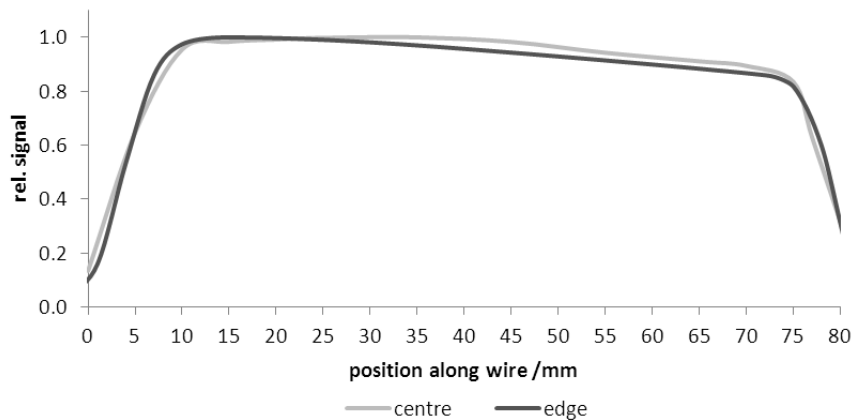


Figure 6-8: Scan along a central wire and a wire at the edge of the first prototype at the x-ray test stand

At the end of the tests a control measurement on the central wire showed that the series of measurements were stable as the deviation to the first measurement was below 1 %

6.3.2 Linear Accelerator

Figure 6-9 shows the measured values and interpolated profile of two consecutive measurements at 25 MV (black and grey lines). The maximal deviation between the two measurements at 25 MV is 1.6 %. Figure 6-10 shows a measurement at 6 MV (black line). Moreover a profile of a 6 MV beam measured during another measuring series by Gafchromic EBT film is included for comparison (red line).

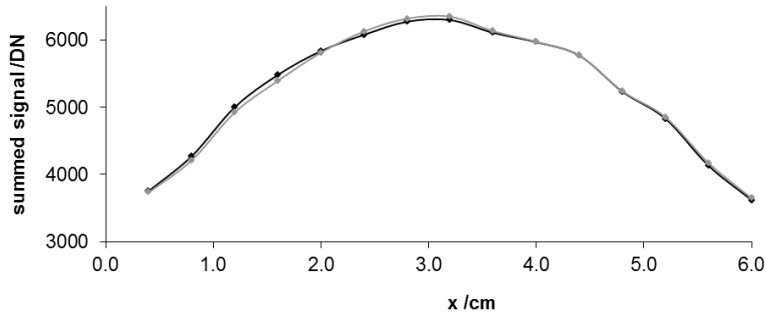


Figure 6-9: Measured values with prototype 1 at 25 MV

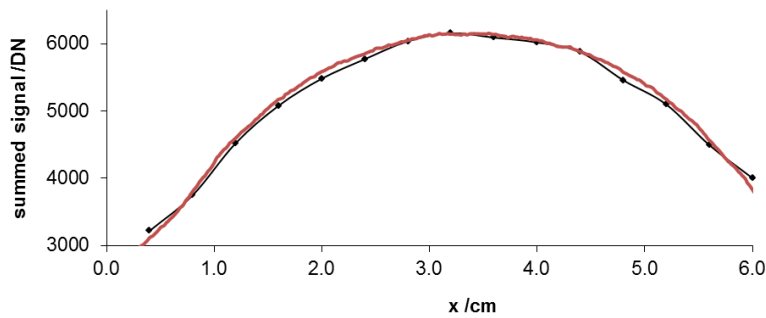


Figure 6-10: Measured values with prototype 1 at 6 MV (black line) and profile measured with Gafchromic EBT film (red line)

When steering the beam, for 25 MV the change in the profile is clearly visible and linear (figure 6-11). For 6 MV the difference in profile before and after steering is not as clear as for 25 MV. The height of the signals is reduced and at the edges of the chamber a change in profile is visible.

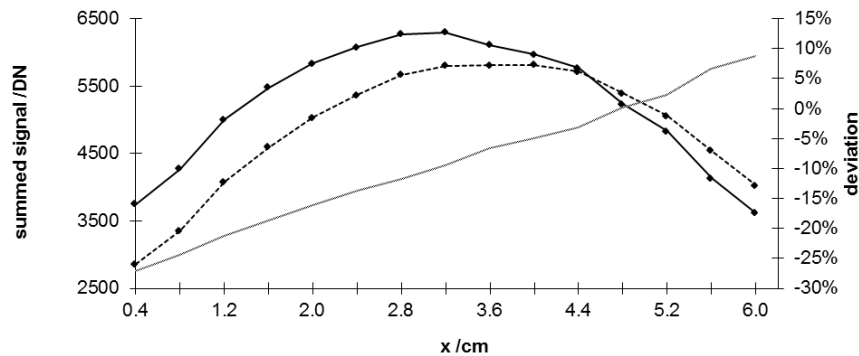


Figure 6-11: Original (solid line) and steered (dashed line) signal at 25 MV; percentage deviation of these (grey line)

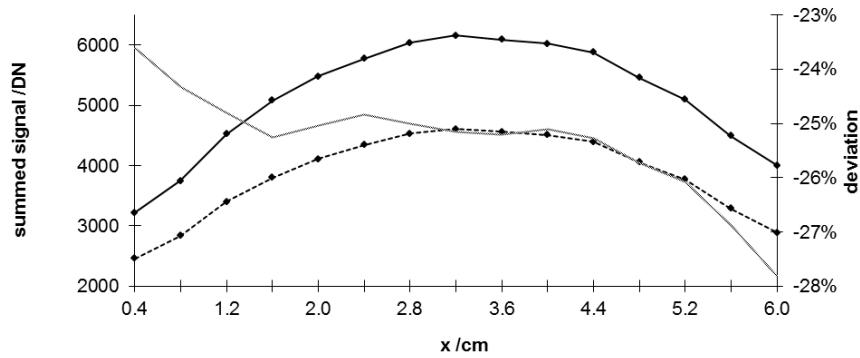


Figure 6-12: Original (solid line) and steered (dashed line) signal at 6 MV; percentage deviation of these (grey line)

In order to design the electronics for the second prototype accordingly, the expected induced charge Q in the volume Vol of the first prototype at a distance of 12 cm from the exit window for 6 MV and 25 MV beams at 220 Hz and 3 Gy/min is derived.

$$Q = 0.034 \frac{C}{Gy * m^3} * DPP * Vol * k_{Int}$$

$$= 0.034 \frac{C}{Gy * m^3} * \frac{3 Gy}{60 s * 220 Hz} * \left(\frac{100}{12}\right)^2 * 1.35 * 10^{-5} m^3 * 0.84 = 6.1 nC$$

As the dose rate at isocentre is measured in the centre of the beam, but the intensity is not homogeneous across the profile, as can be seen in figure 6-13, the scaling factor k_{Int} was introduced to scale the dose per pulse to the average intensity over the chamber volume (corresponding to the grey line in figure 6-13). For both energies the factor is similar and assumed to be the same for the above estimation.

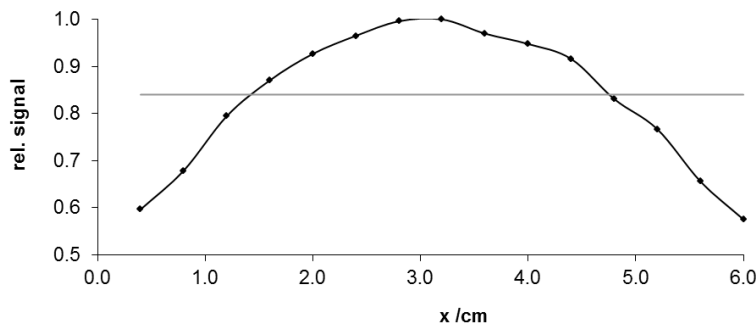


Figure 6-13: Beam profile at 25 MV (black line) and average intensity (grey line)

As the measurements were done at 40 % and 31 % of the normal dose rate for 6 MV and 25 MV, respectively, the expected values were scaled accordingly. 2.44 nC and 1.89 nC are expected for 6 MV and 25 MV, respectively.

From the measurements 2.45 nC were calculated for 6 MV which is equivalent to the theoretical value. For 25 MV the measured induced charge was determined to be 2.51 nC, i.e. 133 % of the theoretical value.

6.4 Discussion and Conclusion

From the measurements with the first prototype one can conclude that a wire chamber is suitable to monitor the radiation beam of a linear accelerator. The tests showed a homogeneous response of the wires. Nevertheless the electronic channels have to be calibrated.

As the wires were not parallel to the axis, the homogeneity along a wire could not be shown directly. But the results show a decrease of the signal from one end of the chamber to the other of 10 % which agrees well with the loss in signal when the x-ray beam is 1 mm off the wire.

Moreover a channel distance of 4 mm seems to be sufficient to detect shifts in a profile as shown by steering the beam. As the profile could not be monitored sufficiently in the isocentre, further measurements with the second prototype have to show how sensitive the chamber is to changes in beam profile.

The tests showed that the profile of the beam can be detected well. As here the measured 6 MV profile was compared to a film measurement taken at another machine at a different point in time, further measurements comparing the detected profile to the true profile have to show how good both profiles agree.

The induced charges determined during the measurements at the linear accelerator are in good agreement with theoretically derived values. For 25 MV the induced charge is higher than the theoretically expected value which might be due to the uncertainties in dose rate determination at the position of the chamber. Nevertheless, the good agreement in order of magnitude between theoretically derived and measured values for the induced charge allows the development of the electronics for the second prototype based on theoretically calculated values.

From the experience with the first prototype, a second, more sophisticated prototype including adequate electronics was designed.

7 Second Prototype of UDC

7.1 Construction

The second prototype is an airtight chamber which was designed to test different gas fillings and to perform tests in the head of a linac. Figure 7-1 shows the assembled chamber.

The basic layout is shown in figure 7-2. The HV layer (yellow foil in dark green layer) is situated in the middle of the chamber. Symmetrically, two signal planes (light green) are stacked on bolts. Consecutively, shielding planes (light yellow) are mounted on the bolts. The casing (grey) has a Kapton window (yellow) where the beam hits the chamber. For filling the chamber with different gases, gas inlet (yellow connector with brown tube) and outlet passages (filled with yellow plug) are added to the housing. Each volume can be filled separately.

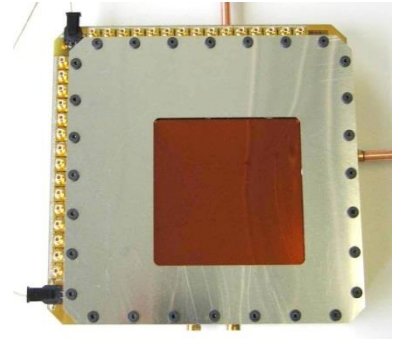


Figure 7-1: Assembled prototype 2

The outer diameter is 160 mm x 160 mm, the central area for beam sensing is 76 mm x 76 mm.

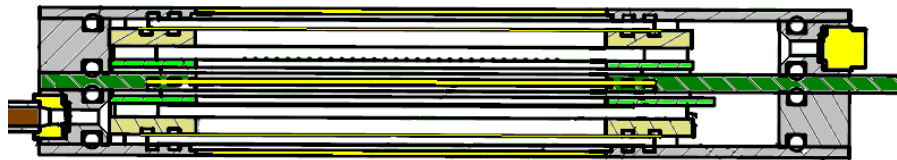


Figure 7-2: Sectional drawing of prototype 2

A signal plane consists of 38 parallel gilded tungsten wires with 100 μm diameter and 2 mm distance between the wires. Each channel consists of two wires, which gives a better sampling as shown in chapter 4.3.1.4. In total 19 channels are available. The electronic readout was limited to 32 channels, so that only 15 channels are read out per plane.

For the first measurements, the wire plane was inserted such that the distance between wires and HV was 4.2 mm. For the following measurements, the wire plane was placed in the chamber such that the distance between wires and HV was 2.7 mm.

Following the signal plane, spacer rings with 1 mm thickness (made from PVC instead of PEEK due to material availability) were inserted, followed by a shielding plane.

For all measurements, the upper side, on which the connectors are located, was labelled volume 1. The lower side is volume 2, respectively. The channels were labelled from 1-01 to 1-15 and from 2-01 to 2-15, counting from the HV supply connector outwards.

Details on the construction can be found in appendix F.

7.2 Electronics

7.2.1 Hard- and Software

For analysing the signals per radiation pulse from each channel, the designed electronics with 30 read-out channels were constructed by HBS (Rudolstadt, Germany). These were connected with a computer via two cRIO modules in a chassis with an FPGA and a NI cRIO9004 real-time controller. The read-out programme was programmed with LabView. In figure 7-3 the signal flow chart is plotted.

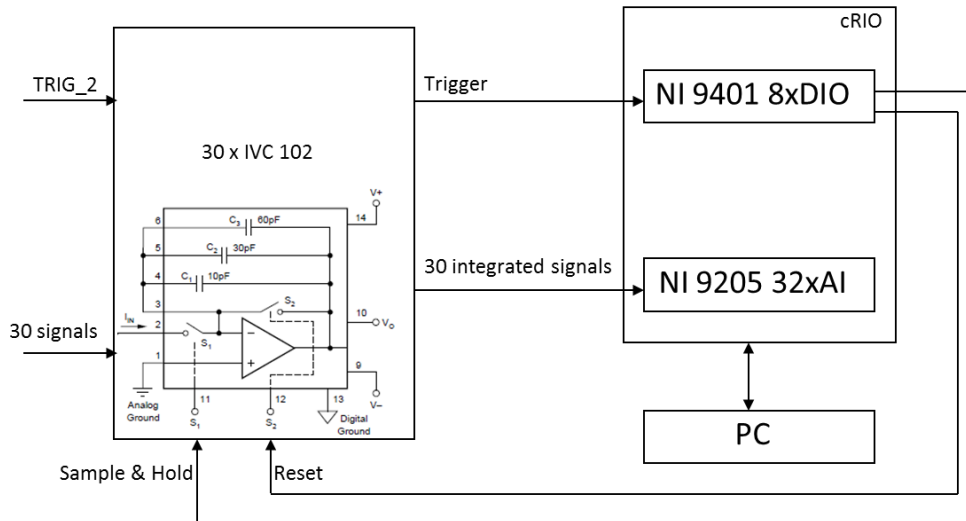


Figure 7-3: Signal processing for prototype 2

The electronics first of all convert the -15 V analogue trigger signal TRIG_2 from the linear accelerator to a +5 V TTL signal which is fed into the LabView programme via the NI 9401 DIO module, which has a maximum clock frequency of 10 MHz. This signal is used for timing the integrate, hold and reset phases of the 30 integrators (IVC 102) on the electronics board.

When the TRIG_2 latches, the integration on IVC 102 starts after the time t_1 “delay integration”, which is normally set to zero, by opening the switch S_1 . After a defined time t_2 (“integration time”) the switch S_1 is closed such that the signal is held on the integrator. A defined time t_3 (“delay sample”) later, the software samples the values from all 32 channels on the NI 9205 during the “sample time”. To ensure that all signals are read, t_3 should be longer than 32 times $4 \mu\text{s}$ (the switching time between channels of the NI 9205). A “delay reset” time may be introduced before the integrator is reset during the “reset time” by closing switch S_2 . An example of the charging curve and timing scheme is given in figure 7-4.

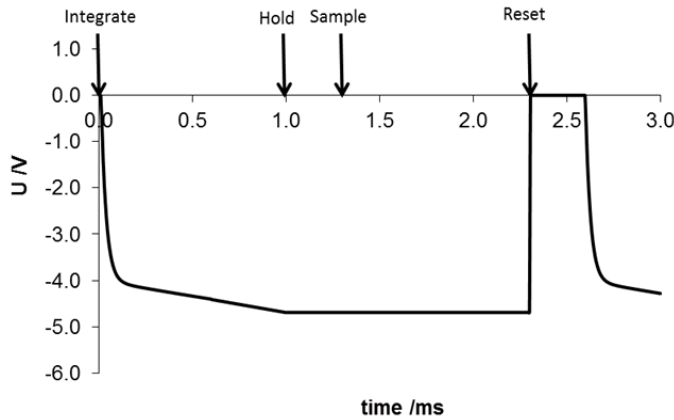


Figure 7-4: Timing for electronics of prototype 2

The capacitance was first of all kept at 100 pF for the functionality tests. For the measurements under pulsed radiation the capacitance was increased to 250 pF per channel to allow measurements at high dose rates. The NI 9205 samples the analogue input with 16 bit resolution and 250kS/s. The input range is ± 10 V.

The main programme on the FPGA samples the values at the 32 analogue input channels continuously and hands them over to the real-time programme. Moreover the time, when sampling is allowed is defined at this level. From the stream of sample values those during the “sample time” are picked and this stream of sample values for each pulse is sent to the host PC. On the real-time symmetry, flatness, total dose and dose of each side of a profile are calculated. Besides this option, these calculations were done for the final analysis with the raw data sent to the host PC.

The programme is operated from a user interface on the host PC. Figure 7-5 shows this user interface, where the integration, hold and reset times are entered. The programme supports an internal trigger which triggers as fast as possible, i.e. after the sum of all manually entered times passed. This option is used for testing the electronics with a constant current where no external trigger is available. Moreover the number of sets, i.e. the number of pulses that should be logged has to be defined. Status displays for the TCP/IP connection between cRIO and computer are shown as well. The “Array” shows the sampled values. After starting the measurement the “transfer” button allows the values to be sent from the real-time to the host PC. After having logged the desired number of pulses, the data is saved by pressing the “save” button. A dialogue appears in which an appropriate folder and filename can be selected. After having saved the data, the programme stops and has to be restarted before the next measurement.

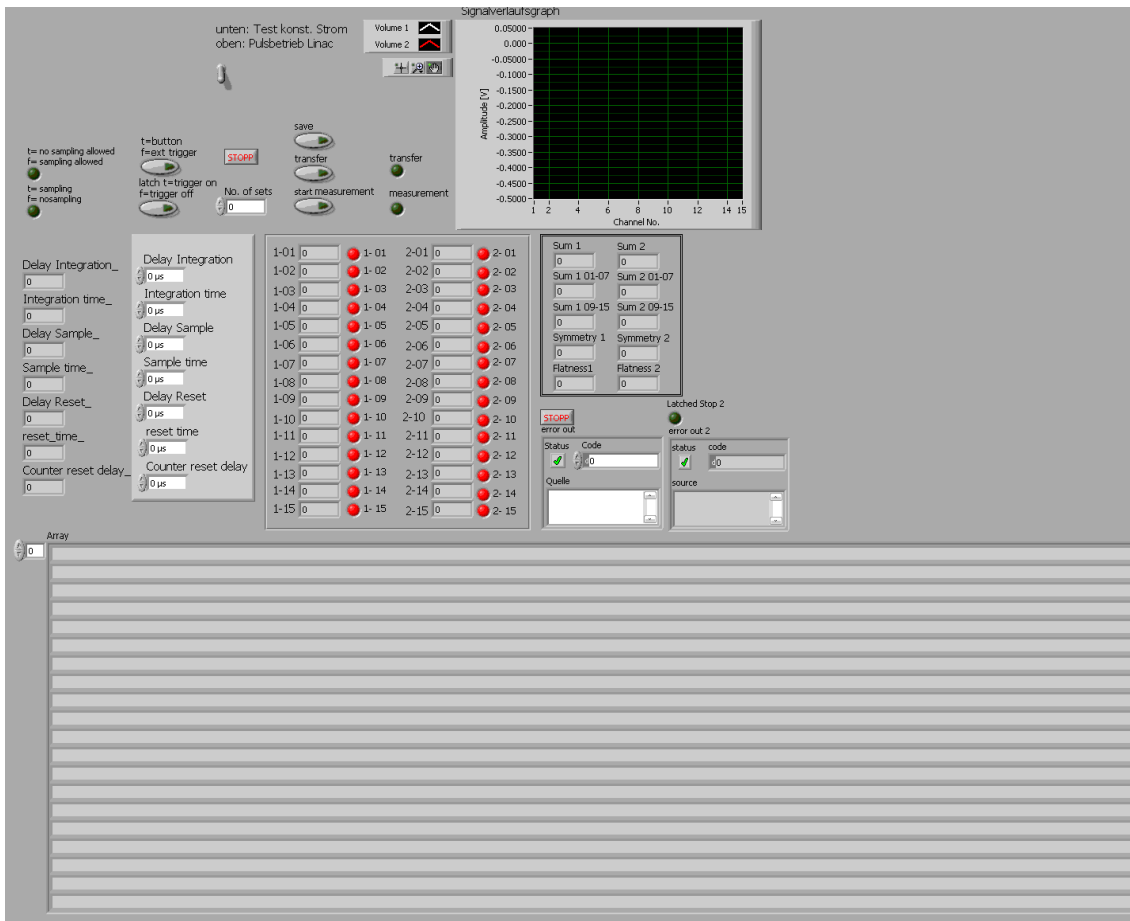


Figure 7-5: User interface of read-out programme

7.2.2 Accuracy

The charge integrated on the IVC102 integrating amplifier is held during the hold period. During this time the voltage slightly drops. The droop rate for 250 pF capacitor is around 0.4 nV/ μ s [Texas Instruments 2000]. As the first sample during the hold period is logged, the maximum time until sampling is 300 μ s (“delay sample”) plus 32 times 4 μ s (switching time of the NI9205). The voltage droop is therefore below 170 nV, i.e. negligible. Moreover the noise voltage is around 10 - 30 μ V_{rms}.

Nonlinearity is specified to be below ± 0.005 % when using the internal capacitances. The specified gain error is ± 5 %. By adding additional 150 pF this gain error is altered and investigated together with nonlinearity in the following chapter.

The absolute accuracy of the NI 9205 is defined as

$$\begin{aligned} \text{Absolute accuracy} \\ &= \text{Reading} * \text{GainError} + \text{Range} * \text{OffsetError} \\ &+ \text{NoiseUncertainty} \end{aligned} \quad (51)$$

with $\text{GainError} = \text{ResidualGainError} + \text{GainTempco} * \Delta T_{int} + \text{RefTempco} * \Delta T_{ext}$

$\text{OffsetError} = \text{ResidualOffsetError} + \text{OffsetTempco} * \Delta T_{int} + \text{INL_Error}$

$$\text{NoiseUncertainty} = \frac{\text{RandomNoise} * 3}{\sqrt{100}}$$

for a coverage factor of 3σ and averaging 100 points

ΔT_{int} Temperature change from last internal calibration

ΔT_{ext} Temperature change from last external calibration

For a nominal range of ± 10 V, the following values are given by the manufacturer [National Instruments 2010]

ResidualGainError	115 ppm
Gain Tempco	11 ppm/ $^{\circ}$ C
RefTempco	5 ppm/ $^{\circ}$ C
Residual Offset Error	20 ppm of Range
OffsetTempco	44 ppm of Range/ $^{\circ}$ C
INL Error	76 ppm of Range
RandomNoise	240 μ V _{rms}

Assuming a ΔT_{ext} of 20 $^{\circ}$ C and a ΔT_{int} of 1 $^{\circ}$ C

$$\begin{aligned} \text{Absolute accuracy} &= \text{Reading} * 226 \text{ ppm} + 10 \text{ V} * 140 \text{ ppm} + 72 \mu\text{V} \\ &= \text{Reading} * 226 \text{ ppm} + 1.472 \text{ mV} \end{aligned}$$

which leads to an absolute accuracy of 3.7 mV at 10 V, i.e. a relative accuracy of 0.037 %. The relative accuracy at 1 V is 0.17 % and 0.05 % at 5 V.

The total accuracy of the measurement chain including gain error is therefore 5.2 % or less above 1 V. The gain error for each channel is determined in the next chapter, so that the accuracy of the measurement is below 0.2 % for measured values above 1 V. The accuracy of the measurement is then determined by the noise of the integrating amplifier and the offset error and noise uncertainty of the NI 9205.

$$\text{Accuracy} = \text{Noise}_{IVC102} + \text{OffsetError}_{NI\ 9205} + \text{Noise}_{NI\ 9205} = 30 \mu\text{V} + 1400 \mu\text{V} + 72 \mu\text{V} = 1.52 \text{ mV}$$

7.2.3 Tests

To test the linearity of all channels and their offset, a function generator providing continuously -0.225 V , was connected via a $1\text{ M}\Omega$ resistor with each of the input channels of the electronics. This results in a continuous current of 225 nA charging the capacitor on the electronics. Integration time was varied between $100\text{ }\mu\text{s}$ and 10 ms while keeping the reset time at $300\text{ }\mu\text{s}$. The channels were tested with a capacitance at the integrator of 250 pF .

The relation between integration time and accumulated charge is linear ($R^2=1.0000$) but varies between channels. The voltage at the integrator is on average $-0.8969\pm 0.0200\text{ V/ms}$ or $-3.99\pm 0.089\text{ mV/pC}$. The offset is between -3.5 mV and $+7.3\text{ mV}$. Figure 7-6 shows the linear relationship for the channels of volume 1.

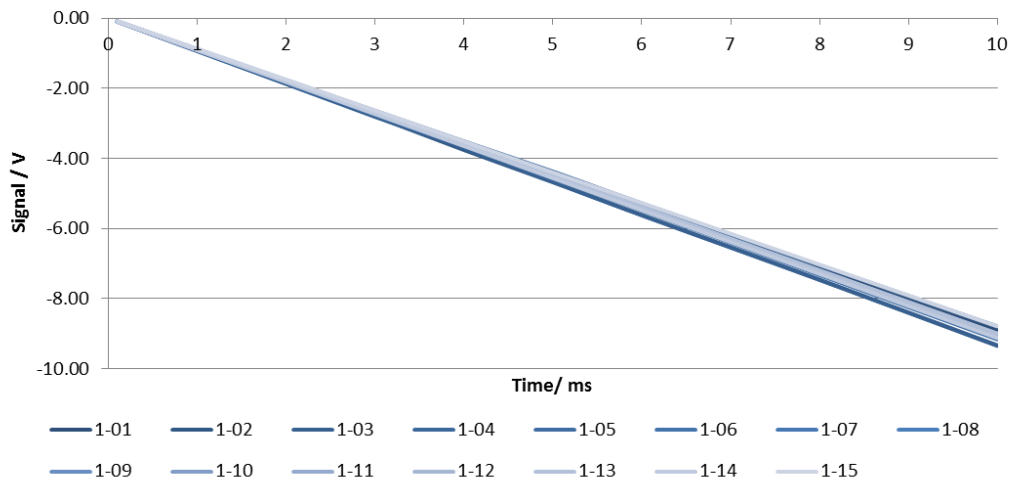


Figure 7-6: Integration time -voltage relationship for charging the capacitors of the channels of volume 1

The channel characteristics are summarized in table 7-1. The maximum gain error is found for channel 2-13 with -4.9% .

Table 7-1: Channel characteristics of electronics

Channel	mV/pC	Offset /mV	Channel	mV/pC	Offset /mV
1-01	-3.95	5.6	2-01	-3.84	1.8
1-02	-4.15	-1.2	2-02	-3.99	3.7
1-03	-4.15	-3.5	2-03	-3.93	1.9
1-04	-3.91	-0.6	2-04	-4.06	0.0
1-05	-4.04	-0.6	2-05	-3.84	0.3
1-06	-4.07	1.1	2-06	-4.08	2.7
1-07	-4.03	2.7	2-07	-3.87	2.6
1-08	-4.04	0.9	2-08	-3.86	0.8
1-09	-4.01	-0.2	2-09	-4.00	-0.2
1-10	-4.02	-3.3	2-10	-4.00	0.5
1-11	-4.03	7.3	2-11	-4.07	-0.5
1-12	-4.00	1.7	2-12	-3.97	0.9
1-13	-4.00	1.2	2-13	-3.80	2.4
1-14	-4.05	3.0	2-14	-4.05	-1.3
1-15	-3.91	4.5	2-15	-3.91	1.1

To account for the different gains, correction factors are introduced (see table 7-2).

$$\text{Correction factor} = \frac{1}{100\% - \text{GainError}} \quad (52)$$

Table 7-2: Correction factors due to gain error

Channel	Correction factor	Channel	Correction factor
1-01	1.014	2-01	1.040
1-02	0.963	2-02	1.003
1-03	0.965	2-03	1.018
1-04	1.024	2-04	0.985
1-05	0.991	2-05	1.042
1-06	0.983	2-06	0.982
1-07	0.992	2-07	1.034
1-08	0.991	2-08	1.038
1-09	0.998	2-09	0.999
1-10	0.995	2-10	1.000
1-11	0.993	2-11	0.983
1-12	1.000	2-12	1.009
1-13	1.001	2-13	1.052
1-14	0.987	2-14	0.988
1-15	1.023	2-15	1.024

As the charging curve under pulsed radiation could not be tracked directly, it was measured at channel 1-10 with 100 pF capacitance by increasing the integration time in small steps from 1 μs to 150 μs . The beam was from a waveguide with a nominal 6 MV photon beam used in Tomotherapy systems (Accurray Incorporated, USA). Figure 7-7 shows the measured values (black crosses) and the fitted charging curve. The fit of the measured values gives

$$y = -3.95 + 2.39e^{-\frac{t}{22.77}} \quad (53)$$

which gives a time constant of 22.77 μs , i.e. an integration time of 120 μs should be sufficient to collect the charge of the pulse. As the capacitance for the main measurements is 250 pF (see chapter 7.2.1), an integration time of at least 300 μs has to be chosen.

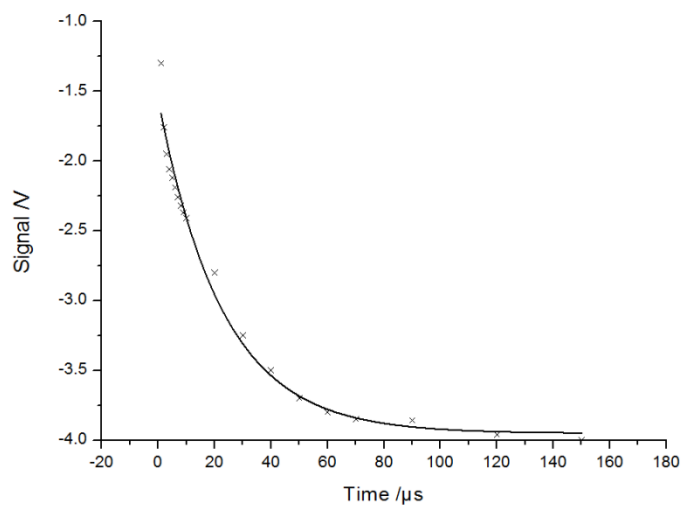


Figure 7-7: Charging curve of IVC102 (100 pF) under pulsed radiation

7.3 Measurements

The second prototype was first of all tested under photon and electron radiation at a test stand. Aim of these measurements in chapter 7.3.1 was to determine the best filling gas for the chamber. Moreover the signal strength at the highest dose rate used in standard settings at a linac was determined in order to assess the necessary capacitor values for the electronics for the performance measurements.

During the performance measurements in a linear accelerator head given in chapter 7.3.2, the main focus was on the response of the chamber to different settings, i.e. tilted fields or different field sizes, linearity of signals to applied dose and stability. By these measurements the capability of the Unified Dose Chamber to meet the main requirements like sensing the beam profile and detection of changes in beam symmetry are checked. Moreover the effect of the wires on the beam was evaluated.

7.3.1 Determination of Gas Filling

To find a suitable filling gas for the chamber, nitrogen, a nitrogen-carbon-dioxide mixture and an argon-carbon-dioxide mixture were compared. These provide a reasonable number of electron-ion pairs and are non-hazardous materials (see chapter 4.5).

7.3.1.1 Materials and Methods

7.3.1.1.1 Photon Radiation

For testing the second prototype under photon radiation, a linear accelerator used in Tomotherapy systems (Accuray Incorporated, USA), which emits 7-8 MV photon radiation, mounted on a test coach was used. At an SSD of 84 cm a solid water phantom out of RW3 was placed and semiflex ionisation chambers in 1.5 cm ($\approx D_{max}$) and 10 cm (D_{10}) depth were mounted (see figure 7-8 on the left). The prototype 2 of the Unified Dose Chamber was placed on an aluminium holder with a rectangular hole larger than the exit window of the chamber to let the beam pass through. Threaded rods were used to vary the distance between target and chamber and by this vary the dose rate at the position of the chamber (figure 7-8 on the right).

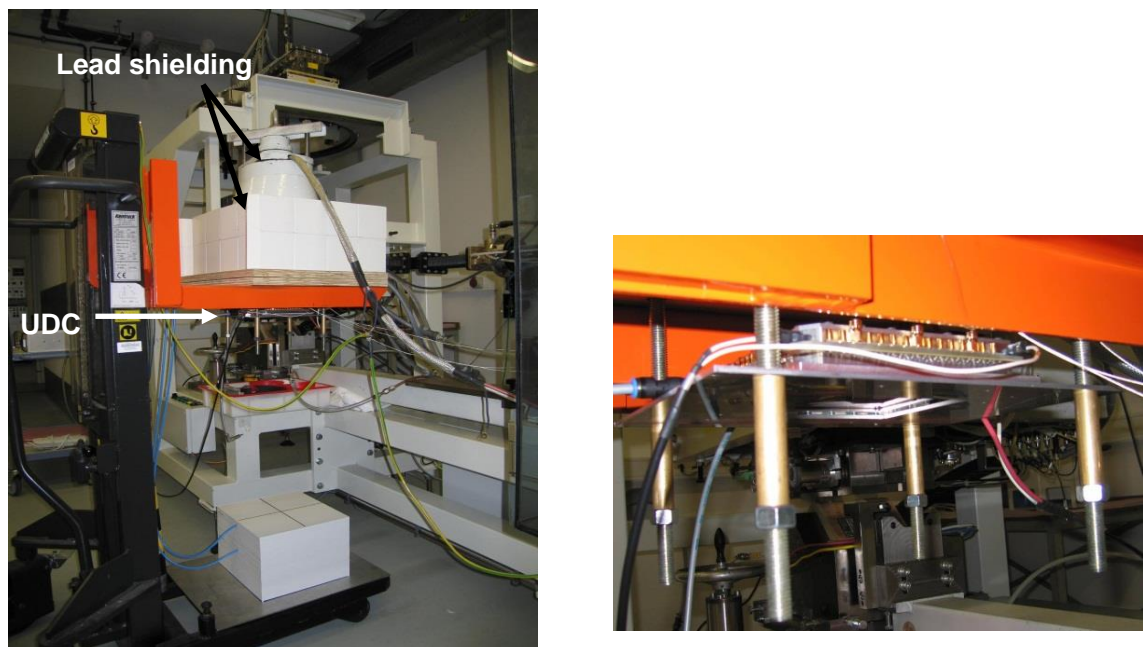


Figure 7-8: Test stand for photon radiation (left) and close-up of UDC in test stand (right)

For these measurements, some of the 30 channels were connected via coaxial cables to the operator station outside the bunker. Three channels were then connected at a time to a digital oscilloscope outside the bunker via an internal 1 M Ω resistance.

First of all, the functionality of the chamber after assembly was tested. The chamber surface was at 15.6 cm from the target, dose rate measured at D_{\max} was 5.7 Gy/min at 50 Hz. The distance d between the wires and HV was 4.2 mm and the chamber filled with nitrogen.

For the following measurements channels 1-15, 2-01 and 2-10 were read out. The peak of the signal on the oscilloscope as well as the area under the curve was analysed. Initially, the HV supply of the chamber was varied from 50 V to 1000 V to determine the operating voltage for the chamber to be in the ionisation region. Then the proportionality of the signal to the dose rate was analysed at 1000 V. Finally, the HV was increased up to 1500 V.

After these functionality tests the signal layer in the dose chamber was turned, such that the distance d between HV and signal plane was now 2.7 mm.

In order to determine the future gas filling for the chamber, measurements with three gases were performed: N₂, N₂-CO₂ (80 % - 20 %) and Ar-CO₂ (80 % - 20 %). For all three gases, the HV was varied from 50 V – 1200 V for different dose rates. From this data, the plateau region was determined. Moreover the linearity of signal vs. applied dose per pulse was analysed. Furthermore signal levels were compared.

At the time of measurement gas volume one was not gastight and was therefore intentionally not filled with the probe gas, but the air from the clean room was left inside. Thus a direct comparison of the measurements in volume one was possible to control the variation in dose per pulse. Volume two was filled with the probe gas at 10 mbar (N₂), 11 mbar (Ar-CO₂) and 12.5 mbar (N₂-CO₂) above air pressure which was constant between 1027 mbar and 1030 mbar during the measurements.

For the functionality tests the distance between UDC and target was varied to achieve higher dose rates (see table 7-3). The distance from UDC to target was only changed to 9.8 cm for nitrogen to achieve higher dose rates due to constraints in construction that were solved after the first measurement series. The operational settings of the linear accelerator, such as Klystron current Kly I and radiofrequency power are given as well in table 7-3. From the measured D_{10} values the corresponding equivalent beam energy is given in the last column.

Table 7-3: Test conditions for photon radiation (prototype 2)

Distance d UDC - Target /cm	Kly I /A	RF Power /MW	DR@ D_{\max}	DR@ D_{\max}	DR@ D_{\max}	D_{10}	Energy /MeV
			/(Gy/min) N ₂	/(Gy/min) Ar-CO ₂	/(Gy/min) N ₂ -CO ₂		
11.0	70.8	1.8	0.630	0.637	0.635	64.7 - 66.7%	7.13 - 8.02
11.0	70.8	1.8	1.650	1.650	1.652	64.1 - 65.5%	6.87 - 7.48
11.0	74.7	2.2	3.630	3.600	3.607	64.3 - 64.8%	6.96 - 7.17
9.8 (N ₂)	78.9	2.9	4.710			65.4 - 66.2%	7.44 - 7.80
9.8 (N ₂)	78.9	2.9	6.000			64.6 - 65.2%	7.08 - 7.35
8.9	78.9	2.9		4.749	4.753	65.4 - 66.2%	7.44 - 7.80
8.9	78.9	2.9		5.835	5.750	64.6 - 65.2%	7.08 - 7.35

The dose rates were chosen such that the dose per pulse (DPP) at the chamber is 81 times the dose that would be measured at D_{\max} at SSD 100 cm for different common dose rates (see table 7-4). For 14 MV UF and 6 MV UF the measured DPP are given for N₂-CO₂ and Ar-CO₂ only. For N₂, the values are 1.39 mGy and 1.77 mGy, respectively. As recombination is only a function of dose per pulse and not energy [Bruggmoser, et al. 2007, Burns and McEwen 1998], the effect of using 7-8 MV instead of the intended energy is negligible for these measurements.

Table 7-4: Equivalent system settings for photon radiation (prototype 2)

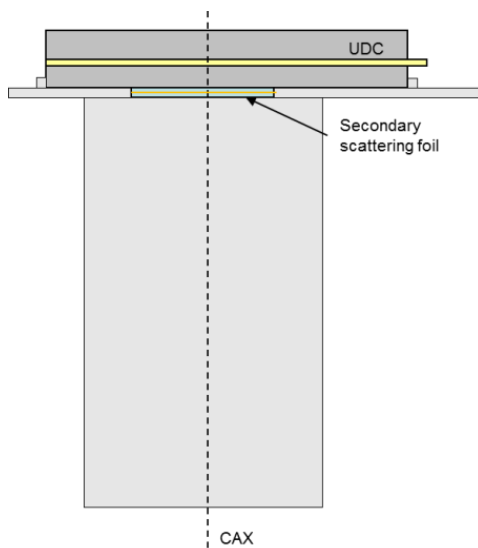
Equivalent System Setting	Equivalent DPP at D_{max} at SSD 100 /mGy	Measured DPP scaled to D_{max} at SSD 100 /mGy
6MV 200 MU/min	0.15	0.14
15MV 500 MU/min	0.38	0.37
7MV UF 500 MU/min	0.83	0.80 - 0.81
14MV UF 2000 MU/min	1.67	1.60 - 1.68
6MV UF 4000 MU/min	2.22	1.96 – 1.99

The output of the accelerator was adjusted during the measurements by varying the beam current such that the dose rate in D_{max} was approximately constant.

For analysing the linearity between dose per pulse and measured signal level, the values for different dose rates at 1000 V were compared. Moreover, for Ar-CO₂ and N₂-CO₂, the dose per pulse was varied at a fixed klystron setting of 74.7 A. Moreover, the pulse shapes for different dose rates were compared.

7.3.1.1.2 Electron Radiation

For testing the second prototype under electron radiation, a support for the chamber was constructed. Measurements were only done at 6 MeV as for this energy no primary scattering foil is necessary. At the test stand a waveguide without linac head was available.



The chamber was mounted on a plate with a circular passage through which the radiation can pass. In this passage the secondary scattering foil is mounted. To keep a distance of 11 cm between exit window and chamber entrance window, the plate is mounted on a cylinder which can be attached to the waveguide (see figure 7-9). Moreover this cylinder is required for shielding as otherwise stray radiation to nearby electronics would be too high. The centre of the chamber entrance window is aligned with the central axis of the radiation beam.

The applied dose rate is measured with the 1-D water phantom buddleship (Wellhöfer, Schwarzenbruck, Germany) which is readily available at the test stand. Due to the missing feedback from the electron dose chamber the dose rate varied during the measurements.

Figure 7-9: Support for electron measurements with prototype 2

For signal transmission the same path as for the measurements with photon radiation was used. Volume two was filled with the probe gas with a pressure of 10 mbar (Ar-CO₂ and N₂-CO₂) and 15 mbar (N₂) above air pressure. The air pressure was constant between 1027 mbar and 1031 mbar.

Measurements were done at 90 Hz and a dose rate of 3 Gy/min at D_{max} at SSD 100 which are the standard settings for low dose rate. The applied voltage to the prototype was varied from 50 V – 1200 V and signal levels were compared.

7.3.1.2 Results

7.3.1.2.1 Photon Radiation

When varying the applied voltage during the functionality tests, the values above 1000 V are scaled by the dose rate measured during the respective measurement. The accelerator output varied for the measurements above 1000 V, such that the curves in figure 7-10 are not constant before and after 1000V. Figure 7-10 shows that the signal strength increases with voltage up to approx. 1200 V. Therefore the wire plane was turned after the functionality tests to reduce the distance from the wires to the HV plane.

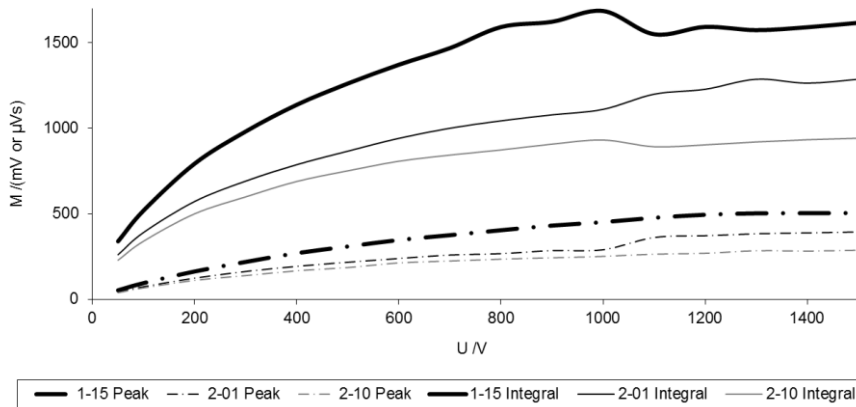


Figure 7-10: Signal M (peak value in mV or area in μ Vs) over varying U for $d = 4.2$ mm

As can be seen in figure 7-11, the signals of the three channels varied approximately linearly with dose per pulse. The dose at D_{max} was scaled to a distance of SSD 100 to ensure comparability with requirements from system.

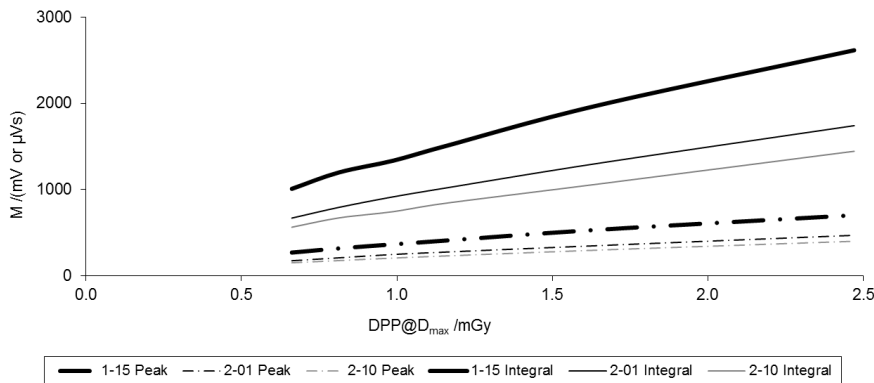


Figure 7-11: Signal M (peak value in mV or area in μ Vs) over varying DPP for $d = 4.2$ mm and $U = 1000$ V

When comparing the different gas fillings with a distance between HV plane and wire plane of $d = 2.7$ mm, the plateau region starts at approx. the voltages given in table 7-5.

Table 7-5: Plateau region for prototype 2

Equivalent DPP /mGy	N2	Ar-CO2	N2-CO2
0.15	300 V	500 V	400 V
0.38	700 V	500 V	500 V
0.83	800 V	700 V	900 V

For 1.67 mGy and 2.22 mGy per pulse the plateau region was not reached, although the curves seem to settle somewhere beyond 1400 V.

Figure 7-12 shows the measured peak values and figure 7-13 the measured area under the curve for 0.83 mGy per pulse in D_{max} at SSD 100. The measured data for volume 1, which is filled with air, are approximately the same for all three measurements. The area under the curve was determined with a larger uncertainty as the value displayed on the oscilloscope was fluctuating rapidly. Graphs for all dose rates can be found in appendix F.

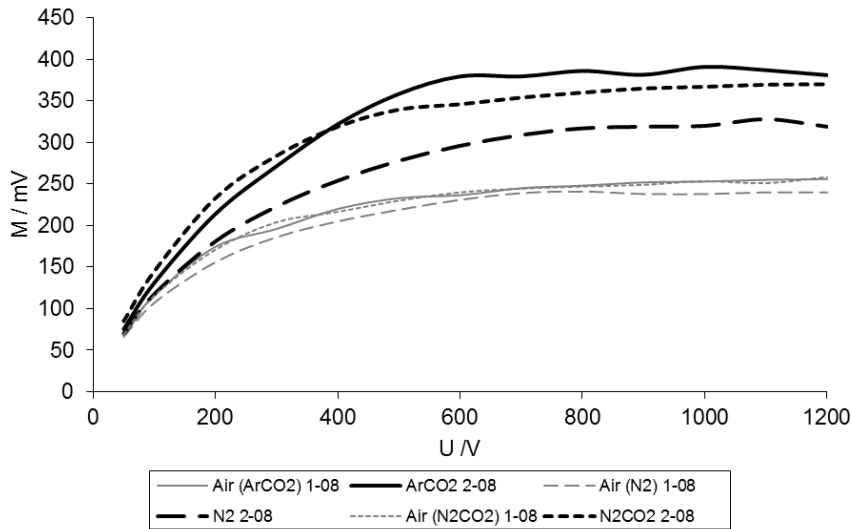


Figure 7-12: M-U diagram for 0.83 mGy/pulse in D_{max} at SSD100; M= peak value

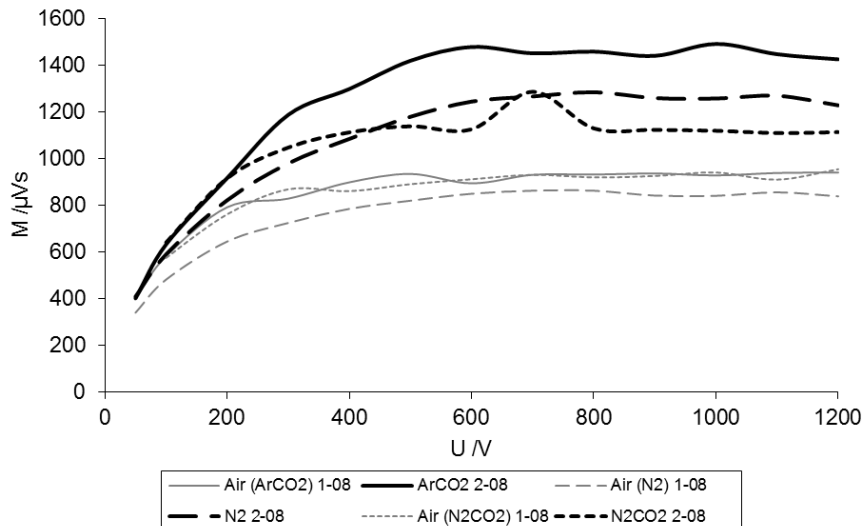


Figure 7-13: M-U diagram for 0.83 mGy/pulse in D_{max} at SSD100; M= area under the curve

When looking at the linearity of the signal with increasing dose per pulse, the curves for the area under the curve are fairly linear up to 1.67 mGy, although having different steepness (see figure 7-14).

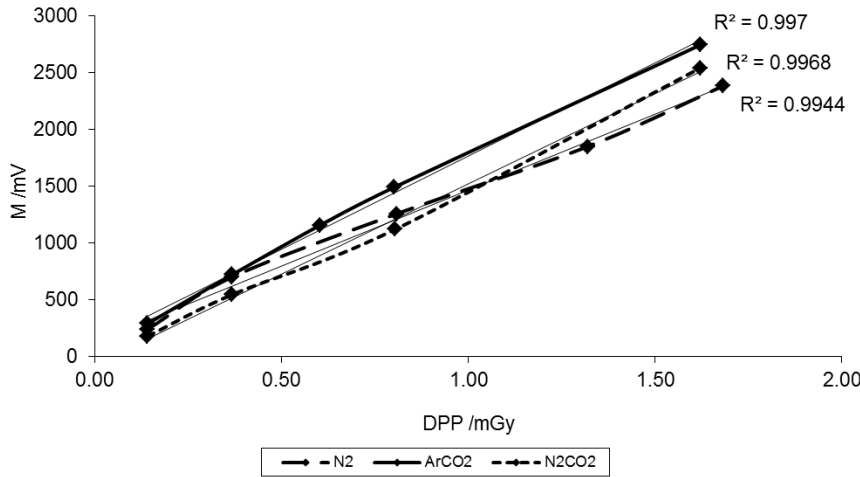


Figure 7-14: DPP linearity from measurements at $U=1000V$; $M=$ area under the curve

By varying the dose per pulse when keeping the klystron setting constant, it was ensured that the energy stayed the same. In figure 7-15 it is shown that the measured values in the volume filled with air are the same for both measurements. The peak signal level for Ar- CO_2 filled volume 2 compared to N₂- CO_2 filled volume 2 is approximately 12 % higher.

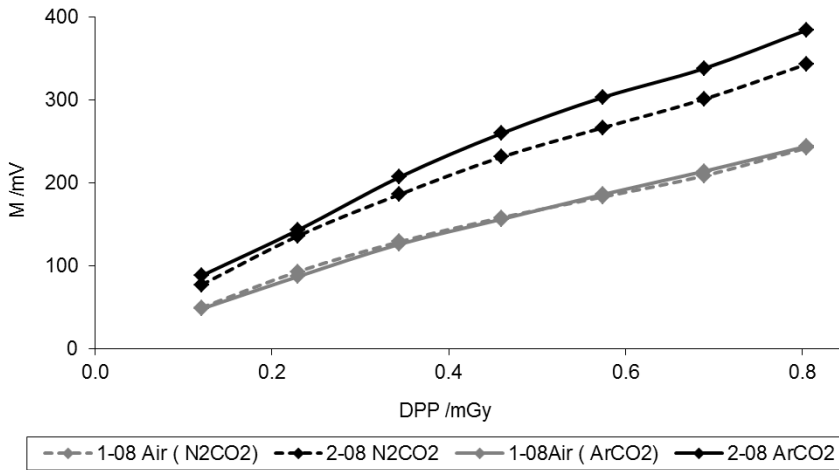


Figure 7-15: DPP linearity (Ar- CO_2 and N₂- CO_2)

Figure 7-16 and figure 7-17 show the dose pulses at the oscilloscope at 0.15 mGy/pulse and 0.83 mGy/pulse for the three gases. For low doses per pulse, the peak of Ar- CO_2 is higher than for N₂- CO_2 which is higher than the N₂ peak. This difference decreases with high doses per pulse. The area under the curve is approximately the same for Ar- CO_2 and N₂ and lower for N₂- CO_2 at low doses per pulse. At high doses per pulse, the area under the curve is largest for N₂, followed by Ar- CO_2 and then N₂- CO_2 .

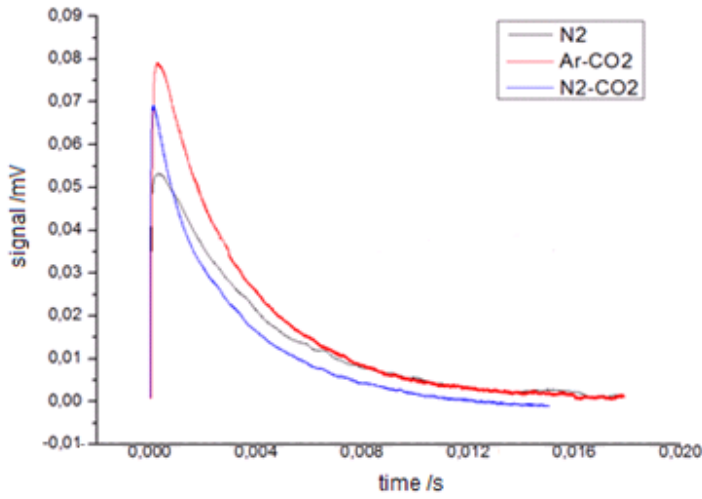


Figure 7-16: Measured dose pulses from oscilloscope for a dose per pulse of 0.15 mGy

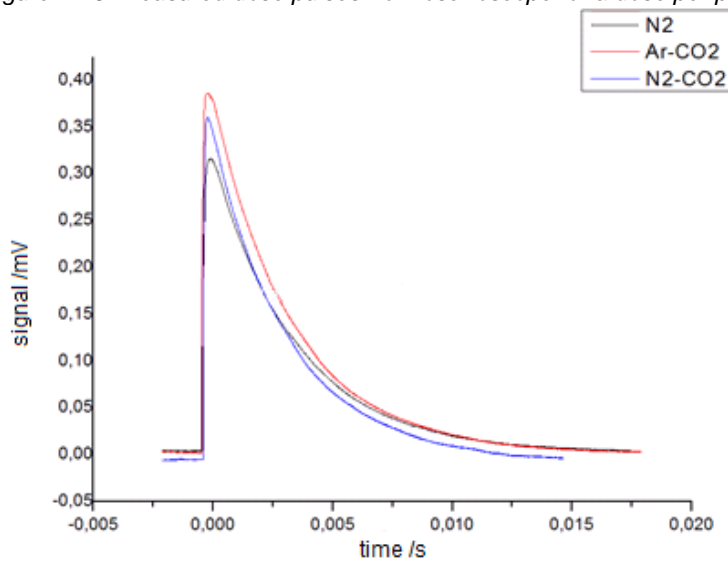


Figure 7-17: Measured dose pulses from oscilloscope for a dose per pulse of 0.83 mGy

7.3.1.2.2 Electron Radiation

When varying the applied voltage, the saturation region was not reached. Figure 7-18 shows the peak value of the pulses for varying voltage U for the three probe gases as well as for the pulses from volume one (filled with air). As the dose rates varied between the measurements, the values for air differ.

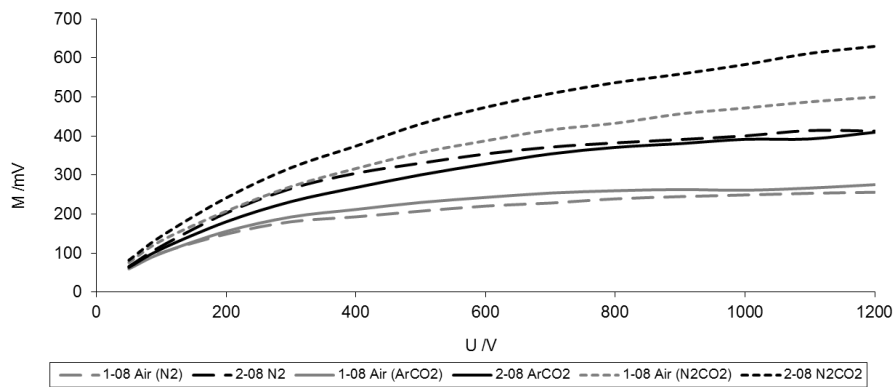


Figure 7-18: M-U diagram for electron radiation in D_{max} at SSD100. M= peak value

As the dose rate varied between the measurements, the signal curves of channel 2-08 were normalized to the peak and area of 1-08, respectively, i.e. to the value in the air filled volume (see figure 7-19 for peak values). The peak signals of channel 2-08 at 1000 V are 61 %, 50 % and 24 % higher and the area under the curve 40 %, 37 % and 18 % higher than for channel 1-08 for N_2 , Ar- CO_2 and N_2 - CO_2 , respectively. Figure 7-19 shows the curves from the oscilloscope for all three gases.

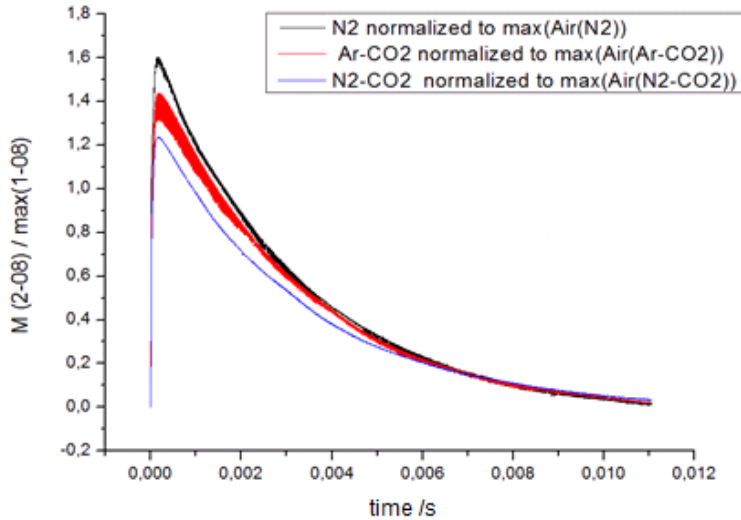


Figure 7-19: Channel 2-08 normalized to the maximum of channel 1-08 (6 MeV)

7.3.1.3 Discussion

The differences in pulse shape at different doses per pulse are due to the different recombination effects and ion mobilities in the three gases. In Ar and CO_2 , initially more electron-ion pairs are produced than in N_2 , but the free electrons present in the gas after ionisation do not attach to N_2 or Ar, but form negative ions with CO_2 . CO_2 binds the electron on average for 0.7 ms [Sauli 1977], i.e. longer than the transit time in the chamber. Thus more negative ions are present in N_2 - CO_2 and Ar- CO_2 than in N_2 . This increases the probability of volume recombination between negative and positive ions in the gas volume which leads to a loss in signal.

Dinter and Tesch claim that in technically pure gases, like the N_2 used here, the concentration of impurities is high enough to ensure electron attachment to those molecules [Dinter and Tesch 1974]. But newer investigations by Boag showed, that in gases like N_2 the free electrons lead to an increase in collection efficiency [Boag, Hochhäuser and Balk 1996]. With increasing dose per pulse, the probability of volume recombination increases due to a higher charge density. Thus the effect of CO_2 -admixture is more profound.

The values for ion mobilities given in the literature vary (see chapter 4.5.3). In N_2 the ionisation leads to the formation of N_2^+ ions which can combine with neutral N_2 to N_4^+ . Moreover N^+ and N_3^+ may be formed by elastic collisions and dissociation [Saporoschenko 1965]. In ionized gas mixtures, the charge is quickly transferred to the ions with lowest ionisation energy, i.e. CO_2 in the case of Ar- CO_2 and N_2 - CO_2 ($IE_{CO_2}=13.7$ eV; $IE_{N_2}=15.6$ eV; $IE_{Ar}=15.8$ eV) [Sauli 1977]. Thus after 100-1000 collisions, CO_2^+ ions dominate the ion drift.

For electron radiation measurements, the higher pressure in volume two during the measurements with N_2 explain the higher signal as probably the HV foil was blown up more than for the other two gases and thus increasing the gap between the HV foil and the electrodes. See chapter 7.3.2.2.5 for the effect of varying pressure on chamber signals.

For all three gases, the signal is proportional to the dose per pulse up to 1.67 mGy/pulse, which corresponds to 2000 MU/min at normal clinical settings (see table 7-4 on page 99). For low dose rates, the peak of the signal is higher for Ar-CO₂, but sparks were observed at higher voltages. The area under the curve, which gives the total charge, is approximately the same for Ar-CO₂ and N₂. The values for N₂-CO₂ are lower.

For further chamber designs, a gas filling of N₂ is advised, as here no sparks at high voltages were observed and the total signal (amount of collected charge) is higher than for N₂-CO₂.

7.3.2 Performance Measurements

7.3.2.1 Materials and Methods

The second prototype was re-opened in the clean room before measurements at a test bunker and checked for changes on wires or foils. Subsequently the chamber was closed again and the gas inlets were squeezed so that the measurement volumes were filled with dry clean room air during the following tests. As no mid-term tests of chamber tightness could be done, it was decided to leave air in the chamber. In this way, signal changes cannot be due to slow gas loss from the chamber volume. The integrating capacitance was adjusted to 250 pC to allow measurements with high doses per pulse.

In the test bunker, the gantry of an Siemens Oncor linear accelerator with 82 MLC was at gantry angle 180° and the UDC was positioned on the chamber slide with the original chambers removed. The power supply of the original chambers was short-circuited and the linear accelerator was operated in open loop, i.e. without feedback loop from the monitor chambers. An external power supply for the UDC with an external potentiometer was used (see figure 7-20). This supplied a constant voltage of +1000 V. The 30 signal wires as well as the power supply cable were connected with the electronics and power supply, respectively. The trigger signal from the linear accelerator was connected to the electronics which were on their part joined with the cRIO. A network cable connected the cRIO with a laptop outside the bunker. The electronics were shielded with lead plates.

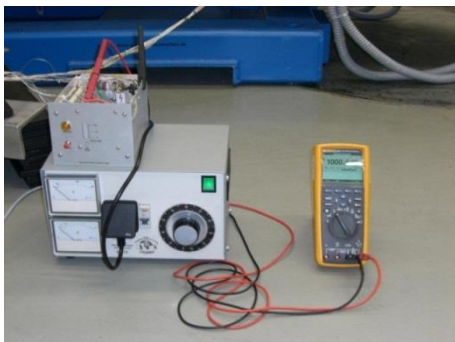


Figure 7-20: Power supply of prototype 2 during performance measurements

First of all, measurements with 6 MV and 23 MV photon beams with flattening filter were performed. Therefore the UDC was placed in a fixture which was mounted on the chamber slide (see figure 7-21). Afterwards, the UDC was dismantled in order to remove the flattening filter. Following measurements with 7 MV UF and 17 MV UF, the UDC was again dismantled and put above the opening for electron radiation. To prevent movement of the chamber slide during the measurements, for unflat beams the head control board was removed, for electron measurements the connection to the slide motors was disconnected such that the electron energy could still be changed. In all three configurations the centre of the entrance window was aligned as good as possible with the central beam axis. Due to the fixture, the entrance window of the UDC was 12 mm above the chamber slide. This results in a distance of 13.86 cm of the first

wire plane (volume 2) from the target. Therefore the dose rate at this plane is 62 % of the dose rate in the current photon chamber.

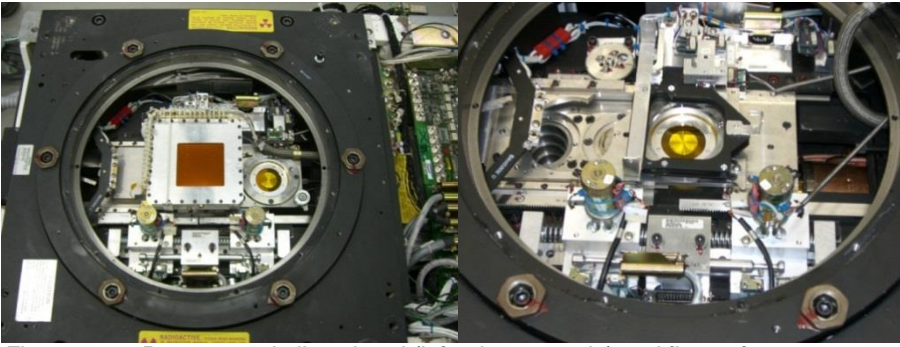


Figure 7-21: Prototype 2 in linac head (left: photon mode) and fixture for prototype 2 (right: electron mode)

To characterize the performance of the second prototype, the following measurements were performed for the nominal energies given in table 7-6.

- Repeatability
- Backscatter into the chamber volume from jaws and MLC
- Detectability of errors in symmetry (steered beam)
- Beam profile
- Stability over the day and after high absorbed dose

In table 7-6 the dose rate, pulse repetition frequency (prf) and dose per pulse (DPP) are given. Moreover, for photon radiation D_{\max} and for electron radiation the reference depth Z_{ref} are stated. The built-up was chosen such that the measurement point for the reference chamber was behind D_{\max} or Z_{ref} .

Table 7-6: Measurement configurations for performance measurements

Nominal Energy	Dose Rate /(Gy/min)	prf /Hz	DPP@100cm /mGy	Nom. D_{\max} or Z_{ref} /cm	Build-up* /cm
6 MV	0.5	40	0.21	1.5±0.2	2.43
	3	220	0.23	1.5±0.2	2.43
23 MV	5	20	0.42	3.5±0.2	4.43
7 MV UF	5	100	0.83	1.7±0.2	1.93
	20	220	1.52	1.7±0.2	1.93
17 MV UF	5	100	0.83	3.1±0.2	3.43
8 MeV	9	187	0.80	1.8	2.0
10 MeV	3	80	0.63	2.1	2.0
	9	130	1.15	2.1	2.0
16 MeV	3	72	0.69	3.8	4.0
	9	147	1.02	3.8	4.0
21 MeV	3	58	0.86	4.8	5.0
	9	122	1.23	4.8	5.0

* for photon radiation: 1.2 cm Plexi (1.43 cm water equivalent) plus RW3 (solid water); For electron radiation: RW3 only

For photon radiation a fixture with a 1.2 cm plexi plate in the beamline was used on which additional RW3 (solid water) was placed as build-up and backscatter material (figure 7-22). A Farmer chamber (type 30013, PTW-Freiburg, Germany) connected to a Unidos webline (PTW-Freiburg, Germany) was used as a reference dosimeter. For measuring the beam profile, a StarCheck (type T10032, PTW-Freiburg, Germany) was used.



Figure 7-22: Test set-up for photon radiation for performance measurements (left: Farmer chamber in RW3; right: StarCheck with RW3 built-up and backscatter)

For electron radiation the set-up of backscatter, Roos chamber (type 34001, PTW-Freiburg, Germany) and build-up was fixed to a mobile table top. Measurements with the StarCheck were done closer to the target, as the StarCheck plus build-up was placed on the applicator (figure 7-23).

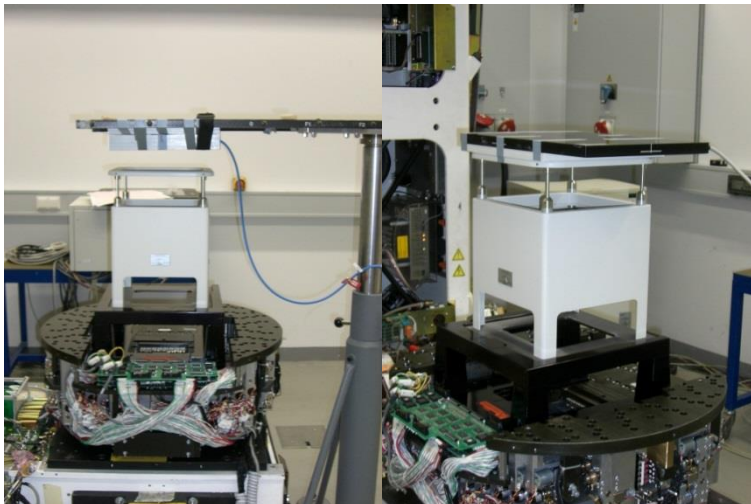


Figure 7-23: Test set-up for electron radiation for performance measurements (left: Roos chamber in RW3; right: StarCheck with RW3 built-up)

Moreover the beam profile was sensed for each energy with GafChromic EBT2 films above the UDC while sensing the profile with the UDC and StarCheck. Furthermore film measurements were performed for steered beams. The films were scanned with a VIDAR VXR-16 Dosimetry Pro scanner with 16 bits per pixel and a resolution of 0.009 cm with FilmScan software (PTW-Freiburg, Germany). The films were analysed with VeriSoft (version 2.1, PTW-Freiburg, Germany).

To analyse the effect of the wires on the beam, films were placed in air and with backscatter material into the beam at SSD 95 for electron radiation (figure 7-24).



Figure 7-24: Film measurements in air (left) and with backscatter (right) for analysing the effect of the wires on electron radiation

7.3.2.2 Measurements and Results

7.3.2.2.1 Repeatability

To observe the repeatability of the chamber signals at fairly constant dose per pulse, ten consecutive measurements per energy were made while logging 15 to 50 pulses each time and noting the dose rate measured at isocentre. Field size was 10 cm x 10 cm for photons and 20 cm x 20 cm for electrons.

When normalizing the signals to the dose rate, the relative standard deviation over the ten measurements is within 0.5 % for 23 MV, except for channels 1-10, 1-13 and 1-15. For 6 MV problems occurred with the same channels and in 2-01. The variation for all other channels was below 0.7 %. The variability between pulses is higher for volume 2. Channels 1-01 and 2-01 fluctuate more than the other channels from their respective plane, whereas the mean is within expected values. The signal of channel 1-15 is nearly twice the signal from channel 1-01 which is not expected from a symmetrical field.

For unflat photon beams problems only occurred with channel 1-15, where the dose in two of the ten measurements was 4 % higher than in the other eight. The signal from this channel is again higher than expected. Channel 2-01 showed a high relative standard deviation of around 2 % over 40-50 pulses. The mean was again within expected values.

For electron beams the relative standard deviation over ten measurements was below 0.7 %, except for channel 2-15. Again, the relative standard deviation of channel 2-01 over several pulses was higher than for the other channels.

Figure 7-25 shows the variability of the signals of a 23 MV low dose rate flat photon beam from ten measurements, each averaged over approximately 40 pulses. The signals are normalized to measured dose rate at isocentre and to the mean of the ten measurements. As dose rate was fluctuating, the dose rate during the 40 pulses was taken with a certain inaccuracy. The signals from all channels vary synchronously and the fluctuation between the channels is smaller than 1 %. Only for channels 1-13 and 1-15 (black and grey line in figure 7-25) fluctuations were higher.

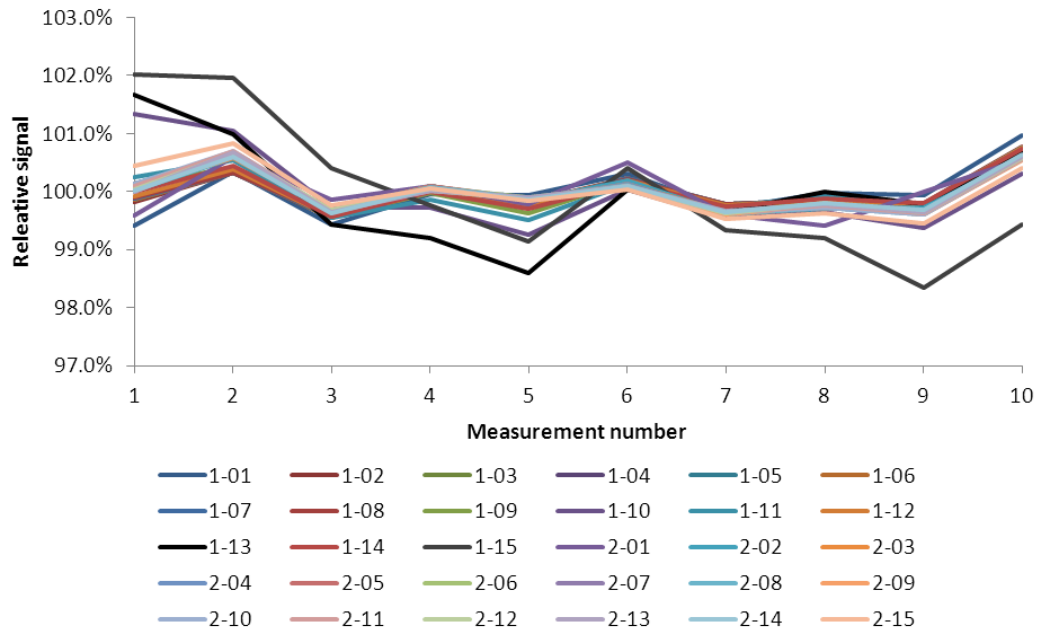


Figure 7-25: Short-term stability of signals

7.3.2.2.2 Backscatter

To observe the dependence of the signal on the field size, it was varied for all energies to five sizes from 2 cm x 2 cm to 40 cm x 40 cm. For each field size, 5 measurements over 50-100 pulses were made and corrected by the calibration factors determined in chapter 7.2.3. As temperature and pressure did not vary significantly ($<0.5^{\circ}\text{C}$ and <1 Torr), the following data are not corrected for these.

As can be seen in figure 7-26 the signals of the channels, normalized to a 40 cm x 40 cm field size, increase with decreasing field size. At the edges the signal increases more than in the centre.

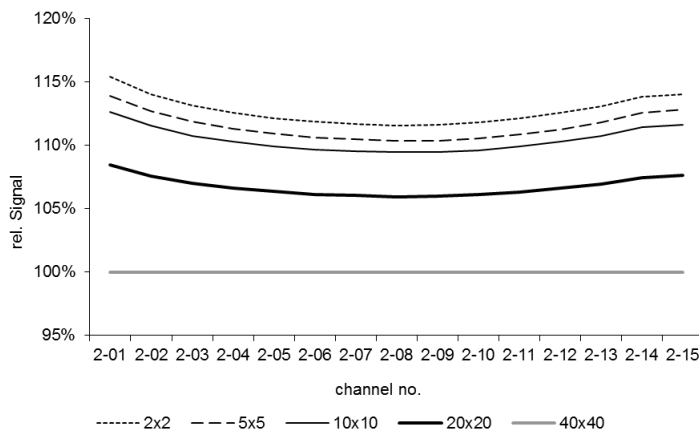


Figure 7-26: Relative signal for 6 MV LDR for varying field size

By normalizing the signals to the signal from channel 2-08, the centre of the beam can be observed (figure 7-27). The central axis of the beam traverses the chamber at the positions given in table 7-7. For photon beams the beam central axis (CAX) hits the chamber between channels 1-09 and 1-10, i.e. 6 mm off the central position of the chamber in the direction of channel 1-15. Also in the orthogonal direction, a shift of the chamber with respect to central axis is observed. For electrons, only a shift in inplane direction was observed.

Table 7-7: Position of beam CAX in chamber

	Volume 1 (crossplane)	Volume 2 (inplane)
6/23 MV	6 mm (-> 1-15)	1 mm (-> 2-15)
7/17 MV UF	6 mm (-> 1-15)	3 mm (-> 2-15)
Electrons	0 mm	3 mm (-> 2-01)

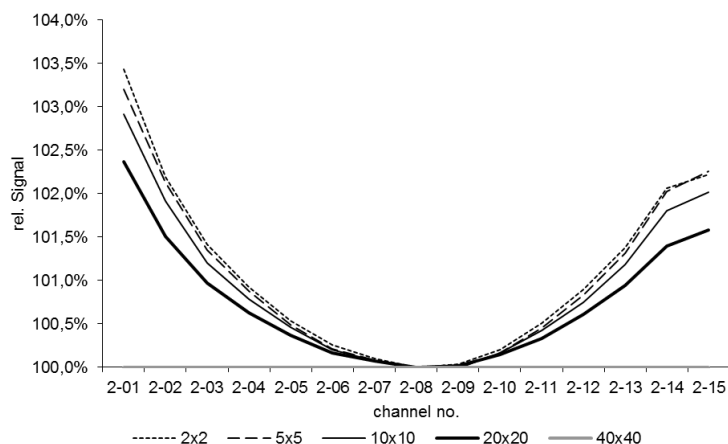


Figure 7-27: Signal for 6 MV LDR normalized to central channel for varying field size

For a 2 cm x 2 cm field and a 6 MV flat photon beam, the signal at channel 2-01 is approx. 3.5 % higher than for channel 2-08 (figure 7-27). Generally, for photon radiation, the signal for a 2 cm x 2 cm field is in the centre about 12 % higher than for a 40 cm x 40 cm field, and approx. 15 % at the edges (for 6 MV LDR see figure 7-26). For electron radiation, the signal increase depends on the energy and varies from 2 % for 21 MeV to 10 % for 10 MeV in the centre. The signal at the edges is again 2 – 5 % higher than in the centre. Graphs for all energies can be found in appendix F.

As simulated and measured in chapters 3.1.2.2 and 3.2.2.2 the amount of backscatter depends on the field size. For squared field sizes the relationship is linear (see figure 7-28).

Besides square field sizes, also rectangular fields were analysed. The field size was kept at 40 cm in one direction and the other direction was varied from 2 cm to 40 cm. In figure 7-29 it can be seen that the change in signal is significantly higher when the y-jaws are moved. This effect was expected, as the y-jaws are closer to the chamber and thus more radiation is scattered back at smaller field sizes.

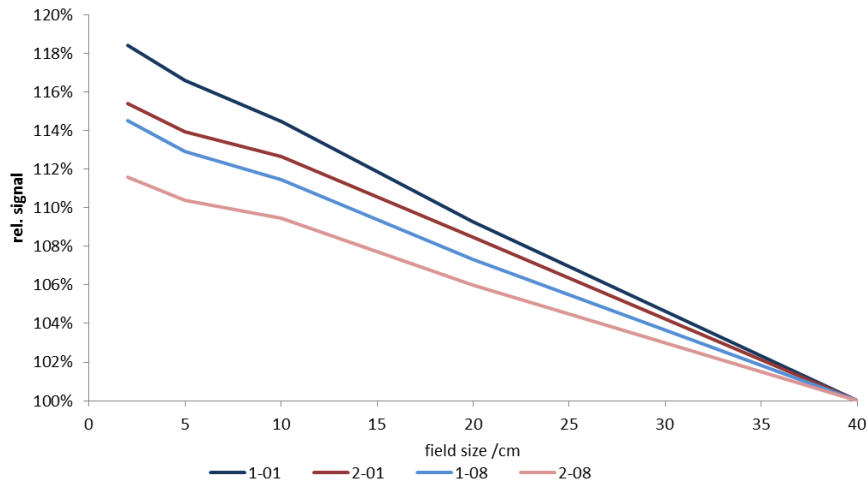


Figure 7-28: Variation of signal with square field size (6 MV LDR)

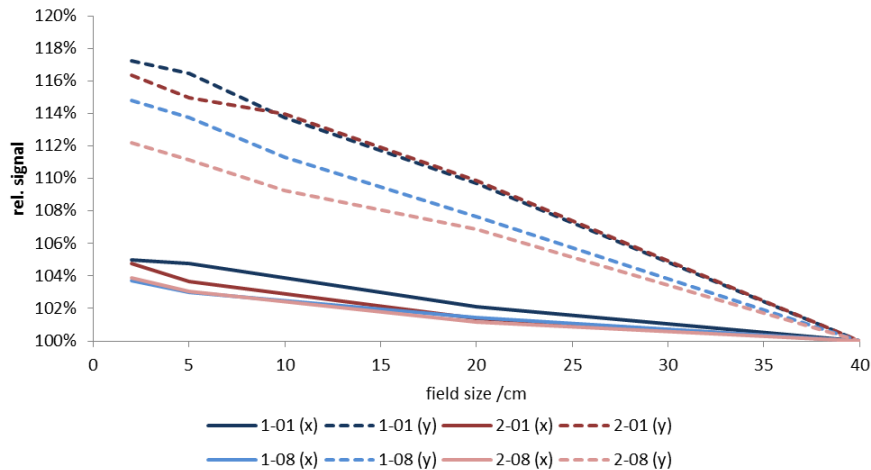


Figure 7-29: Variation of signal with field size while keeping the other direction constant at 40 cm (6 MV LDR)

7.3.2.2.3 Detection of Symmetry Changes

By steering the beam, the ability of the UDC to detect changes in symmetry was analysed. To compare the change in signal from the UDC with the real change in beam profile, a StarCheck was placed at SSD 100 and SSD 90 for photon and electron radiation, respectively (see figure 7-22 and figure 7-23). Moreover GafChromic EBT2 films were placed on top of the chamber.

To steer the beam, the current through the steering coils was changed, i.e. the STC parameter at the control console was varied. The resulting profile was measured with the StarCheck over an integration time of 10 seconds. The UDC logged around 50 pulses. For each STC setting the mean of these was divided by the mean of the pulses from the STC setting where the field was symmetric, i.e. the relative change was analysed. Each channel was normalized to channel 2-08. By steering the beam only changes in inplane direction can be realized.

For 6 MV, STC 381 defined a symmetric field. The curves in figure 7-30 are relative to these signals, i.e. for STC 0 the relative signal in channel 2-01 with respect to channel 2-08 is 1.5 % higher than for STC 381. In table 7-8 the values for the symmetry of the field measured with the StarCheck are given.

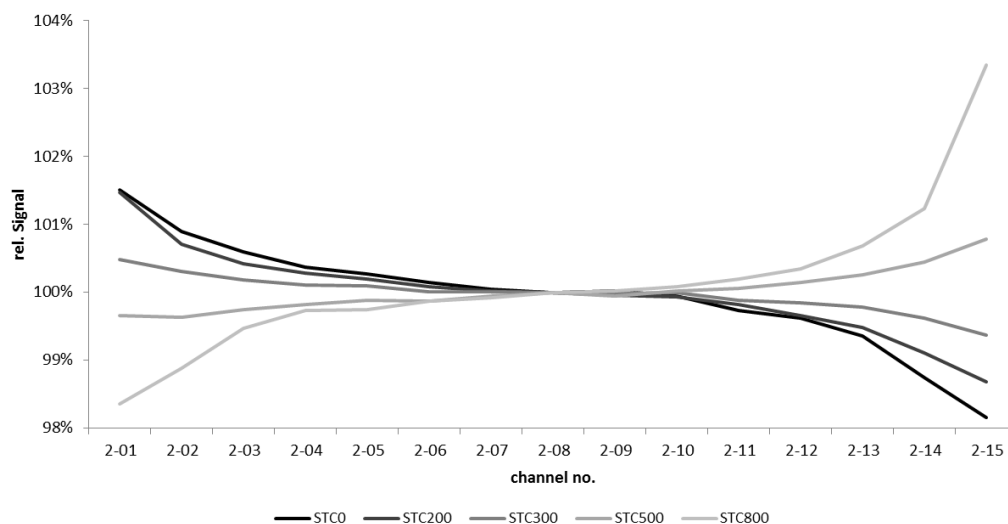


Figure 7-30: Relative signal for steered beams of 6 MV

Table 7-8: Symmetry values at patient plane for steered beams of 6 MV

	Symmetry ([IEC 60976]) /%	Symmetry (Siemens) /%
STC 0	106.41	4.15
STC 200	104.76	2.95
STC 300	102.76	1.42
STC 381	101.19	0.07
STC 500	102.89	1.64
STC 800	109.09	6.06

As can be seen from figure 7-30 and table 7-8, the change in signal of the UDC is not as high as the change in signal measured with the StarCheck. For a symmetry value of 110 %, a signal change at the edges of the field of ± 5 % is expected. For 6 MV the change in signal is around 1.5 %, when neglecting channel 2-15. The determined symmetry by comparing channels 2-02 and 2-14 is nonetheless proportional to the symmetry measured with the StarCheck (except for STC 800), for IEC 60976 as well as Siemens defined symmetry.

$$\frac{2-02}{2-14} \approx 42 - 48\% \text{Sym}(IEC)$$

$$\frac{2-02}{2-14} \approx 52 - 57\% \text{Sym}(Siemens)$$

For the film measurements only a few pulses were applied as the film rapidly darkens. It was observed, that the steering coils do not have an immediate effect on the beam so that the film measurements are not comparable to the measurements under continuous radiation.

The fluctuations when measuring several times a flat profile is constant within 0.5 %, except for the outermost channel (compare figure 7-31). The values are not corrected for the changes in linear accelerator performance which is in the order of 0.5 % [IEC 60977 2008].

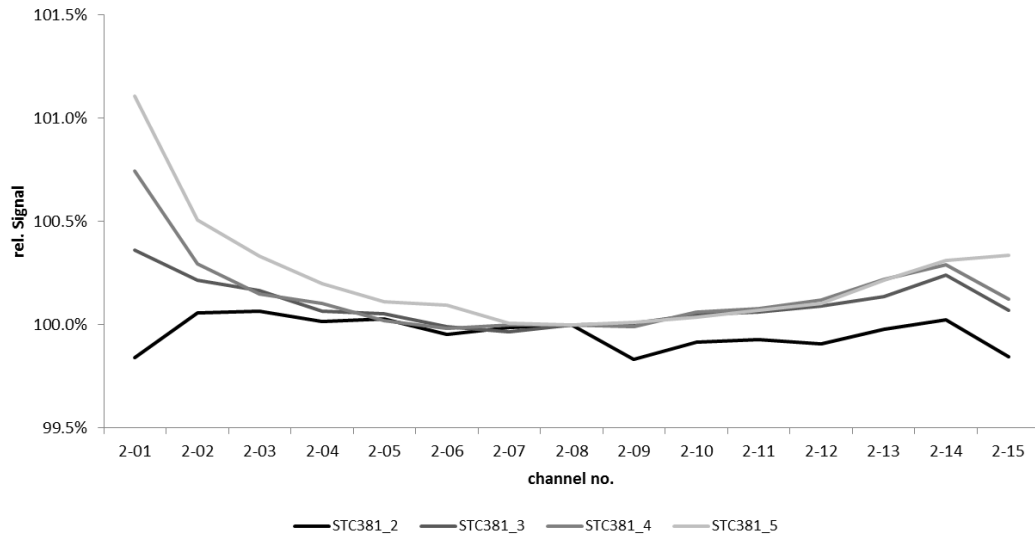


Figure 7-31: Relative signal for steered beams of 6 MV at STC 381 (symmetric and flat beam) normalized to first measurement (STC381_1)

For 23 MV the change in signal is also fairly proportional to the change in symmetry at isocentre. Here channel 2-04 and 2-12 were compared as here the largest signal change occurs (as symmetry is defined by IEC 60976).

For 7 MV UF and 17 MV UF the signals of channel 2-04 and 2-14 were compared, i.e. channels symmetric around channel 2-09. Again, the change in measured symmetry is fairly proportional to the change in symmetry at isocentre.

In figure 7-32 the measured profiles of a flat (STC 5200) and tilted (STC 4500, 4000 and 2000) 21 MeV electron beam can be seen, which correspond to symmetries of 102 %, 105 %, 107 % and 110 %, respectively, according to IEC 60976 symmetry definition. The values are normalized to channel 2-07. The change in symmetry is not proportional to the change in symmetry at the isocentre for the measured electron energies.

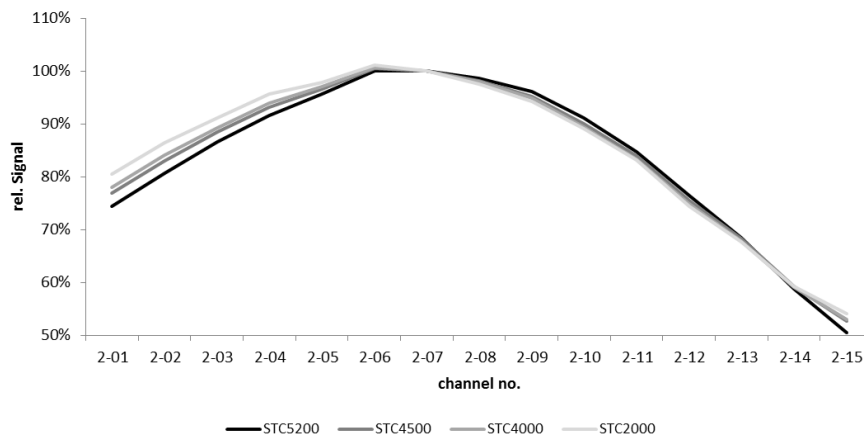


Figure 7-32: Measured beam profiles (volume 2) for a flat (STC5200) and tilted 21 MeV beams. Signal values normalized to channel 2-07

7.3.2.2.4 Beam Profile

The UDC measures a projection of the beam profile. When neglecting channels 1-10, 1-13 and 1-15 for photon radiation, the beam profiles given in figure 7-33 are measured (normalized to channel 1-08).

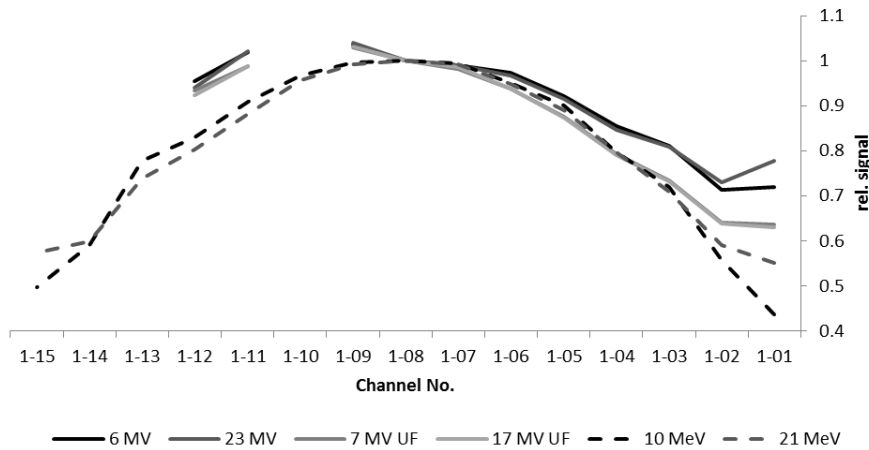


Figure 7-33: Measured beam profiles (volume 1)

The measurement of these signals are also subject to the signal changes observed in the chapter 7.3.2.2.5. As the chamber was sealed with an air pressure of 1035 mbar and most probably volume two is not sealed (see chapter 7.3.2.3), the HV foil is most probably bend towards volume two during the film measurements as the ambient air pressure was between 929 mbar and 970 mbar during these measurements. This means that the profile of volume one is too peaked and of volume two too flat. Nevertheless, major distortions in the profile could be observed. In the profile of a 6 MV photon beam in figure 7-34 an elevation on the left hand side can be seen. The signals from the UDC are also higher at these points. The measurement points of volume one are projected to the plane of the film. Values for channel 1-10 and 1-13 are interpolated and marked with open circles in figure 7-34, figure 7-35 and figure 7-36.

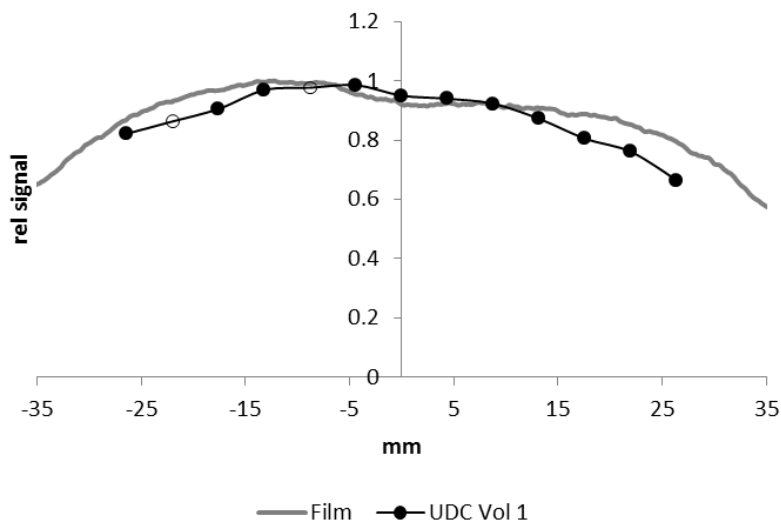


Figure 7-34: Profile of a 6 MV photon beam, measured with film and UDC (volume 1)

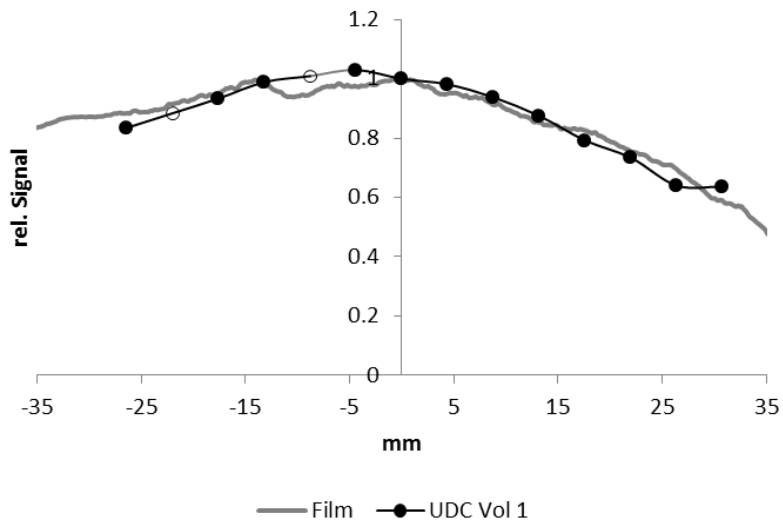


Figure 7-35: Profile of a 7 MV UF photon beam, measured with film and UDC (volume 1)

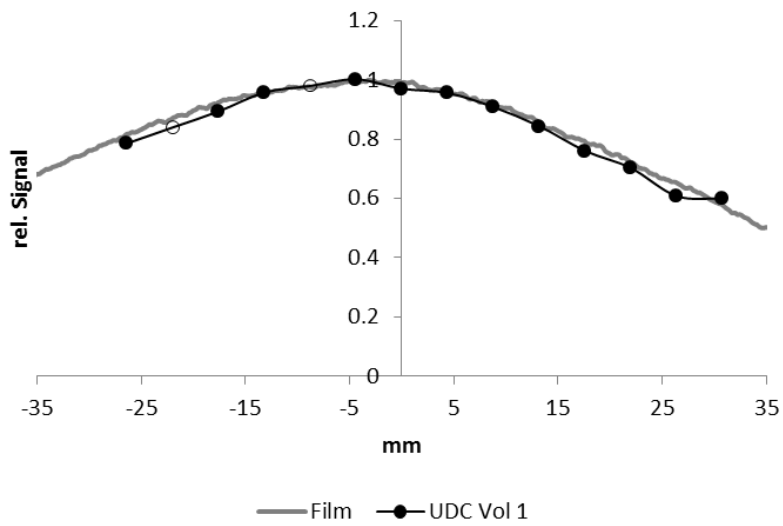


Figure 7-36: Profile of a 17 MV UF photon beam, measured with film and UDC (volume 1)

7.3.2.2.5 Stability Over the Day and After High Absorbed Dose

The complete measurement system was tested for stability over the day and after high absorbed dose.

For 6 MV 30 measurements on five consecutive days were made, for 7 MV UF 15 measurements on three days. 40 cm x 40 cm fields were used and the average over several pulses was taken. Both energies were measured at the same days. For electron energies, five consecutive measurements were made on five days each morning and afternoon. Moreover, for 10 MeV a series of measurements after applying high doses or waiting for several hours without radiation were made. Values were corrected for dose rate measured at the isocentre.

It was observed that values from volume one increased over the day by 2-4 % for photon radiation and up to 11 % for electron radiation. From day to day, the signal decreased by around 5 % for photon radiation and stayed fairly constant over the week for electron radiation with a slight increase from Monday to Tuesday morning as the temperature in the linac head was higher on Tuesday morning. For the effect of temperature and pressure changes see discussion in chapter 7.3.2.3.

On the other hand, the signals from volume two decreased over the day by up to 21 %, but increased from day to day for photon radiation by up to 16 %. For electron radiation a drop from Monday to Tuesday was observed. The signals recovered over the week. A summary can be found in table 7-9.

Table 7-9: Signal changes during the stability measurements

	Volume 1		Volume 2	
	Morning/afternoon	Day-to-day	Morning/afternoon	Day-to-day
6 MV	+(1...4) %	-(3...7) %	-(2...10) %	+(4...16) %
7 MV UF	+(0.5...2.5) %	≈ - 4 %	-(3...10) %	+(5...10) %
10 MeV	+(2...11) %	≈ 0 % (+2.6 % Mon-Tue)	-(2...21)%	≈ 0 % (-4.4 % Mon-Tue)
21 MeV	+(2...8) %	≈ +1 % (+3 % Mon-Tue)	-(6...20) %	-(2...5) %

Figure 7-37 and figure 7-38 show the change in signal for a 10 MeV beam over the day and over the week. The day and time of measurement are given on the x-axis. On Friday the measurements for backscatter for 10 MeV LDR and HDR were performed between the two measurement sessions. On Monday, backscatter experiments for all other electron energies were performed. On Tuesday first of all, 10 Gy were applied before the first five measurements. The next series of five measurements is taken after applying additional 20 Gy. Before the next series, another 80 Gy were applied to determine the effect of high doses. After waiting for two hours, the fourth series was measured (13:10). Approx. 1.5 hours (14:50) and 3.5 hours (16:40) afterwards, series five and six were taken without applying any additional dose in between. In volume one the signal changes steadily (see figure 7-37), while for volume two the signal's decrease is less after noon (see figure 7-38). On Wednesday, the steering measurements for all energies were done plus some film measurements between the two measurement series.

The changes in signal are in opposite direction for volume one and two.

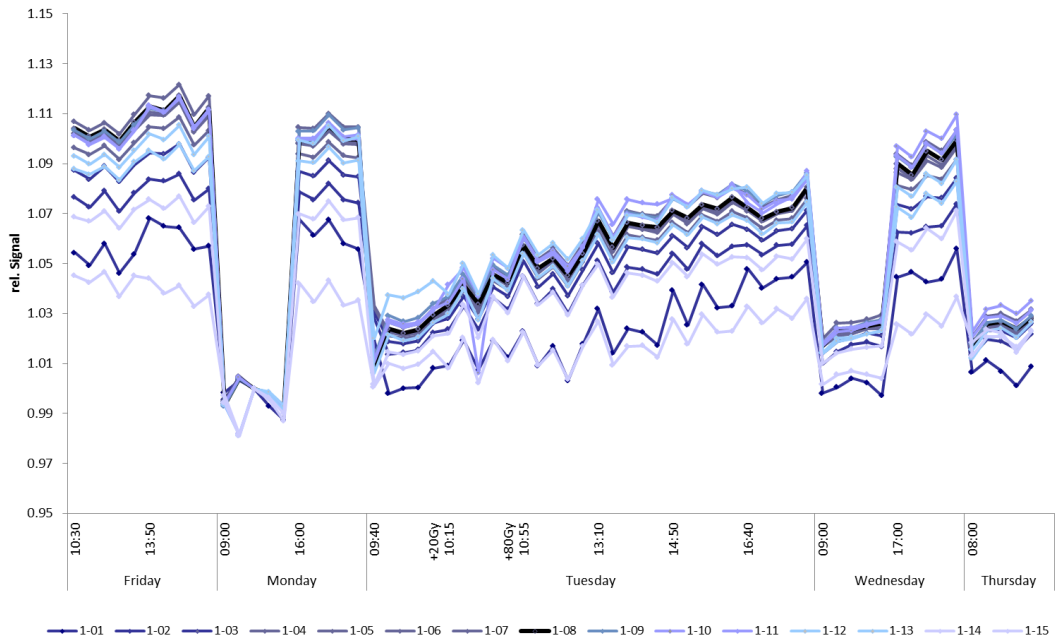


Figure 7-37: Stability of signal from a 10 MeV beam: volume 1

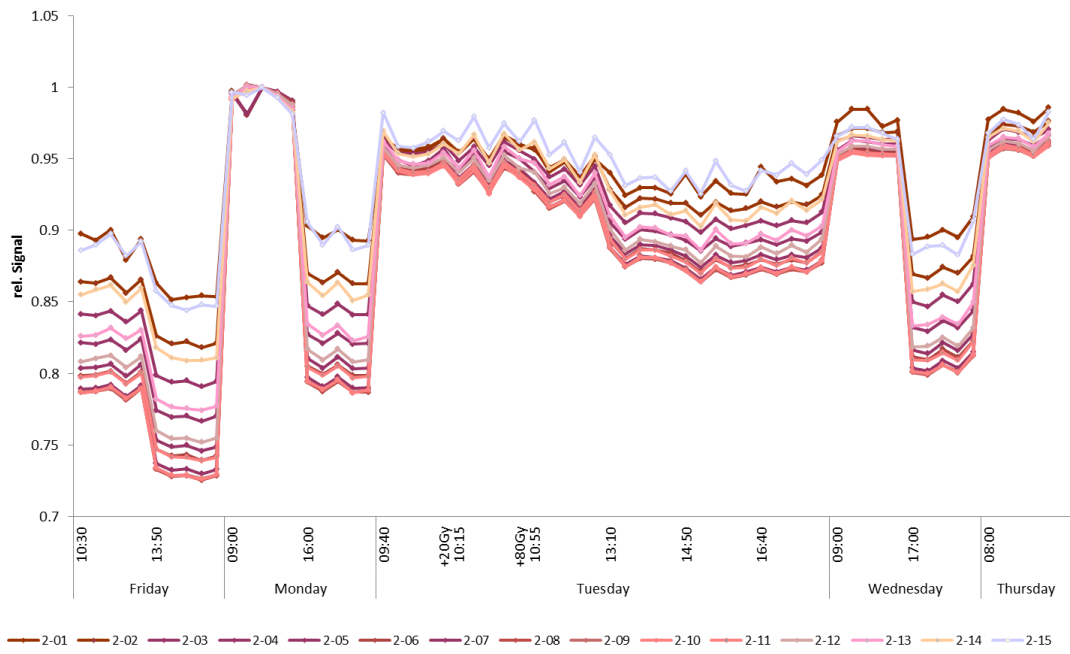


Figure 7-38: Stability of signal from a 10 MeV beam: volume 2

7.3.2.2.6 Effect of Wires on Beam

For photon radiation the effect of the wires on the beam is negligible. Figure 7-39 shows a film placed on the chamber and the respective profile. The films are normalized to the central beam axis value.

For electron radiation, the grid of wires is clearly visible on the film as well as on a measured profile (see figure 7-40). Near the patient plane this effect vanishes due to multiple scattering and is thus not dosimetrically relevant. Figure 7-41 shows the measured profile with backscatter at SSD 95 in comparison to a profile of an unused film. No significant differences are observed.

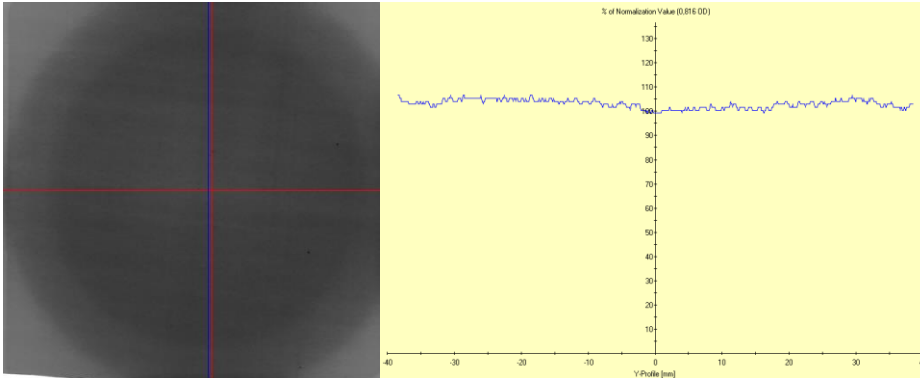


Figure 7-39: Film and measured profile (blue line) for a 6 MV photon beam

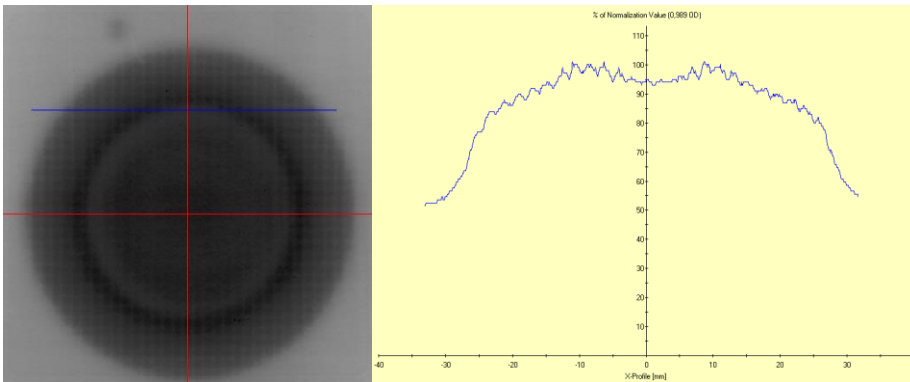


Figure 7-40: Film and measured profile (blue line) for a 6 MeV electron beam

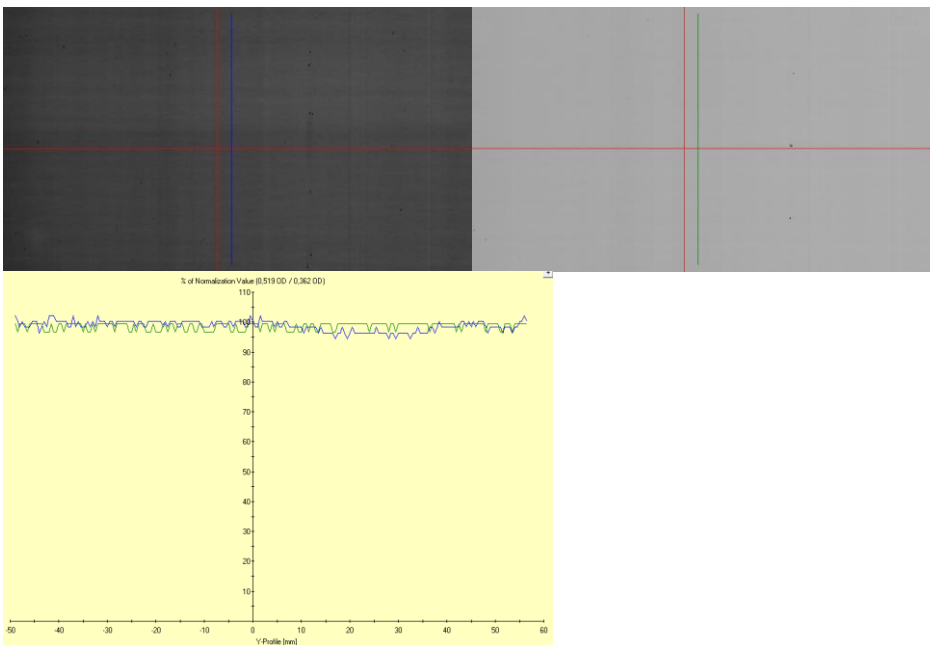


Figure 7-41: Film at SSD 95 with 3.5 cm RW3 backscatter (upper left film; blue line) compared to unused film (upper right film; green line) for a 6 MeV electron beam; normalized to central axis value

7.3.2.3 Discussion

During the dose rate measurements it was observed that in general the relative standard deviation of individual pulse measurements is higher for channels 1-01 and 2-01. The signals of all channels are fairly proportional to the dose per pulse as the variations are approximately the same for all wires in a plane and might be due to the inaccuracy in reading the dose rate during the ten pulses, as the display was fluctuating. This is true for all channels, except 1-10, 1-13, 1-15 and 2-01 for photon radiation and 2-15 for electron radiation.

The problems in channels 1-10, 1-13 and 1-15 might be due to bad soldering, kinks and spikes on some of the wires (see appendix F, page F-18). A more thorough production as well as a better design of the signal planes could minimize these problems. Large variation in signal in channels 1-01, 2-01 and 2-15 is most likely due to fluctuations in the beam. These channels are at the very edge and as the CAX is not at channel x-08, larger variation might occur only on one side of the UDC.

As the reproducibility of the output of the linear accelerator varies within 0.5 % [IEC 60977 2008] and the fluctuating dose rate at isocentre was noted at a certain point in time during the measurement, the differences in channel signals are partly due to changes in linear accelerator performance.

The backscatter experiments showed that the effect of backscattered radiation is higher at the edges of the chamber and is mainly caused by radiation from the y-jaws, as expected. The relationship between backscattered radiation and field size is linear. This is in agreement with the findings of Sanz et al. who also found a linear relationship between backscattered radiation and field size [Sanz, Alvarez and Nelli 2007].

The Unified Dose Chamber is suitable for detecting symmetry changes of the beam profile. As shown, the change in calculated symmetry is proportional to the change in symmetry at isocentre for photon radiation. The fluctuations in measuring the profile in figure 7-31 are due to fluctuations in linac output but are also owed to the drift of chamber signals (see chapter 7.3.2.2.5). For electron radiation the change in signal is not proportional to the change at isocentre. Nevertheless small symmetry changes can be detected, such that nonsymmetric beams can be identified.

Moreover the beam profile itself can be measured. The small deviations between the profile measured by film and by the UDC are due an effect observed during the measurements of the stability over the day.

During these measurements the signals from both volumes drift in opposite directions. The signals from volume one increase faster in the morning and then drift with time and dose over the day (for photon and electron radiation) as can be seen in figure 7-42 for 10 MeV. If a temperature correction is applied, suggesting that the volume is open to air, the signal changes get worse. The signals increase over the day as temperature does. For open chambers a decrease in signal with increasing temperature is expected as the density would decrease.

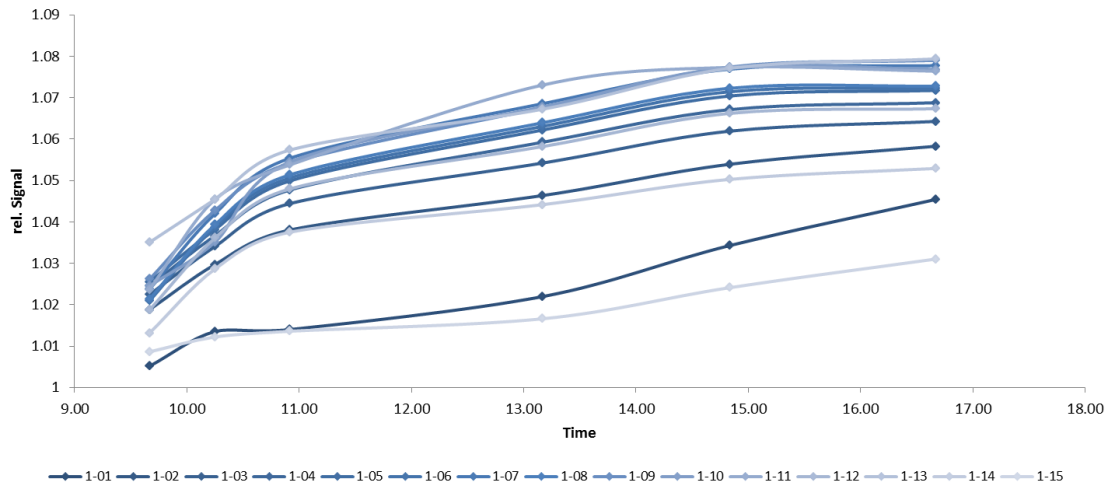


Figure 7-42: Stability of signal from a 10 MeV beam: volume 1. Measurement points are the averages of 5 consecutive measurements and normalized to Monday morning (see figure 7-37)

Nevertheless the changes are higher on days on which more dose is applied. Moreover the changes over the day in the central channels are higher than at the edges. Figure 7-43 shows the change in signal from morning to afternoon for 10 MeV on three days. It can be clearly seen that the changes are higher in the centre. On day 1 more dose was applied than on day 3 and the smallest amount of dose on day 2.

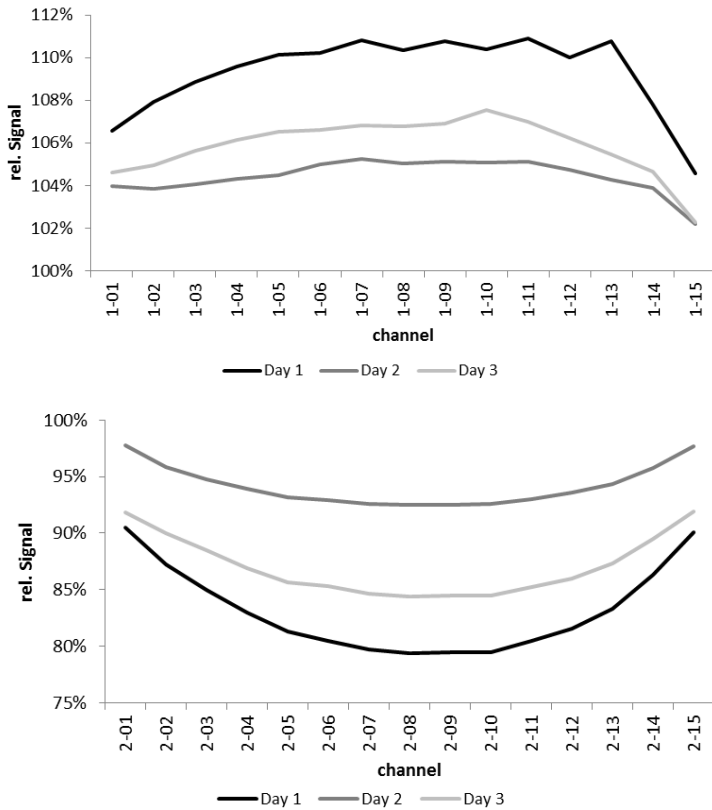


Figure 7-43: Change of signals from volume one (top) and two (bottom) from morning to afternoon for a 10 MeV beam

In volume two a temperature and pressure correction reduces the changes. As the temperature measurement in the head is not directly at the chambers, the temperature at the prototype might be higher than the measured one. This is especially true for the electron measurements where the temperature sensor had to be put aside in order to fix the UDC to the slide. The temperature is measured in this case around 10 cm from the UDC.

From these findings it is assumed that volume one is sealed and volume two is open to air. This is reasonable as when opening volume two the last time before the performance measurements for repairing a channel, three screws could not be tightened properly because they slipped.

During the day the temperature in the head rises, the higher the more radiation is applied. Therefore the air in volume one expands and bloats the Kapton foils (window and HV foil). The HV foil expands as well, as volume two is open to air. This leads to a signal increase in volume one and a signal decrease in volume two, as the distances between electrodes and HV foil change. As the foil bends more in the centre, the changes are higher in central channels. During the night the temperature falls again to the morning level.

During the electron measurements from Monday to Thursday the air pressure stayed fairly constant over the days and thus the signal levels in the morning are comparable. For the measurements with photon radiation, the air pressure in the bunker stayed constant during the day but increased over night. From Tuesday to Wednesday the pressure raised from 929 mbar to 935 mbar. On Thursday morning 955 mbar were measured. This leads to a signal loss in volume one as the HV foil is bent inwards by an increased pressure from volume two. The dose-rate normalized signals of volume one during these three days can be seen in figure 7-44.

The air pressure rose from Tuesday morning to Wednesday noon by 1 %. The temperature difference in this time is 2.2 °C, which is a temperature rise of 0.72 % which counteracts the pressure influence. This explains that the signal level on Wednesday noon is only around 1 % below the normalization value. The percental changes in volume two are higher than in volume one as these signals are lower. I.e. a change of 0.1 V means a 10 % change in volume one (with 1 V level in the morning) and 20 % in volume two (0.5 V level in the morning).

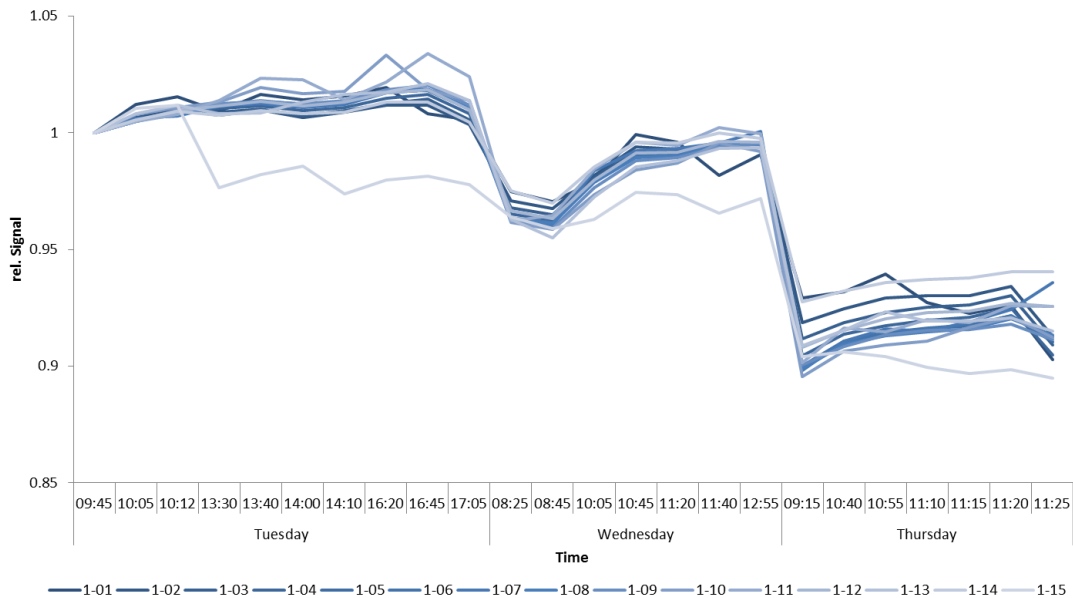


Figure 7-44: Stability of signal from 6 MV beam (volume 1)

It can be concluded that the drift of the chamber signals is due to temperature and pressure changes. The effect of changes in opposite direction occurs as volume one is sealed and volume two is open to air. Would volume two be sealed as well, the HV foil would not bend. Only a pressure correction for the bending Kapton entrance and exit windows would have to be applied.

The measurements for backscatter and steered beams were made within a short time and several measurements were made which were averaged to minimize the effects from the instability of the signals.

7.3.3 Conclusion

With the current design of the UDC, a beam profile can be gathered. The effect of backscatter is clearly visible, and changes in beam profile due to steering can be examined.

Nevertheless the stability of the signals has to be improved by thoroughly sealing the chamber and applying corrections to the signals. If both volumes are closed, the HV foil should not bend due to temperature or pressure changes, thus keeping the distance between HV and electrodes constant. However, with the current design the outer Kapton windows will bend with pressure or temperature changes and thus changing the gas density in the sensitive volume. Either a temperature and pressure correction has to be applied or a more rigid construction of the windows has to be found (e.g. by increasing the pretension of the foils). Ideas for improvement of the dose chamber are given in appendix F.

In future measurements proper alignment of the chamber with the beam central axis is essential. It is expected that nonsymmetry can be detected with the design of this chamber when signal drifts as observed with this prototype are excluded. For calculating the symmetry of the radiation field, the IEC 60976 definition (maximum ratio of symmetric channels) should be used.

When analysing the signals, backscatter from the y-jaws and MLC has to be taken into account. Either an algorithm for determining a field size dependent correction factor has to be found or a shielding plate when using photon radiation has to block the backscattered radiation. For the former, further investigations on the field size dependence of the backscatter should be performed to verify the linear relationship observed here.

It was shown that the dose determination per pulse is possible, even for high dose rates if the chamber voltage is raised, and that the measured dose rates are proportional to the ones measured by an external dosimeter. The measured beam symmetry is proportional to the beam symmetry measured at isocentre. Moreover the beam profile can be sensed with the chamber. With the second prototype an exact determination of the profile was not possible due to volume two not being gastight and the resulting pressure and temperature effects on the HV-foil.

7.4 Conclusion on Applicability of the New Dose Monitor Concept

The main criteria for a new dose monitoring system are requirements concerning comparability to current dose chambers, serviceability and lifetime, adherence to IEC 60601-2-1 and capability to monitor the recommended performance of linear accelerators given by IEC 60976/60977:

- 1) sensing of beam profile
- 2) detection of changes in beam symmetry and flatness at least as good as current system
- 3) reliable measurement of applied dose
- 4) fit into current linear accelerator head
- 5) not disturb the beam in unwanted fashion
- 6) lifetime of at least several years, preferably 10 years

IEC 60601-2-1

- 7) Two independent dose monitoring systems which can independently terminate radiation
- 8) Malfunctioning of one system shall not affect the other system
- 9) Performance for absorbed dose rate up to twice the specified maximum included in technical description if linear accelerator is under any circumstance capable of producing this dose rate
- 10) At least one transmission detector centred on reference axis on patient side of all field flattening and beam scattering filters shall be provided
- 11) Hermetically sealed detectors should be sealed independently of one another
- 12) Detectors shall detect symmetrical and non-symmetrical changes of dose distribution
- 13) Means shall be provided to terminate irradiation before additional 0.25 Gy is delivered, when absorbed dose distribution is distorted by more than 10 % or the signals from the radiation detectors indicate a change >10 % in absorbed dose distribution

IEC 60976/60977 (recommended performance stated in brackets)

- 14) Reproducibility (0.5 %)
- 15) Proportionality (2 %)
- 16) Dependence on the shape of radiation field (statement sufficient)
- 17) Stability after high absorbed dose (2 %)
- 18) Stability throughout the day (2 %)
- 19) Stability throughout the week (2 %)
- 20) Flatness and symmetry of radiation field (symmetry: photons 103 %; electrons 105 %)

The Unified Dose Chamber presented in this work fits into the current Siemens linear accelerator head as was seen in chapter 7.3.2. Its diameter was chosen not to disturb the beam (see chapter 4.2.1) and the diameter of the wires is chosen small enough not to have an adverse effect on the beam profile as shown in chapter 7.3.2.2.6. The two ionisation volumes are transmission detectors which are centred on the reference axis on patient side of all field flattening and beam scattering filters. These ionisation volumes are independently sealed as shown by filling one volume by nitrogen, nitrogen + carbon dioxide or by argon and leaving the other volume filled with ambient air (chapter 7.3.1). This also shows that malfunctioning of one system does not affect the other, as excessive radiation could still be detected, besides the effects seen in chapter 7.3.2.2.5. Moreover the ionisation volumes have independent electronics (see chapter 7.2) such that radiation can be independently terminated.

Materials for the dose chamber were chosen such that the lifetime is as long as possible, especially concerning ageing of the materials with respect to applied dose to these (see chapter 4.6).

The construction of the dose monitor chamber and its electronics therefore fulfils criteria 4), 5), 6), 7), 8), 10) and 11).

As the linear accelerators under investigation in this work are not capable of producing twice the specified dose rate, criterion 9) was not investigated in this work.

Concerning the performance it was shown that the UDC can detect changes in symmetry of the radiation field. In chapter 7.3.2.2.3 it was shown that the dose chamber signals of wires 2-02 and 2-14 change by $\pm 0.8\%$ when changing the symmetry by 3%. This signal change is higher than the repeatability such that these changes in symmetry can be detected.

The capability to detect changes in symmetry was theoretically compared to the current dose chambers in chapter 4.3.3 which shows a better detectability by the UDC if the outer wires are used for measurement. Measurements show that the change in symmetry for photon beam is proportional to the change detected at isocentre for the UDC and that the detectability is better compared to the current Siemens photon dose chamber (compare chapter 3.2.2.4 for photon chamber and chapter 7.3.2.2.3 for UDC). The detectability of symmetry changes under electron radiation was not proportional to the changes in symmetry at isocentre. Nevertheless signal changes were seen. This fulfils criteria 12), 13) and 20) and partially criterion 2).

The repeatability of the dose chamber signals is within the reproducibility of the linear accelerator and the proportionality to applied dose is within the required 2% for all three investigated gas fillings (see chapters 7.3.2.2.1 and 7.3.1.2.1). This ensures a reliable measurement of the applied dose and fulfils criteria 3), 14) and 15).

Concerning criterion 16) it can be stated that varying field sizes have an effect on the chamber performance in photon mode, as shown in chapter 7.3.2.2.2, as the entrance and exit windows of the UDC are made from foils. As these changes are proportional to the field size, a correction like it is used for other chamber types is possible. Moreover the backscattered electrons can be blocked by inserting a sufficiently thick plate between monitor chamber and secondary collimators.

The stability of the linac after high absorbed dose, throughout the day and throughout the week (criteria 17), 18) and 19)) could not be monitored with the prototype two of the UDC as one of the ionisation volumes was open to air. This led to signal changes due to changes in temperature in the linac head and ambient air pressure. During further investigations with a gas-tight chamber the effect of temperature and pressure on the signals could be further examined.

In this work for the first time a possibility to sense the beam profile as required by criterion 1) is realized with the UDC. Preliminary tests with the first prototype in chapter 6.3.2 showed that the measured profile agrees well with a film measurement of a 6 MV beam.

In chapter 7.3.2.2.4 a direct comparison of chamber signal to beam profile measured by film at the same time was made. Due to the influences of temperature and pressure and the resulting bending of the HV-foil, it was not possible to measure the exact profile. Nevertheless, major distortions in the profile could be observed.

8 Summary and Outlook

The aim of this work was to develop a new dose monitoring system for medical linear accelerators which gains more information on the beam besides the required parameters applied dose, symmetry and flatness.

After giving an overview on the signal generation in ionisation chambers and introducing flatness and symmetry monitoring conventions as well as normative requirements in chapters 2.1 to 2.3, examples of dose monitor chambers were given in chapter 2.4. The external influences on these were presented in chapter 2.5.

To analyse the drawbacks and capabilities of the current dose monitor chambers used by Siemens to monitor the radiation beam and to gain information on the ambient radiation field in the linear accelerator head, simulations and measurements with these chambers were done in chapter 3.

Chapter 4 focused on the design of the new dose monitor chamber. First of all, a new beam sensing principle was introduced which senses the beam by wires or strip electrodes instead of radially segmented electrodes. Afterwards the geometric dimensions as well as the channel and wire distance were determined.

Moreover a pre-selection on suitable filling medium was done, based on required signal level and ion mobility. These investigations revealed that a fluid is not suitable for this kind of chamber and as filling gases nitrogen, a nitrogen-carbon dioxide mixture as well as an argon-carbon dioxide mixture are best suited.

The materials of the chamber were selected such that they do not adversely alter the beam profile, have a long durability even after applying high doses and form a favourable electric field. This was achieved by 100 μm thick wires with a small wire distance of 2 mm, thin entrance and exit foils of 100 μm and HV-foil of 25 μm thickness and by selecting radiation resistant foils, gasket material and adhesive.

By changing the concept from two monitor chambers to a single one, alternative solutions for the secondary scattering foil in electron mode and the mirror in photon mode had to be found. A concept for a secondary scattering foil and a mirror permanently in the beam path were presented in chapter 5.

Based on the results in chapter 4 and first measurements with a multi-wire proportional chamber operated in ionisation mode, a first basic prototype open to air was built to show the feasibility of using a wire chamber to monitor the beam profile of a medical linear accelerator in chapter 6. With this prototype it was shown that a channel distance of 4 mm is sufficient.

Finally a second prototype with sealed ionisation chambers was investigated in chapter 7. For this suitable electronics were developed and the three gas fillings selected in chapter 4 were analysed. These measurements showed that nitrogen is the best suited gas.

During measurements with the second prototype in the head of a medical linear accelerator the performance concerning repeatability, detection of symmetry changes and measurement of the beam profile were analysed. Moreover the effect of varying field size on the chamber signals was investigated.

The investigations in this work showed that a Unified Dose Chamber for photon and electron radiation with wire electrodes can monitor the beam adequately and fulfil the main criteria for such a chamber.

The drawback of two monitor chambers on a moving slide prone to mechanical errors can be overcome by integrating the secondary scattering foil and a foil mirror into the setup.

For the further development in linear accelerators this chamber is well suited as this dose monitor system could also be used for precise steering and failure analysis as more detailed information on beam profile and changes therein is available, compared to the current dose monitor system. By knowing the change of the beam profile, a feedback loop could be integrated into the linear accelerator control system which compensates the beam distortions or shutting off the beam.

In case of a tilted electron beam caused by a wrong bending magnet current, the beam could be steered by applying a corresponding current to the bending magnet. This would lead to a more precise agreement of applied dose to planned one. This chamber would not only ensure a good agreement between total applied dose to planned one, averaged over the full field size, but also make sure that the spatial distribution is as planned. Smaller changes in symmetry and flatness as detected nowadays could be compensated by this algorithm. This becomes more important in radiation fields sparing critical organs and boosting certain tumour regions.

For a diverging beam the root cause is mostly a problem with the bending magnet and an error message could direct the service technician directly to this problem. In further linear accelerator developments focussing coils might be implemented to counteract these problems.

If the electron beam hits the target or primary scattering foil off-axis, the beam could be stopped and a corresponding error message could be sent to the control console to ease error analysis. If the electron beam is off-axis but parallel to the intended beam path, the main cause is a mechanical displacement of the components in the linear accelerator head relative to each other and cannot be compensated by steering coils. With the UDC this case would be easily detectable as the beam profile is broader for a diverging beam (see chapter 1).

It can be concluded that this new dose monitoring system concept overcomes the drawbacks of current dose monitor chambers and allows for new control loops in the linear accelerator control system for a more stable operation.

Appendix

A Recombination Correction for Continuous Sweeping of Dose Rate

If continuous sweeping of the dose rate is applied, the dose per pulse can be calculated. According to DIN 6800-2 (2008), the correction factor for recombination is

$$k_s = 1 + \frac{\gamma}{U} + \frac{\delta \cdot D^p}{U} \quad (54)$$

The first correction term corresponds to initial recombination, the second one to volume recombination. D^p is the dose to water per pulse, U the applied voltage. γ and δ can be determined from a k_s -DPP plot. $\gamma = k_s(0)$ and δ is the slope. This linear relationship holds up to 130 mGy/pulse for air filled ion chambers [Di Martino, et al. 2005].

In order to determine γ and δ , a k_s -DPP plot has to be drawn. k_s can be derived from a so-called Jaffé-plot. For each DPP under investigation, the applied voltage is varied and $1/U$ is plotted against $1/M$ (M : readings from chamber). By extrapolating U to infinity (i.e. $1/U=0$), k_s can be derived. From these Jaffé plots a k_s value for each investigated DPP can be derived. Plotting k_s vs DPP yields γ and δ .

As recombination is independent of energy and type of radiation [Havercroft and Klevenhagen 1993], this procedure has not necessarily to be conducted for each radiation-energy combination. γ and δ have to be determined only once for the type and not for each manufactured sample.

The chamber measures the signal $M - M_0$ per pulse. As the dose per pulse is [DIN 6800-2 2008]

$$D^p = (M - M_0) \cdot N \cdot \prod_{i=1}^n k_i = (M - M_0) \cdot N \cdot k_s \quad (55)$$

assuming that all correction factors except k_s are one. The first equation then yields

$$k_s = 1 + \frac{\gamma}{U} + \frac{\delta \cdot (M - M_0) \cdot N \cdot k_s}{U} \quad (56)$$

This gives

$$k_s = \frac{U + \gamma}{U - \delta \cdot N \cdot (M - M_0)} \quad (57)$$

By inserting k_s into the equation (55), the dose per pulse is

$$D^p = \frac{(U + \gamma) \cdot (M - M_0) \cdot N}{U - \delta \cdot N \cdot (M - M_0)} \quad (58)$$

B Monte Carlo Simulation

Monte Carlo simulations were conducted with the EGSnrc code version V4-r2-2-5 and BEAMnrc version beam2007. A developer at Siemens Healthcare described the simulation input for a typical Siemens Primus with 3D-MLC in 2001. The data was provided by Siemens in an Excel-sheet and used as is, as no particular linear accelerator had to be simulated, but a typical one. Figure B-1 shows the simulated set-up with an exemplary scoring plane behind the chamber. The Y-jaws are not shown in this view in the xz-plane.

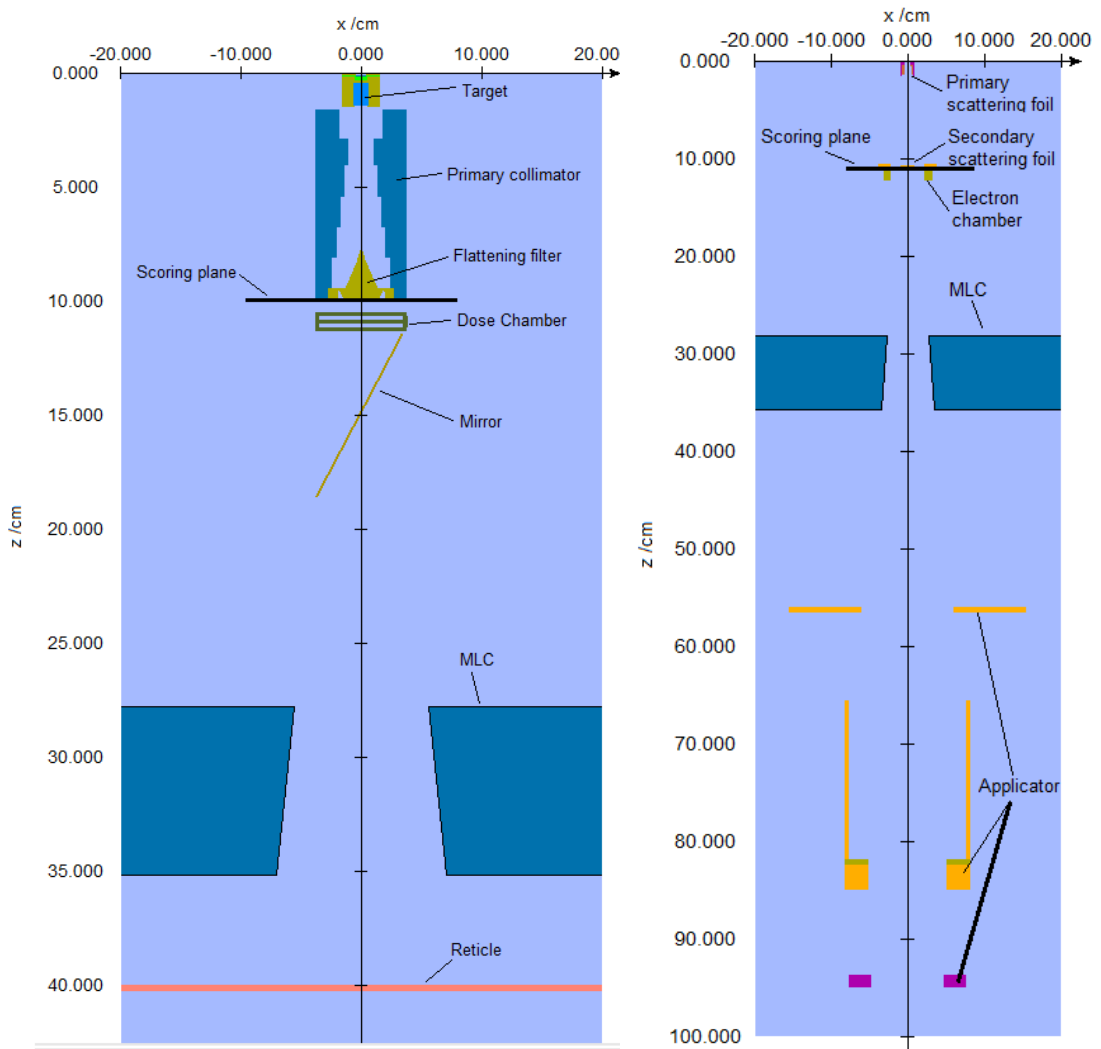


Figure B-1: Simulated linac head with scoring planes; right: 6 MV photon; left: 17 MeV electron

The geometrical dimensions of target/primary foils, absorber, primary collimator, flattening filter, compensator/insert, secondary foil, dose chambers, mirror, Y-jaws, MLC, reticle, and five applicators was given in the Excel-sheet for 6 MV and 15 MV photon radiation as well as 6 MeV, 8 MeV, 12 MeV, 14 MeV and 17 MeV electron radiation. The position of the MLC jaws could be calculated via the Excel-sheet, depending on desired field size.

The mean incident energy on the window was given as well:

Table B-1: Mean incident energy on the exit window for Monte Carlo simulations

Nominal energy	6 MV	15 MV	6 MeV	8 MeV	10 MeV	12 MeV	14 MeV	17 MeV
Mean energy of incident e- /MeV	6.58	13.76	6.87	9.17	11.42	13.18	14.62	19.31

Each component of the linear accelerator was given a different latch bit, such that the origin of particles in each scoring plane could be evaluated. Table B-2 summarizes the component module and latch bit configurations. Latch bits were set by interaction.

Table B-2: Component modules and latch bits for backscatter simulations

Component	Component module number	Latch bit
Target	1	1
Primary collimator	2	2
Flattening filter + absorber	2	3
Monitor chamber	3	4
Mirror/Acrylic glass	4	5
Y-jaws	5	6
MLC	6	7
Reticle	7	8

C Channel and Wire Distance Results

The figures on pages C-2 to C-3 give a comparison of reconstructed, interpolated and original **measured profile** for sampling distances T which ensure a reconstruction within 1.5 % from the original profile for **sampling with a wire with Gaussian transfer function** ($\text{FWHM} = T$).

The green vertical lines in the bottom diagrams show the 5 mm border at the edge of the radiation field or chamber edge which were not included in the analysis of the fit between original and reconstructed profile. The red horizontal lines in the lower right figure show the $\pm 1.5\%$ acceptance criterion.

Analysis **for measured beam profiles** and **sampling with two wires per channel** are given on pages C-4 to C-6.

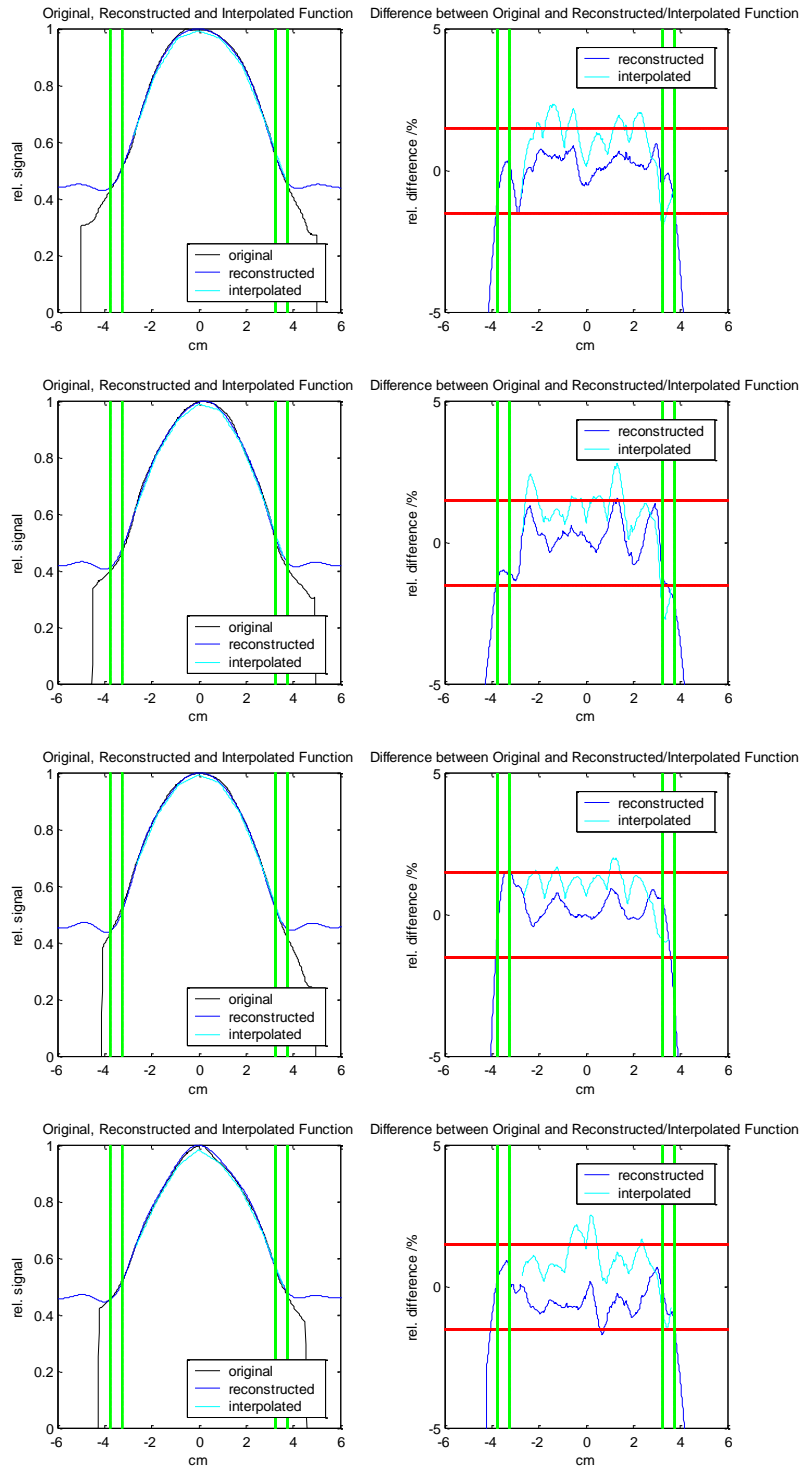


Figure C-1: Sampling of measured profiles of 6 MV, 6 MV UF, 15 MV and 15 MV UF photon beams (top to bottom) with one wire per channel and with sampling distances $T = 9.2$ mm, 9.0 mm, 8.8 mm and 9.0 mm, respectively

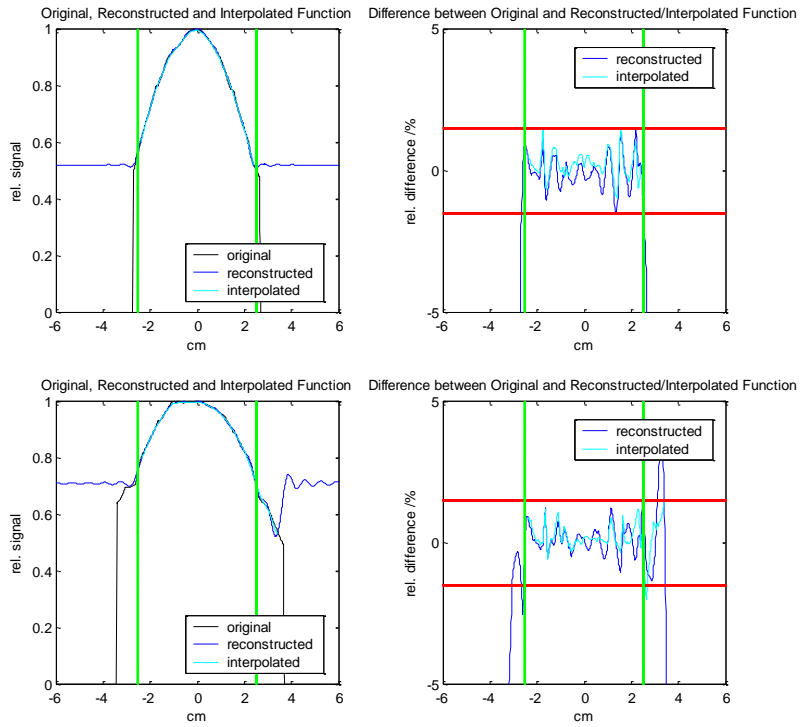


Figure C-2: Sampling of measured profiles of 6 MeV (top) and 15 MeV (bottom) electron beams with one wire per channel and with sampling distances $T = 3.0$ mm and 3.4 mm, respectively

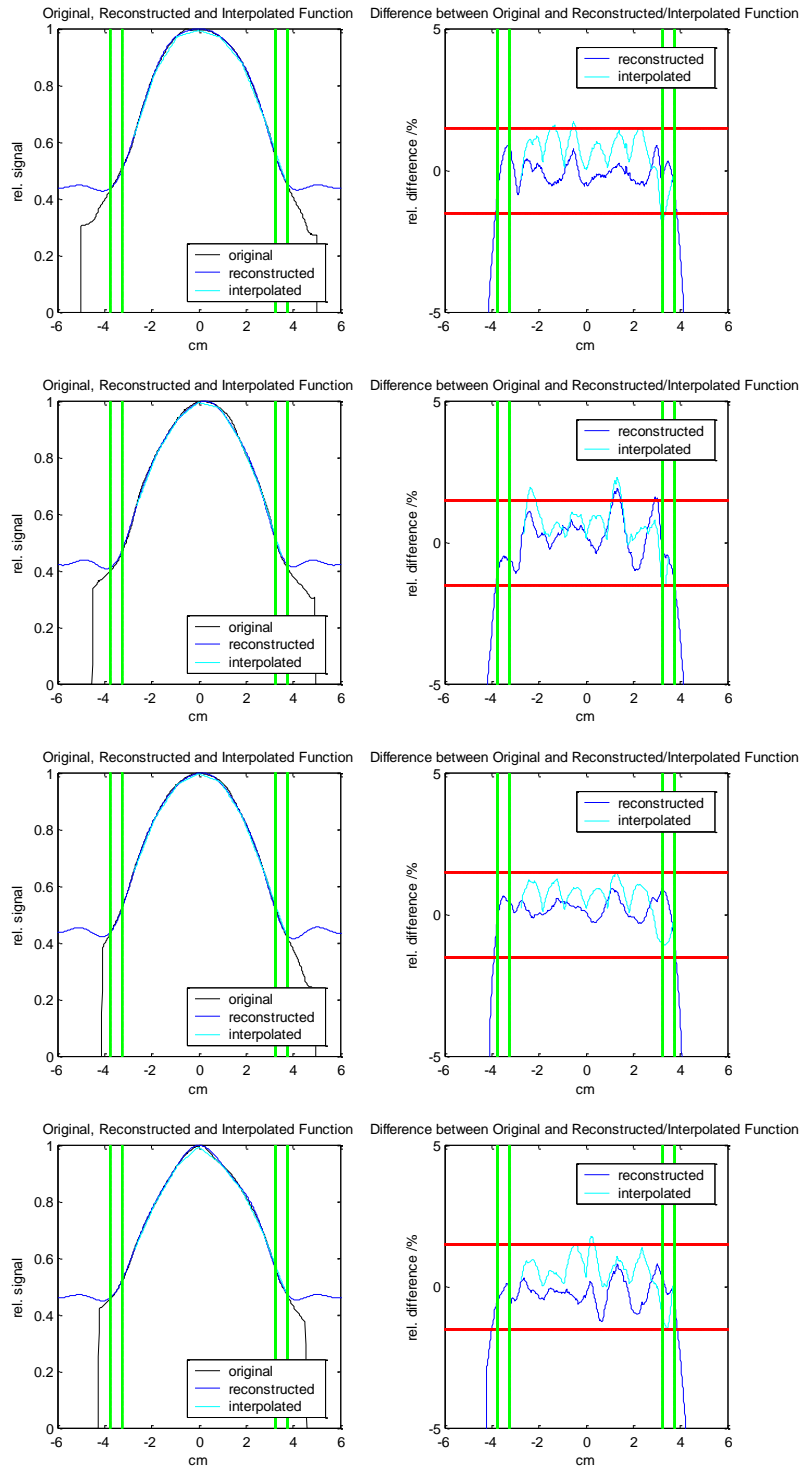


Figure C-3: Sampling of measured profiles of 6 MV, 6 MV UF, 15 MV and 15 MV UF photon beams (top to bottom) with two wires per channel and with sampling distances $T = 9.2$ mm, 9.2 mm, 8.8 mm and 9.2 mm, respectively

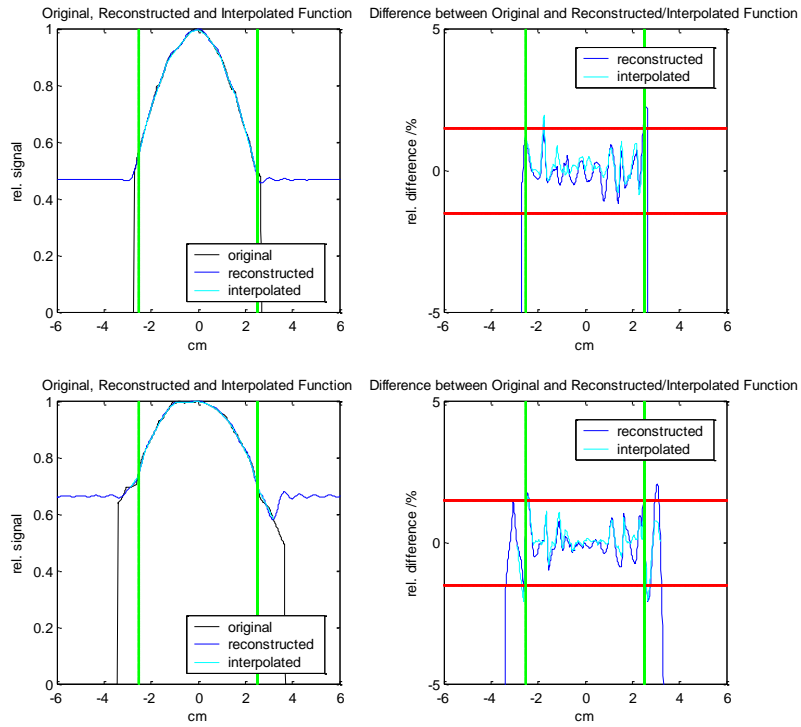


Figure C-4: Sampling of measured profiles of 6 MeV (top) and 15 MeV (bottom) electron beams with two wires per channel and with sampling distances $T = 3.2$ mm

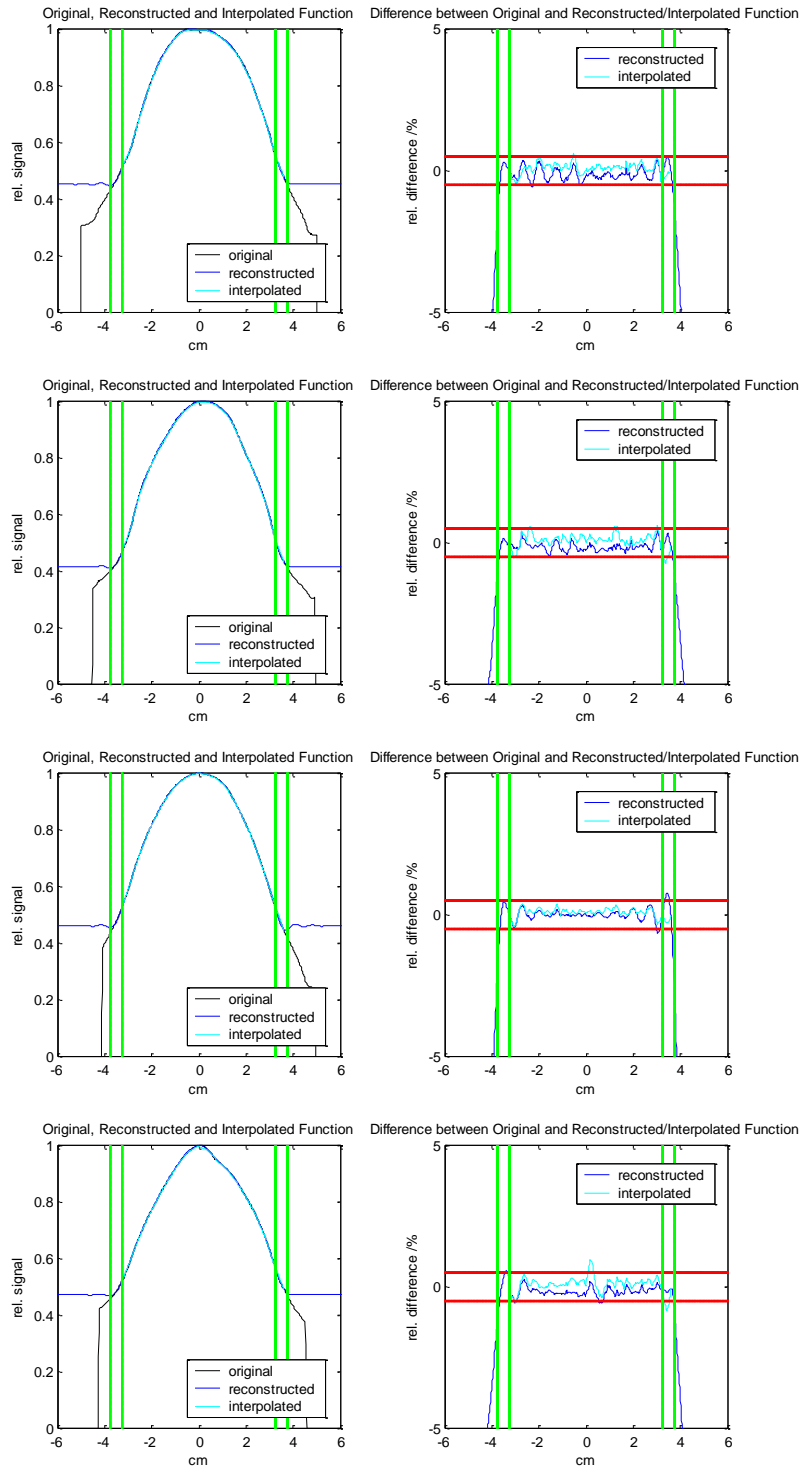


Figure C-5: Sampling of measured profiles of 6 MV, 6 MV UF, 15 MV and 15 MV UF photon beams (top to bottom) with two wires per channel and with sampling distances $T = 3.6$ mm, 3.6 mm, 3.6 mm and 4.0 mm, respectively

D Activation of Chamber Materials

Table D-1 gives the photonuclear reaction properties of some possible chamber materials.

σ_{\max} and E_{\max} of (γ , abs) are partly estimated from the graphs given in the handbook on photonuclear data by the IAEA [IAEA], where no values were given in the tabulated measurements in the same handbook. Estimated values are given as integer numbers, whereas data from the table are given with at least one decimal place. The peak energy and cross sections are stated from different studies, so that if several values for the same peak energy were given, the newest reference is cited. For W-183 and W-184 only total photoneutron cross sections $\sigma(\gamma, \text{sn})$ were available and are cited in the column of γ, n reaction.

Table D-1: Photonuclear reaction properties of some chamber materials (data from [IAEA])

Element (abundance)		γ , abs	γ, n	$\gamma, 2\text{n}$	$\gamma, 3\text{n}$	γ, p
Al-27 (100%)	Threshold /MeV	-	13.06	24.42	41.36	8.27
	E_{\max} /MeV	20.8	21.2	29.74		19.9
	σ_{\max} /mbarn	41.6	19.84 15.8 14.3	34.567 0.6 1.34		17.5
Mo-92	Threshold /MeV	-	12.67	22.78	36.02	7.46
	E_{\max} /MeV	17	16.73	25.67		
	σ_{\max} /mbarn	300	163.8	8.2		
Mo-94	Threshold /MeV	-	9.68	17.75	30.42	8.49
	E_{\max} /MeV	18	16.19	19.98		
	σ_{\max} /mbarn	210	184.9	49.9		
Mo-95 (15.92%)	Threshold /MeV	-	7.37	17.05	25.11	8.63
	E_{\max} /MeV	18				
	σ_{\max} /mbarn	190				
Mo-96 (16.68%)	Threshold /MeV	-	9.15	16.52	26.20	9.30
	E_{\max} /MeV	18	16.46	19.17	29.19	
	σ_{\max} /mbarn	180	190.6	67.9	12.9	
Mo-97 (9.55%)	Threshold /MeV	-	6.82	15.98	23.34	9.23
	E_{\max} /MeV	18				
	σ_{\max} /mbarn	190				
Mo-98 (24.13%)	Threshold /MeV	-	8.64	15.46	24.62	9.79
	E_{\max} /MeV	18	15.37	19.17	28.11	
	σ_{\max} /mbarn	190	194.7	86.0	13.3	
Mo-100 (9.63%)	Threshold /MeV	-	8.29	14.22	22.86	11.15
	E_{\max} /MeV	18	14.29	18.08	28.38	22.5
	σ_{\max} /mbarn	170	163.4	104.8	25.94 27.3	13.16 20.3
W-182 (26.30%)	Threshold /MeV	-	8.07	14.75	23.16	7.10
	E_{\max} /MeV	13-16				
	σ_{\max} /mbarn	425				
W-183 (14.28%)	Threshold /MeV	-	6.19	14.26	20.94	7.22
	E_{\max} /MeV	12.83	14.9 (sn) 12.7(sn)			
	σ_{\max} /mbarn	401.0	390.0 (sn) 290.0 (sn)			
W-184 (26.30%)	Threshold /MeV	-	7.41	13.6	21.67	7.70
	E_{\max} /MeV	12.02 14.44	13.42 (sn) 15.02 (sn)			
	σ_{\max} /mbarn	416.0 407.0	432.1 (sn) 426.2 (sn)			

Element (abundance)		γ, abs	γ, n	$\gamma, 2n$	$\gamma, 3n$	γ, p
W-186 (28.60%)	Threshold /MeV	-	7.19	12.95	20.36	8.40
	E_{max} /MeV	13.47	12.814	15.756	28.299	
	σ_{max} /mbarn	449.0	390.87	256.28	38.03	
Au-197 (100%)	Threshold /MeV	-	8.07	14.71	23.08	5.78
	E_{max} /MeV	13.5	13.504	16.851	27.12	
			16.85			
	σ_{max} /mbarn	540.0	494.15	104.78	13.6	
			104.78			

E Preliminary Investigations with MWPC

Assembly

In monitoring proton and ion beams, the multi-wire proportional chamber MWPC is used as a beam detector and analyses the position and full width at half maximum of the beam spot.

The MWPC is a wire chamber with an active area of 20 cm x 20 cm, a sense wire diameter of 50 μm made of gilded tungsten-rhenium, a wire spacing of 1 mm and a channel distance of 2 mm. In each direction there are 112 channels. The chamber is used in the proportionality region. The high voltage plane is made from 25 μm thick gilded tungsten-rhenium wires, spanned at an angle of 45° to the wires in the sense planes. The volume is continuously purged with Ar-CO₂ as ionisation gas.

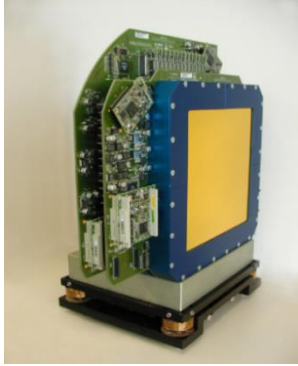


Figure E-1: MWPC

Figure E-1 shows a picture of a MWPC. The chamber is directly mounted on the main board on which the HV supply and electronics are positioned. Every eight channels are processed in an integration and digitalisation module.

In the software, the integration time can be selected. As the proton and ion beam is quasi-continuous, the time of integration T_{int} determines the expected signal level. The measured signal is given in digital numbers which are proportional to the measured current I_{in} . The integration capacity C_{int} is 100 pF and 4095 digital numbers (DN) correspond to 2.5 V on C_{int} . The amplification factor is 2.546.

$$DN = 4095 * \frac{2.546}{2.5} * \frac{I_{\text{in}} T_{\text{int}}}{C_{\text{int}}} \quad (59)$$

Measurements

First of all, the MWPC was used at the MWPC test stand which is normally used to check the parallelism of the wires and check the functionality of each channel. The test stand consists of a table movable in x-y direction and an x-ray tube orthogonal to the movable table. The voltage applied to the HV wire grid was varied from 0 V to 1632 V in order to determine the ionisation region and the beginning of the proportionality region. The x-ray tube was operated at 60 kV and 20 mA and the measurements were averaged over 2048 measurements in 10 seconds. The summed signal from eight channels, over whose centre the x-ray beam was positioned, was used to analyse the voltage dependency of the signals.

After determining the plateau region for x-ray beams, measurements at a linear accelerator in electron mode were conducted to verify the applicability of a wire chamber for monitoring electron beams.

The MWPC was placed in a 6 MeV beam of a linear accelerator (67 Hz pulse repetition frequency, 3.5 μs pulse length). The signals from the chamber were again scored with the test software developed for the MWPCs. For all channels the average signal of 2047 samples in 15 ms, i.e. within one pulse, was calculated.

Results

The offset at zero voltage was 100 digital numbers per channel and was subtracted from the measured values. To evaluate the voltage where the proportional region begins, the inverse of the measured voltage is plotted against the inverse of the applied voltage. Figure E-2 shows such a Jaffé diagram in which the point where the

proportional region begins is clearly visible as the curve bends at the starting point. At an applied voltage of 542 V the chamber operates no longer in the ionisation region.

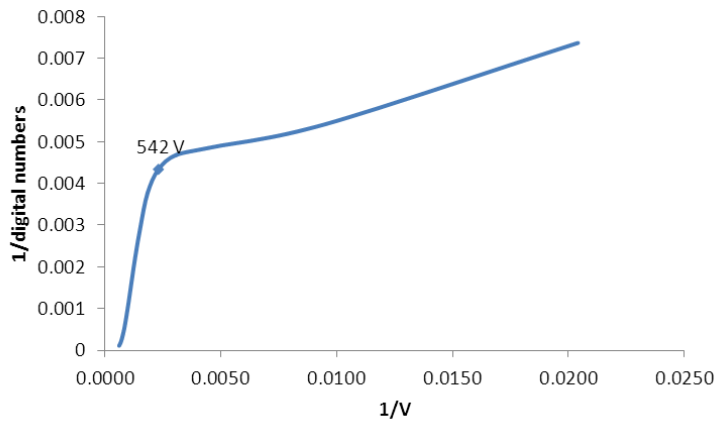


Figure E-2: Jaffé diagram for a MWPC and 6 MeV electron radiation

The Jaffé diagram clearly shows that the ionisation region ends around 500 V to 540 V. As the instantaneous intensity of the electron beam from the linear accelerator is higher than that of the x-ray beam, the proportionality region would start at higher voltages. Therefore 500 V were chosen as applied voltage for the measurements with electron beams.

Figure E-3 and Figure E-4 show the measured beam profiles of the electron beam in x- and y-direction. The FWHM of the fitted Gauss function is 27 mm in x-direction and 25 mm in y-direction. The centre of gravity is at -1.9 mm in x-direction and -4.5 mm in y-direction. As the measurements were conducted without primary or secondary scattering foil the beam profile is of Gaussian shape.

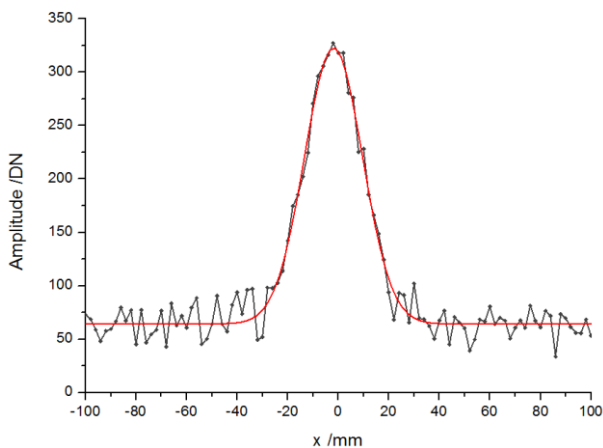


Figure E-3: Beam profile in x-direction (grey line) and fitted gauss function (red line)

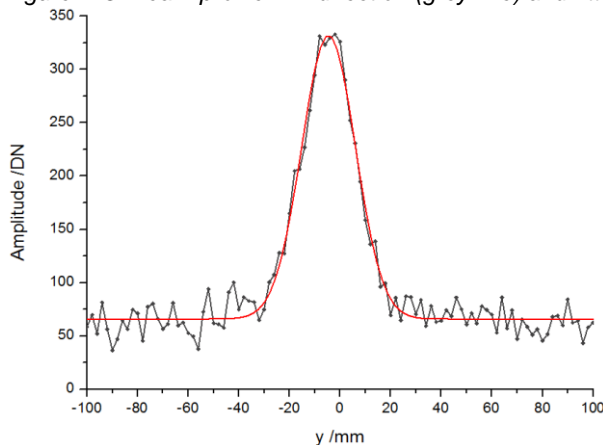


Figure E-4: Beam profile in y-direction (grey line) and fitted gauss function (red line)

F Prototype Two

Details on the construction of the second prototype are given on pages F-2 to F-4.

On pages F-5 to F-8 the measured peak values and the measured area under the curve for 0.15 mGy, 0.38 mGy, 0.83 mGy and 1.67 mGy per pulse in D_{\max} at SSD 100 for the investigated gases are shown. From these measurements the beginning of the **plateau region** was determined as given in table 7-5.

On pages F-9 to F-17 the effect of **backscattered radiation** to the chamber volume in the linac head is shown.

After the measurements the **wires** were **investigated**, see page F-18.

Ideas for improvement of the second prototype are given on page F-19.

Construction of Prototype 2

All assembly steps were performed in a clean room by an experienced Siemens employee.

Figure F-1 shows the basic layout. The HV layer (yellow foil in dark green layer) is situated in the middle of the chamber. Symmetrically, two signal planes (light green) are stacked on bolts. Consecutively, shielding planes (light yellow) are mounted on the bolts. The casing (grey) has a Kapton window (yellow) where the beam hits the chamber. For filling the chamber with different gases, gas inlet (yellow connector with brown tube) and outlet passages (filled with yellow plug) are added to the housing. Each volume can be filled separately. The outer diameter is 160 mm x 160 mm, the central area for beam sensing is 76 mm x 76 mm.

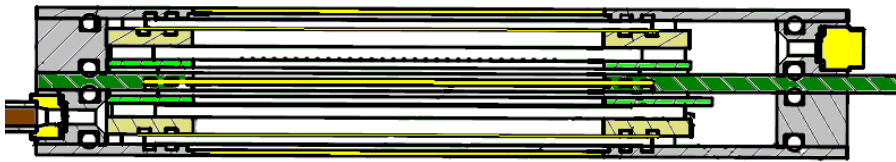


Figure F-1: Sectional drawing of prototype 2

The core of the chamber is the HV board in the middle. It consists of a 3.2 mm thick PCB board which routes the signals from the signal planes to the SMC connectors outside the housing and the high voltage from the external connector to the respective internal sites. Figure F-2 shows the two layers in which signals and HV are routed.

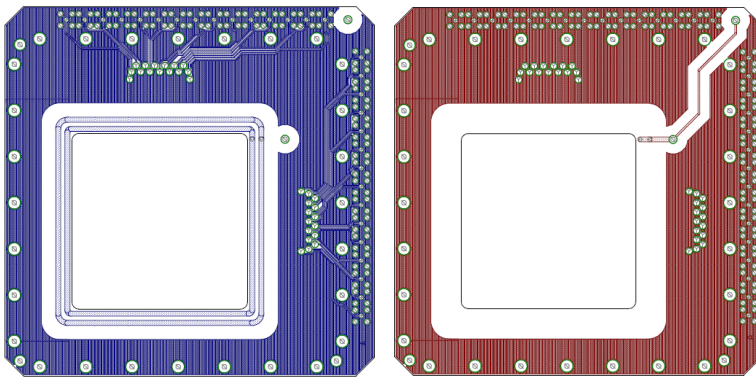


Figure F-2: Internal layers of HV board of prototype 2 (left: signal layer; right: HV-layer)

The HV layer consists of three parts. First of all, the 25 μm Kapton foil which is coated on both sides with aluminium is glued to a small frame which is afterwards glued into the HV plane. Each time the Al-coating connection to the frame is reinforced by conductive silver. Figure F-3 illustrates the layout of the HV layer. The Al-layer is connected to HV on one side from the HV PCB board, and through the small frame from the other side. The connection point on the small frame is connected by conductive silver to a through-hole in the HV board. Figure F-3 shows on the right the Kapton adhesive tape which is put on the conductive silver layer to prevent the HV on this conductive silver layer to arc to the signal wires. After insertion of the HV layer, the bolts for mounting the signal and ground layer were glued into the HV board.

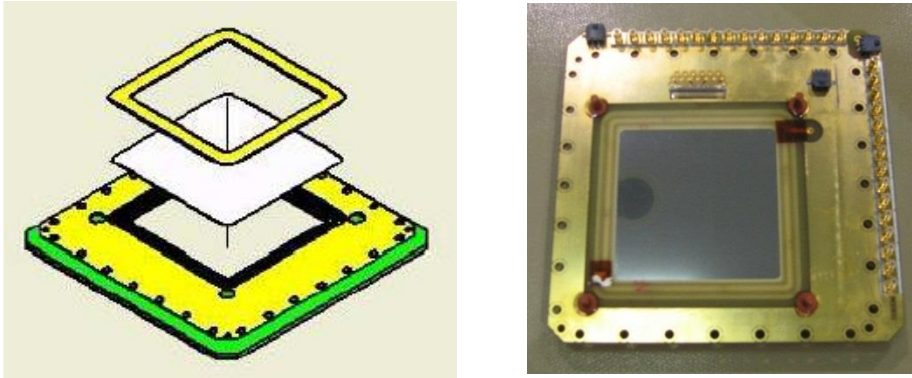


Figure F-3: HV layer of prototype 2. Left: setup of HV board with insert of HV-foil and frame. Right: photo of HV board with bolts (red), connectors and HV connection to frame coated by Kapton adhesive tape

A signal plane consists of 38 parallel gilded tungsten wires with 100 μm diameter and 2 mm distance between the wires. Figure F-4 shows such a signal plane. Each channel consists of two wires, which gives a better sampling as shown in chapter 4.3.1.4. In total 19 channels are available. Due to financial restrictions, the electronic readout was limited to 32 channels, so that only 15 channels are read out per plane. The signal plane is connected to the HV board by a spring connector.

The wire planes are wired with a nominal wire tension of 150 cN and glued to the wire frame (laid out and manufactured by straschu GmbH, Stuhr, Germany). After the glue hardened for at least eight hours, the wires were soldered to the wire frame and cut at the edges of the glue groove.

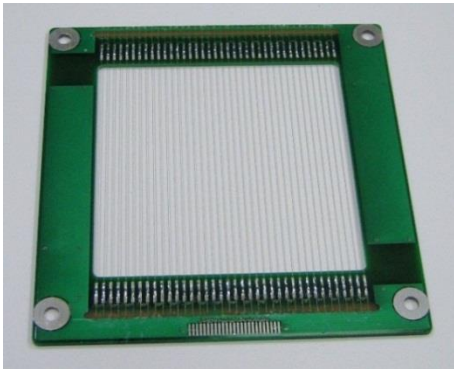


Figure F-4: Signal plane of prototype 2

The assembling of the chamber started on the side on which the smaller HV frame was glued in. On the other side, an aluminium frame was put under the chamber and kept in place by three bolts at the edges of the chamber. Figure F-5 shows some of the building elements.

A signal plane is stacked on the bolts without spacer rings as the base of the bolts stick out of the plane by approximately 1 mm. The signal planes can be mounted with the wires face up or down. For the first measurements, the wires faced outwards, i.e. away from the HV plane. This results in a distance of 4.2 mm between wires and HV. For the following measurements, the wires faced the HV, resulting in 2.7 mm between wires and HV.

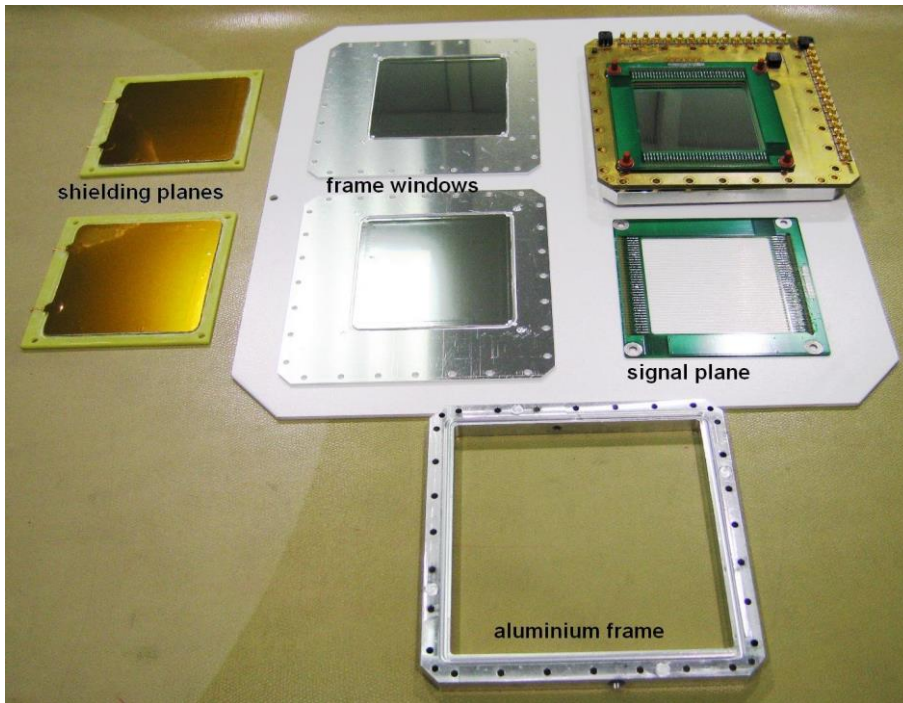


Figure F-5: Building elements of prototype 2

Following the signal plane, spacer rings with 1 mm thickness (made from PVC instead of PEEK due to material availability) are stacked on the bolts, followed by a shielding plane from prototype 1. The foils were renewed for prototype 2. The shielding plane is then connected to the ground socket. Finally, spacer rings with a total thickness of 3 mm are mounted on the bolts. For this side of the chamber it was shown in the first measurements that 3 mm spacer rings are not sufficient. Therefore one layer of 1 mm spacer rings was replaced by 1.5 mm spacer rings after the first measurements. Now the other aluminium frame is put on the chamber, curved washers and the sealing ring are put in the respective places. Afterwards, the frame window is fixed on the chamber by 28 screws. These screws also fix the lower frame to the chamber.



Finally, the chamber is turned upside down and on the other side the layers are stacked accordingly. The chamber is sealed the same way and 28 shorter screws fix the frame window to the aluminium frame.

For the gas supply a spring washer and sealing ring were put in each gas supply passage. Copper tubes with soldered brass thread were screwed in one of the holes for each gas volume. The other two holes are closed with a brass blind plug when filling the chamber. Figure F-6 shows the gas plug which was mounted on the copper tubes for filling the chamber with different gases to ease gas exchange. For the performance measurements in the linac head the copper tubes were squeezed.

Figure F-6: Gas supply of prototype 2 for measurements with different gas fillings

Plateau Region

0.15 mGy per pulse

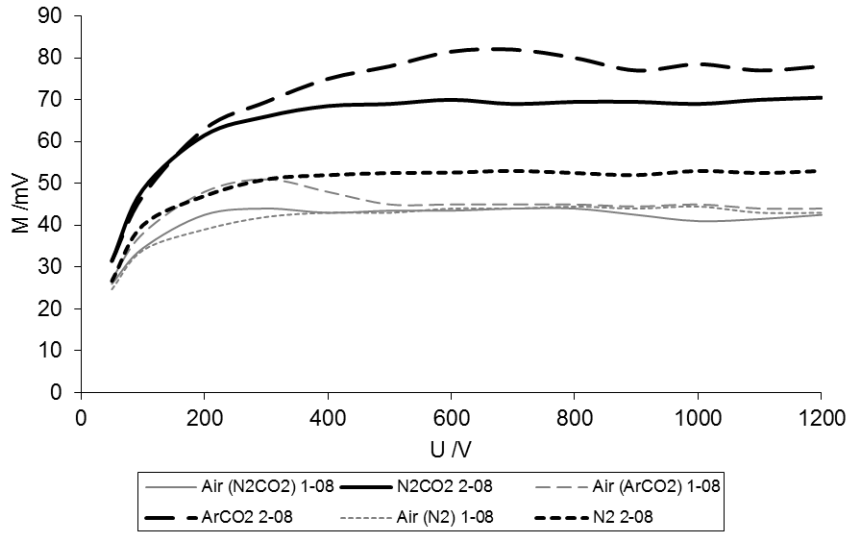


Figure F-7: M-U diagram for 0.15 mGy/pulse in D_{max} at SSD100; M = peak value

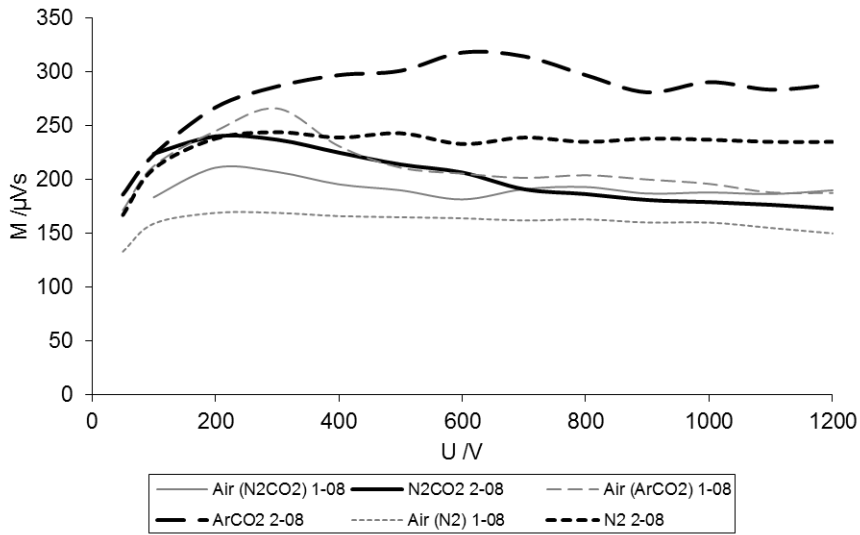


Figure F-8: M-U diagram for 0.15 mGy/pulse in D_{max} at SSD100; M = area under the curve

0.38 mGy per pulse

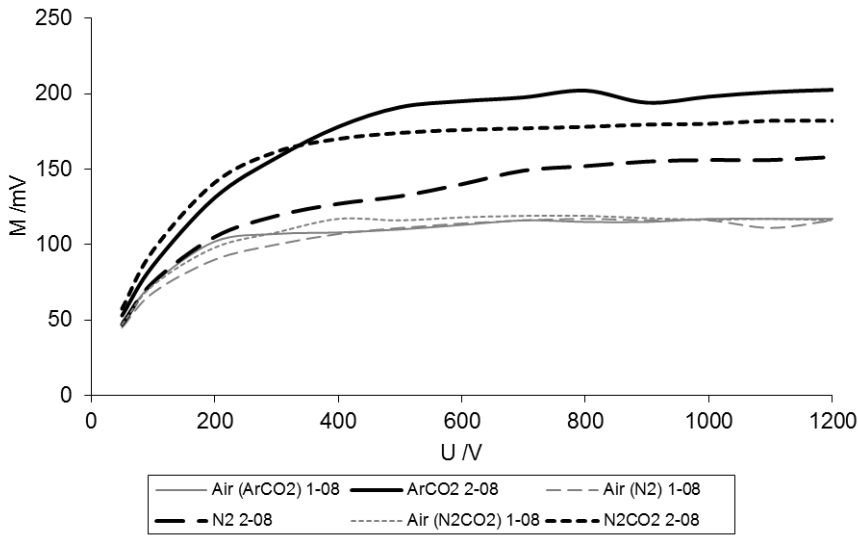


Figure F-9: M-U diagram for 0.38 mGy/pulse in D_{max} at SSD100; M = peak value

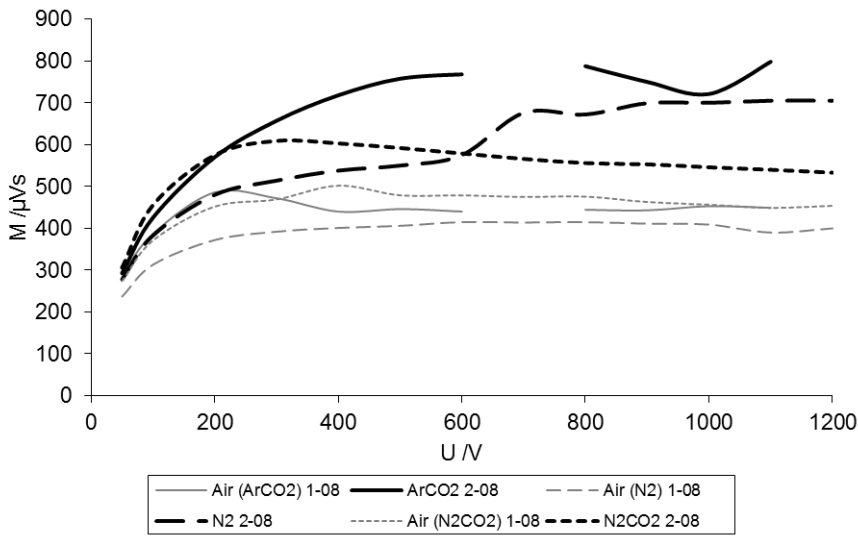


Figure F-10: M-U diagram for 0.38 mGy/pulse in D_{max} at SSD100; M = area under the curve

0.83 mGy per pulse

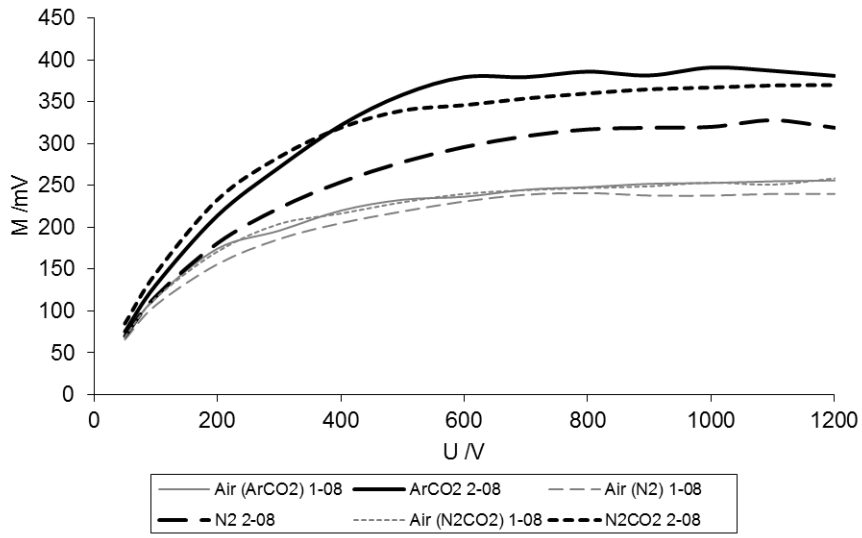


Figure F-11: M-U diagram for 0.83 mGy/pulse in D_{max} at SSD100; M = peak value

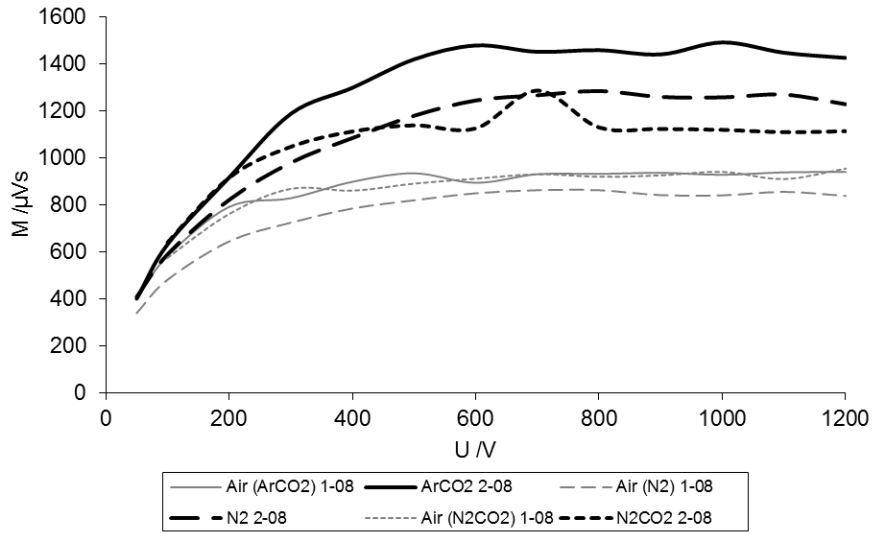


Figure F-12: M-U diagram for 0.83 mGy/pulse in D_{max} at SSD100; M = area under the curve

1.67 mGy per pulse

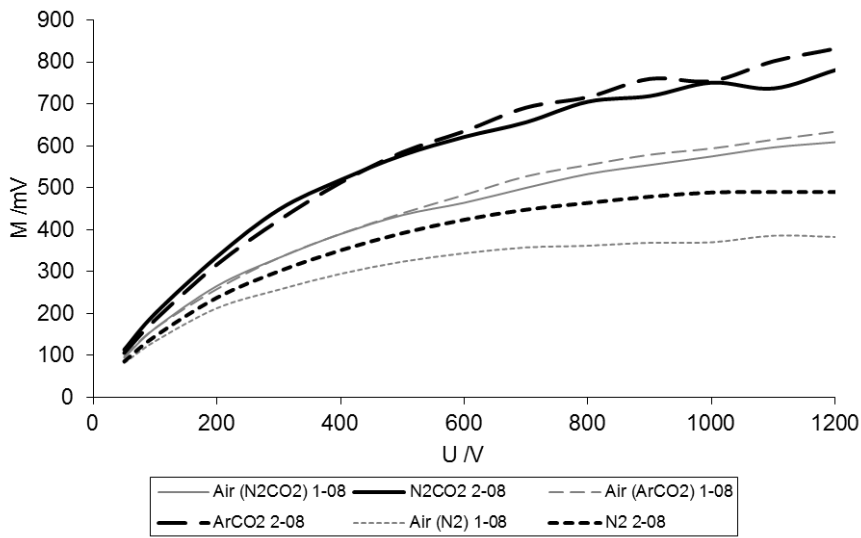


Figure F-13: M-U diagram for 1.67 mGy/pulse in D_{max} at SSD100; M= peak value

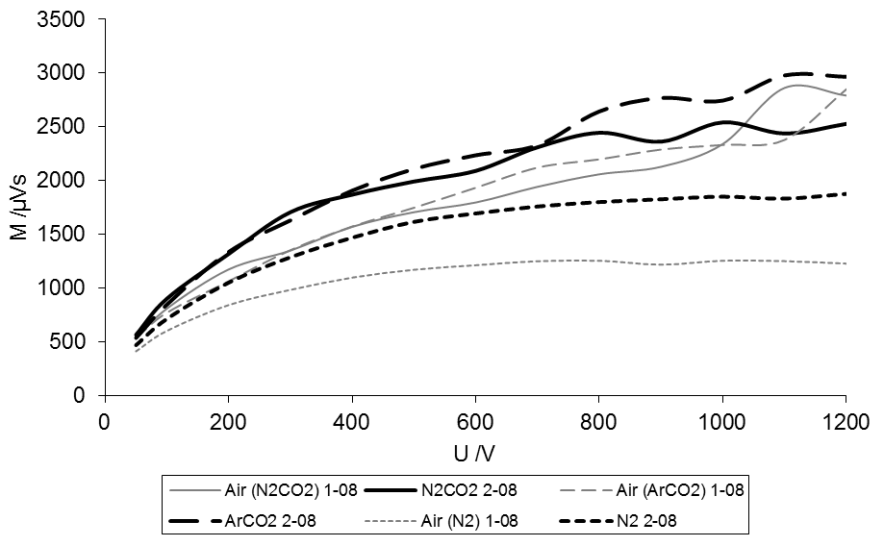


Figure F-14: M-U diagram for 1.67 mGy/pulse in D_{max} at SSD100; M= area under the curve

Backscatter

6 MV LDR

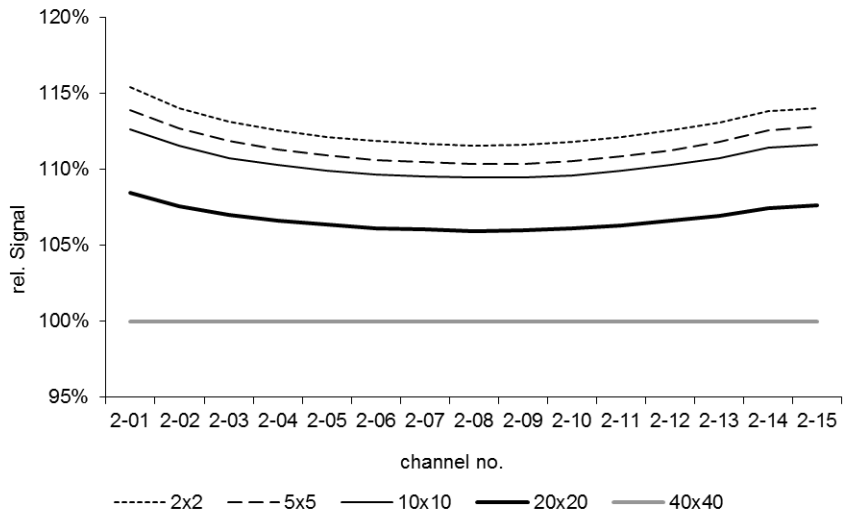


Figure F-15: Relative signal for 6 MV LDR for varying field size

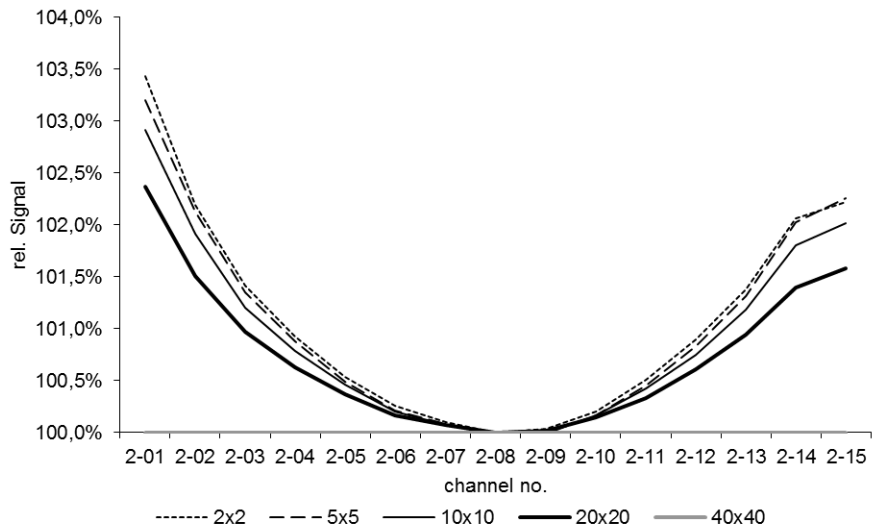


Figure F-16: Signal for 6 MV LDR normalized to central channel for varying field size

6 MV HDR

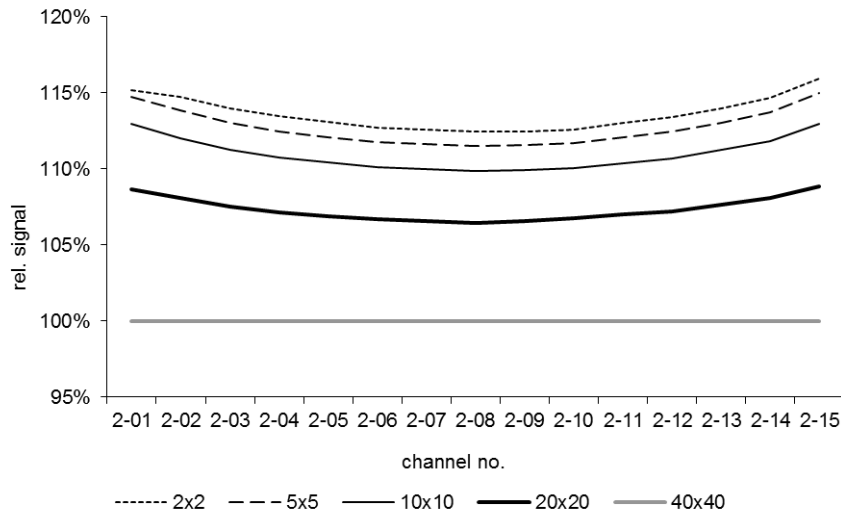


Figure F-17: Relative signal for 6 MV HDR for varying field size

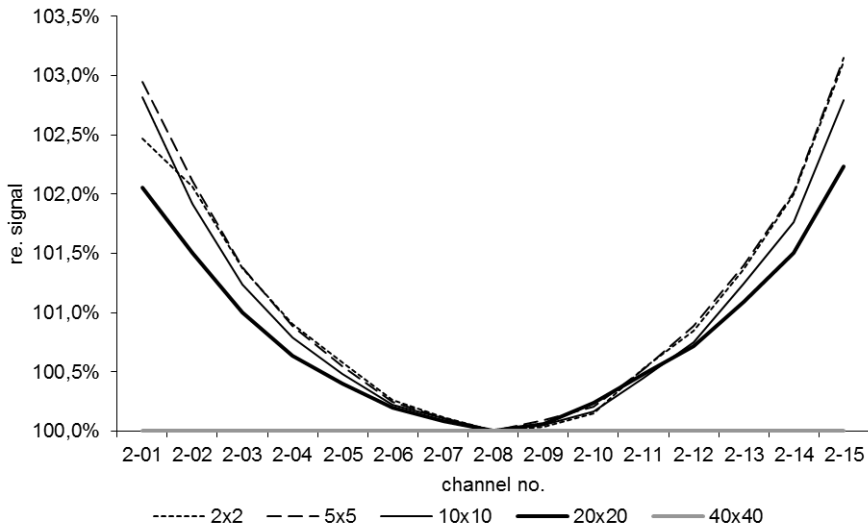


Figure F-18: Signal for 6 MV HDR normalized to central channel for varying field size

23 MV LDR

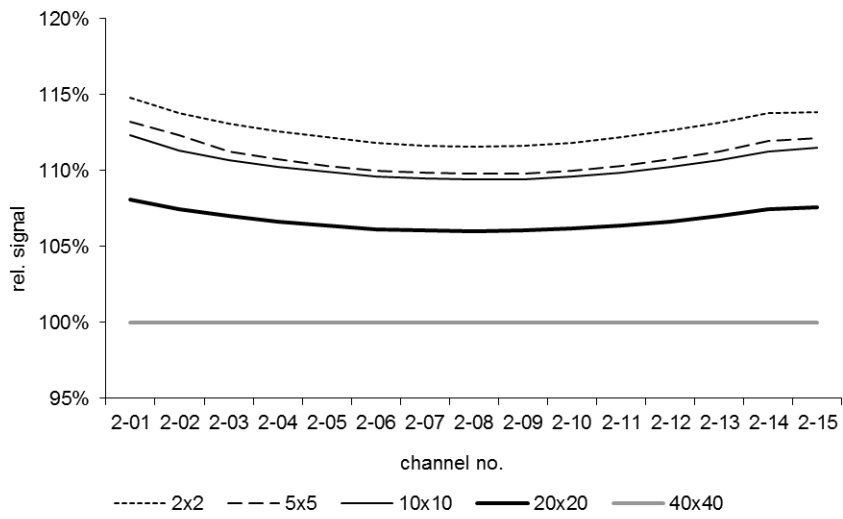


Figure F-19: Relative signal for 23 MV LDR for varying field size

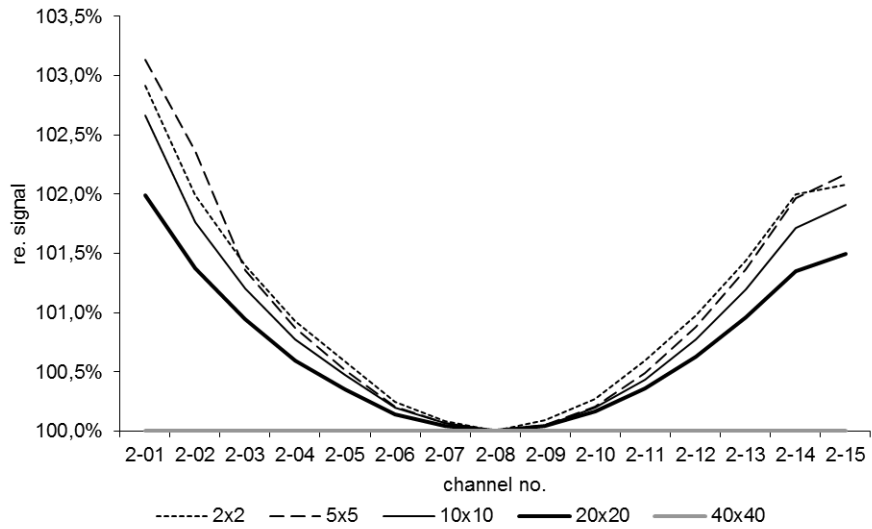


Figure F-20: Signal for 23 MV LDR normalized to central channel for varying field size

7 MV UF LDR

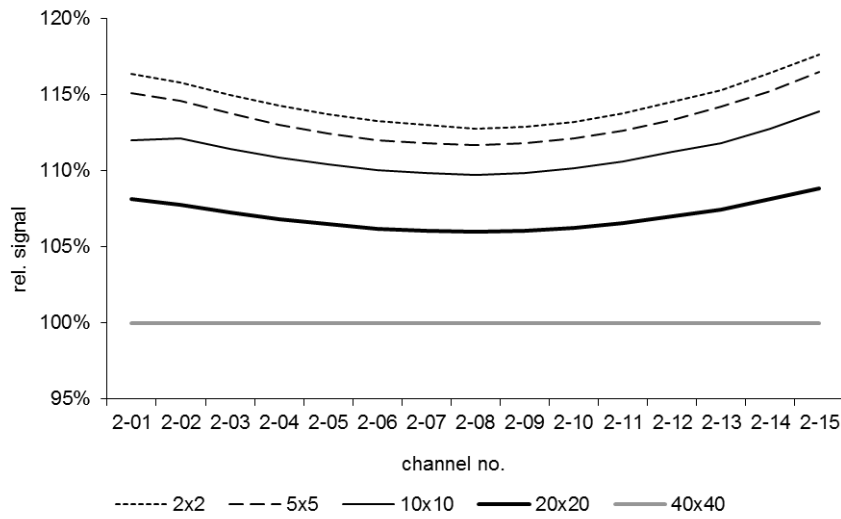


Figure F-21: Relative signal for 7 MV UF LDR for varying field size

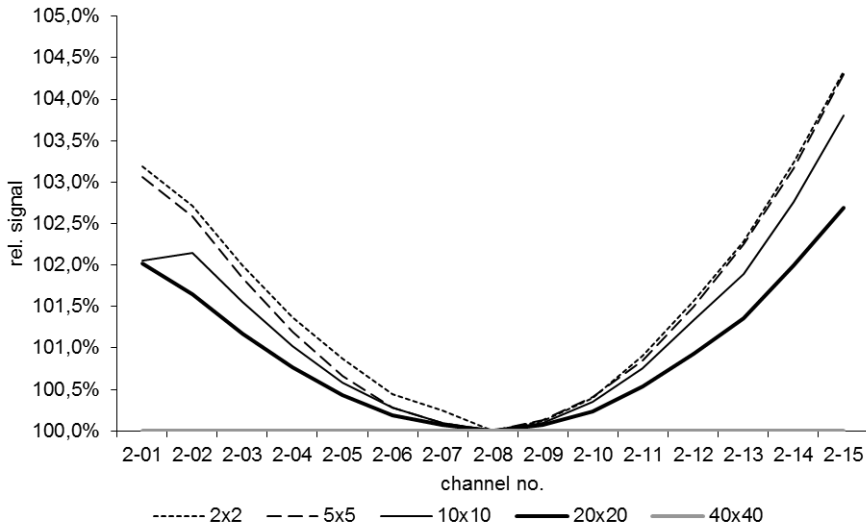


Figure F-22: Signal for 7 MV UF LDR normalized to central channel for varying field size

7 MV UF HDR

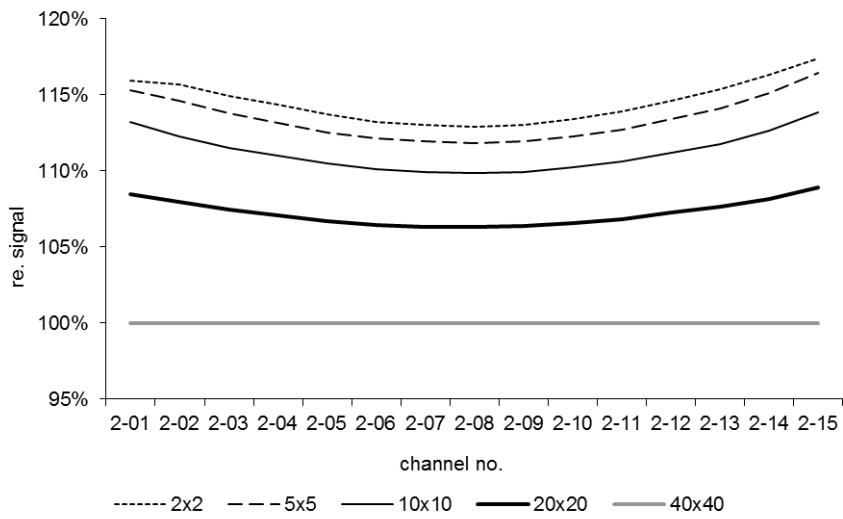


Figure F-23: Relative signal for 7 MV UF HDR for varying field size

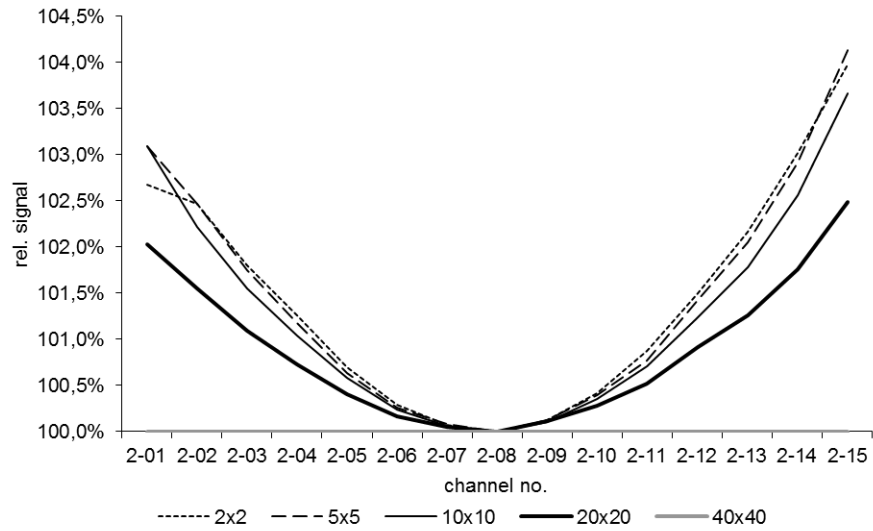


Figure F-24: Signal for 7 MV UF HDR normalized to central channel for varying field size

17 MV UF LDR

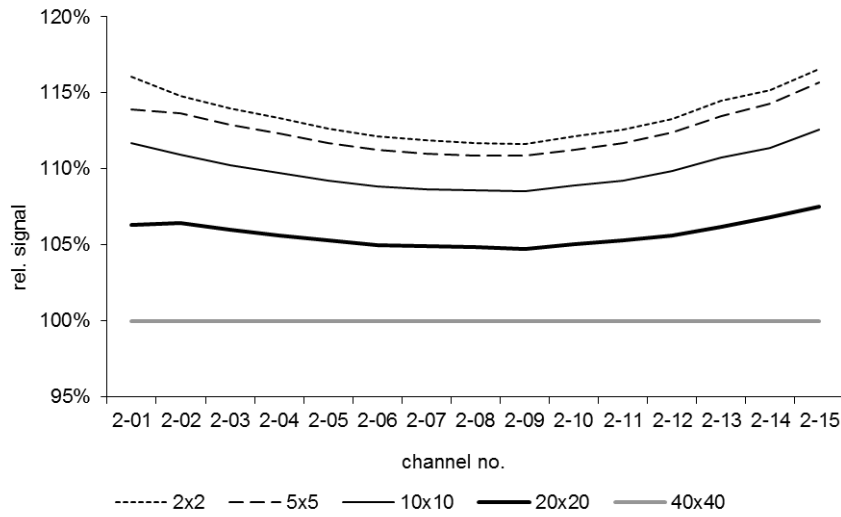


Figure F-25: Relative signal for 17 MV UF LDR for varying field size

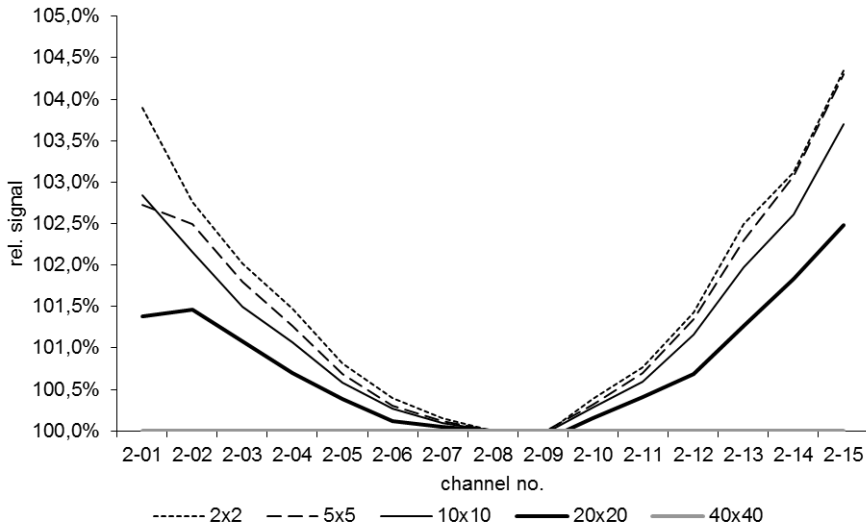


Figure F-26: Signal for 17 MV UF LDR normalized to central channel for varying field size

10 MeV LDR

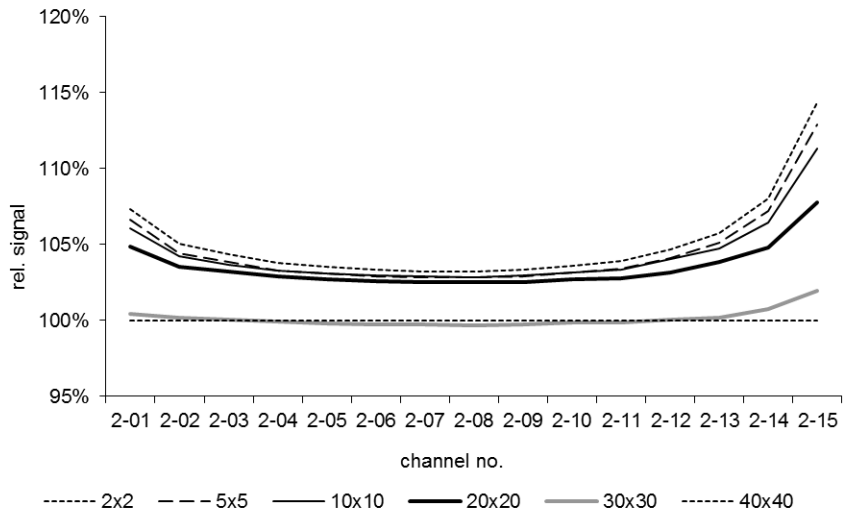


Figure F-27: Relative signal for 10 MeV LDR for varying field size

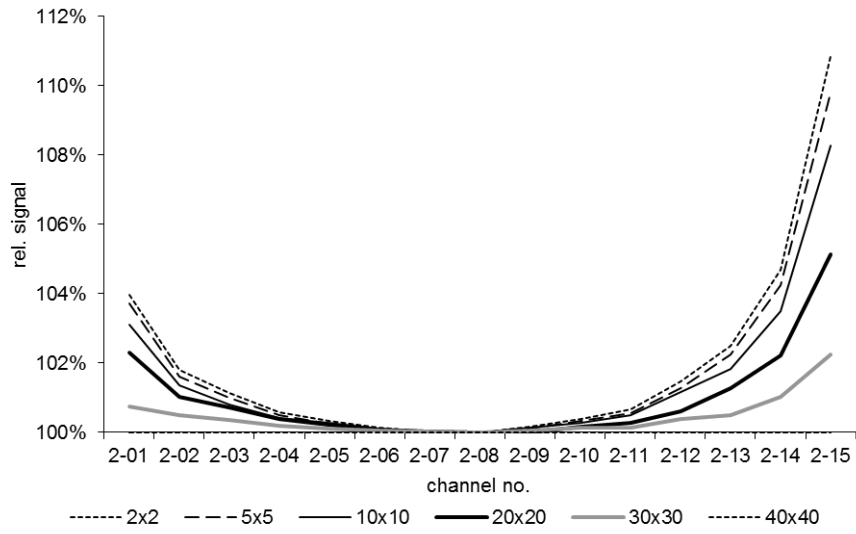


Figure F-28: Signal for 10 MeV LDR normalized to central channel for varying field size

10 MeV HDR

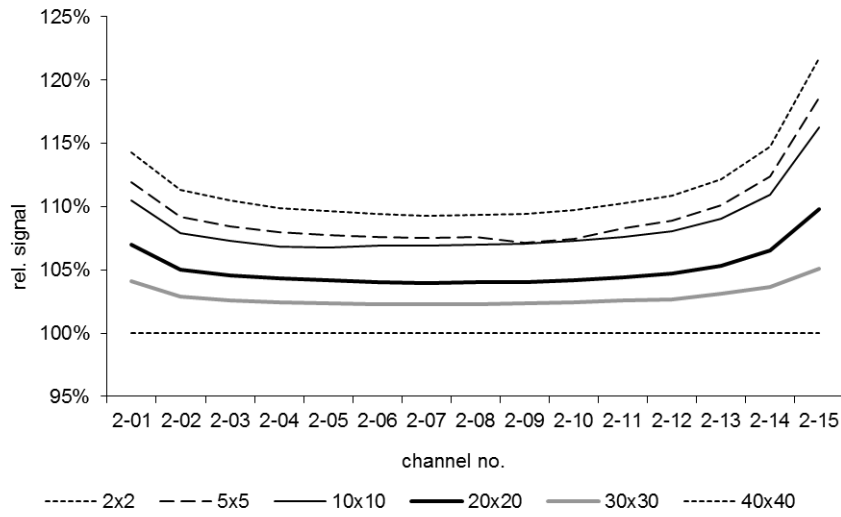


Figure F-29: Relative signal for 10 MeV HDR for varying field size

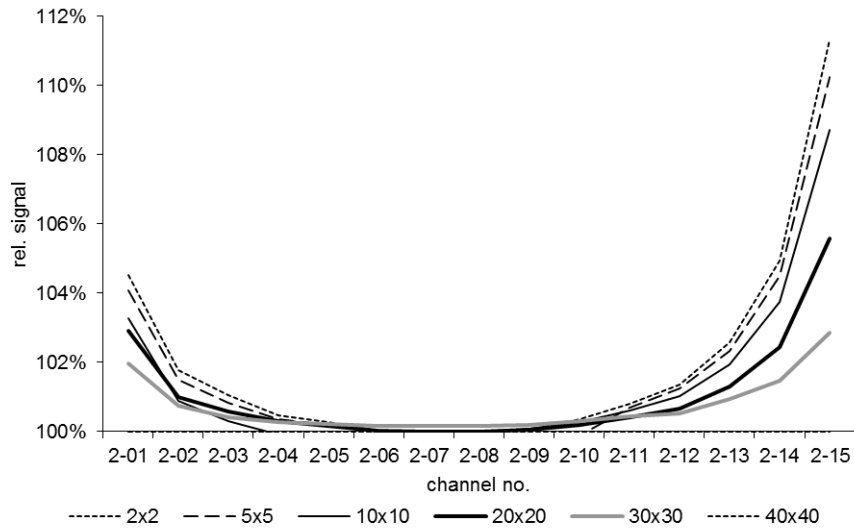


Figure F-30: Signal for 10 MeV HDR normalized to central channel for varying field size

21 MeV HDR

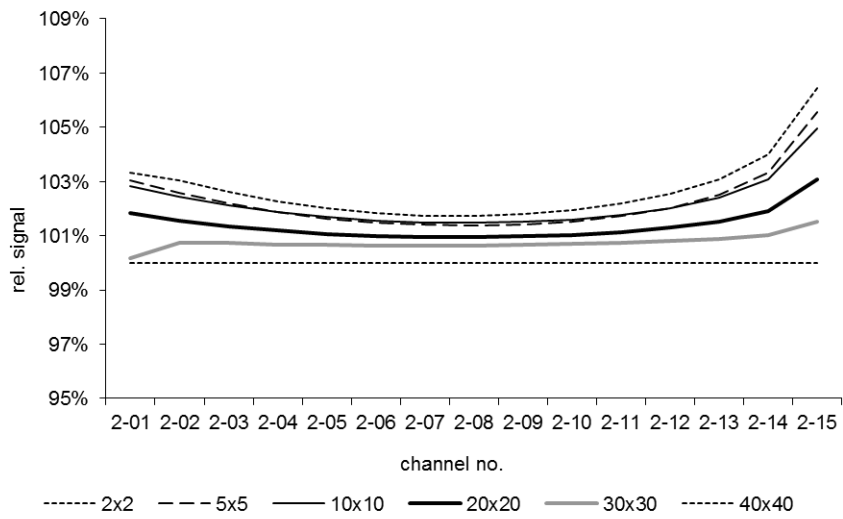


Figure F-31: Relative signal for 21 MeV HDR for varying field size

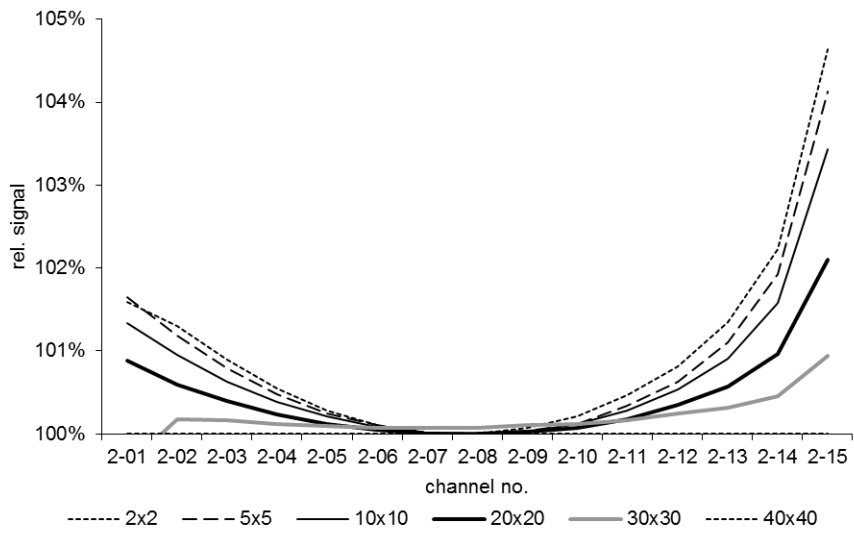


Figure F-32: Signal for 21 MeV HDR normalized to central channel for varying field size

Investigation of Wires after Measurements

After having completed the measurements, the wires of volume one were analysed under a microscope. Figure F-33 shows that on two wires (12 and 16 from the right, i.e. channels 1-04 and 1-06) a deposit of material, presumably plastic, was observed. This might be due to the use of PVC instead of PEEK for the spacer rings and the outgassing of PVC after high applied doses (see chapter 4.8).

Some wires showed a soldering not holding the wire in the flute which is not critical but might disturb the profile measurement slightly. Moreover, some wires are not fully in contact with solder. This is observed for wires of channel 1-10 and 1-15.

Figure F-34 shows that wire 10 from the left (channel 1-13) is kinked at the edge of the signal plane and a spike of wire material is observed.

These findings might explain the variations in signal for channels 1-10, 1-13 and 1-15.

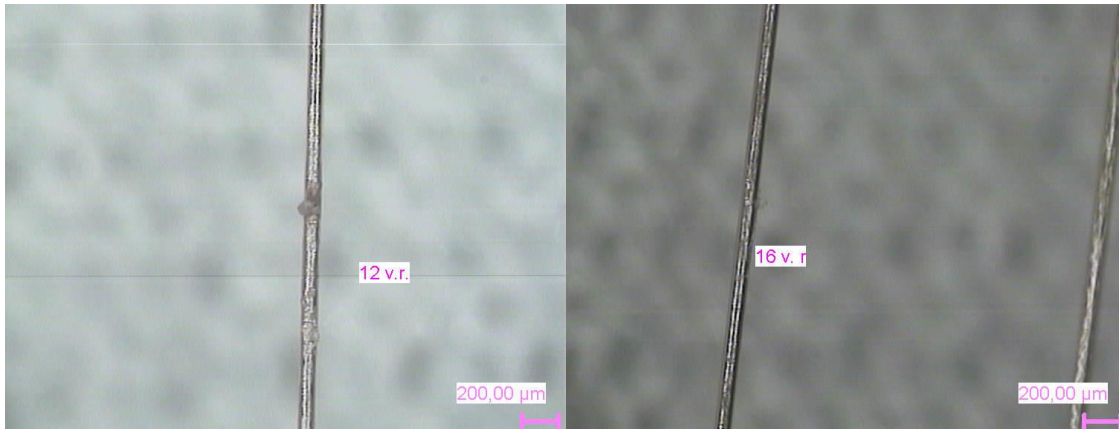


Figure F-33: Deposit on wires 12 and 16 (from right side; channels 1-04 and 1-06)

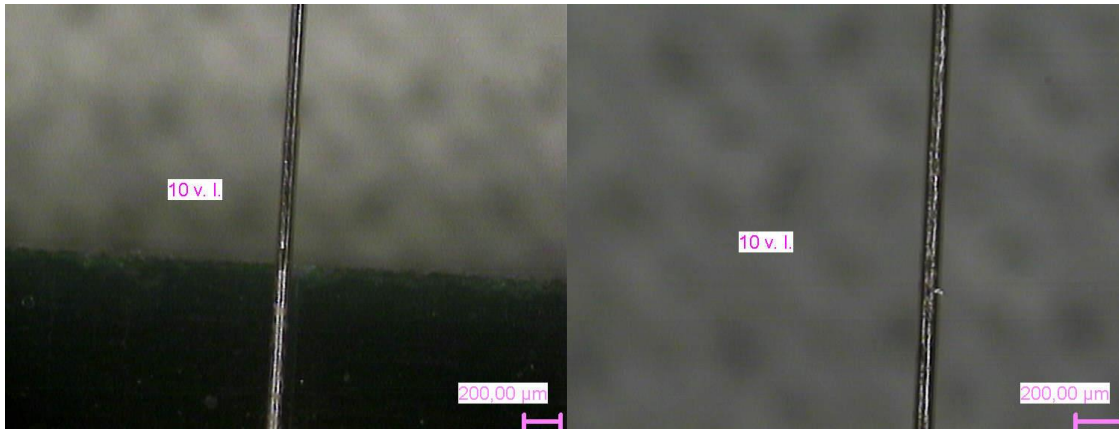


Figure F-34: Kink and spike on wire 10 from the left side (channel 1-13)

Ideas for Improvement

During the construction of the second prototype several ideas for improvement came up. First of all, the second prototype is quite large. As in a future design the gas will not be exchanged, the design of the gas inlets can be different to reduce the height. The gas inlets could be for example on the top and bottom and not on the sides and be plane with the chamber after sealing. Moreover, the first ground plane is not necessary as the casing is grounded, too. Therefore the total height could be reduced to

$$h_{\text{new}} = h_{\text{HVlayer}} + 2 \times h_{\text{ionisation volume}} + 2 \times h_{\text{signal plane}} + 2 \times h_{\text{space}} + 2 \times h_{\text{frame}} = \\ 3.2 \text{ mm} + 2 \text{ mm} + 2.8 \text{ mm} + 2 \text{ mm} + 4 \text{ mm} = 14 \text{ mm}$$

To reduce the dimensions in x and y direction, the signal, HV and ground cables could be directly mounted and not via SMC connectors. Moreover, as no ground connection in the gas volume is necessary, the frame dimensions could be reduced to the outer dimensions of the signal planes plus connector to HV plane.

In the clean room while assembling the chamber, it was proposed that the bolts should be threaded in the future to be able to thoroughly fix the planes with a screw nut. Moreover, the glue groove for the frame window should be replaced by a plane glue area.

The spacer rings and bolts should be made from PEEK as initially planned, as deposits on some wires might be due to outgassing PVC.

The wire tension ought to be around 100-120 cN, as the wire is brittle. The pad structure on the wire frame should be higher than the current 150µm and lead-free. Grooves should be added to the design on both sides of the pad structure to glue the wires, as well as an edge to cut the wires.

Glossary and Abbreviations

CAX	Central axis
Closed loop	Normal operating mode of linac in which the dose rate is controlled via a feedback loop that keeps the applied dose rate at the specified value
Crossplane	Direction in radiation field perpendicular to the direction of the waveguide
Dose	Amount of radiation, per unit mass, to be delivered to a target or identified structure
D ₁₀	Percentage of ionisation, as compared to the maximum dose, at 10 cm depth in water
D _{max}	Depth of maximum dose in water (10 cm x 10 cm field)
DPP	Dose per pulse
Field size	Separation of the 50% dose level points on the profile
Flatness	see chapter 4.1.2
Gantry	Moving part of the linac that contains the waveguide and the target
Inplane	Direction in radiation field parallel to the direction of the waveguide
Linac	Linear accelerator
Linearity	The maximum deviation (expressed in %) of the measured absorbed dose and the value of the dose monitor units from the ideal linear relationship as described in the formula: $D = S \cdot U$ where D is the absorbed dose, S is the proportionality factor and U is the value of the dose monitor unit
Monitor unit	Measure for delivered dose. Primary ionisation chamber is adjusted to read 1.00 monitor unit per 1 cGy of delivered dose using a suitable dosimetry protocol. Setup: SSD 100cm, depth: D _{max} , field size 10 cm x 10 cm in water
MU	Monitor unit
Open loop	Operating mode of linear accelerator in which the applied dose rate is not controlled; not used for patient treatment
prf	Pulse repetition frequency
Repeatability	A measure of the ability to achieve a commanded response over a series of attempts. Generally specified as the maximum deviation from the average response
Reproducibility	Repeatability measured over an extended period of time or across multiple systems
SID	Source to isocentre distance
SSD	Source to surface distance
Symmetry	see chapter 4.1.2
UF	Unflat

Table of Figures

Figure 1-1: Potential errors in beam symmetry and flatness for flattened beams: (a) correct beam direction and divergence, (b) tilted incident electron beam, (c) displaced incident electron beam, (d) divergent beam (adapted from [Krieger 2005]).....	2
Figure 1-2: Potential errors in beam symmetry and flatness for unflattened beams: (a) correct beam direction and divergence, (b) tilted incident electron beam, (c) displaced incident electron beam, (d) divergent beam (adapted from [Krieger 2005]).....	3
Figure 2-1: Pulse shape dependence on RC	9
Figure 2-2: Electric field of a MWPC	10
Figure 2-3: Siemens photon chamber (left) and segmentation of electrode two (right).....	14
Figure 2-4: Siemens electron chamber (left) and segmentation of electrode two (right).....	15
Figure 2-5: Schematic cross-section of Varian mica chamber (adapted from [Duzenli, McClean and Field 1993])	15
Figure 2-6: Schematic cross-section of Varian Kapton chamber (adapted from [Duzenli, McClean and Field 1993])	15
Figure 2-7: Segmentation of Varian chamber (adapted from [Chapman 2005])	16
Figure 2-8: Segmentation of the Elekta dose monitor chamber (adapted from [Barth 2007])	16
Figure 2-9: Schematic of chamber with two electrodes (adapted from [Taumann 1984]).....	17
Figure 2-10: Schematic of chamber with four inner (I1-I4) and four outer segments (O1-O4) (adapted from [McIntyre 1974])	17
Figure 2-11: Schematic of chamber with strip electrodes. left: electrode 1 with segments e11 to e14; right: electrode 2 with segments e21 to e24 (adapted from [Boux 1976])	17
Figure 2-12: Segmentation of liquid filled chamber of German Research Cancer Centre (adapted from [Hofmann 2003])	18
Figure 2-13: Schematic drawing of a linear accelerator head	20
Figure 3-1: Simulated linac head with scoring planes; right: 6 MV photon; left: 17 MeV electron.....	24
Figure 3-2: Energy fluence vs. position behind the dose chamber for 6 MV beams.....	25
Figure 3-3: Energy fluence vs. position behind the dose chamber for 15 MV beams...	26
Figure 3-4: Energy fluence per incident particle behind the dose chamber for 6 MV beams	26
Figure 3-5: Energy fluence vs. position behind the dose chamber for 6 MV backscattered radiation	27
Figure 3-6: Energy fluence vs. position of radiation scattered back to monitor chamber from Y-jaws, MLC or reticle for a 6MV beam.....	27
Figure 3-7: Energy fluence vs. position of radiation scattered back to monitor chamber from Y-jaws, MLC or reticle for a 15MV beam.....	28
Figure 3-8: Dosimetry electronics	29
Figure 3-9: Set-up for evaluation of current dose monitor chambers	30
Figure 3-10: Foil chamber signals for 1 MU at 6 MV UF.....	31
Figure 3-11: Foil chamber signals for 1 MU at 6 MeV	31
Figure 3-12: Backscatter to Monitor 1	32
Figure 3-13: Backscatter to segments.....	32
Figure 3-14: Sum of dose chamber voltage pulses per charge at isocentre for 1 MU to 10 MU.....	33
Figure 3-15: Simulated beam profile of a 6 MV photon beam scored at chamber position non-tilted (black line) and tilted by 1° (grey line)	34

Figure 3-16: Simulated beam profile of a 17 MeV electron beam scored at chamber position, non-tilted (black line) and tilted by 1° (grey line).....	35
Figure 4-1: Fourier transformation of a continuous (top), sampled (middle) and undersampled (bottom) signal.....	39
Figure 4-2: Schematic diagram of beam symmetry and flatness detection by current Siemens chamber	39
Figure 4-3: Beam profiles in chamber plane of incident radiation for 6 MV and 6 MV UF (top) and 6 MeV and 17 MeV (bottom) beams	41
Figure 4-4: Measured 6 MV beam profiles with and without flattening filter	42
Figure 4-5: X-Y scatter plot of 6 MV beam. Red lines indicate the position of wires on central beam axis and at the edge of the radiation field	43
Figure 4-6: Sampling principle of a dirac comb	45
Figure 4-7: Fourier spectra of Gaussian distribution with FWHM=75mm.....	45
Figure 4-8: Sampling of a Gaussian profile with a dirac comb with sampling distance $T = 25.0$ mm (top), $T = 10.0$ mm (middle) and $T = 5.0$ mm (bottom).....	47
Figure 4-9: Induced current caused by a pencil beam incident at $x = 0$ mm	48
Figure 4-10: Sampling principle of a wire chamber	49
Figure 4-11 Film exposure, 3D profile and projected profiles in x- and y-direction of a 6 MV photon beam at the position of the chamber carriage.....	49
Figure 4-12: Sampling of a 6 MV photon beam film exposure profile with $T=4.0$ mm in the inner 7.5 cm of the radiation field and reconstruction without (top) and with (bottom) subtraction of outermost signal	50
Figure 4-13: Sampling of measured profile of a 6 MV flattened photon beam with wires with Gaussian transfer function with $T = 9.2$ mm	51
Figure 4-14: Sampling principle of multi-wire channels	51
Figure 4-15: Sampling of measured profile of a 6 MV flattened photon beam with two wires with Gaussian transfer function per channel with $T = 9.2$ mm	52
Figure 4-16: Film exposure of a 15 MeV electron beam at the position of the chamber carriage.....	52
Figure 4-17: Sampling of measured profile of a 6 MV flattened photon beam with two wires with Gaussian transfer function per channel with $T = 3.6$ mm	53
Figure 4-18: Film exposure of a 6 MV photon beam (left) and the same beam with homogeneous background (right) at the position of the chamber carriage.....	54
Figure 4-19: Projected profiles of film exposure and hypothetical film exposure with homogenous background of a 6 MV photon beam at the position of the chamber carriage.....	54
Figure 4-20: Original and by 10% tilted profile of an 6 MV photon beam.....	55
Figure 4-21: Difference between a symmetric profile and a profile with 100.73 % symmetry (blue line), the respective sampled values (black) and interpolated profiles (green) for sampling distances of $T = 10.0$ mm (top) and $T = 4.0$ mm (bottom).....	56
Figure 4-22: Sampling of measured and tilted profile of a 6 MV flattened photon beam with a symmetry of 107.51 % with two wires with Gaussian transfer function per channel with $T = 3.6$ mm	57
Figure 4-23: Ion velocity in a wire chamber with 1000 V applied to the electrodes, wire length $l = 7$ cm, wire spacing $s = 3$ mm, gap size $d = 4$ mm and at position $x = 0$	59
Figure 4-24: Total number of electron-ion pairs per centimetre in different filling gases (calculated from data from [Berger, et al. 2009] and [Kolanoski 2004])	61
Figure 4-25: Chamber geometry and simulation parameters for Garfield simulations	65
Figure 4-26: Radiation resistance of foil materials. For meaning of abbreviations see table 4-16 [Domininghaus 1998] and [Bay. Forschungsverbund Materialwissenschaften 2007].....	67
Figure 4-27: Total stopping power for polyimide (dark grey), polyethylene-terephthalate (grey) and polycarbonate (light grey) [NIST 2009]	69

Figure 4-28: Energy fluence at isocentre of a 6 MeV beam for different combined thicknesses of entrance and exit foil	70
Figure 4-29: Energy fluence vs. position at isocentre of a 6 MeV beam for different combined thicknesses of entrance and exit foil	70
Figure 4-30: Total attenuation with coherent scattering for different entrance and exit foil thicknesses.....	71
Figure 5-1: Secondary foil.....	77
Figure 5-2: Simulated foil chamber.....	78
Figure 5-3: Detail of simulation set-up for a 6 MV flat photon beam with secondary scattering foil in place	78
Figure 5-4: Difference in energy fluence between a simulated 6 MV flat photon beam without and with secondary foil in beam path, scored at 100 cm SSD in air (left) and in 10 cm of water (right). Black lines indicate a 4 th order polynomial fit.....	79
Figure 5-5: Energy fluence distribution for a 6 MV flat photon beam at 100 cm SSD with silicon (dark grey) or polyimide (light grey) mirror	80
Figure 6-1: Layout of prototype 1 [Schirmer 2010].....	81
Figure 6-2: Photo of prototype 1	81
Figure 6-3: Displacement of wires of prototype 1	82
Figure 6-4: Prototype 1 with MWPC electronics	82
Figure 6-5: Set-up of prototype 1 at linear accelerator (left: chamber in head; right: electronics on accessory holder).....	83
Figure 6-6: Signal levels of channels of prototype 1 at x-ray test stand	84
Figure 6-7: Scan of the x-ray beam from the test stand with a single channel of prototype 1	85
Figure 6-8: Scan along a central wire and a wire at the edge of the first prototype at the x-ray test stand	85
Figure 6-9: Measured values with prototype 1 at 25 MV	86
Figure 6-10: Measured values with prototype 1 at 6 MV (black line) and profile measured with Gafchromic EBT film (red line)	86
Figure 6-11: Original (solid line) and steered (dashed line) signal at 25 MV; percentage deviation of these (grey line).....	86
Figure 6-12: Original (solid line) and steered (dashed line) signal at 6 MV; percentage deviation of these (grey line).....	87
Figure 6-13: Beam profile at 25 MV (black line) and average intensity (grey line).....	87
Figure 7-1: Assembled prototype 2	89
Figure 7-2: Sectional drawing of prototype 2.....	89
Figure 7-3: Signal processing for prototype 2	90
Figure 7-4: Timing for electronics of prototype 2.....	91
Figure 7-5: User interface of read-out programme.....	92
Figure 7-6: Integration time -voltage relationship for charging the capacitors of the channels of volume 1.....	94
Figure 7-7: Charging curve of IVC102 (100 pF) under pulsed radiation.....	96
Figure 7-8: Test stand for photon radiation (left) and close-up of UDC in test stand (right).....	97
Figure 7-9: Support for electron measurements with prototype 2.....	99
Figure 7-10: Signal M (peak value in mV or area in μ Vs) over varying U for d = 4.2 mm	100
Figure 7-11: Signal M (peak value in mV or area in μ Vs) over varying DPP for d = 4.2 mm and U = 1000 V	100
Figure 7-12: M-U diagram for 0.83 mGy/pulse in D_{max} at SSD100; M= peak value	101
Figure 7-13: M-U diagram for 0.83 mGy/pulse in D_{max} at SSD100; M= area under the curve	101
Figure 7-14: DPP linearity from measurements at U=1000V; M= area under the curve	102
Figure 7-15: DPP linearity (Ar-CO ₂ and N ₂ -CO ₂)	102

Figure 7-16: Measured dose pulses from oscilloscope for a dose per pulse of 0.15 mGy	103
Figure 7-17: Measured dose pulses from oscilloscope for a dose per pulse of 0.83 mGy	103
Figure 7-18: M-U diagram for electron radiation in D_{max} at SSD100. M= peak value..	103
Figure 7-19: Channel 2-08 normalized to the maximum of channel 1-08 (6 MeV).....	104
Figure 7-20: Power supply of prototype 2 during performance measurements	105
Figure 7-21: Prototype 2 in linac head (left: photon mode) and fixture for prototype 2 (right: electron mode)	106
Figure 7-22: Test set-up for photon radiation for performance measurements (left: Farmer chamber in RW3; right: StarCheck with RW3 built-up and backscatter)	107
Figure 7-23: Test set-up for electron radiation for performance measurements (left: Roos chamber in RW3; right: StarCheck with RW3 built-up	107
Figure 7-24: Film measurements in air (left) and with backscatter (right) for analysing the effect of the wires on electron radiation.....	108
Figure 7-25: Short-term stability of signals	109
Figure 7-26: Relative signal for 6 MV LDR for varying field size	109
Figure 7-27: Signal for 6 MV LDR normalized to central channel for varying field size.....	110
Figure 7-28: Variation of signal with square field size (6 MV LDR)	111
Figure 7-29: Variation of signal with field size while keeping the other direction constant at 40 cm (6 MV LDR).....	111
Figure 7-30: Relative signal for steered beams of 6 MV	112
Figure 7-31: Relative signal for steered beams of 6 MV at STC 381 (symmetric and flat beam) normalized to first measurement (STC381_1).....	113
Figure 7-32: Measured beam profiles (volume 2) for a flat (STC5200) and tilted 21 MeV beams. Signal values normalized to channel 2-07.....	113
Figure 7-33: Measured beam profiles (volume 1)	114
Figure 7-34: Profile of a 6 MV photon beam, measured with film and UDC (volume 1).....	114
Figure 7-35: Profile of a 7 MV UF photon beam, measured with film and UDC (volume 1).....	115
Figure 7-36: Profile of a 17 MV UF photon beam, measured with film and UDC (volume 1).....	115
Figure 7-37: Stability of signal from a 10 MeV beam: volume 1	117
Figure 7-38: Stability of signal from a 10 MeV beam: volume 2	117
Figure 7-39: Film and measured profile (blue line) for a 6 MV photon beam	118
Figure 7-40: Film and measured profile (blue line) for a 6 MeV electron beam	118
Figure 7-41: Film at SSD 95 with 3.5 cm RW3 backscatter (upper left film; blue line) compared to unused film (upper right film; green line) for an 6 MeV electron beam; normalized to central axis value.....	118
Figure 7-42: Stability of signal from a 10 MeV beam: volume 1. Measurement points are the averages of 5 consecutive measurements and normalized to Monday morning (see figure 7-37)	120
Figure 7-43: Change of signals from volume one (top) and two (bottom) from morning to afternoon for a 10 MeV beam	120
Figure 7-44: Stability of signal from 6 MV beam (volume 1).....	121
Figure B-1: Simulated linac head with scoring planes; right: 6 MV photon; left: 17 MeV electron.....	B-1
Figure C-1: Sampling of measured profiles of 6 MV, 6 MV UF, 15 MV and 15 MV UF photon beams (top to bottom) with one wire per channel and with sampling distances $T = 9.2$ mm, 9.0 mm, 8.8 mm and 9.0 mm, respectively	C-2
Figure C-2: Sampling of measured profiles of 6 MeV (top) and 15 MeV (bottom) electron beams with one wire per channel and with sampling distances $T = 3.0$ mm and 3.4 mm, respectively	C-3

Figure C-3: Sampling of measured profiles of 6 MV, 6 MV UF, 15 MV and 15 MV UF photon beams (top to bottom) with two wires per channel and with sampling distances $T = 9.2$ mm, 9.2 mm, 8.8 mm and 9.2 mm, respectively	C-4
Figure C-4: Sampling of measured profiles of 6 MeV (top) and 15 MeV (bottom) electron beams with two wires per channel and with sampling distances $T = 3.2$ mm.....	C-5
Figure C-5: Sampling of measured profiles of 6 MV, 6 MV UF, 15 MV and 15 MV UF photon beams (top to bottom) with two wires per channel and with sampling distances $T = 3.6$ mm, 3.6 mm, 3.6 mm and 4.0 mm, respectively	C-6
Figure E-1: MWPC.....	E-1
Figure E-2: Jaffé diagram for a MWPC and 6 MeV electron radiation	E-2
Figure E-3: Beam profile in x-direction (grey line) and fitted gauss function (red line)	E-2
Figure E-4: Beam profile in y-direction (grey line) and fitted gauss function (red line)	E-2
Figure F-1: Sectional drawing of prototype 2	F-2
Figure F-2: Internal layers of HV board of prototype 2 (left: signal layer; right: HV-layer)	F-2
Figure F-3: HV layer of prototype 2. Left: setup of HV board with insert of HV-foil and frame. Right: photo of HV board with bolts (red), connectors and HV connection to frame coated by Kapton adhesive tape.....	F-3
Figure F-4: Signal plane of prototype 2	F-3
Figure F-5: Building elements of prototype 2	F-4
Figure F-6: Gas supply of prototype 2 for measurements with different gas fillings	F-4
Figure F-7: M-U diagram for 0.15 mGy/pulse in D_{max} at SSD100; M= peak value	F-5
Figure F-8: M-U diagram for 0.15 mGy/pulse in D_{max} at SSD100; M= area under the curve	F-5
Figure F-9: M-U diagram for 0.38 mGy/pulse in D_{max} at SSD100; M= peak value	F-6
Figure F-10: M-U diagram for 0.38 mGy/pulse in D_{max} at SSD100; M= area under the curve	F-6
Figure F-11: M-U diagram for 0.83 mGy/pulse in D_{max} at SSD100; M= peak value.....	F-7
Figure F-12: M-U diagram for 0.83 mGy/pulse in D_{max} at SSD100; M= area under the curve	F-7
Figure F-13: M-U diagram for 1.67 mGy/pulse in D_{max} at SSD100; M= peak value.....	F-8
Figure F-14: M-U diagram for 1.67 mGy/pulse in D_{max} at SSD100; M= area under the curve	F-8
Figure F-15: Relative signal for 6 MV LDR for varying field size	F-9
Figure F-16: Signal for 6 MV LDR normalized to central channel for varying field size.....	F-9
Figure F-17: Relative signal for 6 MV HDR for varying field size.....	F-10
Figure F-18: Signal for 6 MV HDR normalized to central channel for varying field size.....	F-10
Figure F-19: Relative signal for 23 MV LDR for varying field size	F-11
Figure F-20: Signal for 23 MV LDR normalized to central channel for varying field size.....	F-11
Figure F-21: Relative signal for 7 MV UF LDR for varying field size	F-12
Figure F-22: Signal for 7 MV UF LDR normalized to central channel for varying field size	F-12
Figure F-23: Relative signal for 7 MV UF HDR for varying field size.....	F-13
Figure F-24: Signal for 7 MV UF HDR normalized to central channel for varying field size	F-13
Figure F-25: Relative signal for 17 MV UF LDR for varying field size	F-14
Figure F-26: Signal for 17 MV UF LDR normalized to central channel for varying field size	F-14
Figure F-27: Relative signal for 10 MeV LDR for varying field size	F-15
Figure F-28: Signal for 10 MeV LDR normalized to central channel for varying field size.....	F-15

Figure F-29: Relative signal for 10 MeV HDR for varying field size.....	F-16
Figure F-30: Signal for 10 MeV HDR normalized to central channel for varying field size.....	F-16
Figure F-31: Relative signal for 21 MeV HDR for varying field size.....	F-17
Figure F-32: Signal for 21 MeV HDR normalized to central channel for varying field size.....	F-17
Figure F-33: Deposit on wires 12 and 16 (from right side; channels 1-04 and 1-06) .	F-18
Figure F-34: Kink and spike on wire 10 from the left side (channel 1-13)	F-18

Table of Tables

Table 2-1: W-values for different gases [Kolanoski 2004]	7
Table 2-2: Parameters for calculating flattened area for photon beams (data from [IEC 60976]).....	12
Table 3-1: Resistor on G42 for flat and unflat photon beams	30
Table 3-2: Output change for steered beams.....	33
Table 3-3: Symmetry changes for steered 6 MV, 6 MV UF and 6 MeV beams	34
Table 4-1: Doses per pulse at patient plane and resulting dose at chamber and induced charge for an air-filled chamber for typical linac settings.....	43
Table 4-2: Required sampling distance T_{\max} for sampling measured profiles with wires.....	50
Table 4-3: Required sampling distance T_{\max} for sampling measured profiles with two wires per channel within $\pm 1.5\%$	52
Table 4-4: Required sampling distance T_{\max} for sampling measured profiles with two wires per channel within $\pm 0.5\%$	53
Table 4-5: Detected symmetry changes for tilted profiles of a 6 MV flattened photon beam for different sampling distances T in %.....	55
Table 4-6: Detected symmetry changes for tilted profiles of a 6 MeV electron beam for different sampling distances T in %	57
Table 4-7: Symmetry detection by UDC and Siemens photon chamber in inner 3.4 cm of radiation field	58
Table 4-8: Symmetry detection by UDC in inner 7.5 cm of radiation field.....	58
Table 4-9: Ion mobilities for filling liquids (in $\text{m}^2 \text{V}^{-1} \text{s}^{-1}$).....	60
Table 4-10: Collision stopping power dE/dx , mean energy to produce an electron-ion pair W and resulting total number of electron-ion pairs per centimetre n_t for different filling gases for a minimal ionising particle	61
Table 4-11: Number of primary electron-ion pairs [Kolanoski 2004] and resulting inefficiency	62
Table 4-12: Mobility $\mu / (10^{-4} \text{m}^2 \text{atm}/(\text{Vs}))$ of ions in gases at zero field	63
Table 4-13: Properties of typical wire materials	64
Table 4-14: Simulated electric field strengths, sag and deflection for varying wire diameter.....	65
Table 4-15: Typical values for elongation and sag for different wire materials	66
Table 4-16: Properties of foil materials [Domininghaus 1998].....	68
Table 4-17: Permeability coefficients for different gases for Kapton in ($\text{cm}^3 \text{mm}$) / ($\text{m}^2 \text{day atm}$)	71
Table 4-18: Properties of materials suited for metallisation	72
Table 4-19: Radiation resistance of materials used for ionisation chambers	73
Table 4-20: Permeability constants for nitrogen [Massey 2003].....	73
Table 7-1: Channel characteristics of electronics	94
Table 7-2: Correction factors due to gain error	95
Table 7-3: Test conditions for photon radiation (prototype 2)	98
Table 7-4: Equivalent system settings for photon radiation (prototype 2)	99
Table 7-5: Plateau region for prototype 2.....	100
Table 7-6: Measurement configurations for performance measurements.....	106
Table 7-7: Position of beam CAX in chamber	110
Table 7-8: Symmetry values at patient plane for steered beams of 6 MV	112
Table 7-9: Signal changes during the stability measurements.	116
Table B-1: Mean incident energy on the exit window for Monte Carlo simulations.....	B-2
Table B-2: Component modules and latch bits for backscatter simulations	B-2
Table D-1: Photonuclear reaction properties of some chamber materials (data from [IAEA]).....	D-1

References

- Arndt, U W, and M P Kyte. "Ionization chambers for monitoring the position and tilt of X-ray beams." *J Appl Cryst*, 2000: 986-987.
- Barth, A. *Betrachtung der Dosislinearität und Strahlhomogenität im Niederdosisbereich therapeutischer Photonen an Wanderwellenbeschleunigern*. Diploma thesis, Gießen: University of Applied Sciences Gießen-Friedberg, 2007.
- Bay. Forschungsverbund Materialwissenschaften. *Werkstoffsuche und Kompetenzsuche mit M-Line 2*. 23 March 2007. www.werkstoffe.de [accessed June 20, 2010].
- Becker, J, E Brunckhorst, and R Schmidt. "Photoneutron production of a Siemens Primus linear accelerator studied by Monte Carlo methods and a paired magnesium and boron coated magnesium ionization chamber system." *Phys Med Biol*, 2007: 6375-6387.
- Berger, M J, J S Coursey, M A Zucker, and J Chang. *Stopping-Power and Range Tables for Electrons*. 07 October 2009. <http://physics.nist.gov/PhysRefData/Star/Text/ESTAR.html> [accessed March 14, 2011].
- Berghöfer, Th, J Engler, J M Milke, and J R Hörandel. "A liquid ionization chamber as monitor in radiotherapy." *Proceedings of the 9th Conference on Astroparticle, Particle, Space Physics, Detectors and Medical Physics Applications*. Como, 2005.
- Blad, B, P Nilsson, and T Knöös. "The influence of air humidity on an unsealed ionization chamber in a linear accelerator." *Phys Med Biol*, 1996: 2541-2548.
- Boag, J W. Vol. 2, in *The Dosimetry of Ionizing Radiation*, by K R Kase, B E Bjarngard and F H Attix, 169-244. London: Academic Press, 1987.
- . "Ionization measurements at very high intensities. I. Pulsed radiation beams." *Br J Radiol*, 1950: 601-611.
- Boag, J W. *Radiation Dosimetry - Ionization chambers*. Vol. 2, in *Radiation Dosimetry*, by F H Attix and W C Roesch. London: Academic Press, 1966.
- Boag, J W, E Hochhäuser, and O A Balk. "The effect of free-electron collection of the recombination correction to ionization measurements of pulsed radiation." *Phys Med Biol*, 1996: 885-897.
- Boggula, R, et al. "Experimental validation of of a commercial 3D dose verification system for intensity-modulated arc therapies." *Phys. Med. Biol.*, 2010: 5619-5633.
- Böhm, J. "Saturation correction for plane-parallel ionization chambers." *Phys Med Biol*, 1976: 754-759.
- Boux, R. Device for monitoring the position, intensity, uniformity and directivity of an ionizing radiation beam. United States Patent 3,997,788. 14 December 1976.
- Bruggmoser, G, R Saum, A Schmachtenberg, F Schmid, and E Schüle. "Determination of the recombination correction factor k_s for some specific plane-parallel and cylindrical ionization chambers in pulsed photon and electron beams." *Phys Med Biol*, 2007: N35-N50.
- Buchner, Norbert. *Verpackung von Lebensmitteln*. Berlin Heidelberg: Springer, 1999.
- Burns, D T, and M R McEwen. "Ion recombination corrections for the NACP parallel-plate chamber in a pulsed electron beam." *Phys Med Biol*, 1998: 2033-2045.
- Buryakov, I A. "Determination of kinetic transport coefficients for ions in air as function of electric field and temperature." *Tech Phys*, 2004: 967-972.
- Butz, Tilman. "Das Sampling-Theorem." In *Fouriertransformation für Fußgänger*, 109-110. Wiesbaden: Vieweg+Teubner, 2009.
- Chaney, E L, T J Cullip, and T A Gabriel. "A Monte Carlo study of accelerator head scatter." *MedPhys*, 1994: 1383-1390.
- Chang, J, et al. "A method for online verification of adapted fields using an independent dose monitor." *Med. Phys.*, 2013: 072104-1 - 072104-8.

- Chapman, A. *Dosimetric verification of intensity modulated radiation therapy*. Master thesis, Wollongong: University of Wollongong, 2005.
- Charpak, G, R Bouclier, T Bressati, J Favier, and C Zupancic. "The use of multiwire proportional counters to select and localize charged particles." *Nucl Instr Meth*, 1968: 262-268.
- Choppin, G, J-O Liljenzin, and J Rydberg. "1-CH07NY3.pdf." *JOL*. 2002. <http://jol.liljenzin.se/KAPITEL/CH07NY3.PDF> [accessed March 03, 2014].
- Christo, S. *note89-013.pdf*. 21 September 1989. http://www.jlab.org/Hall-B/notes/clas_notes89/note89-013.pdf [accessed May 12, 2011].
- Di Martino, F, M Gianelli, C Traino, and M Lazzen. "Ion recombination correction for very high dose-per-pulse high-energy electron beams." *Med Phys*, 2005: 2204-2210.
- DIN 6800-2. *Dosismessverfahren nach der Sondenmethode für Photonen- und Elektronenstrahlung – Teil 2: Dosimetrie hochenergetischer Photonen- und Elektronenstrahlung mit Ionisationskammern*. Standard, Normenausschuss Radiologie (NAR) im DIN, 2008.
- Dinter, H, and K Tesch. "Calculation of the current of an ionization chamber exposed to a pulsed electromagnetic radiation field and comparison with measurements." *Nucl Instr Meth*, 1974: 113-119.
- Domininghaus, Hans. *Die Kunststoffe und ihre Eigenschaften*. 5th ed. Berlin Heidelberg: Springer, 1998.
- dos Santos, J M F, J F C A Veloso, and C M B Monteiro. "Permeability measurements in undergraduate vacuum laboratories: a simple experiment using a He leak detector." *Eur J Phys*, 2004: L1-L3.
- Dotan, I, D L Albritton, W Lindinger, and M Pahl. "Mobilities of CO₂⁺, N₂H⁺, H₃O⁺, H₃O⁺ H₂O and H₃O⁺ (H₂O)₂ ions in N₂." *J Chem Phys*, 1976: 5028-5030.
- Duncombe, P B, and J M Nieminen. "On the field-size dependence of relative output from a linear accelerator." *Med Phys*, 1992: 1441-1444.
- Duzenli, C, B McClean, and C Field. "Backscatter into the beam monitor chamber: Implications for dosimetry of asymmetric collimators." *Med Phys*, 1993: 363-367.
- Eberle, K, J Engler, G Hartmann, R Hofmann, and J R Hörandel. "First tests of a liquid ionization chamber to monitor intensity modulated radiation beams." *Phys Med Biol*, 2003: 3555-3564.
- Eenboom, F. ÜberwachungsVorrichtung und Verfahren zur Überwachung eines insbesondere medizinischen Bestrahlungsfeldes und Bestrahlungsvorrichtung mit einer solchen ÜberwachungsVorrichtung. Germany Patent DE 10 2011 077 978 A1. 27. 12 2012.
- Ensinger. "Ensinger-Handbuch_01.pdf." *Technische Kunststoffe und Hochleistungskunststoffe*. October 2012. http://www.ensinger-online.com/uploads/media/Ensinger-Handbuch_01.pdf [accessed March 03, 2014].
- Faddegon, Bruce. *Siemens Proposed Radiosurgery Beamline*. Siemens internal report, 2005.
- Fischer, H W, B E Tabot, and B Poppe. "Activation processes in a medical linear accelerator and spatial distribution of activation products." *Phys Med Biol*, 2006: N461-N466.
- Fischer, H, and K Peick. "Fischer_FS2003.pdf." *Radioactivity Measurements Laboratory*. 2003. www.radioaktivitaet.uni-bremen.de/downloads/Fischer_FS2003.pdf [accessed May 11, 2010].
- Fu, W, J Dai, D Han, and Y Song. "Delivery time comparison for intensity-modulated radiation therapy with/without flattening filter: a planning study." *Phys med Biol*, 2004: 1535-1547.
- Galbraith, D M, E S Martell, T Fueurstake, B Norrlinger, H Schwendener, and J A Rawlinson. "A dose-per-pulse monitor for a dual-mode medical accelerator." *Med Phys*, 1990: 470-473.

- Goodfellow. *Gold - Properties and Uses - Supplier Data by Goodfellow*. 05 May 2003. <http://www.azom.com/article.aspx?ArticleID=1965> [accessed May 12, 2011].
- Hackam, R. "Mobility and diffusion cross section of atomic xenon ion in xenon." *J Phys B (Atom Molec Phys)*, 1969: 790-797.
- Haryanto, F. *Monte-Carlo-Simulation des Strahlungstransports im Strahlerkopf eines Elektronenlinearbeschleunigers*. Dissertation, Tübingen: University of Tübingen, 2003.
- Havercroft, J M, and S C Klevenhagen. "Ion recombination corrections for plane-parallel and thimble chambers in electron and photon radiation." *Phys Med Biol*, 1993: 25-38.
- Hearty, C. "BABAR drift chamber wire tension." *BABAR Note 301 - TNDC-96-43*. 16 May 1996.
- Helm, H, and M T Eford. "The mobility of Ar⁺ ions in argon and the effect of spin-orbit coupling." *J Phys B: At Mol Phys*, 1977: 3849-3851.
- Hochhäuser, E, and O A Balk. "The influence of unattached electrons on the collection efficiency of ionisation chambers for the measurement of radiation pulses of high dose rate." *Phys Med Biol*, 1986: 223-233.
- Hofmann, R. „Ein System zur Online-Qualitätssicherung in der Strahlentherapie.“ Dissertation, Heidelberg, 2003.
- Hoppe, A. *Elemente im Periodensystem der Elemente*. 16 March 2011. <http://www.periodensystem.info/elemente> [accessed May 12, 2011].
- Hounsell, A R. "Monitor chamber backscatter for intensity modulated radiation therapy using multileaf collimators." *Phys Med Biol*, 1998: 445-454.
- Huang, P H, J Chu, and E Bjärngard. "The effect of collimator backscatter radiation on photon output of linear accelerators." *Med Phys*, 1987: 268–269.
- IAEA. *International Atomic Energy Agency (IAEA)*. n.d. <http://www-nds.iaea.org/photonuclear> [accessed May 11, 2010].
- IEC 60601-1. *IEC 60601-1: Medical electrical equipment – Part 1: General requirements for basic safety and essential performance*. International Standard, Geneva: International Electrotechnical Commission, 2000.
- IEC 60601-1-2. *IEC 60601-1-2: Medical electrical equipment – Part 1-2: General requirements for basic safety and essential performance – Collateral standard: Electromagnetic compatibility – Requirements and tests*. International Standard, Geneva: International Electrotechnical Commission, 2007.
- IEC 60601-2-1. *IEC 60601-2-1: Medical electrical equipment - Part 2-1: Particular requirements for the safety of electron accelerators in the range of 1 MeV to 50 MeV*. International Standard, Geneva: International Electrotechnical Commission, 1998.
- IEC 60976. *IEC 60976: Medical electrical equipment - Medical electron accelerators - Functional performance characteristics*. International Standard, Geneva: International Electrotechnical Commission, 2007.
- IEC 60977. *IEC/TR 60977: Medical electrical equipment - Medical electron accelerators - Guidelines for functional performance characteristics*. International Standard, Geneva: International Electrotechnical Commission, 2008.
- Inox, Euro. *Tables_TechnicalProperties_EN.pdf*. 02 May 2007. http://www.euro-inox.org/pdf/map/Tables_TechnicalProperties_EN.pdf [accessed May 12, 2011].
- Islam, M K, et al. „An integral quality monitoring system for real-time verification of intensity modulated radiation therapy.“ *Med. Phys.*, 2009: 5420-5428.
- Johns, H E, und J R Cunningham. *The Physics of Radiology*. Springfield, IL: Thomas, 1974.
- Kairn, T, S B Crowe, C M Poole, and A L Fielding. "Effects of collimator backscatter in an Elekta linac by Monte Carlos simulation." *Australas Phys Eng Sci Med*, 2009: 129-135.

- Keller, G E, D W Martin, and E W McDaniel. "General considerations concerning apparent mobilities in mixed ion populations: drift velocities of mass-identified N⁺, N²⁺, N³⁺, and N⁴⁺ ions in nitrogen." *Phys Rev*, 1965: A1535--A1546.
- Knoll, G. *Radiation detection and measurement*. 3rd ed. New York: John Wiley & Sons, Inc., 2000.
- Kolanoski, Hermann. "gasdet01.ps.gz." *DESY*. 24 May 2004. www-zeuthen.desy.de/~kolanosk/det04/skripte/gasdet01.ps.gz [accessed November 09, 2009].
- Krieger, H. *Strahlungsquellen für Technik und Medizin*. Wiesbaden: B. G. Teubner, 2005.
- Kubo, H. "Telescopic measurements of backscattered radiation from secondary collimator jaws to a beam monitor chamber using a pair of slits." *Med Phys*, 1989: 295-298.
- Kubo, H, and K K Lo. "Measurement of backscattered radiation from Therac-20 collimator and trimmer jaws into beam monitor chamber." *Med Phys*, 1989: 292-294.
- Lam, K L, M S Muthuswamy, and R K Ten Haken. "Measurement of backscatter to the monitor chamber of medical accelerators using target charge." *Med Phys*, 1998: 334-338.
- . "Flattening-filter based empirical methods to parametrize the head scatter factor." *MedPhys*, 1996: 343-352.
- Liu, H H, T R Mackie, and E C McCullough. "Calculating output factors for photon beam radiotherapy using a convolution/superposition method based on a dual source photon beam model." *Med Phys*, 1997: 1975-1985.
- . "Modelling photon output caused by backscattered radiation in the monitor chamber from collimator jaws using a Monte Carlo technique." *Med Phys*, 2000: 737-744.
- Loi, G, et al. "Neutron production from a mobile linear accelerator operating in electron mode for intraoperative radiation therapy." *Phys Med Biol*, 2006: 695-702.
- Looe, H K, D Harder, A Rühmann, K C Willborn, and B Poppe. "Enhanced accuracy of the permanent surveillance of IMRT deliveries by iterative deconvolution of DAVID chamber signal profiles." *Phys Med Biol*, 2010: 3981-3992.
- Looe, H K, T S Stelljes, S Foschepoth, D Harder, K Willborn, and B Poppe. "The dose response functions of ionization chambers in photon dosimetry - Gaussian or non-Gaussian?" *Z Med Phys*, 2013: 129-143.
- Los Alamos National Laboratory. *NIS/photonuclear*. 08 April 2008. <http://t2.lanl.gov/data/photonuclear.html> [accessed May 12, 2010].
- Luxton, G, and M A Astrahan. "Output factor constituents of high energy photon beam." *Med Phys*, 1988: 88-91.
- Madson, J M, and H J Oskam. "Mobility of argon ions in argon." *Phys Lett A*, 1967: 407-408.
- Markert, J. *Untersuchung zum Ansprechverhalten der Vieldraht-Driftkammern niedriger Massenbelegung des HADES Experimentes*. Dissertation, Frankfurt: Universität Frankfurt, 2005.
- Massey, L K. *Permeability properties of plastics and elastomers: a guide to packaging and barrier materials*. 2nd ed. Norwich, NY, USA: William Andrew, 2003.
- McGinnis, R. *Rad Pro Calculator: Free Online X-Ray, Dose-Rate and Shielding Calculator*. 24 May 2009. www.radprocalculator.com/XRay.aspx [accessed July 10, 2009].
- McIntyre, R D. Transmission ion chamber. United States Patent 3,852,910. 03 December 1974.
- McIntyre, R D, und S W Johnson. In-line electron beam energy monitor and control. United States Patent 0 366 330 A1. 02. May 1990.
- Mohan, R, C Chui, and L Lidofsky. "Energy and angular distribution of photons from medical linear accelerators." *Med Phys*, 1985: 592-597.
- Moseley, J T, P C Cosby, and J R Peterson. "Mobilities and reactions of negative ions in CO₂ gas." *J Chem Phys*, 1976: 4228-4229.

- Moseley, J T, R M Snuggs, D W Martin, and E W McDaniel. "Mobilities, diffusion coefficients, and reaction rates of mass-identified nitrogen ions in nitrogen." *Phys Rev*, 1969: 240-248.
- Muralidhar, K R, P N Murthy, N V M Sresty, P K Dixit, R Kumar, and A K Raju. "Measurement of back-scattered radiation from micro multileaf collimator into beam monitor chamber from dual energy linear accelerator." *J Med Phys*, 2007: 65-67.
- Naeem, S F. "syed_hw12.pdf." *Idaho State University*. 18 December 2006. http://www2.cose.isu.edu/~tforest/Classes/NucSim/Day11/syed_hw12.pdf [accessed December 2007, 10].
- National Instruments. "NI_Datasheet-ds-190.pdf." 04 June 2010. <http://sine.ni.com/ds/app/doc/p/id/ds-190/lang/de> [accessed July 01, 2010].
- NIST. *NIST Physical Reference Data*. 15 July 2009. <http://www.nist.gov/pml/data/index.cfm> [accessed September 05, 2009].
- O'Kelly, G D. *Detection and Measurement of Nuclear Radiation*. Subcommittee on Radiochemistry, National Academy of Sciences-National Research Council, 1962.
- Olofsson, J, D Georg, and M Karlsson. "A widely tested model for head scatter influence on photon beam output." *Radiother Oncol*, 2003: 225-238.
- Ott, R J. "Wire chambers revisited." *Eur J Nucl Med*, 1993: 348-358.
- Pardo, J, et al. "Development and operation of a pixel segmented liquid-filled linear array for radiotherapy quality assurance." *Phys Med Biol*, 2005: 1703-1716.
- Patterson, M S, and P C Shragge. "Characteristics of an 18 MV photon beam from a Therac 20 Medical Linear Accelerator." *Med Phys*, 1981: 312-318.
- personal communication: HBS (Rudolstadt). [2008].
- Pettifer, R F, M Borowski, and P W Loeffen. "The physics of ionization chambers - or how to improve your signal-to-noise ratio for transmission EXAFS measurements." *J Synchrotron Rad*, 1999: 217-219.
- Piermattei, A, et al. "The saturation loss for plane parallel ionization chambers at high dose per pulse values." *Phys Med Biol*, 2000: 1869-1883.
- Pierson, H O. *Handbook of carbon, graphite, diamond, and fullerenes: properties, processing, and applications*. Park Ridge, NJ, USA: Noyes Publication, 1993.
- Podgorsak, E B, and G H Hartman. "Slides to Radiation Oncology handbook - IAEA NAHU." *Nuclear Sciences and Applications - IAEA*. August 2007. <http://www-naweb.iaea.org/nahu/DMRP/slides.html> [accessed January 08, 2008].
- Poppe, B, et al. "DAVID - a translucent multi-wire transmission ionization chamber for in vivo verification of IMRT and conformal irradiation techniques." *Phys Med Biol*, 2006: 1237-1248.
- Ravikumar, M, and R Ravichandran. "Measurement of backscattered radiation from secondary collimator jaws into the beam monitor chamber from a dual energy linear accelerator." *Strahlenther Onkol*, 2001: 670-675.
- Reich, H. *Dosimetrie ionisierende Strahlung*. Stuttgart: B. G. Teubner, 1990.
- Rhenium Alloys Inc. *rhenium alloys, moly-rhenium alloys, tungsten alloys, copper alloy, fabricated products, fabricated componenets, molybdenum, chemical powders*:. 2011. http://rhenium.com/properties.asp?menu_id=4&pic_id=1 [accessed May 27, 2011].
- Roos, M, and K Derikum. "The recombination correction and the dependence of the response of plane parallel chambers on the polarizing voltage in pulsed electron and photon beams." In *IAEA-TECDOC-1173*, 53-64. Vienna: International Atomic Energy Agency, 2000.
- Sanz, D E, G D Alvarez, and F E Nelli. "Ecliptic method for the determination of backscatter into the beam monitor chambers in photon beams of medical accelerators." *Phys. Med. Biol.*, 2007: 1647-1658.
- Saporoschenko, M. „Mobility of Mass-Analyzed N+, N2+, N3+ and N4+ Ions in Nitrogen Gas." *Phys Rev*, 1965: A352-A356.
- Sauli, F. *Principles of operation of multiwire proportional and drift chambers*. Lecture notes, Geneva: CERN, 1977.

- Schirmer, R. *Aufbau und Test eines Funktionsmusters einer Ionisationskammer für den Einsatz in einem Dosisüberwachungssystem*. Diploma thesis, FH Schmalkalden, Schmalkalden: University of Applied Sciences Schmalkalden, 2010.
- Science at home. *Molybdän - Wiki*. 11 March 2011. <http://www.science-at-home.de/wiki/index.php/Molybdän> [accessed May 12, 2011].
- Scientists, The Society for Amateur. *Engineering Material Properties*. 2004. <http://www.sas.org/engineerByMaterial.html> [Zugriff am 12. 05 2011].
- Seilnacht, Thomas. *Elektrische Leitfähigkeit von Metallen*. 08 March 2011. <http://www.seilnacht.com/Lexikon/leitf.htm> [accessed May 12, 2011].
- Sharma, A. „Properties of some gas mixtures used in tracking detectors.“ *SLAC-J-ICFA-16-3*, 1998.
- Sharpe, M B, D A Jaffray, J J Battista, and P Munro. “Extrafocal radiation: A unified approach to the prediction of beam penumbra and output factors for megavoltage x-ray beams.” *Med Phys*, 1995: 2065-2074.
- Sheikh-Bagheri, D, and D W O Rogers. “Monte Carlo calculation of nine megavoltage photon beam spectra using the BEAM code.” *Med Phys*, 2002: 391-402.
- Sixel, K E, and B A Faddegon. “Calculation of x-ray spectra for radiosurgical beams.” *Med Phys*, 1995: 1657-1661.
- Sjörger, R, M G Karlsson, and M Karlsson. “Methods for the determination of effective monitor chamber thickness.” *Med Phys*, 1999: 1871-1873.
- Taumann, L. Dose monitor chamber for electron or x-ray radiation. United States Patent 4,427,890. 24 January 1984.
- Texas Instruments. „ivc102.pdf.“ *Analog, Embedded Processing, Semiconductor Company, Texas Instruments - TI.com*. 27. September 2000. <http://www.ti.com/lit/ds/symlink/ivc102.pdf> [Zugriff am 14. August 2009].
- The Engineering Toolbox. *Elastic Properties and Young Modulus for some Materials*. 28 February 2011. http://www.engineeringtoolbox.com/young-modulus-d_417.html [accessed May 12, 2011].
- Thomas, M D R, and J R N Symonds-Taylor. “Characterization of a transmission ionization beam-imager for radiotherapy verification.” *Phys Med Biol*, 2003: 2633-2644.
- Tilly, N, et al. “Development and verification of the pulsed scanned proton beam at The Svedberg Laboratory Uppsala.” *Phys Med Biol*, 2007: 2741-2754.
- Titov, M, M Hohlmann, C Padilla, and N Tesch. “Summary and outlook of the international workshop on aging phenomena in gaseous detectors.” *IEEE Transactions on Nuclear Science*, 2002: 1609-1621.
- Titt, U, O N Vassiliev, F Pönisch, S F Kry, and R Mo. “Monte Carlo study of backscatter in a flattening filter free clinical accelerator.” *Med Phys*, 2006: 3270-3273.
- Titt, U, O N Vassiliev, F Pönisch, L Dong, H Liu, and R Mohan. “A flattening filter free photon treatment concept evaluation with Monte Carlo.” *Med Phys*, 2006: 1595-1602.
- Townsend, J. *Electrons in gases*. London: Hutchinson, 1947.
- van Herk, M. “Physical aspects of liquid-filled ionization chamber with pulsed polarizing voltage.” *Med Phys*, 1991: 692-702.
- Varney, R N. “Drift velocities of ions in krypton and xenon.” *Phys Rev*, 1952: 362-364.
- Vassiliev, O N, U Titt, S F Kry, F Pönisch, M T Gillin, und R Mohan. „Monte Carlo study of photon fields from a flattening filter free clinical accelerator.“ *Med Phys*, 2006: 820–827.
- Veenhof, R. *Simulation of gaseous detectors*. 01 September 1984. <http://garfield.web.cern.ch/garfield/>.
- Verhaegen, F, and I J Das. “Monte Carlo modelling of a virtual wedge.” *Phys Med Biol*, 1999: N251–N259.
- Verhaegen, F, R Symonds-Taylor, H H Liu, and A E Nahum. “Backscatter towards the monitor ion chamber in high-energy photon and electron beams: charge integration versus Monte Carlo simulation.” *Phys Med Biol*, 2000: 3159-3170.

- Watts, D L, and G S Ibbott. "Measurement of beam current and evaluation of scatter production in an 18-MeV accelerator." *Med Phys*, 1987: 662-664.
- Wickman, G, and H Nyström. "The use of liquids in ionization chambers for high precision radiotherapy dosimetry." *Phys Med Biol*, 1992: 1789-1812.
- Wikipedia. *Thermal expansion - Wikipedia*. 13 May 2011. http://en.wikipedia.org/wiki/Thermal_expansion#Thermal_expansion_coefficients_for_various_materials [accessed May 16, 2011].
- Yi Yao, J. Ionization chamber having off-passageway measuring electrodes. United States Patent 5,672,878. 30 September 1997.
- Yu, M K, R S Sloboda, and F Mansour. "Measurement of photon beam backscatter from collimators to the beam monitor chamber using target-current-pulse-counting and telescope techniques." *Phys Med Biol*, 1996: 1107-1117.
- Zhu, T C, B E Bjärngard, Y Xiao, and C J Yang. "Modeling the output ratio in air for megavoltage photon beams." *Med Phys*, 2001: 925-937.
- Zhu, T C, et al. "Report of AAPM Therapy Physics Committee Task Group 74: In-air output ratio, S_c , for megavoltage photon beams." *Med. Phys.*, 2009: 5261-5291.
- Zhu, X R, Y Kang, and M T Gillin. "Measurement of in-air output ratios for a linear accelerator with and without the flattening filter." *Med Phys*, 2006: 3723-3733.

Erklärungen

Hiermit versichere ich, dass ich die vorliegende Arbeit selbständig verfasst und nur die angegebenen Hilfsmittel benutzt habe.

Erlangen, Dezember 2014

Alle in dieser Dissertation verwendeten Firmen- und/oder Produktnamen sind Warenzeichen und/oder eingetragene Warenzeichen ihrer jeweiligen Hersteller in ihren Märkten und/oder Ländern.

Curriculum Vitae

Personal data

Name	Frauke Eenboom
Date of birth	17 th September 1981, Eutin (Plön)
Nationality	German
Address	Hofmannstr. 11g, 91052 Erlangen

Schooling

09/1988 – 07/1992	Grundschule an der Ammer, Weilheim (Oberbay)
09/1992 – 07/2001	Gymnasium Weilheim, Weilheim (Oberbay), Abitur

University

10/2001 – 07/2004	University of Oldenburg Bachelor of Engineering in Engineering Physics (BEng)
09/2003 – 02/2004	University of Nottingham Biomedical and economic courses
10/2004 – 05/2007	University of Oldenburg Master of Science in Engineering Physics (M.Sc.)

Professional activity

09/2005 – 01/2007	Intern at Department for Radiotherapy, Pius Hospital, Oldenburg
07/2007 – 11/2010	Doctoral researcher at Siemens AG, Rudolstadt
02/2011 – 12/2011	Siemens AG, Erlangen/Forchheim, R&D Radiotherapy
01/2012 – 04/2015	Siemens AG, Forchheim, R&D Computed Tomography
05/2015 – today	Siemens Healthcare GmbH, Forchheim, R&D Computed Tomography